

Waves and turbulence on wavy coastal seabeds
inducing vertical scalar transport

Dissertation

zur

Erlangung des akademischen Grades

Doktor-Ingenieur (Dr.-Ing.)

der Fakultät für Maschinenbau und Schiffstechnik
der Universität Rostock

vorgelegt von

Nils Karow, geb. am 02.04.1990 in Rostock

aus Rostock

Rostock, 07.03.2019

Gutachter:

Prof. Dr.-Ing, habil. Sven Grundmann, Universität Rostock, Fakultät für Maschinenbau und Schiffstechnik, Lehrstuhl Strömungsmechanik

Prof. Dr. Inna Sokolova, Universität Rostock, Mathematisch-Naturwissenschaftliche Fakultät, Lehrstuhl Meeresbiologie

Jahr der Einreichung: 2019

Jahr der Verteidigung: 2019

Acknowledgements

Firstly, I would like to express my sincere gratitude to my advisor Dr. M. Brede for the continuous support of my Ph.D study and related research. He always helped me with his extra ordinary commitment, motivation and immense knowledge. His guidance helped me in all the time of research and writing of this thesis.

Besides my advisor, I would like to thank Prof. S. Grundmann for his advises and knowledge. He always had an ear for questions and problems. My sincere thanks also goes to Dr. S. Forster who always tried to help me in interdisciplinary contexts.

I would like to thank Dr. A. Wolter, J. Wenzlaff, U. Grebin and A. Fretwurst who gave access to the laboratory and research facilities and who supported me with technical equipment, assembling of setups and their technical knowledge. Without their precious support it would not be possible to conduct this research.

A very special gratitude goes to H. Schade for the intensive cooperation with the wave measurement device and the measurement of the porous medias. I also want to thank X. Lange for the intense discussions, his intense knowledge and great conferences together. Special thank also to R. Strehse who helped me with the tracer solution and his commitment. I would like to pay special thankfulness to all members of the Baltic Transcoast graduate school for their great expertise and the opportunity of interdisciplinary research.

A very special thanks goes out to the German Research Foundation for helping and providing the project in the graduate school of Baltic Transcoast.

I would like to show my greatest appreciation to my students, T. Bestier, J. Groß and L. Kandler for their support, nice discussions and help with the experiments.

Last but not the least, I would like to thank my family: my mother Grit and my wife Josi, who were always there when I needed someone to talk to and the rest of my family for supporting me spiritually throughout writing this thesis and my life in general. I also want to thank my friends who supported me and had fun with me during the last three years.

Abstract

In the project *waves and turbulence on wavy coastal seabeds inducing vertical scalar transport* as part of the graduate school Baltic Transcoast, the mixing and transport mechanism of submarine groundwater discharge into a water column of a Baltic Sea model is investigated. The experiments are conducted in the water channel of the chair of fluid mechanics at the University of Rostock. An adjustable artificial seabed is placed in the channel. Furthermore, a wave generator will generate different intermediate water waves for the experiments. Rhodamine 6G is pumped through the artificial seabed as a model for the submarine groundwater discharge. In the measurements, the velocity field is captured with the Particle Image Velocimetry (PIV). Simultaneously the concentration field of the Rhodamine 6G inflow is captured with the Laser Induced Fluorescence technique (LIF). In the experiments, the slope angle, the artificial seabed and the waves are varied.

The transport and mixing behavior of the submarine groundwater discharge is described with the Reynolds-flux model and the mixing length model. Furthermore, the mixing length model delivers parameters which may be used for numerical simulations of a Baltic Sea model.

Contents

Acknowledgements	I
Abstract	II
Contents.....	III
List of figures	VI
List of tables	X
List of symbols	XI
1 Introduction	- 1 -
1.1 Objective	- 2 -
1.2 State of research	- 3 -
2 Physical background	- 5 -
2.1 Laser optical measurement techniques.....	- 5 -
2.1.1 Particle image velocimetry (PIV).....	- 5 -
2.1.2 Laser induced fluorescence (LIF).....	- 7 -
2.1.3 Combination of PIV and LIF.....	- 9 -
2.2 Submarine Groundwater Discharge (SGD).....	- 10 -
2.3 Ground properties.....	- 12 -
2.3.1 Porosity.....	- 12 -
2.3.2 Darcy's law.....	- 14 -
2.3.3 Permeability.....	- 14 -
2.4 Wave theory	- 16 -
2.4.1 General specification of mechanical waves.....	- 16 -
2.4.2 Ocean waves.....	- 18 -
2.4.3 Potential function as a basis for wave theories.....	- 21 -
2.4.4 AIRY theory	- 23 -
2.4.5 Stokes theory	- 25 -
2.5 Turbulence.....	- 27 -
2.5.1 Averaging and fluctuation values.....	- 27 -
2.5.2 Reynolds-averaged Navier-Stokes equation (RANS)	- 28 -

2.5.3	Mixing length model	- 29 -
2.5.4	Reynolds-flux model	- 30 -
2.6	Mixing and transport mechanisms.....	- 34 -
2.6.1	Transport mechanism	- 34 -
2.6.2	Mixing mechanisms.....	- 36 -
2.7	Oceanic Boundary Layer.....	- 37 -
2.7.1	The benthic boundary layer	- 37 -
2.7.2	Boundary layer above a permeable medium	- 38 -
2.7.3	Oscillating bottom boundary layer	- 39 -
2.7.4	Influence of the shape of the ground	- 40 -
3	Experimental setup.....	- 42 -
3.1	Water channel.....	- 42 -
3.2	Wave channel elements	- 43 -
3.2.1	Wave generator.....	- 43 -
3.2.2	Wave absorber	- 44 -
3.2.3	Control and triggering devices	- 45 -
3.2.4	Tracer pump system	- 45 -
3.3	Channel floor concept	- 47 -
3.3.1	Overview and requirements.....	- 47 -
3.3.2	Porous Media Application Basin (PMAB).....	- 50 -
3.4	Artificial seabed	- 54 -
3.5	Measurement concept.....	- 56 -
4	Methods.....	- 58 -
4.1	Wave dataset analysis.....	- 58 -
4.2	Main measurement procedures.....	- 63 -
4.3	Data analysis concepts.....	- 65 -
4.3.1	Image settings via Dynamic Studio	- 65 -
4.3.2	Diffusion analysis in Matlab	- 67 -
4.3.3	Turbulence analysis in Matlab.....	- 69 -
5	Results.....	- 73 -

5.1	Analysis of the concentration development.....	- 73 -
5.2	Reynolds-flux development and dependencies	- 80 -
5.3	Mixing length models.....	- 86 -
5.3.1	Concentration gradients.....	- 86 -
5.3.2	Velocity fields	- 88 -
5.3.3	Velocity gradients.....	- 90 -
5.3.4	Mixing length	- 91 -
5.4	Phase specific Reynolds-Fluxes and Mixing length.....	- 94 -
5.4.1	Phase specific Reynolds-fluxes	- 94 -
5.4.2	Phase specific mixing length	- 98 -
5.5	Bottom friction and turbulence.....	- 100 -
5.5.1	Bottom Friction factor	- 100 -
5.5.2	Turbulent Kinetic Energy (TKE).....	- 102 -
6	Discussion	- 105 -
6.1	Concentration boundary development.....	- 105 -
6.2	Reynolds-flux development.....	- 107 -
6.3	Mixing length quantities for the scalar transport.....	- 110 -
6.4	Phase specific Reynolds-fluxes and mixing length	- 111 -
6.5	Bottom friction and turbulence.....	- 113 -
7	Summary and future research	- 114 -
	References	XV
	Appendix	XXII
	Appendix A: List of LIF-Calibration steps	XXII
	Appendix B: Frequency analysis.....	XXIII
	Appendix C: Reynolds-flux diffusions.....	XXIX
	Appendix D: Concentration maps	XXXII
	Appendix E: LDA results	XXXV
	Appendix F: Phase specific TKE	XXXVII

List of figures

Figure 2-1: General PIV setup.....	- 6 -
Figure 2-2: Emission states [Menzel 2010].....	- 8 -
Figure 2-3: Combined PIV-PLIF setup	- 9 -
Figure 2-4: Categorization of submarine groundwater discharge following [Robinson et al. 2007] ..	- 11 -
Figure 2-5: Overview of the pore volume of different materials after [Spektrum 2000]	- 12 -
Figure 2-6: General exposure of a plain harmonic wave.....	- 16 -
Figure 2-7: Orbital path.....	- 18 -
Figure 2-8: Categorization of ocean waves	- 19 -
Figure 2-9: Wave shape comparison [Le Méhauté 1976]	- 25 -
Figure 2-10: Reynolds-flux model	- 31 -
Figure 2-11: Reynolds-flux model with additional inflow condition.....	- 32 -
Figure 2-12: Benthic boundary layer.....	- 37 -
Figure 2-13: Boundary layer above a permeable bed.....	- 38 -
Figure 2-14: Comparison of wave and tide induced velocity profiles	- 39 -
Figure 2-15: Symmetric orbital ripples	- 40 -
Figure 3-1: Water channel.....	- 42 -
Figure 3-2: Wave generator.....	- 43 -
Figure 3-3: Wave absorber	- 44 -
Figure 3-4: Overview of the tracer pump configuration.....	- 45 -
Figure 3-5: Old floor of the water channel.....	- 47 -
Figure 3-6: Subassemblies of the new floor structure	- 49 -
Figure 3-7: CAD model of the PMAB; side view	- 50 -
Figure 3-8: Reservoir plate.....	- 51 -
Figure 3-9: Volume-reducing concepts	- 52 -
Figure 3-10: Detailed view of the AAB	- 53 -
Figure 3-11: Constant head method	- 54 -
Figure 3-12: Measurement setup.....	- 56 -
Figure 4-1: Position of the acoustic wave and current profiler	- 58 -
Figure 4-2: Geometrical dimensions of the AWAC.....	- 59 -
Figure 4-3: Histogram of the orbital velocity	- 61 -
Figure 4-4: Overview of the measurements	- 63 -
Figure 4-5: Program flow chart.....	- 67 -
Figure 4-6: Phase angle decomposition [Kandler 2018]	- 70 -
Figure 4-7: Realignment of image matrices	- 72 -
Figure 5-1: Comparison of mean spread behavior	- 73 -

Figure 5-2: Amplitude spectrum of measurement with 10PPI and mean wave scenario, 50% boundary line	- 74 -
Figure 5-3: Low pass filtered signal of measurement with 10PPI and mean wave scenario at frequency 0.02Hz	- 75 -
Figure 5-4: Low pass filtered signal of measurement with 10PPI and mean wave scenario at frequency 0.001Hz	- 76 -
Figure 5-5: Comparison of diffusion during different wave events for measurements with 10PPI and 0° slope angle	- 77 -
Figure 5-6: Comparison of the diffusion analysis for the 10% line	- 78 -
Figure 5-7: Mean phase averaged Reynolds-flux of 10PPI mean 0°	- 80 -
Figure 5-8: Scatter plot of centers for Reynolds-flux hotspots	- 81 -
Figure 5-9: Comparison of the integral Reynolds-flux mass and the mean boundary area	- 82 -
Figure 5-10: comparison of averaged Reynolds-fluxes for the 10PPI measurements	- 84 -
Figure 5-11: Scatter plot of the averaged Reynolds-fluxes of 10PPI and the boundary growth rate	- 85 -
Figure 5-12: Concentration gradients for different wave scenarios of the 10PPI medium	- 86 -
Figure 5-13: Comparison of the phase averaged velocity fields from [Kandler 2018]	- 88 -
Figure 5-14: Velocity gradients for the mean wave scenario	- 90 -
Figure 5-15: Comparison of the Mixing length	- 91 -
Figure 5-16: Scatter plot of the boundary growth rate over the mixing length	- 93 -
Figure 5-17: Phase averaged Reynolds-flux maps	- 95 -
Figure 5-18: Polar diagram of averaged phase specific Reynolds-fluxes	- 96 -
Figure 5-19: Polar diagram of mean wave scenario for 10PPI under different slope angles	- 97 -
Figure 5-20: Phase specific mixing lengths for measurement 10PPI, 0° slope angle and mean wave scenario	- 98 -
Figure 5-21: Median of phase specific mixing lengths for all measurements	- 99 -
Figure 5-22: Wave friction over bottom stress	- 100 -
Figure 5-23: Wave friction over Reynolds-flux	- 101 -
Figure 5-24: Reynolds-stress over turbulent kinetic energy	- 102 -
Figure 5-25: Phase specific TKE	- 103 -
Figure 5-26: Phase specific TKE of 0° slope angle measurements	- 104 -
Figure 7-1: frequency analysis measurement 10PPI, 0° slope	XXIII
Figure 7-2: frequency analysis measurement 10PPI, 3° slope	XXIII
Figure 7-3: frequency analysis measurement 10PPI, 7° slope	XXIII
Figure 7-4: frequency analysis measurement 10PPI, 14° slope	XXIII
Figure 7-5: frequency analysis measurement 45PPI, 0° slope	XXIV
Figure 7-6: frequency analysis measurement 45PPI, 3° slope	XXIV
Figure 7-7: frequency analysis measurement 45PPI, 7° slope	XXIV

Figure 7-8: frequency analysis measurement 45PPI, 14° slope	XXIV
Figure 7-9: frequency analysis measurement 10PPI, 0° slope	XXV
Figure 7-10: frequency analysis measurement 10PPI, 3° slope	XXV
Figure 7-11: frequency analysis measurement 10PPI, 7° slope	XXV
Figure 7-12: frequency analysis measurement 10PPI, 14° slope	XXV
Figure 7-13: frequency analysis measurement 45PPI, 0° slope	XXVI
Figure 7-14: frequency analysis measurement 45PPI, 3° slope	XXVI
Figure 7-15: frequency analysis measurement 45PPI, 7° slope	XXVI
Figure 7-16: frequency analysis measurement 45PPI, 14° slope	XXVI
Figure 7-17: frequency analysis measurement 10PPI, 0° slope	XXVII
Figure 7-18: frequency analysis measurement 10PPI, 3° slope	XXVII
Figure 7-19: frequency analysis measurement 10PPI, 7° slope	XXVII
Figure 7-20: frequency analysis measurement 10PPI, 14° slope	XXVII
Figure 7-21: frequency analysis measurement 45PPI, 0° slope	XXVIII
Figure 7-22: frequency analysis measurement 45PPI, 3° slope	XXVIII
Figure 7-23: frequency analysis measurement 45PPI, 7° slope	XXVIII
Figure 7-24: frequency analysis measurement 45PPI, 14° slope	XXVIII
Figure 7-25: Reynolds-flux diffusion for the calm scenarios and the 10PPI porous media.....	XXIX
Figure 7-26: Reynolds-flux diffusion for the mean scenarios and the 10PPI porous media.....	XXIX
Figure 7-27: Reynolds-flux diffusion for the stormy scenarios and the 10PPI porous media.....	XXX
Figure 7-28: Reynolds-flux diffusion for the calm scenarios and the 45PPI porous media.....	XXX
Figure 7-29: Reynolds-flux diffusion for the mean scenarios and the 45PPI porous media.....	XXXI
Figure 7-30: Reynolds-flux diffusion for the stormy scenarios and the 45PPI porous media.....	XXXI
Figure 7-31: Concentration maps for the calm scenarios and the 10PPI porous media	XXXII
Figure 7-32: Concentration maps for the mean scenarios and the 10PPI porous media	XXXII
Figure 7-33: Concentration maps for the stormy scenarios and the 10PPI porous media.....	XXXIII
Figure 7-34: Concentration maps for the calm scenarios and the 45PPI porous media	XXXIII
Figure 7-35: Concentration maps for the mean scenarios and the 45PPI porous media	XXXIV
Figure 7-36: Concentration maps for the stormy scenarios and the 45PPI porous media.....	XXXIV
Figure 7-37: LDA velocity profiles of the 45PPI porous media	XXXV
Figure 7-38: LDA turbulence profiles of the 45PPI porous media	XXXV
Figure 7-39: LDA velocity profiles of the 10PPI porous media	XXXVI
Figure 7-40: LDA turbulence profiles of the 10PPI porous media	XXXVI
Figure 7-41: Phase specific TKE of 3° slope angle and 10PPI porous medium	XXXVII
Figure 7-42: Phase specific TKE of 7° slope angle and 10PPI porous medium	XXXVII
Figure 7-43: Phase specific TKE of 14° slope angle and 10PPI porous medium	XXXVIII
Figure 7-44: Phase specific TKE of the calm wave scenario and 10PPI porous medium.....	XXXVIII

Figure 7-45: Phase specific TKE of the mean wave scenario and 10PPI porous medium.....	XXXIX
Figure 7-46: Phase specific TKE of the stormy wave scenario and 10PPI porous medium	XXXIX

List of tables

Table 1-1: Greek letters.....	XI
Table 1-2: Latin letters	XII
Table 1-3: Operators.....	XIII
Table 1-4: Indices.....	XIV
Table 1-5: Acronyms.....	XIV
Table 2-1: Overview of porosity parameters for different soil textures after [Koch 2004].....	- 13 -
Table 2-2: Typical values of permeability for different types of pervious materials after [Bear 2013]... -	15 -
Table 2-3: Overview of linear transport processes by [Stierstadt 2010]	- 35 -
Table 3-1: Requirements for new floor concept.....	- 48 -
Table 3-2: Parameters of the porous materials	- 55 -
Table 4-1: Parameters of the wave scenarios	- 62 -
Table 4-2: Overview of the specific parameters for the adaptive PIV setup.....	- 66 -
Table 4-3: Tracking lines of the spread analysis	- 68 -

List of symbols

Table 1-1: Greek letters

Symbol	Name	Description	SI unit
Γ, γ	gamma	specific flow property	
Z	Amplitude	amplitude or maximum elongation	m
O	omicron	porosity of a porous medium	%
$\Phi(t)$	phase angle	time dependent phase angle	°
$\Psi(x, t)$	stochastic function	stochastic function for different values	
α	alpha	specific angle for geometries or others	°
γ	gamma	boundaries for the concentration lines	m
δ	delta	bottom boundary layer thickness	m
ε	Reynolds-flux	Reynolds-flux for different scalars, lateral fluxes	mm/s*μg/l
$\zeta(t)$	elongation	elongation of a particle in a wave	m
η, H	eta	count variables for different aspects	
θ, Θ	theta	specific angle for geometries or others	°
κ	constant of Karman	constant in turbulent boundary layer flows	
λ	wavelength	length of a mechanical wave	m
μ	dynamic viscosity	dynamic viscosity of the fluid	N*s/m ²
ν	kinematic viscosity	kinematic viscosity of the fluid	m ² /s
ν_d	kinematic durability	specific variable in the kinetic theory of gases	m ² /s
ν_t	turbulent eddy viscosity	specific variable in the Boussinesq hypothesis for turbulent flows	m ² /s
ξ	xi	variable for u, v, w, c	m/s, μg/l
ρ	density	density of a fluid or solid	kg/m ³
τ_t	shear stress	general shear stress in a fluid or solid	Pa, N/m ²
τ_w	bottom stress	shear stress of the fluid with the bottom (for example the seabed)	Pa, N/m ²
φ	phase angle	specific phase angle	°
χ	chi	fluctuation values	value specific
ψ	psi	random variable for different aspects	
ω	angular velocity	change of the angular displacement during a time interval	rad/s

Table 1-2: Latin letters

Symbol	Name	Description	SI unit
A	surface	surface area	m ²
a	axis	axis of ellipsoid	m
B, b	variable	count variables for different parameters	
C	concentration	concentration of the tracer fluid	µg/l
c_p	heat capacity	heat capacity of a fluid	kg/m ² * K/s
D	diffusion coefficient	specific diffusion coefficient	m ² /s
E	energy	energy level of molecules	J
h_v	energy flux	energy flux as light or general energy transfer	J/s
f	frequency	frequency of a signal	Hz
F_i	force	conservative force in Reynolds equations	N
f_r	friction factor	general friction factor for different parameters	
f_w	friction factor	wave friction factor for the friction between the water waves and the seabed	
F_y	variable	specific transport variable	variable specific
g	gravitational acceleration	earth gravitational acceleration	m/s ²
h	heat transfer coefficient	proportionality constant for the flow of heat	W/(m ² *K)
h_D	mass transfer coefficient	proportionality constant for the flow of mass	m/s
I	intensity	intensity of the light source or fluorescence	W/m ²
J_x	transport parameter	variable for different transport parameters	parameter specific
K	permeability	permeability of a porous medium	m ²
k	wave number	wave number	
k_f	hydraulic conductivity	proportionality constant for the flow of water through a porous medium	m/s
l_c	mixing length	mixing length for the tracer concentration	m
l_m	mixing length	mixing length of Prandtl	m
l_M	path	mean free path between molecules in gases	m
L_{xy}	kinematic coefficient	coefficient for different transport equations	
m	mass	mass of a specific volume	kg
ṁ	mass flux	mass flux of a specific volume	kg/s
M_S	spectral moment	spectral moment of the power density function of waves	
n, N	variable	count variables for different parameters	parameter specific

$\underline{\underline{o}}$	matrix	transformation matrix	
\mathbf{P}	potential	potential function for different parameter	
p	pressure	specific pressure	Pa
\mathbf{PCB}	variable	percentage of the concentration boundaries	%
pd	variable	probability diffusion	
\dot{q}	heat flux	flux of heat/energy per unit of area and time	W/m ²
R_K	cross correlation function	specific function of the cross correlation	
s	thickness	thickness of a material, probe or others	m
$S(f)$	function	spectral density function	
S_M	state	state of molecules	
\mathbf{SWH}	significant wave height	height of the third highest waves in a spectrum	m
t	time	time of a measurement or other processes	s
T	wave period	period of a water wave	s
t^*	variable	time variable for the integration	
\mathbf{U}	velocity	velocity vector with components (u, v, w)	m/s
V	volume	volume of the fluid	m ³
\dot{V}	volume flux	volume flux of the fluid	m ³ /s
$v(t)$	wave speed	speed of the water wave	m/s
V_F	volume	volume of solid substances	m ³
V_H	volume	percentage of voids	m ³
V_{sf}	parameter	solid volume fraction	
\mathbf{WD}	water depth	depth of the water column	m
\mathbf{WH}	wave height	height of the water waves	m
x,y,z	coordinates	cartesian coordinates	

Table 1-3: Operators

Symbol	Name	Description
Δ	Delta	difference between parameters
\mathbf{grad}	gradient	gradient of parameters

Table 1-4: Indices

Symbol	Name	Description
10	10%-line	concentration line the 10% concentration line
C	concentration	concentration boundary line
horz	horizontal	indices for horizontal velocity component
vert	vertical	indices for vertical velocity component
i, j	sum convention	parameters of the sum convention standing for 1, 2, 3
tot	total	for example, the total mass of a volume
x, y	coordinates	cartesian coordinates specific
mea	measurement	data from measurements
ph	phase	phase specific or orbital specific values (for example the velocity)
ad	additional	additional mass flux or volume flux

Table 1-5: Acronyms

Acronym	Description
TKE	turbulent kinetic energy
PIV	particle image velocimetry
LIF	laser induced fluorescence
CCD	charge coupled device
LDA	laser doppler anemometry
RMS	root mean square
RANS	Reynolds averaged Navier-Stokes equations

1 Introduction

Our environment is changing more and more every day. Climate change has been of interest in different research groups during the last decades. And it is known and discussed that the effects of this change will influence the environment, the animals and also the human being significantly [Schubert 2006]. In the coastal zones, the sea level rise [Nerem et al. 2018] has one of the greatest impacts.

In the graduate school Baltic Transcoast, the impact of the climate change on the sea-land interaction is investigated on a nature reserve which was formerly used for agriculture. The Hüttelmoor is a coastal fen, which interacts with the Baltic Sea and has been investigated over several years [Miegel et al. 2016]. The fen has been subjected to numerous rewetting processes, allowing for a detailed analysis of the environmental changes resulting from them. Furthermore, the fluxes between the land and sea can be investigated. Because of the erased coastal protection measures, the possibility of flooding rises. This would in principal show which environmental effects could occur if the sea water rise lead to flooding events elsewhere. On the other hand, the flow of submarine groundwater into the sea is of importance. The impact of the submarine groundwater onto the environment is mentioned by [Moore 2010] and the [IOC et al. 2004]. With the submarine groundwater discharge (SGD) the delivery of nutrients, pollutions, water and other particles into the coastal environment is intensified. Hence, landside changes of the environment near the coast have a strong impact on the marine environment. [Burnett et al. 2006], [Leote et al. 2008], [Moore 2010], [Burnett et al. 2001] and [Robinson et al. 2007] mentioned SGD as a significant source of nutrients for the Baltic Sea.

The input of SGD into the coastal zone influences the local flora and fauna, but the diffusion and transport of these inputs are not fully understood. It is known that the bottom boundary layer of an oceanic seabed is controlled by the tidal and wave motion of the upper lying water column. In the Baltic Sea, the tidal movement is very low compared to the wave action. Thus, in this area the wave motion will be the dominant factor for the occurrence of the bottom boundary layer and the turbulent motion near the ground.

In this project, the mixing and transport processes which are relevant for the diffusion of the SGD into the water column, are investigated within a laboratory experiment. In a wave channel at the chair of fluid mechanics of the University of Rostock, the submarine groundwater discharge is simulated under three different wave conditions, with two artificial seabeds and four different slope angles. Furthermore, the velocity and concentration fields are measured with a combined laser light-based measurement system. The particle image velocimetry (PIV) delivers the velocity field and the laser induced fluorescence (LIF) delivers the concentration field of the tracer *Rhodamine 6G*, which simulates the SGD input.

1.1 Objective

The objectives of this project is the development of an experimental setup, the measurement of the velocity and concentration field under different aspects and the investigation of possible models and parameters for a numerical simulation of a Baltic Sea model.

The experimental setup has to facilitate a variable adjustment of different parameters which influence the bottom boundary layer. The main parameters are the wave action, the artificial seabed, the slope angle and the inflow conditions. Hence, the existing wave generator system has to be optimized. Furthermore, the construction of the ground has to be renewed such that the artificial seabed can be changed, and the slope angle can be adjusted quickly. Moreover, the inflow is controlled by different pumps and the inflow area can be varied by using different inflow elements.

Secondly, the measurement of the velocity and concentration fields are done under different conditions to estimate the dependencies of the transport and mixing behavior. The laser and camera system with controlling elements already existed and were used for the experiments. The measurement procedure and the orientation of the field of view was tested and optimized for this case.

Finally, different models and parameters for a possible numerical ocean simulation have to be calculated. The focus lies on the Reynolds-flux model as method to interpret the turbulent transport and the mixing length model of [Prandtl 1925] as a parameter for the numerical simulation. The postprocessing algorithm and data management were developed and optimized.

1.2 State of research

In the current state of research, no equivalent project is found with the same contexts and types of measurements. Because of the interdisciplinary research topic, the field of science in which possible parallels are found differ strongly.

The flow field over and in porous media due to a steady current is well known. The focus lies mostly on the transition zone between the porous media inner flow (Darcy's law) and the outer boundary layer flow. This zone is called Brinkman layer after [Brinkman 1949]. [Beavers and Joseph 1967] delivers one of the first investigations of this transition zone. They used a flow channel which was separated into two zones. In the underlying zone, a porous media was placed. In the overlying zone, a steady current was generated. In the outflow area, the mass fluxes of both zones were measured. The results of their investigations were that the boundary layer affects the mass flux strongly and that this boundary layer depends strongly on the porous material. [Ochoa-Tapia 1995] defined mathematical models and boundary conditions for the transition zone and compared the results with the data of [Beavers and Joseph 1967]. The main aspect of their investigations was the momentum transport from the porous media into the free stream. Further work on this topic was done by [Alazmi and Vafai 2001]. They used the mathematical models and boundary conditions of [Ochoa-Tapia 1995] and developed new solutions for their models. The result of their calculation shows, that the velocity field is more influenced by the type of the porous media than the heat transfer in the transition zone.

Another laboratory experiment was conducted by [Huettel et al. 1996]. He investigated the advection of particulate matter from the porous media into the open flow. He used a water channel with 160l of freshwater with a steady current of 10cm/s. In the channel, dyed sediment was placed in different zones. Furthermore, the sediment movement and the diffusion of the different sediments were monitored.

[Gupte and Advani 1997] used a miniature flow channel with a Hele-Shaw-cell of fiberglass material to investigate the transition zone. They used the laser Doppler velocimetry to measure the velocity field in this zone. They also mentioned that this area depends mostly on the type of porous media.

With the development of the particle image velocimetry, several working groups used an artificial seabed with the same refraction index of the overlying fluid to measure the complete flow field in and above the bed. [Goharzadeh et al. 2005] used glass spheres with varying diameters in a water channel for their investigations. The dependency of the boundary layer flow on the diameter was significant for their results. A further development of their experiment was done by [Morad and Khalili 2009]. They used a glass sphere bed with different diameters of the spheres. The result was the same, with the transition and boundary layer zone thickness strongly depending on the mean diameter of the spheres. Another kind of porous bed was developed and investigated by [James and Davis 2001], [Tachie et al. 2003], [Agelichaab et al. 2006] and [Arthur et al. 2009]. They used several vertical standing cylinders

in a defined distance to build up a well-defined porosity of the seabed. They all used the same water channel and continuously developed the respective experiments. [Arthur et al. 2009] summarized the investigations and gives an overview of the state of research. Furthermore, he concluded that the flow is blocked by the cylinders if the volume friction factor is higher than 0.22. [Carotenuto and Minale 2011] used a rheometer to measure velocity profiles above different porous media. They compared their results to the models of [Ochoa-Tapia 1995] and proved their equations for the tension jump in the boundary layer. [Keramaris and Pechlivanidis 2015] used a water channel and a 2D-PIV system to measure the velocity profile above different types of grounds. They compared the vertical cylinder experiments from [Arthur et al. 2009] to a ground of grass and a granulated material. They showed that the vertical cylinders disturb the flow significantly. Furthermore, the longitudinal and vertical turbulence intensity is influenced by the kind of porous media.

[Precht and Huettel 2003] investigated the advective pore water exchange with sandy sediment under wave action. The experiments were conducted with sediment from the North Sea in a water channel. Like in [Huettel et al. 1996], parts of the sediments were dyed with Rhodamine 6G to mark the oxygen level in the sandy sediments. It was seen that the oxygen mixing interacts with the speed at which ripples are built up. Furthermore, the waves increase the exchange of fluid between the sediments and the overlying water column. A reason for this may be a pressure gradient, which occurs because of the interaction between the oscillating boundary layer and the creation of the ripple structure. Moreover, [Huettel et al. 1996] shows that because of a pressure gradient, fluid from the open flow is pushed into the ripple structure.

The pore water exchange and the velocity structures around ripple structures were also investigated in field studies. There are numerous varying publications in the literature, of which only a few projects are described here briefly. The used sediment in [Precht and Huettel 2003] was collected during the investigations of [Rusch et al. 2000] near the Island of Sylt. In this study, core probes were sampled over the course of a year to estimate the change of particulate organic matter with respect to the outer environment. One result was that the specific matter concentration changes with the averaged flow velocity. [Smyth 2002] conducted measurements with acoustic doppler velocimetry at a pocket beach. He investigated the influence of ripples and waves on the turbulent structures in the water column. He found that the ripples in this specific area show no significant influence on the turbulence. Another investigation with an acoustic doppler anemometer was done by [Lorke et al. 2003]. In addition to the velocity measurement an oxygen sensor was installed. Hence, the oxygen concentration and the turbulent dissipation rate were compared. With this analysis, he concluded that knowledge of the mixing due to waves over a permeable seabed is required to understand the balance of the transport mechanism. [Feddersen 2012] used acoustic doppler velocimetry to investigate turbulent effects near a beach. He installed 8 measurement stations orthogonally to the beach in the shallow area. He concluded that in the deeper surf zone, the development of the turbulence is caused by friction effects with the seabed.

2 Physical background

In this chapter the fundamentals of the particle image velocimetry and the laser induced fluorescence technique are presented. Furthermore, the experimental realization of the submarine groundwater discharge is mentioned. Also, the ground properties such as the permeability are defined. The used wave theories are described with respect to the experiment and the Reynolds-averaged Navier-Stokes equations are given. The Reynolds-flux model is defined for the description of the transport phenomena.

2.1 Laser optical measurement techniques

According to [Nitsche and Brunn 2006] Laser optical measurement techniques are all techniques, which use a light source with high intensity (for example a laser) and do not disturb the flow conditions. In the project “Waves and turbulence on wavy coastal seabeds inducing vertical scalar transport” the particle image velocimetry and the laser induced fluorescence technique are combined.

2.1.1 Particle image velocimetry (PIV)

Particle image velocimetry is one of the modern laser optical measurement techniques which is used in different kinds of fluids. Furthermore, it is a field measurement technique due to the determination of a complete flow field in two or three dimensions within one snapshot. Following [Nitsche and Brunn 2006], PIV works in two stages:

At first, the imaging stage is elaborated. In this stage, the images are captured which are needed for the following stage. The method involves taking double images. This includes two snapshots of the flow field within a well-defined time step Δt . To make the flow field visible, additional particles are needed in the flow. These particles underly different requirements. It is of importance that they follow the fluid without any reaction time. Moreover, they should not show a natural drift or substantial drop in the surrounding fluid. Furthermore, they must reflect the laser light adequately to stand out from the surrounding fluid. Because of these requirements and the multiple applications for PIV within a variety of different fluids, a lot of different types of tracer particles are available. For the application in water, the synthetic material VESTOSINT ® has very good properties. These particles are mixed into the working fluid and illuminated by a high intensity light source such as a laser light which is normally used in these applications. The laser light is spread out into a plain which illuminates an area within the fluid flow. In this area, the tracer particles reflect this light. In a specific angle to the point of view, one or more cameras capture the field. The number of cameras depends on the number of required velocity components. For the two-dimensional two components PIV measurement only one camera is needed. The light source and the camera are triggered together, such that the maximum illumination and the image capturing come together, allowing the maximum resolution to be accomplished. The time interval between the double images is adjusted to the main velocities in the flow field. The faster the flow, the shorter the time interval between the double images.

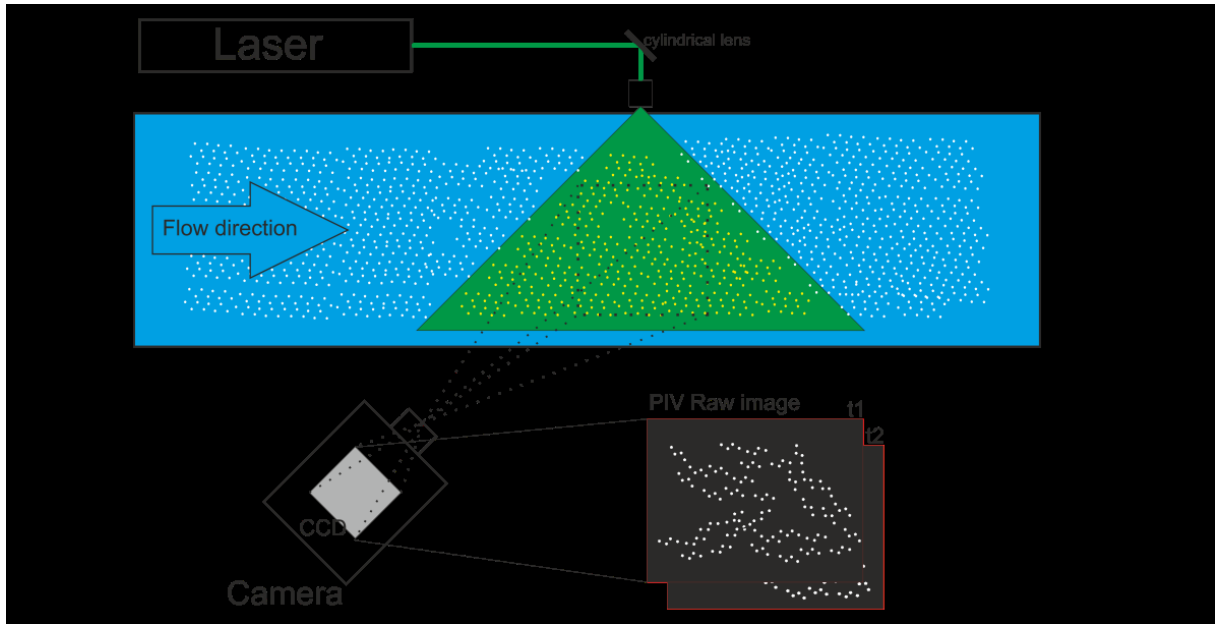


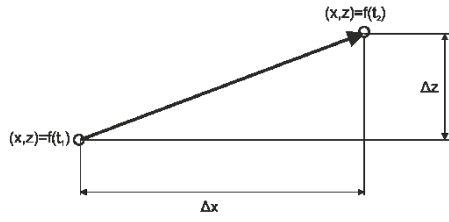
Figure 2-1: General PIV setup

The laser is guided into a fluid flow and spread out with a cylindrical lens. The tracer particles are illuminated within the laser light sheet. A camera takes pictures of the light sheet and the resulting greyscale images are shown in this figure.

In the second stage, the images are analyzed. The algorithm is based on an enhanced cross-correlation of the light intensity diffusion I between the respective double-images. The simple cross-correlation is defined by

$$R_K(b, n) = \sum_{b=-B}^B \sum_{n=-N}^N I(b, n) \cdot I'(b + x, n + z) \quad \text{Eq. (2.1)}$$

In the time interval between the double-images, the particles in the fluid are moving. Hence, the light intensity diffusion in the image changes. Due to a higher resolution of the vector field, the field of view is subdivided into interrogation areas (IA). These IA are correlated if R_K reaches its maximum. This maximum shows that the statistical accordance is the best by a given displacement. Hence, a displacement vector is calculated for the defined IA in one double-images. With this vector and the defined time step between the images, the velocity vector is calculated with the following equations.



$$u = \lim_{t_2 \rightarrow t_1} \frac{x_2 - x_1}{t_2 - t_1} = \lim_{\Delta t \rightarrow 0} \frac{\Delta x}{\Delta t}$$

$$w = \lim_{t_2 \rightarrow t_1} \frac{z_2 - z_1}{t_2 - t_1} = \lim_{\Delta t \rightarrow 0} \frac{\Delta z}{\Delta t}$$

Eq. (2.2)

The smaller the IA, the higher the resolution of the flow field. The minimum size of the IA depends on the maximum number of particles within the IA, the diameter of the particles and the time between the laser bursts. The cross-correlation is a statistical algorithm. Thus, it is obvious that a minimum number of particles has to be in the IA. If there are too few, the correlation peak will not be unique enough to show the right displacement. On the other hand, if the IA is too large, the small-scale velocity vectors will not be detected, resulting in the flow field being averaged over a large area. This effect can be used for a first orientation on how the flow field is oriented, for example in wave experiments.

2.1.2 Laser induced fluorescence (LIF)

The laser induced fluorescence technique is a laser-based measurement technique which uses the induced fluorescence of tracers. According to [Zare 2012] this technique is well known in different disciplines and was successfully used to make tracers visible. Examples for practical uses in chemistry are given by [Guilbault 1990].

Basically, LIF works similar to PIV. A tracer is introduced into the investigated fluid and a laser illuminates the measurement area. Furthermore, a CCD camera is placed perpendicular to the light sheet and takes images of the illuminated flow area. Because of the similar structure, the PIV and LIF measurement techniques can be combined (see 2.1.3). The difference between these measurement techniques lies in the type of used phenomena. In PIV, the reflection of light on the tracer particles is used. For LIF, the fluorescence of the tracer is of importance. Furthermore, the tracer does not have to be mixed into the fluid before the measurement, as it can also be mixed in during the measurement. Thus, LIF is normally used to investigate mixing mechanisms of fluids, for example in [Menzel 2010] or [Walker 1987].

In this experiment, LIF is used by creating a planar laser light sheet (planar laser induced fluorescence PLIF). The laser light source is the same as for the PIV setup, namely a NdYAG laser with a wavelength of 532 nm. The tracer *Rhodamin 6G*, which is used in this experiment, is most fluorescent at this wavelength. The tracer is excited, and the fluorescent light is captured with a camera setup.

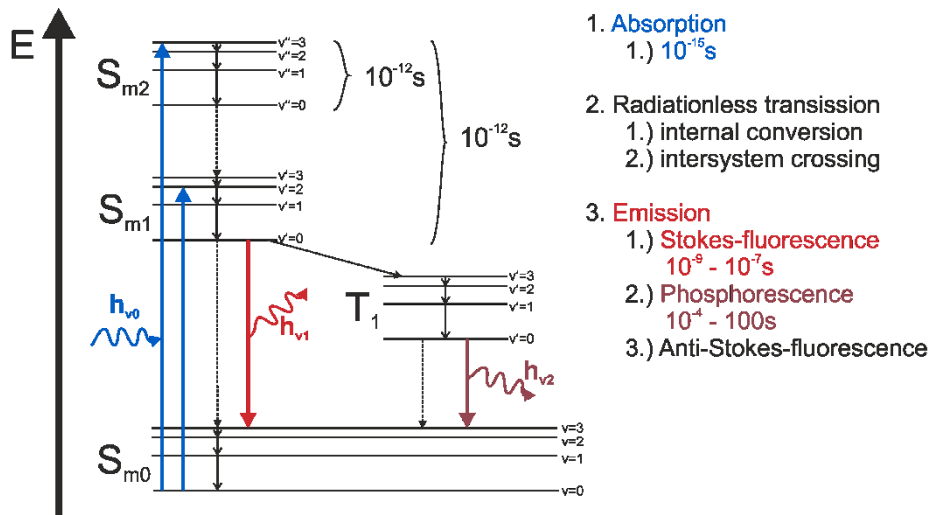


Figure 2-2: Emission states [Menzel 2010]

The excitation of molecules leads to different types of reactions, with fluorescence being one possibility. The reaction depends on how long the electron can hold the higher energy state S_m . If the time exceeds 10^{-9} s, the energy h_ν is emitted. The Stokes-fluorescence is used for the LIF technique.

The excitation of fluorescent molecules is based on the change of state S of the outer electron [Walker 1987]. This electron jumps from the ground state S_{m0} to a higher energetic S_{m2} state during the excitation with the laser light with the energy $E = h_{\nu 0}$. The electron cannot hold this state and jumps back to the stable ground state S_{m0} or after a short residence time to the first singlet (S_{m1}) or triplet (T_1)¹ state. From this state, the molecule jumps back to the stable ground state S_{m0} after a longer residence time. During this process, the excess energy $E_1 = h_{\nu 1}$ or $E_2 = h_{\nu 2}$ is discharged as light. The wavelength of this light differs from the laser light which formerly excited the tracer. Hence, it is seen as fluorescence light. For the LIF technique, the Stokes-fluorescence is used. This means that the electrons hold their higher energetic state for 10^{-9} - 10^{-7} s until they jump back to the ground state. The emitted light during this process has a smaller wavelength than the laser light. For this reason, a bandpass filter is used in front of the camera in order to filter out every unnecessary wavelength. Moreover, it is easily possible to combine the PIV and LIF measurement techniques in one setup.

¹ Singlet or triplet states describe the status of the electron spin of a molecule, for further information see fundamental works in theoretical physics, such as Nolting [2009].

2.1.3 Combination of PIV and LIF

The combination of the PIV and the PLIF measurement techniques delivers the possibility to measure the velocity field and the concentration field of a measured area simultaneously. The advantages are obvious: With little effort, the measurement time is halved. In this experiment, the camera setup includes two cameras. The first one is used to capture the PIV images and the second one is used for the PLIF images. Both cameras use the same lens. For the second camera, a semi-reflecting mirror guides the light to a bandpass filter and the following CCD. Because of the filter, only the fluorescence light reaches the CCD of the second camera and the reflected light of the tracers for the PIV are not visible in the post processing. The PIV camera is sensitive to all wavelengths of the light in the measurement, but the reflections of the particles are more intense than the fluorescence, such that the post-processing is not affected by this light.

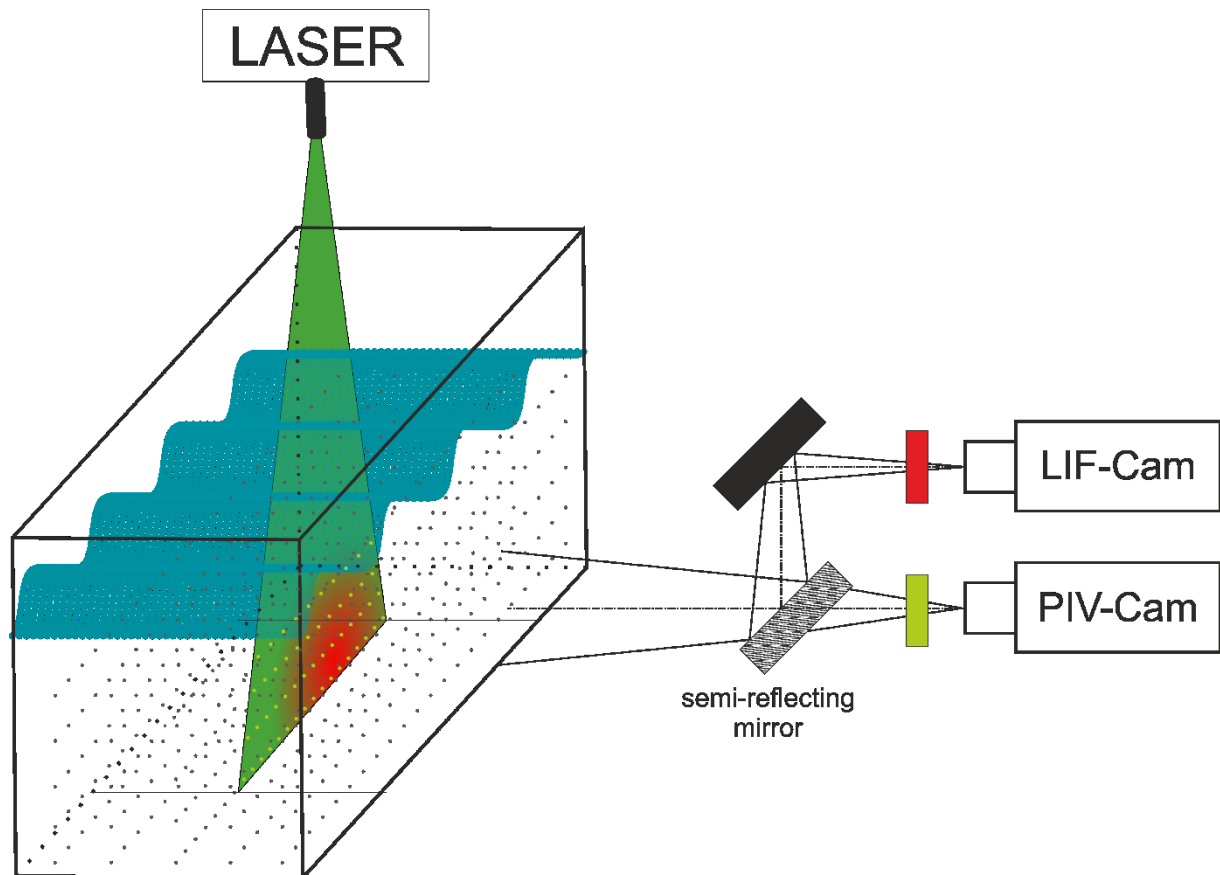


Figure 2-3: Combined PIV-PLIF setup

On the left-hand side of the figure, a wave channel with tracer particles in the fluid is shown. From the inflow tracers reach the channel. The grey particles reflect the green laser light and the other tracers fluoresce in a red light due to being illuminated by the green laser light. On the right-hand side, the camera setup is placed. The PIV camera sees every wavelength of the experiment, while the LIF camera sees only the red light of the image.

2.2 Submarine Groundwater Discharge (SGD)

In the coastal ecosystem, the topic of submarine groundwater discharge (SGD) has received more and more attention during the last twenty years. [Moore 2010] mentioned this in a review with reference to a significant increase in published articles related to the topic of SGD. The definition of SGD is also specified by [Moore 2010]: “*SGD includes any and all flow of water on continental margins from the seabed to the coastal ocean, with scale lengths of meters to kilometers regardless of fluid composition or driving force.[...] The definition of SGD does not include such processes as deep-sea hydrothermal circulation, deep fluid expulsion at convergent margins, and density-driven cold seeps on continental slopes.*” Accordingly, the term SGD describes freshwater flows into the bottom boundary layer as well as mixed brackish water flows.

Based on this definition, the SGD has a strong impact on the ecosystem in several very different aspects. On the one hand, the directly transported nutrients from the fertilizer, pesticides and wastewater from the landside have a huge impact on the marine environment. On the other hand, the chemical reactions, which occur in the sediments themselves when brackish and freshwater zones are mixed and come in contact with different reactants, will also have a high impact on the ecosystem. The importance of nutrient input with SGD in the coastal zone was investigated by several scientists. [Leote et al. 2008] studied the inflow of nitrogen, phosphorus and silicon into a lagoon surrounded by intensely used algacultural land. [Slomp and van Cappellen 2004] mentioned the SGD as a highly important source for nutrients in the coastal zone. [Burnett et al. 2001] describes the significance of the SGD as a nutrient source. There are a lot of area specific studies on the impact of SGD on local ecosystems such as in [Beck et al. 2016], [Burnett et al. 2006], [Rapaglia et al. 2012], [Robinson et al. 2007] or [Taniguchi et al. 2006]. [Moore 2010] describes all of these studied impacts of SGD in detail.

The amount of the submarine groundwater depends mainly on the hydraulic gradient from land to the sea. This gradient depends on different factors, such as the swell, the ground properties and the hydrogeological processes, for example the development of rivers or precipitation. The ground consists of different layers and aquifers. Hence, the permeability and porosity of these structures are important for the hydraulic gradient and as a consequence of this also for the amount of SGD coming from the land side. These factors also control the nutrient input into the SGD flux and chemical reactions within the layers.

The submarine groundwater discharge consists of two main types: the terrestrial freshwater SGD and the seawater recirculation SGD. The first type includes every freshwater input flowing through aquifers from the land into the sea. The second type consists of the water which is recirculated in the permeable ground on the sea side and the interface between the sea and the land side. Following [Robinson et al. 2007], the SGD is divided into two more subtypes. In Figure 2-4 the different types of SGD are illustrated.

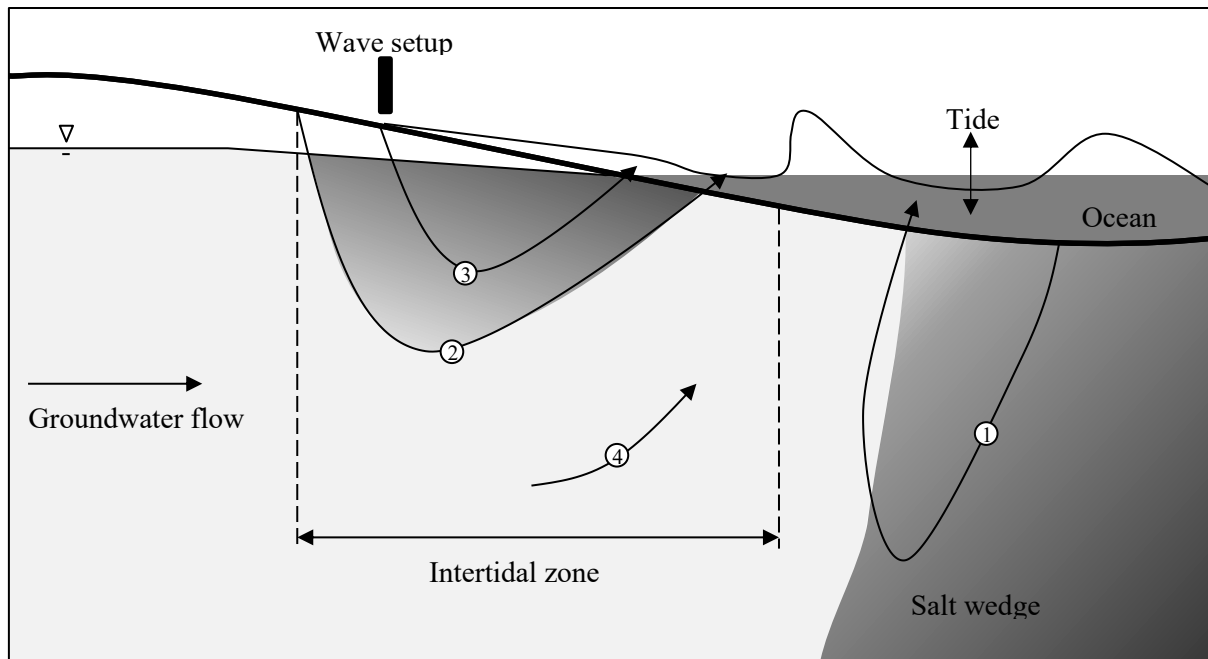


Figure 2-4: Categorization of submarine groundwater discharge following [Robinson et al. 2007]

The SGD is divided into the direct flow (4) and the recirculated seawater (1), (2) and (3). (2) is mixed with rain water coming from the beach, (3) includes the up-running wave water in the surf zone and (1) contains of the mixed water from the salt wedge zone.

The biggest part of the SGD (nearly 95%) consists of the recirculated seawater [Santos et al. 2008]. This leads to the division of this main type into subtypes. In Figure 2-4, the first three flows are part of the recirculating seawater SGD. The first circulation is driven by density gradients along the path. It occurs between freshwater flow of terrestrial SGD and the salt wedge in the ocean zone. The second circulation is induced by the tide of the ocean. And the third circulation is driven by the wave setup.

The measurement of SGD is a big problem and still scientific work in progress. [Moore 2010] describes the most common and important measurement techniques to define the amount of outcoming SGD fluxes. To detect an SGD flux, thermal imaging is the most common technique. For this, thermal images are taken from satellites or drones. If a cold area is captured on the beach side, this is a possible cold groundwater outflow. Electromagnetic techniques lead to a detection of pore water salinity near the surface on the beach side. When a low salinity is detected, this is a possible area of outflowing freshwater. As a direct measurement method, seepage meters are used. These boxes are placed in the area of outcoming SGD and the amount of freshwater flowing into them shows the discharge in the specific area. The disadvantage of this technique is that it only works in a section where SGD is flowing out. A more regional working technique is the tracer technique with isotopes. Further information on this technique can be found in [Moore 2010]. With this it is possible to integrate the flux over a large area. Another common method is the modelling of groundwater flow and estimating the SGD fluxes. A more detailed description is given by [Burnett et al. 2006].

2.3 Ground properties

The properties of the seabed in the various regions of the Baltic Sea differ in many aspects. Even in a very small area in front of the Hüttelmoor the ground changes its shape and properties in different directions. For the description of these changes, the two most common properties are described here exemplarily.

2.3.1 Porosity

In general, the porosity O is defined as the percentage of voids of a material. Following [Engelhardt 1960] this definition equates to the absolute porosity defined as the quotient of the percentage of voids of a rock mass to the total volume.

$$O = \frac{V_H}{V_H + V_F} \quad \text{Eq. (2.3)}$$

In Eq. (2.3) V_H is the percentage of voids and V_F is the volume of solid substance. In [Engelhardt 1960], the percentage of voids is divided into several subspaces. Hence, the effective useable pore volume is reduced by the occurrence of adhesive water. This water is bound onto the surrounded rock material through adhesive forces and cannot move. The ratio of the adhesive water to the percentage of voids depends on the properties of the rock material. This includes the shape of the grain material, bulk density and diagenesis². Thus, the space in which fluid is able to flow in a porous media is the result of the difference of the percentage of voids and the adhesive water.

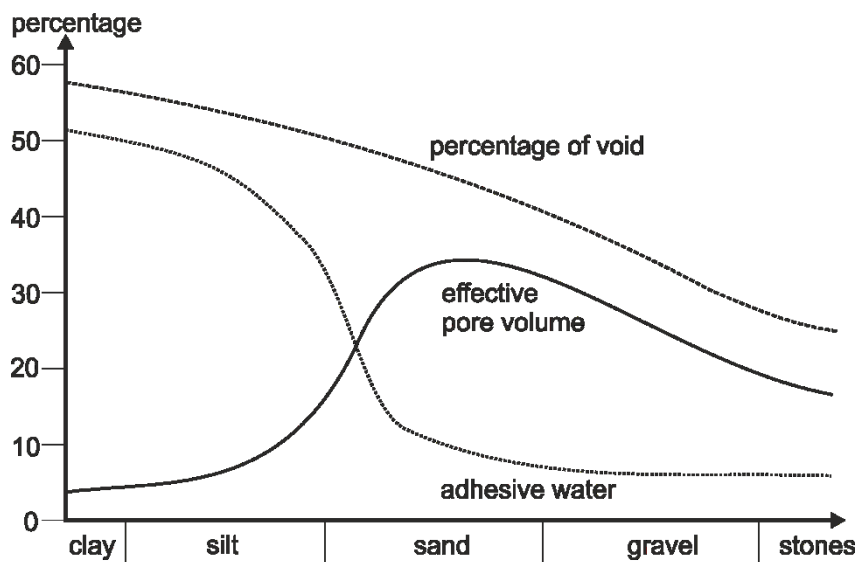


Figure 2-5: Overview of the pore volume of different materials after [Spektrum 2000]


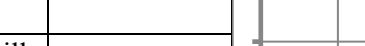
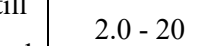
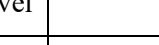
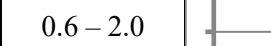
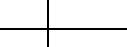
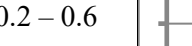
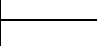
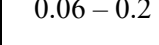

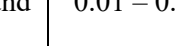









² “Diagenesis comprises a broad spectrum of physical, chemical and biological post-depositional processes by which original sedimentary assemblages and their interstitial pore waters react in an attempt to reach textural and geochemical equilibrium with their environment” (Burley and Worden [2003]).

In Figure 2-5, the different ratios of the pore volumes for different materials are shown. Hence, the effective pore volume increases with the more grained materials like sand and gravel. On the other hand, the adhesive water decreases to a minimum value of around 10% of the complete volume. Thus, the percentage of void and the effective pore volume are nearly at the same level in sandy materials. As such, the porosity delivers an important parameter for the properties of the seabed.

In different studies in the field of the analysis of flow fields over and within porous media, the so-called volume friction factor is named. The studies of [Agelichaab et al. 2006], [Arthur et al. 2009], [Alazmi and Vafai 2001], [Carotenuto and Minale 2011], [Gupte and Advani 1997], [Tachie et al. 2003] and others use this specific parameter for the categorization of the investigated porous material. The definition of the solid volume fraction V_{sf} is the following:

$$V_{sf} = 1 - 0 \quad \text{Eq. (2.4)}$$

Table 2-1: Overview of porosity parameters for different soil textures after [Koch 2004]

Soil texture	Diameter limits [mm]	Volume of void [Vol - %]	
Pure gravel	20 - 60		
Sandy fine till medium gravel	2.0 - 20		
Coarse sand	0.6 - 2.0		
Medium sand	0.2 - 0.6		
Fine sand	0.06 - 0.2		
Very fine sand	0.01 - 0.02		
Silty clay	0.006 - 0.01		
Silt	0.002 - 0.006		
Clay	0.001 - 0.002		
Effective porosity	Ineffective porosity		

In Table 2-1, the different porosities for the most common soil textures are given. In beach areas with sandy sediments, the porosity range is between the values of coarse and very fine sand. For the reference area in front of the Hüttelmoor, porosities between 0.36 and 0.41 have been measured at different stations [Schade, personal communication].

2.3.2 Darcy's law

The flow through a permeable medium is defined by Darcy's law. Following [Allen 2001] this law is valid for small Reynolds numbers.

$$\dot{V} = - \frac{K * A \Delta p}{\nu s} \quad \text{Eq. (2.5)}$$

The flow \dot{V} is defined by the permeability K multiplied with the surface area through which the water flows divided by the kinematic viscosity. The second term of the equation consists of the pressure difference between the start and the end point of the material divided by the thickness of it. Hence, the percolation is linear to the hydraulic conductivity and dependant on the material behaviour. For further reading, [Simmons 2008] illustrates the investigations of Darcy in a detailed review.

2.3.3 Permeability

The permeability of porous media is described as the possibility of a fluid going through a defined thickness of this media. Hence, this parameter defines a resistance of a solid structure against a fluid flow. Following [Bear 2013], the permeability of a porous media is calculated with the hydraulic conductivity k_f , the dynamic viscosity μ , the density ρ and the gravity acceleration g .

$$K = k_f \frac{\mu}{\rho * g} \quad \text{Eq. (2.6)}$$

The coefficient K can be determined experimentally or empirically. The experimental calculation of this parameter can be done with two different methods: the constant head method and the constant pressure method.

In the following Table 2-2, typical values for permeabilities of different porous media are given.

Table 2-2: Typical values of permeability for different types of pervious materials after [Bear 2013]

Permeability	Pervious				Semi-Pervious					Impervious			
Unconsolidated sand and gravel	Well sorted gravel		Well sorted sand or sand and gravel		Very fine sand, silt, loess, loam								
Unconsolidated clay and organic					Peat		Layered clay			Unweathered clay			
Consolidated rocks	Highly fractured rocks				Oil reservoir rocks			Fresh sandstone		Fresh limestone, dolomite		Fresh granite	
K(cm ²)	10 ⁻³	10 ⁻⁴	10 ⁻⁵	10 ⁻⁶	10 ⁻⁷	10 ⁻⁸	10 ⁻⁹	10 ⁻¹⁰	10 ⁻¹¹	10 ⁻¹²	10 ⁻¹³	10 ⁻¹⁴	10 ⁻¹⁵

2.4 Wave theory

Following [Demtröder 2006], a “mechanical wave is a process, in which an oscillation propagates in space from the place of its excitation, due to a coupling on an adjacent, oscillatory system. The propagation speed depends on the strength of the coupling and on the mass of the oscillating systems”.

The ocean surface waves are a type of mechanical waves. To describe the properties of such a wave, the general parameters are given in this chapter. Furthermore, the most common wave theories are specified. Both the linear wave theory of [Airy 1845] and the Stokes theory named after [Stokes 2009] are described.

2.4.1 General specification of mechanical waves

Mechanical waves describe a multitude of different wave types. In general, the wave type depends on the propagation characteristics and the sort of transport medium. Examples are longitudinal waves, transverse waves, acoustic waves, waves in gases, surface waves and others. All of these waves can be basically be described by the following sketch for a plain harmonic wave:

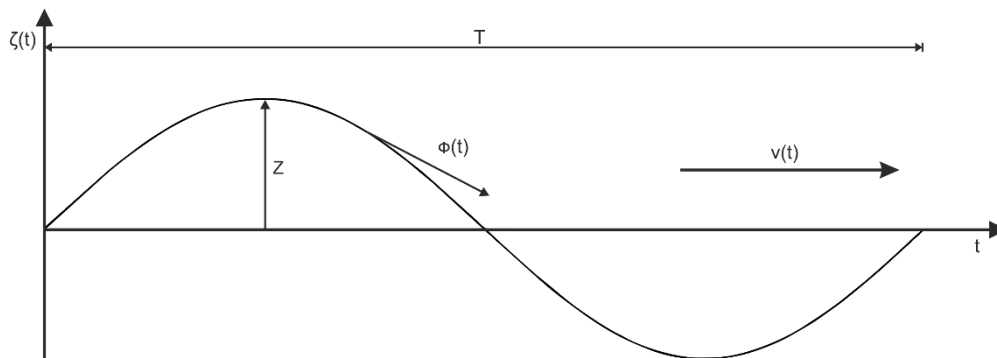


Figure 2-6: General exposure of a plain harmonic wave

A schematic overview of one period T of a sine wave with its amplitude Z , phase $\Phi(t)$ and wave speed $v(t)$ as elongation over time t .

In this figure, the x-axis shows the time and the y-axis the time dependent elongation. The most important parameters of the wave are the amplitude Z , the phase $\Phi(t)$ and the wave speed $v(t)$. The length between two points of the same phase is called the wavelength λ . With these parameters, characteristic factors are calculated. The frequency f is defined as the reciprocal of the period T .

$$f = \frac{1}{T} \quad \text{Eq. (2.7)}$$

The wave number k is defined as the period of 2π divided by the wavelength.

$$k = \frac{2\pi}{\lambda} \quad \text{Eq. (2.8)}$$

Analogously to the wave number, the angular frequency is defined:

$$\omega = \frac{2\pi}{T} \quad \text{Eq. (2.9)}$$

All these characteristic factors are combined in the definition of the wave speed in the following equation.

$$v(t) = \frac{\lambda}{T} = \frac{\omega}{k} = \lambda * f \quad \text{Eq. (2.10)}$$

With the characteristic equation for the plain harmonic wave, the wave is completely described with all of its properties.

$$\zeta(x, t) = Z * \cos(kx - \omega t) \quad \text{Eq. (2.11)}$$

These relationships are general terms of mechanical waves. In order to describe ocean waves, additional theoretical assumptions must be made (see Ocean waves).

2.4.2 Ocean waves

Ocean waves are a special type of mechanical waves. This type is a combination of transverse and longitudinal waves. To define the specific behavior of the ocean wave, a water particle in the water column is considered. This particle is moved with the water and, as an idealization follows an orbital path. This wave orbital is shown in Figure 2-7 for a sine shaped wave.

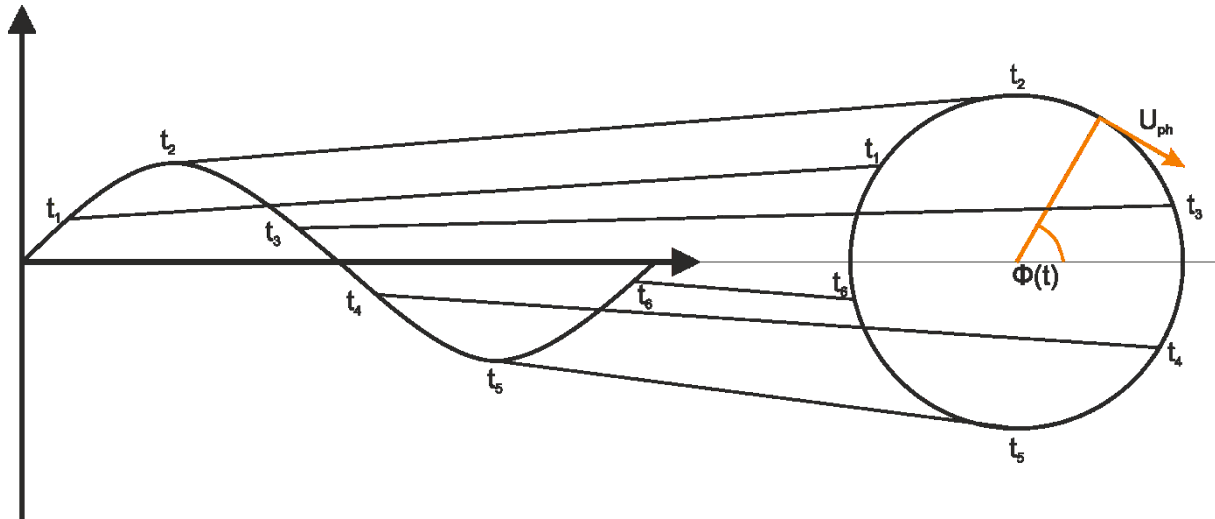


Figure 2-7: Orbital path

The standard sine shaped wave with the idealized orbital movement as a circle, which is typical for a deep-water wave, for different time steps t_n during the period of 2π and the phase $\Phi(t)$.

On the left-hand side, the movement of a sine wave over a period of 2π is plotted. On the right-hand side, the equivalent circular orbital path of the moving particle is drawn. The speed of the particle on its orbital path is defined as the orbital speed u_ϕ and shows how fast a particle moves on the orbital path during a wave period.

In oceanography, typical ocean waves are categorized by the typical shape of the orbital movement of the water particles. The shape depends on the predominant velocity field of the wave, but the water depth and the wavelength affect the movement of the water particles even more. Hence, the descriptions of the typical shapes of the orbital movement are distinguished by the ratio of the water depth h to the wavelength λ . Thus, when the water becomes shallow, the ratio becomes smaller, because of the constant wavelength and the decreasing water depth. Hence, the shallow water zone starts at a ratio smaller than 0.05. On the other hand, the deep-water zone is defined for deep water columns and long wavelengths, so the ratio is larger than 0.5. In Figure 2-8, the categorization of the zones is depicted.

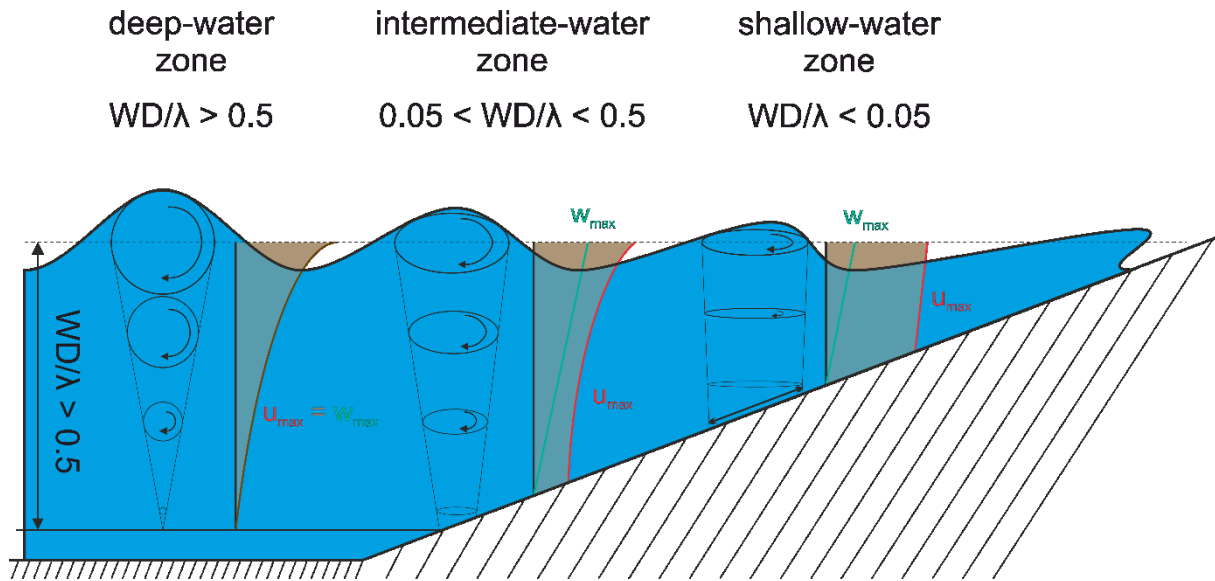


Figure 2-8: Categorization of ocean waves

From left to right, the development of typical ocean waves is shown. The deep-water zone starts at a ratio of WD/λ larger than 0.5. The shallow zone starts at a ratio smaller than 0.05. Between these, the intermediate zone is defined.

The three zones differ in the shape of the orbital path and the predominating velocity field. In the deep-water the idealized orbital of the water particles is circular. With decreasing water depth, the orbital is stretched to an ellipsoid. The shallower the water, the more the ellipsoid is flattened. This development of the particle's path leads to typical velocity components for this wave type. In the deep-water zone with circular orbital movement, the maximum horizontal and the maximum vertical velocity components are equal along the water column. Furthermore, the velocity components decrease equally with increasing distance from the water surface until the wave motion is negligible. In shallow waters, the physics changes. The orbital path develops into a flat ellipsoid. With this shape, the velocity components change their behavior. The maximum horizontal velocity component is much greater than the maximum vertical velocity component along the entire water column. With increasing water depth, the maximum velocity components decrease. In contrast to the development of the components in the deep-water zone, the velocity components in the shallow-water zone do not decrease equally. The maximum horizontal velocity component decreases more slowly than the maximum vertical component. Thus, the horizontal velocity is still dominant near the ground. On the other hand, the vertical velocity component vanishes almost completely. Hence, in the shallow-water zone, the movement of the water above the seabed appears to be only in the horizontal direction parallel to the ground. In the intermediate zone between the described regions, a mix of both developments occurs. The shape of the orbital path is ellipsoid but less flat than in the shallow-water zone. The development of the velocity components along the water column is not equal and corresponds to the development in the shallow-water zone. Hence the influence of the horizontal velocity component above the seabed is very strong, but less so

than in the shallow zone. Furthermore, the vertical velocity component in the immediate vicinity of the ground is not zero.

In summary, the influence of the horizontal velocity component of the wave motion is very high in the intermediate and shallow coastal zone. The wave movement has an impact on the seabed in these zones, in contrast to the deep-water zone. Thus, in shallow areas, ocean surface waves have the main impact on the velocity field and the benthic boundary layer near the seabed are ocean surface waves.

The description of ocean surface waves is a complex problem. For this reason, a lot of different wave theories have been developed. For the deep-water zone, mostly two theories are common, but for the shallower areas, the numbers of theories increase with the increasing complexity of the problem. [Le Méhauté 1976] gives an overview of the different wave theories and the specific aspects of them. In [Ausschuß für Küstenschutzwerke 2002], the mostly used theories are mentioned. In order to decide which theory is the best for a specific case, the URSELL-parameter can be used.

$$Ur = \left(\frac{WH}{\lambda} \right) \left(\frac{\lambda}{WD} \right)^3 = \frac{WH * \lambda^2}{WD^3} \quad \text{Eq. (2.12)}$$

2.4.3 Potential function as a basis for wave theories

Wave theories are important for the analysis of wave action in the oceans. All the commonly used theories have an analytical solution. Thus, it is obvious that a lot of assumptions are made. Following [Graw 1995], the following simplifications are used for most wave theories:

- The fluid is frictionless and incompressible
- The surface tension is negligible
- The pressure above the free surface is constant
- The fluid is ideal, i.e. zero viscosity
- The waves are not influenced by other water movements
- The ground is horizontal and impermeable
- The wave does not change its shape in transverse direction
- The problem is considered only in 2D
- The wave movement can be described by a potential flow

The potential theory presumes a potential difference between two points of a physical value in a space. The difference between these points is described by a potential function. This function is fitted to the physical phenomena. The potential theory is based on the force field and the derivation of this theory was made by [Clausius 1885].

In fluid mechanics, the potential theory postulates a frictionless and rotation-free flow. This is a strong simplification of the problem. Hence, the wave theory always includes errors. In the first step, the vector quantities are replaced by scalars, the potentials. Following [Malcherek 2010], the potential P and the velocity are connected via the gradient of P .

$$\vec{U} = \text{grad}(P) \quad \text{Eq. (2.13)}$$

This potential is used in the continuity equation which subsequently yields the Laplace equation.

$$\frac{\partial^2 P}{\partial x^2} + \frac{\partial^2 P}{\partial y^2} + \frac{\partial^2 P}{\partial z^2} = 0 \quad \text{Eq. (2.14)}$$

In addition to the velocity potential, a simplification for the pressure is needed to modify the conservation of momentum. For this, the gravitational force is replaced by a potential. Hence, the conservative force is described by the following equation.

$$\vec{F} = -\text{grad}(P_F) \quad \text{Eq. (2.15)}$$

This potential is completely known, except for the value of z_0 .

$$P_F = g(z - z_0) \quad \text{Eq. (2.16)}$$

With equations 2.13, 2.14, 2.15, and 2.16, the potential theory for the calculation of water waves are defined as following:

$$\frac{\partial^2 P}{\partial x^2} + \frac{\partial^2 P}{\partial y^2} + \frac{\partial^2 P}{\partial z^2} = 0 \quad \text{Eq. (2.17)}$$

$$\frac{\partial P}{\partial t} + g(z - z_0) + \frac{p}{\rho} = 0 \quad \text{Eq. (2.18)}$$

The wave theories, which are described in the following chapters, are all based on these equations for the conservation of mass (Eq. (2.17)) and the conservation of momentum (Eq. (2.18)).

2.4.4 AIRY theory

The linear wave theory or Airy wave theory named after [Airy 1845] is one of the most important and used wave theories. In oceanography, especially in the deep-water zone, these equations are very accurate. Hence, the theory is very often used for initial estimations. A detailed description of the derivations of the equations is not given in this work, but they can be found in [Salmon 2018] or [Malcherek 2010].

The AIRY theory is based on the potential theory. Thus, the assumptions and simplifications from chapter 2.4.3 also apply for AIRY waves. In addition to these, several assumptions for the shape of the wave are important. Following [Ausschuß für Küstenschutzwerke 2002], the following assumptions are used for the AIRY theory:

- Symmetric wave profile (ideal sinusoidal surface)
- Small amplitudes ($WH \ll \lambda$ and $WD \gg WH$)
- Even ground
- Ideal fluid (frictionless, incompressible, homogeneous)
- Air movement has no impact on the wave movement

Based on these requirements, the equations for the AIRY theory are derived. [Ausschuß für Küstenschutzwerke 2002] differentiates between the three categories deep-water, intermediate-water and shallow-water. The deep-water zone and the shallow-water zone are special cases with additional assumptions which further simplify the equations. The general terms are used in the intermediate zone and are given in the following overview.

The elongation of the water surface is defined via the wave height and the specific phase angle. This is the general assumption for AIRY waves. There is no difference between the separate zones.

$$\zeta(t) = \frac{WH}{2} * \cos(\Phi(t)) \quad \text{Eq. (2.19)}$$

The wave speed is defined as the ratio between the wavelength and the wave period. Hence, the general equation for AIRY waves is as follows.

$$v(t) = \frac{\lambda}{T} = \frac{g}{\omega} * \tanh(k * WD) = \sqrt{\frac{g}{k} * \tanh(k * WD)} \quad \text{Eq. (2.20)}$$

Furthermore, the wavelength is given as:

$$\lambda = \frac{g}{\omega} * T * \tanh(k * WD) \quad \text{Eq. (2.21)}$$

The horizontal component of the orbital velocity of a water particle in the water column is given as

$$u_{\Phi, \text{horz}} = \frac{WH}{2} * \omega * \frac{\cosh[k * (z + WD)]}{\sinh(k * WD)} * \cos(\Phi) \quad \text{Eq. (2.22)}$$

And the vertical component as:

$$u_{\Phi, \text{vert}} = \frac{WH}{2} * \omega * \frac{\sinh[k * (z + WD)]}{\sinh(k * WD)} * \sin(\Phi) \quad \text{Eq. (2.23)}$$

In addition to the orbital velocity, [Büsching 2002] derived the following equations to describe the axes of the orbit of the water particles with the horizontal axis a_{horz} and the vertical axis a_{vert} . The coordinate z is defined from the ocean surface in positive direction towards the sky.

$$a_{\text{horz}} = WH * \frac{\cosh\left(\frac{2\pi}{\lambda}(z + WD)\right)}{\sinh\left(\frac{2\pi}{\lambda} * WD\right)} \quad \text{Eq. (2.24)}$$

$$a_{\text{vert}} = WH * \frac{\sinh\left(\frac{2\pi}{\lambda}(z + WD)\right)}{\sinh\left(\frac{2\pi}{\lambda} * WD\right)} \quad \text{Eq. (2.25)}$$

2.4.5 Stokes theory

A further development of the wave theory of [[Airy 1845, 1952 [reprint]] from 1845 is the theory of [Stokes 2009] from 1847. The main difference between these two theories is that [Stokes 2009] considers the nonlinear terms. This is important, because the linear theory is only valid for small amplitudes and this condition changes when the waves travel in shallow-water zones and change their shape and behavior. In Figure 2-9, typical wave shapes are shown.

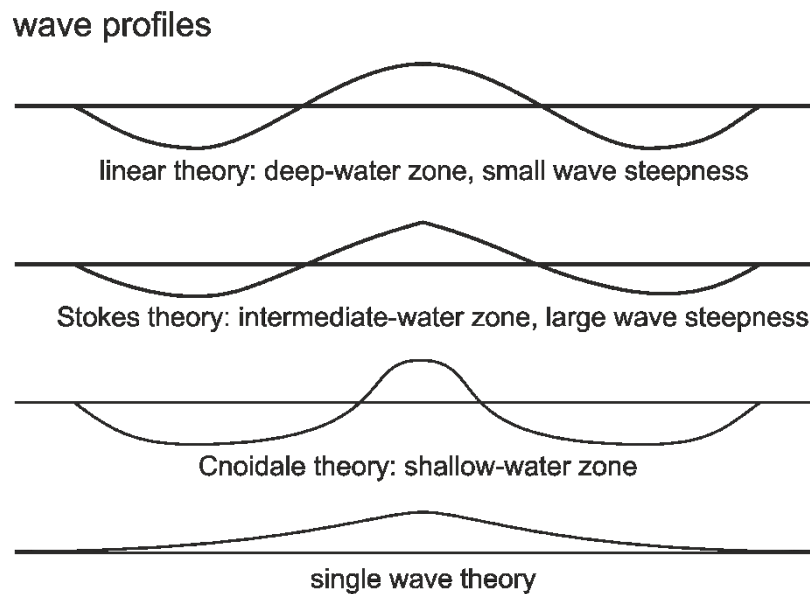


Figure 2-9: Wave shape comparison [Le Méhauté 1976]

Comparison of different typical wave shapes. In the first row, the sinusoidal wave is shown, which is assumed in the linear theory. The second row shows a wave with a larger steepness as considered by [Stokes 2009]. The third row shows a very long wave, which is typical in shallow-water regions and which is calculated with the cnoidal theory, because the Stokes theory is not valid anymore. In the last row, a single wave is shown, which is another extreme case for the typical wave theories. This kind is typical for tsunamis.

Just as the theory of [Airy 1845] the Stokes theory is based on the potential theory. Hence, every assumption of the potential theory (see 2.4.3) is also a requirement for the Stokes theory. Thus, the Laplace equation, the Bernoulli equation and the boundary conditions at the ground and the surface of the water column are equal. Such as it is obvious that this theory is also not exact, but for specific cases it is more accurate than the linear wave theory. A detailed derivation of the Stokes theory would be beyond the scope of this work. [Graw 1995] gives a short overview of the derivation and an overview of the cases for which this theory is useful. In [Fenton 1979], a higher order Stokes theory is derived. In this thesis, the third order Stokes theory was used. In the following, the general equations of the theory are given from [Ausschuß für Küstenschutzwerke 2002].

The profile of the free surface of the water consists of three terms and includes not the wave height, as in the linear theory, but the amplitude A instead.

$$\begin{aligned}\zeta(t) = & Z * \cos(\Phi(t)) \\ & + \frac{k}{4} Z^2 * \frac{\cosh(k WD)[2 + \cosh(2k WD)]}{\sinh^3(k WD)} * \cos(2\Phi(t)) \\ & + \frac{3}{64} k^2 Z^3 * \frac{1 + 8 \cosh^6(k WD)}{\sinh^6(k WD)} * \cos(3\Phi(t))\end{aligned}\quad \text{Eq. (2.26)}$$

The wave speed is described as follows:

$$v(t) = \sqrt{\frac{g}{k} \tanh(k WD) \cdot \left[1 + k^2 Z^2 \frac{8 + \cosh(4k WD)}{8 \sinh^4(k WD)} \right]}\quad \text{Eq. (2.27)}$$

Hence, the wavelength, which is defined as the product of the wave speed c and the period T , is given as

$$\lambda = \frac{g}{\omega} T * \tanh(k WD) \cdot \left[1 + k^2 Z^2 \frac{14 + \cosh^2(2k WD)}{16 \sinh^4(k WD)} \right]\quad \text{Eq. (2.28)}$$

The horizontal orbital velocity is given as

$$\begin{aligned}u_{\Phi, \text{horz}} = & v(t) * \left[k * Z * \frac{\cosh[k(z + WD)]}{\sinh(k WD)} * \cos(\Phi(t)) \right. \\ & + \frac{3}{4} k^2 Z^2 * \frac{\cosh[2k(z + WD)]}{\sinh^4(k WD)} * \cos(2\Phi(t)) \\ & \left. + \frac{3}{64} k^3 Z^3 * \frac{11 - 2 \cosh(k WD)}{\sinh^7(k WD)} * \cosh[3k(z + WD)] * \cos(3\Phi(t)) \right]\end{aligned}\quad \text{Eq. (2.29)}$$

and the vertical orbital velocity is defined as

$$\begin{aligned}u_{\Phi, \text{vert}} = & v(t) * \left[k * Z * \frac{\sinh[k(z + WD)]}{\sinh(k WD)} * \cos(\Phi(t)) \right. \\ & + \frac{3}{4} k^2 Z^2 * \frac{\sinh[2k(z + WD)]}{\sinh^4(k WD)} * \cos(2\Phi(t)) \\ & \left. + \frac{3}{64} k^3 Z^3 * \frac{11 - 2 \cosh(k WD)}{\sinh^7(k WD)} * \sinh[3k(z + WD)] * \cos(3\Phi(t)) \right]\end{aligned}\quad \text{Eq. (2.30)}$$

2.5 Turbulence

Turbulence surrounds us every day. It is a keyword for every chaotic and fast fluctuating thing in our lives, such as the movement of leaves in the wind or fast-moving people in a crowded street. In fluid mechanics, turbulent flow is characterized as chaotic motion with strong eddies and intense mixing. Following [Kornev 2013], it is a three-dimensional unsteady flow with chaotic trajectories of the fluid particles, strong mixing and fluctuations arising due to high Reynolds numbers. In this chapter, a brief overview of the general turbulence modeling assumptions is given. First, the basics of averaging are discussed. Secondly, the Reynolds-averaged Navier-Stokes equations are described. Furthermore, the mixing length model of Prandl is explained. Finally, the Reynolds flux model is described.

2.5.1 Averaging and fluctuation values

The description of turbulent effects requires averaging methods due to strong fluctuating values. The most important averaging methods are mentioned in the following section.

2.5.1.1 Time average

The time averaging defines an average of a stochastic function (for example $U(x,t)$) within a defined time interval. For a stationary flow, this type of average leads to an abstraction of the turbulent fluctuations. In the instationary case, it is also known that the choice of the time interval ΔT influences the possibility of losing information on the mean velocity. For these reasons, it is recommended to perform an ensemble average in a strong instationary flow field. The averaging over a time period is useful to get a first impression of the mean flow in a field. The mathematical expression in this work is the bar over the averaged variable.

$$\bar{U}(x) = \lim_{t \rightarrow \infty} \frac{1}{t} \int_0^t U(x, t^*) dt^* \quad \text{Eq. (2.31)}$$

2.5.1.2 Ensemble average

Following [Fiedler, Prof. Dr.-Ing. H. E. 2003], the ensemble average is defined as the arithmetic mean of a large number H of values of a stochastic function $\psi(x,t)$. These mean values are chosen at different times or at well-defined identical conditions of the fluid flow or the process. This type of averaging is used for instationary flows or processes. The mathematical expression in this work is defined by a caret over the averaged variable.

$$\hat{\psi} = \hat{\psi}(x, t) = \lim_{H \rightarrow \infty} \frac{1}{H} \sum_{\eta=1}^H \psi_{\eta}(x, t) \quad \text{Eq. (2.32)}$$

2.5.2 Reynolds-averaged Navier-Stokes equation (RANS)

The calculation and modelling of turbulent flows is still under investigation. The direct numerical simulation (DNS) delivers the most exact solutions for the Navier-Stokes equations, but this kind of calculation needs the most powerful computational effort. One method of modelling turbulent problems involves making use of the Reynolds-averaged Navier-Stokes Equations. These approximations lead to simulations which need only a small part of the computational power compared to DNS. Because of this, RANS simulations are currently the most used for numerical simulations for turbulent flows.

2.5.2.1 Assumptions and derivation of RANS

In a fully developed turbulent flow, the components of the velocity, the pressure and other scalars are split into a mean value and an oscillating value of it.

$$\begin{aligned} u_i &= \bar{u} + u'_i \\ p_i &= \bar{p} + p'_i \\ &\text{etc.} \end{aligned} \tag{2.33}$$

These definitions are inserted into the Navier-Stokes equation

$$\frac{dU_i}{dt} = \frac{\partial U_i}{\partial t} + U_j \frac{\partial U_i}{\partial x_j} = f_i - \frac{1}{\rho} \frac{\partial p}{\partial x_i} + \nu \frac{\partial^2 U_i}{\partial x_j^2} \tag{2.34}$$

and an ensemble average is conducted. The general assumptions and rules of averaging for this problem are well described in [Fiedler, Prof. Dr.-Ing. H. E. 2003], [Spurk and Aksel] or other fundamental text books. The averaging leads to the RANS equations:

$$\frac{\partial U_i}{\partial t} + \bar{U}_j \frac{\partial \bar{U}_i}{\partial x_j} = F_i - \frac{1}{\rho} \frac{\partial \bar{p}}{\partial x_i} + \nu \frac{\partial^2 \bar{U}_i}{\partial x_j^2} - \frac{\partial (\overline{U'_j U'_i})}{\partial x_j} \tag{2.35}$$

In this equation, the term $\partial (\overline{U'_j U'_i}) / \partial x_j$ contains the unknown shear stresses in the flow. Hence, for a normal three-dimensional flow 9 additional unknown values occur.

$$-\rho \overline{U'_i U'_j} = -\rho \begin{pmatrix} \overline{u'^2} & \overline{u'v'} & \overline{u'w'} \\ \overline{v'u'} & \overline{v'^2} & \overline{v'w'} \\ \overline{w'u'} & \overline{w'v'} & \overline{w'^2} \end{pmatrix} \tag{2.36}$$

These values are the Reynolds stresses or turbulent apparent stresses [Spurk and Aksel]. Due to symmetrical reasons, this tensor can be reduced to 6 unknown values. These stresses need closure assumptions for their description.

2.5.2.2 The closure problem and the Boussinesq approximation

The closure problem of the RANS equations has been under investigation since the equation was first described. For this reason, a lot of closure models have been developed. The models are grouped by their complexity, i.e. empirical or zero equations models, one equation model, two equation models and others. The empirical models are mostly based on simple linear assumptions with additional constants known from experiments. The more complex two equation models, such as the k- ϵ -model, use two differential equations, which are numerically modeled and also include empirical constants. Thus, there are a lot of different models, which each have their specific weaknesses and strengths for different flow conditions.

Each of these models rely on the approximation of [Boussinesq 1877]. This approximation expresses the shear stresses through a turbulent eddy viscosity.

$$\tau_t = -\rho \overline{u'v'} = H \frac{\partial \bar{u}}{\partial y} = \rho \nu_t \frac{\partial \bar{u}}{\partial y} \quad \text{Eq. (2.37)}$$

With this assumption a new unknown variable, the turbulent eddy viscosity ν_t , occurs. This is the variable which is modelled within the closure models of the RANS equations.

2.5.3 Mixing length model

The mixing length model was developed by [Prandtl 1925]. His hypothesis leads to a simple description of the turbulent eddy viscosity ν_t . The concept is based on the kinetic theory of gases, in which the kinematic durability is defined as follows

$$\nu_d = \lambda_m \sqrt{\overline{U^2}} \quad \text{Eq. (2.38)}$$

In this equation, the term λ_m is the mean free path between the molecules and U the speed of the molecules. [Prandtl 1925] transferred this relationship onto a fluid parcel in a flow and marked the relationship with its specific properties which depend on the location in the fluid flow. Hence, following [Prandtl 1925], the following equation is determined in general applications:

$$\Gamma = \overline{w'\gamma'} = -l^* \sqrt{\overline{w'^2}} \frac{d\bar{\gamma}}{dz} \quad \text{Eq. (2.39)}$$

The variable Γ describes a specific property of the flow. The most common version uses the momentum and leads to the following equation, known as the 1. Prandtl mixing length hypothesis:

$$\tau_t = -\rho \overline{u'w'} = \rho l^* \sqrt{(\Delta z)^2} \left| \frac{d\bar{u}}{dz} \right| \frac{d\bar{u}}{dz} = \rho l_m^2 \left| \frac{d\bar{u}}{dz} \right| \frac{d\bar{u}}{dz} \quad \text{Eq. (2.40)}$$

[Fiedler, Prof. Dr.-Ing. H. E. 2003] mention other properties which can be described by Γ in Eq. (2.39), for example scalar values such as the temperature or the concentration. In the experiments in this work, the concentration field was measured, and the associated mixing length was determined via the following relationship:

$$\tau_t = -\rho \overline{C'w'} = \rho l^* \sqrt{(\Delta z)^2} \left| \frac{d\bar{u}}{dz} \right| \frac{d\bar{C}}{dz} = \rho l_m^2 \left| \frac{d\bar{u}}{dz} \right| \frac{d\bar{C}}{dz} \quad \text{Eq. (2.41)}$$

This model is valid in plane shear layers. [Fiedler, Prof. Dr.-Ing. H. E. 2003] mention that the theory is most accurate in wall boundary layers. Hence, it is an essential theoretical point of view for the experiments in this work.

2.5.4 Reynolds-flux model

The Reynolds-flux model is described by [Wallis 1967] as a concept which “postulates transverse mixing velocities in order to account for transport phenomena in a one-dimensional flow model”. In transport processes, the fluxes of mass, energy or scalar values are considered with γ . Within the Reynolds-flux model, the Reynolds-fluxes $\overline{\Gamma'U_l'}$ are modeled individually. Furthermore, turbulent effects and mixing are regarded. [Wallis 1967] described the turbulent mixing in terms of a lateral mass flux ε_0 . This flux leaves the main flow in the direction of the wall. On the way to the wall boundary layer, it shares its momentum, energy and composition. When it reaches the wall, the flux is bounced back to the main flow.

With respect to the wall shear stress, heat flux and mass transfer

$$\tau_w = \frac{fr}{2} \rho V^2$$

$$\dot{q} = h \Delta T \quad \text{Eq. (2.42)}$$

$$\dot{m} = h_D \Delta c$$

, which are defined by making use of the friction factor fr , the heat-transfer coefficient h and the mass-transfer coefficient h_D , respectively [Wallis 1967] describes the Reynolds-flux with the Reynolds analogy as follows:

$$\varepsilon_0 = \frac{fr}{2} \rho V = \frac{h}{c_p} = \rho h_D \quad \text{Eq. (2.43)}$$

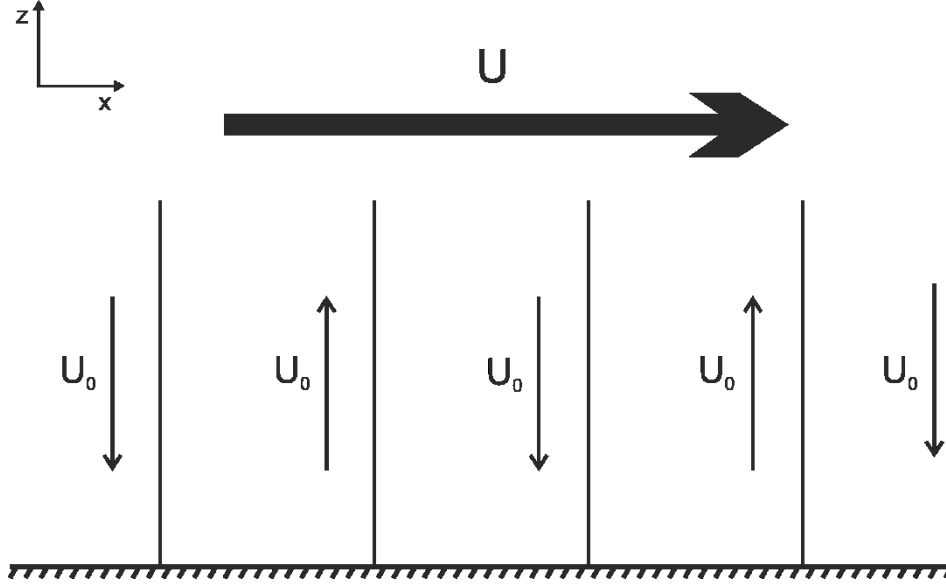


Figure 2-10: Reynolds-flux model

The transversal velocity U_0 leaves the main flow towards the wall. At the wall, it is bounced back again towards the main velocity.

To understand the Reynolds-flux concept, one can imagine a transversal velocity U_0 which leaves the main flow U . [Wallis 1967] assumes that half of the mean transversal flux is moving towards the wall and the other half is bounced back from the wall. Idealized, both fluxes have the velocity U_0 , such that the following relationship between U_0 and the mass flux ε_0 is given:

$$\varepsilon_0 = \frac{1}{2} \rho U_0 \quad \text{Eq. (2.44)}$$

Comparing this relationship with Eq. (2.43) yields

$$U_0 = fr \cdot U = \frac{2h}{\rho c_p} = 2h_D \quad \text{Eq. (2.45)}$$

Thus, the friction factor f can be interpreted as the ratio of the lateral fluctuating velocity to the main stream velocity. [Wallis 1967] mentions, that the flux models in Eq. (2.43) and Eq. (2.45) are the simplest analytical models which account for transfer phenomena in convection. Furthermore, [Wallis 1967] refers to an alternative description which relies on the assumption of a probability diffusion pd of the transverse velocity v .

$$p(v)dv = \frac{1}{U_0} \exp\left(-\frac{v}{U_0}\right) dv \quad \text{Eq. (2.46)}$$

This expression does not change the relationship given in Eq. (2.45), but, following [Wallis 1967], it becomes more important in the context of net mass transfer.

By considering an additional mass flux through a permeable wall, the mixing process is changed

$$\dot{m} = \rho v_{ad} \quad \text{Eq. (2.47)}$$

with v_{ad} being the transverse velocity of the additional flux, which leaves the wall. This changes the mixing process, which is controlled by the transverse velocity v of the main stream. Hence, the respective fluid velocities are superposed.

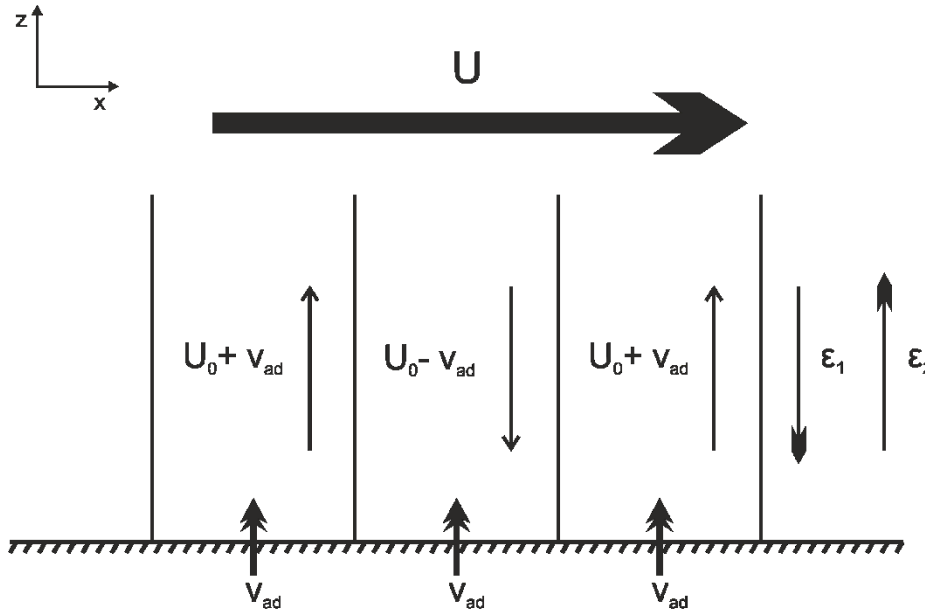


Figure 2-11: Reynolds-flux model with additional inflow condition

The transversal velocity U_0 leaves the main flow towards the wall. At the wall, it is bounced back again towards the main velocity. From the walls, an additional inflow with the velocity v_{ad} is assumed. The velocity components interfere with each other due to superposition.

Following this assumption, it is obvious that the velocity towards the wall is the summation of $U_0 - v_{ad}$ and the velocity from the wall as $U_0 + v_{ad}$. Considering the Reynolds-flux, it is provided by the following two different fluxes:

$$\varepsilon_1 = \frac{1}{2}\rho(U_0 - v_{ad})$$

$$\varepsilon_2 = \frac{1}{2}\rho(U_0 + v_{ad})$$
Eq. (2.48)

Similar to the assumptions for Eq. (2.48), which use the probability diffusion of the velocity v , the solution for the ingoing flux is

$$\varepsilon_1 = \rho \frac{U_0}{2} \exp\left(\frac{-v_{ad}}{U_0}\right)$$
Eq. (2.49)

and for the outgoing flux

$$\varepsilon_2 = \rho v_{ad} + \rho \frac{U_0}{2} \exp\left(\frac{-v_{ad}}{U_0}\right)$$
Eq. (2.50)

By substituting U_0 and v via Eq. (2.44) and Eq. (2.47), respectively the final solutions for the ingoing and outgoing Reynolds-fluxes are

$$\varepsilon_1 = \varepsilon_0 \exp\left(\frac{\dot{m}}{2\varepsilon_0}\right)$$

$$\varepsilon_2 = \dot{m} + \varepsilon_0 \exp\left(\frac{-\dot{m}}{2\varepsilon_0}\right)$$
Eq. (2.51)

2.6 Mixing and transport mechanisms

2.6.1 Transport mechanism

The transport of a material or fluid underlies three different transport mechanisms: the diffusive transport, the convective transport and the turbulent transport.

The diffusive transport is driven by a strong gradient, for example in concentration or temperature. Thereby, a diffusive pressure is generated between the different potentials. Hence, a flux of the exchange value is initiated. The exchange occurs within the Brownian motion of the molecules. The diffusive transport occurs in resting and in flowing media. The most common equation is the diffusion equation according to Fick.

$$\frac{\partial C}{\partial t} = D \frac{\partial^2 C}{\partial z^2} \quad \text{Eq. (2.52)}$$

On the other hand, convective transport occurs only in moving media. The flux of the exchange value depends on the change of the position of the particles in the medium during its movement. Hence, it is obvious that the convective transport in flow direction is much higher than the diffusive flux. Following [Stierstadt 2010], transport processes can be described via a general linear relation:

$$J_x = L_{XY} \mathcal{F}_Y \quad \text{Eq. (2.53)}$$

The first factor is called the kinematic coefficient, which is proportional to the transport coefficients such as the diffusion coefficient D . The second factor \mathcal{F} describes a specific variable of the effect which is transported. [Stierstadt 2010] mentions, that the coefficients rely on measurements and experience. Furthermore, the general equation is only valid for small gradients of L and \mathcal{F} . [Stierstadt 2010] gives an overview of the different transport equations which are based on Eq. (2.53).

Table 2-3: Overview of linear transport processes by [Stierstadt 2010]

$\begin{matrix} \text{F}_{Y,j} \\ J_{X,i} \end{matrix}$	$\begin{matrix} j=1 \\ \nabla(1/T) \\ [K^{-1}m^{-1}] \end{matrix}$	$\begin{matrix} j=2 \\ -\frac{1}{T}\nabla(v) \\ [K^{-1}s^{-1}] \end{matrix}$	$\begin{matrix} j=3 \\ -\frac{1}{T}\nabla(\xi) \\ [JK^{-1}m^{-1}] \end{matrix}$	$\begin{matrix} j=4 \\ -\frac{1}{T}\nabla(\phi_c) \\ [VK^{-1}m^{-1}] \end{matrix}$	$\begin{matrix} j=5 \\ \frac{1}{T}\nabla(E) \\ [VK^{-1}m^{-2}] \end{matrix}$	$\begin{matrix} j=6 \\ \frac{1}{T}\nabla(B) \\ [VsK^{-1}m^{-3}] \end{matrix}$
$\begin{matrix} i=1 \\ J_Q \\ (Jm^{-2}s^{-1}) \end{matrix}$	Heat conduction $L_{QT}(\lambda)$	Shear-thermo-effect L_{Qv}	Diffusion thermo effect $L_{Q\xi}$	Electrocaloric effect $L_{Q\phi_c}$	L_{QE}	L_{QB}
$\begin{matrix} i=2 \\ J_p \\ (Jm^{-3}) \end{matrix}$	Thermo impulse current $L_{pT}(\lambda)$	Viscous shear current L_{pv}	Diffusion impulse current $L_{p\xi}$ {Dufour Effect}	Electro impulse current $L_{p\phi_c}$ {Peltier Effect}	L_{pE}	L_{pB}
$\begin{matrix} i=3 \\ J_N \\ (m^{-2}s^{-1}) \end{matrix}$	Thermo diffusion $L_{NT}(\lambda)$ {Soret Effect}	Shear-diffusion L_{Nv}	Diffusion $L_{N\xi}(D)$	Electro kinetics $L_{N\phi_c}$	L_{NE}	L_{NB}
$\begin{matrix} i=4 \\ J_q \\ (Am^{-2}) \end{matrix}$	Thermocurrent L_{qT}	Shear-electric-effect L_{qv}	Diffusion electric effect $L_{q\xi}$	Electric conductivity $L_{q\phi_c}$	L_{qE}	L_{qB}
$\begin{matrix} i=5 \\ J_{Mt} \\ (Am^{-1}) \end{matrix}$	Thermo polarization current L_{MeT}	Shear polarization current L_{Mev}	Polarization diffusion $L_{Me\xi}$	Electro polarization current $L_{Me\phi_c}$	Polarisation drift $L_{MeE}(D_e)$	L_{MeB}
$\begin{matrix} i=6 \\ J_{Mn} \\ (As^{-1}) \end{matrix}$	Thermo spin current L_{MmT}	Shear-spin-current L_{Mmv}	Spin diffusion $L_{Mm\xi}$	Electro spin current $L_{Mm\phi_c}$	L_{MmE}	Spin drift $L_{MmB}(D_M)$

The turbulent transport occurs in addition to the diffusive and the convective transport due to turbulent effects. Following [Kraume 2012], the turbulent transport is determined by the rebuilding and dissociation of vortices. In turbulent flows, the main flow velocity is overlaid by a fluctuating velocity component. This velocity is based on the occurrence of the vortices. The size of the vortices depends on the space between the walls surrounding the flow field and on the flow conditions. Compared to the convective transport, the size of the vortices is much larger, than the mean free distance between the molecules. [Kraume 2012] mentions, that the turbulent transport can be described as a special type of the convective transport, such that the same mathematical description can be used. [Prandtl et al. 2012] revealed a strong increase of momentum, heat and mass flux due to turbulent fluctuations. The description of the turbulent transport relies on different assumptions and solutions. One of the most common descriptions is the analogy of [Boussinesq 1877] (see 2.5.2.2).

2.6.2 Mixing mechanisms

Mixing describes the connection of two or more different materials or fluids into one homogeneous material or fluid. [Kraume 2012] defines mixing as a result of transport processes and the diffusion of mass in a specific volume. Following the remarks of [Dimotakis 2005], the mixing of fluids takes place in three different stages.

The first stage is the process of entrainment. Entrainment describes the inflow of a resting fluid into a moving one which is flowing over the resting one. [Ellison and Turner 1959] explain this effect with two examples, namely with plumes and with jets. These examples are fully turbulent with a nearly constant, non-turbulent main stream which flows into a resting environment. Hence, in the transition zone, a fully turbulent stream encounters a completely resting fluid. Furthermore, it is observed that the resting fluid is entrained with the turbulent flow. [Turner 1986] mentions a dependency of the inflow of the resting fluid into the turbulent zone. He described a proportional constant (entrainment constant) for the relation between these two zones based on mass, momentum and lift. Due to the complexity of this topic, detailed explanations are waived at this stage. Further information can be found in [Ellison and Turner 1959], [Turner 1986] and others.

The second stage of mixing is the dispersion. This process includes the dispersion of single volume or fluid elements into the surrounding environment. Following [Kraume 2012], this phenomena is defined completely within the linear transport equations.

The last stage is the diffusion. This process relies on the molecular movement of particles and occurs in in every case. In combination with the other stages, the surface between the different fluids is maximized and the diffusion occurs much faster.

2.7 Oceanic Boundary Layer

The bottom boundary layer in oceans is shaped by steady currents, wave action, the ground properties and the shape of the ground itself. This work focuses on the benthic boundary layer which is described first in this chapter. Second, the effect of a steady current on the boundary layer over a random permeable bed is discussed. After this, the oscillating boundary layer is mentioned and at the end, the influence of the shape is briefly described.

2.7.1 The benthic boundary layer

The benthic boundary layer (BBL) is defined by [Boudreau and Jørgensen 2001] as „that part of the marine environment that is directly influenced by the presence of the interface between the bed and its overlying water“. In this layer, most of the action regarding organisms and exchange processes takes place. The environments of the upper ground and the lower marine side converge in this zone. Thus, it is a very important area not only with respect to fluid mechanics with friction and turbulence being at their maximum in this area, but also for organisms which live in the ground and above it. The exchange processes between these bounded environments are under steady investigation with respect to chemical reactions, groundwater fluxes and mixing of heat, energy and pollutions.

Following [Boudreau and Jørgensen 2001], the general benthic boundary layer is layered into 6 sublayers.

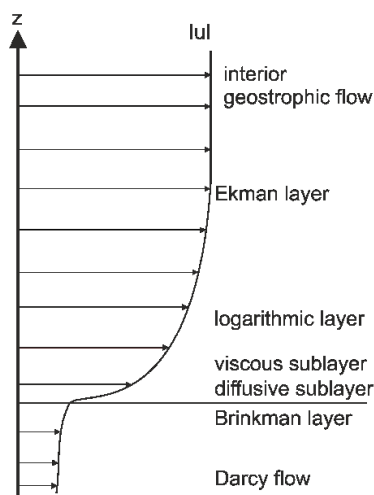


Figure 2-12: Benthic boundary layer

A schematic sketch of the benthic boundary layer. [Boudreau and Jørgensen 2001] split the BBL into 6 sublayers: the interior geostrophic flow as the mean flow, the Ekman layer, the logarithmic sublayer, the viscous and the diffusive sublayer, along with the Darcy flow within the permeable ground and the Brinkman layer as the interface between the inner Darcy flow and the outer flow of the water column.

This profile is valid for a steady current above a seabed. The zone in which the most mixing and turbulent transport of SGD occurs is located directly in and above the permeable seabed.

2.7.2 Boundary layer above a permeable medium

The benthic boundary layer composition of [Boudreau and Jørgensen 2001] is defined from a global point of view. Considering the boundary layer directly above a permeable medium lead to the following structure of the boundary layer.

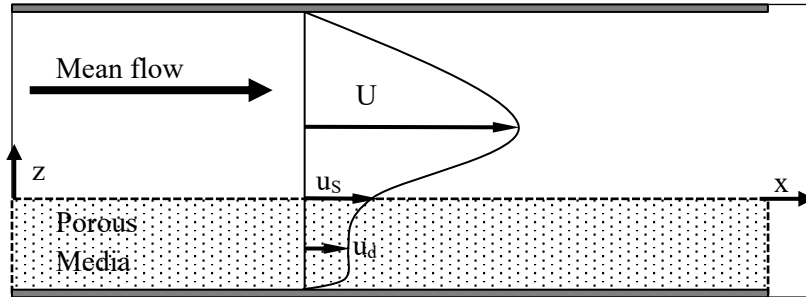


Figure 2-13: Boundary layer above a permeable bed

Boundary layer development above a permeable medium following the experiments of [Agelichaab et al. 2006]. The experiments were conducted under a steady flow above the bed. It is shown that a slip velocity u_s occurs directly at the border between the bed and the freestream.

The profile, which is shown in Figure 2-13, was first developed by [Brinkman 1949], who developed a partial differential equation to couple the known Darcy zone and the free stream zone above it.

$$\frac{\mu U}{\kappa} = -\frac{dp}{dx} + \mu' \frac{d^2 U}{dz^2} \quad \text{Eq. (2.54)}$$

The following investigation of the flow in and above porous media aims to find a solution for the apparent viscosity μ' of [Brinkman 1949]. The work of [Beavers and Joseph 1967] is one of the first experimental studies in this field and the most cited in later works. They used a water channel with a steady current setup and measured the mass flux with different porous materials. The results of the experiments were, that the boundary layer has a great impact on this mass flux and that the used material has the largest influence on the development of this boundary layer. [Ochoa-Tapia 1995] developed new boundary conditions for this problem and compared them to the experimental results of [Beavers and Joseph 1967]. This boundary layer concept was improved by [Alazmi and Vafai 2001]. [Tachie et al. 2003], [Agelichaab et al. 2006] and [Arthur et al. 2009] used the same experimental setup and studied different point of views. They used a porous ground built out of small pipes. These were varied in diameter and distance and so the porosity of the ground model was variable. The results of these experiments were that the thickness of the boundary layer above permeable materials depends on the volume friction factor or rather on the porosity. In all of these studies, the flow field relies on a steady current condition. Following [Nielsen 1994], the wave-induced boundary layer is much thinner than the boundary layer under a steady current. Thus, the wave-induced velocity field has a higher impact on the underlying porous medium.

2.7.3 Oscillating bottom boundary layer

The oscillating boundary or Stokes layer occurs at a boundary which is subjected to oscillating flow conditions. These conditions are the normal case in wave-dominated environments in the ocean. Following [Nielsen 1994], the general equation to define the thickness of a boundary layer is given by the following relation

$$\delta \propto \sqrt{\nu_t T} \quad \text{Eq. (2.55)}$$

where the period T and the eddy viscosity ν_t are the dominating values. The influence of this kind of boundary layer can be explained with the following example. For a tidal flow with a period of 12h, the thickness of the layer due to a constant value of ν_t is approximately sixty-six times thicker than that of a wave with a period of 10s. Hence, the bottom boundary layers under wave motion are always several times thinner than the layers due to a constant flow field. This fact is very important for sediment transport. [Nielsen 1994] mentions, that with a thinner boundary layer, the shear stress at the ground is higher. This may also affect the transport mechanism directly above the ground due to submarine groundwater discharge.

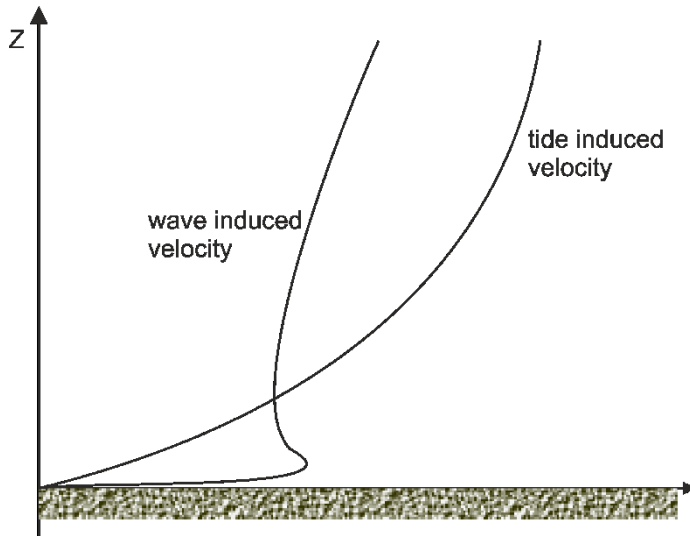


Figure 2-14: Comparison of wave and tide induced velocity profiles

The diagram shows a water column with depth Z . The wave induced velocity profile shows a thinner boundary layer at the bottom than the tide induced velocity profile. The main velocity is higher for the tides, but the influence at the ground is much less.

The typical behavior of the velocity fields is shown in Figure 2-14. It is obvious that the maximum speed of the tidal flow is much higher than the speed under the wavy environment. Considering the bottom boundary layer, it is shown that the tidal bottom boundary layer is much thicker. Hence, the maximum speed near the bottom is much smaller than the maximum speed of the wave-induced velocity profile

near the seabed. The peak in the velocity field for the wave-induced velocity is due to the velocity defect which occurs because of the oscillating behavior of the flow field.

2.7.4 Influence of the shape of the ground

The bottom boundary layer is influenced by the type of flow above it (see 2.7.2 and 2.7.3) and the specific properties of the ground such as the permeability (see section 2.3). Another important impact factor is the shape of the ground. This shape is changed by the occurrence of plants or animals, but the most important change is due to sediment transport processes. This transport can be separated into different types. On the one hand, there is the pure suspended load which rises up in the water column and flows with the main stream. On the other hand, there is the bed load. The bed load describes the skidding, rolling and saltation of sediment particles. With this movement of the upper layer of the seabed, erosion and deposition occur due to mass transport. This mass transport often leads to the development of ripples. Due to the complexity of this topic, only the influence of a typical oscillating ripple structure, which occurs in sandy sediment in shallow zones, will be discussed. Further information can be found in [Karow 2015], [Nielsen 1994], [Allen 2001] and others.

One typical oscillating ripple structure is a symmetric ripple which occurs in shallow waters. It is characterized by the fact that the length from crest to valley is identical on both sides of the ripple crest. Thus, the structure is exactly symmetric. In the following Figure 2-15, a schematic view of such a ripple is given.

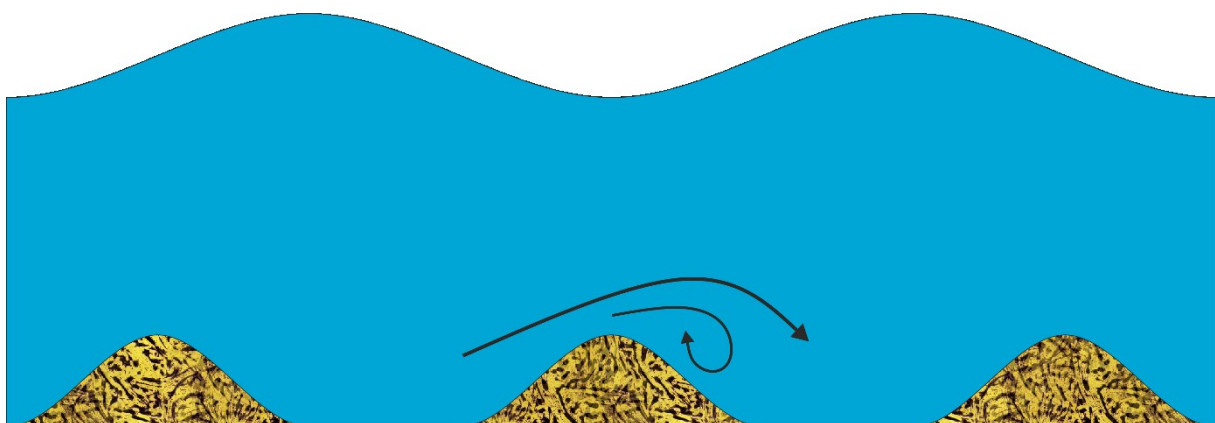


Figure 2-15: Symmetric orbital ripples

The symmetric orbital ripples are shown under a schematic wave. The distance between two ripple crests is called the ripple wavelength. During the flow over a ripple, a vortex is built up behind the crest. This phenomenon occurs in both directions under wavy conditions. Here, only one direction is shown for simplification.

Considering a stream above the ripple in horizontal direction, a vortex is built up behind the ripple crest due to a critical value of the ripple steepness. Under waves, these vortices alternate on both sides of the ripple. [Dingler and Clifton] found out that the ripple wavelength of symmetric orbital ripples linearly depends on to the orbital diameter of the predominating waves. Experiments based on this setup were conducted and analyzed by [Pedersen et al. 2004].

3 Experimental setup

In this section, the experimental setup is described in detail. First, the water channel is described. Secondly, the elements which were used to transform the water channel into a wave channel are explained. After this, the construction of the channel floor and its elements are illustrated. Finally, the setup for the final measurements is explained.

3.1 Water channel

The experiment is conducted in the water channel of the chair of fluid mechanics at the University of Rostock. This channel was formerly used for experiments with stratified fluids and constant flows. In Figure 3-1, the CAD Model of the channel is shown.

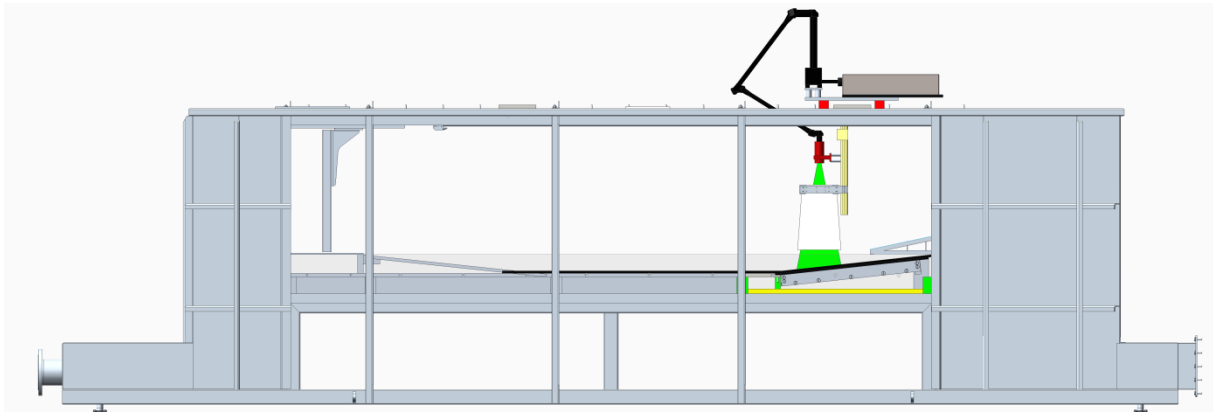


Figure 3-1: Water channel

The water channel is situated at the chair of fluid mechanics at the University of Rostock. It further consist of two additional basins of 4.5m³ volume which are not shown in this figure.

The channel is built of stainless steel and has a length of 5 m and a width of 0.8 m. The height of the visible part of the Channel is 0.88 m. The height of the usable measurement area is reduced by the synthetic ground to a height of 0.78 m. The facility has two water tank systems for filling the channel. This design was developed for stratification experiments in earlier studies. In this work, only one basin was used for mixing and filling water into the water channel. The tank has a filling capacity of 4.5 m³ of water. This water is pumped into the channel with a radial pump with a maximum power of 5.4 kW ($Q = 140 \text{ m}^3/\text{h}$, $H_F = 14.22 \text{ m}$) and a constant filling volume is guaranteed with an additional weir section between the channel and the water basins.

For the experiments on the mixing of groundwater discharge, different reconstructions and additional installations were required, which are described in the following sections.

3.2 Wave channel elements

For the investigation of the turbulent scalar transport above permeable seabeds, wave action is required. The implementation of a wave generator in the water channel requires different elements, which are described in the following section.

3.2.1 Wave generator

In the wave channel, a piston-type wave generator is installed. This generator consists of a linear axis, which is moved with a servo motor controller. On this linear axis, a plate with a size of 770 mm x 650 mm is mounted.

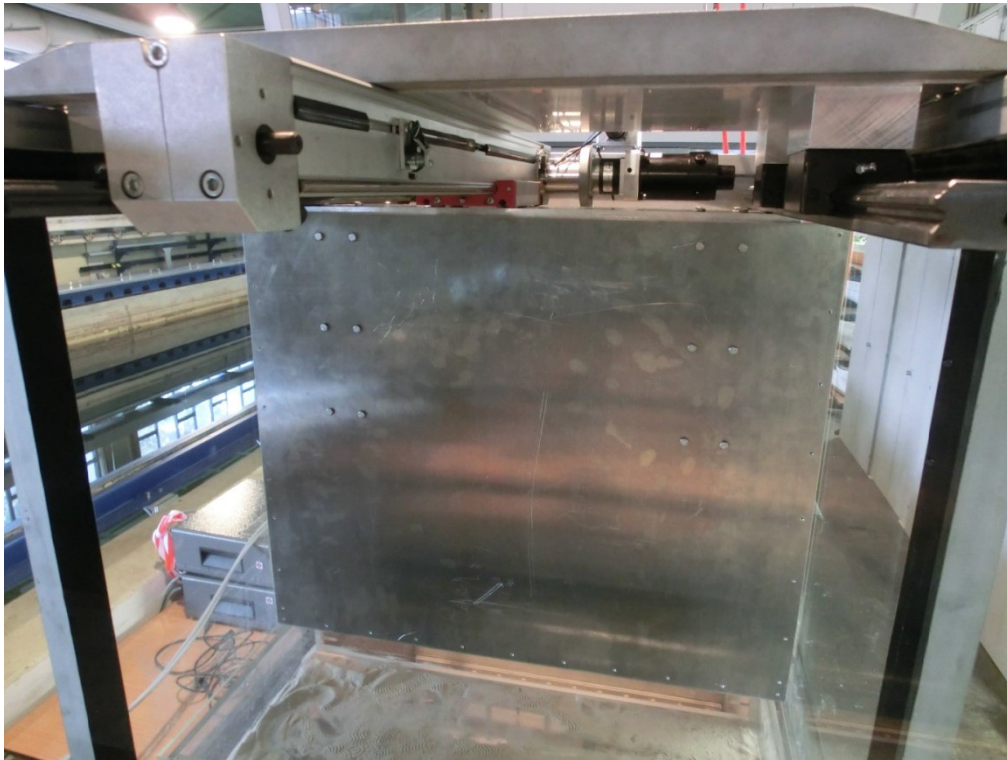


Figure 3-2: Wave generator

The piston type wave generator consists of a generator plate which is mounted on a linear axis. Two additional floating bearings are installed on either side of the linear axis to account for the strong forces during the movement. (Photo by [Bestier 2015])

This application was developed by [Heimbuch 2014]. The piston type wave generator is usually used to generate shallow and intermediate wave setups. The plate is moved and accelerates the whole water column. This movement continues through the channel as a wave front. Then the generator plate moves backwards until it reaches the turning point. From here, the procedure starts again. The acceleration of the water column guarantees a movement of fluid particles directly above the ground. This behavior is a requirement for intermediate or shallow wave types.

3.2.2 Wave absorber

In the experiments, a lot of energy is transferred from the wave generator into the water. In the end, this wave energy has to be removed from the water channel. The biggest problem in wave experiments is that the waves are reflected from solid surfaces. Due to the fact that the measurements should be as undisturbed as possible it is necessary to avoid these reflections. The most common way to reduce these effects is the installation of a wave absorber. In the water channel, a wave absorber based on the research of [Kaufmann 2015] was installed. He compared two different implementations based on the concept of a slightly increasing beach.



Figure 3-3: Wave absorber

Two different wave absorber types were tested based on the concept of a slightly increasing beach. On the left side, a random filling of foam material was used. On the right side, a plate absorber system was used. The single plates increase in size with every step, in order to generate the maximum absorption.

Both systems showed good results regarding the absorption quality [Kaufmann 2015]. Due to the more defined composition of the plate absorber, this type was chosen for the experiments. The absorber will be removed and installed several times between angle setup changes, rendering it is necessary to reproduce the exact behavior of the absorber in every new installation. In the investigations of [Bestier 2015] the mean wave absorption was determined by to be a maximum of 90%. The exact absorption rate is influenced by the wave parameters.

3.2.3 Control and triggering devices

The control of the wave generator system, the tracer pump system and the measurement applications are triggered by several devices. The wave generator consists of the linear axes *LEZ 3* with a maximum traverse path of 798 mm. The power unit is a servo engine EC 86 with 660 W. This engine is controlled by an *iCU-EC* servo controller. All these components are products of the *isel Germany AG*. The controller uses three types of control units: a current controller, a speed controller and an acceleration controller. These units were tuned for the specific case that the water channel is filled to a water level of 30 cm. Furthermore, a PC is integrated into the controller. Hence, every action of the wave generator is controlled by one device. The integrated software application *ProNC* is based on the PAL programming language.

3.2.4 Tracer pump system

In the experiments, a fluorescent tracer medium is pumped into the measurement area. The tracer is stored in a small basin underneath the water channel. The tracer feeding is realized with a parallel connection of two different pumps. The first pump is a gerotor pump m_{zr}-7205F from *HNP Mikrosysteme GmbH*. The second is an immersion pump from *Barwig*. Both are coupled via a three-way valve and are controlled separately.

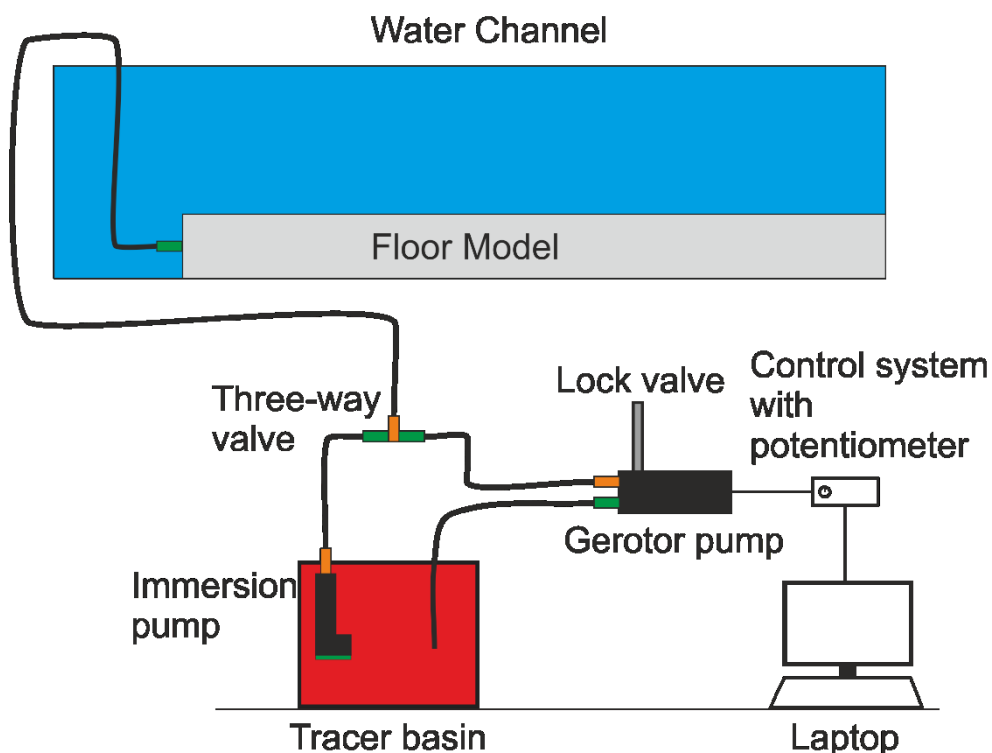


Figure 3-4: Overview of the tracer pump configuration

The figure shows the elements of the tracer pump configuration. The gerotor pump is controlled by a control system or a potentiometer. Additionally, the immersion pump is controlled manually. The pumps are coupled via a three-way valve which also connects them to the water channel.

The immersion pump can realize a maximum flow rate of 22 l/min at a pressure difference of 1,4 bar and is controlled via a laboratory power supply. Hence, the exact fluid quantity during the experiments is measured with an additional experiment. The gerotor pump has a maximum fluid capacity of 288 ml/min at a pressure difference of 30 bar. Furthermore, it has an exactly defined volume flow rate, such that it is possible to deliver an exact amount of tracer with this pump. With this concept, it is possible to work with both pumps at the same time, to work each of them separately or even to change the pump during the experiment. The initial concept was to fill the reservoir underneath the permeable media quickly with the immersion pump and then switch to the gerotor pump to facilitate an exact and constant volume flux during the rest of the experiment. Due to volume reducing concepts and the reduced volume flow rate of the gerotor pump, mainly the immersion pump was used in the final experiments.

3.3 Channel floor concept

3.3.1 Overview and requirements

The water channel is extended by an additional floor which consists of acrylic glass elements. This floor was developed in previous studies to enable the use of sand for scour experiments. Thus, it was built like a basin in which the sand is trapped. The concept is a split into two sections: an underlying section which consists of strong blocks to support the upper structure and the upper section which consists of the wall and ground elements. These sections each include four elements along the channel. All elements are bolted together, and the complete floor is fixed into the channel.

A circular plate is placed in one of the middle elements (see Figure 3-5). This plate is fixed onto ball bearings to enable a rotation of this plate during and between experiments. The control of this part is realized with a wire system lying underneath the upper part of the floor. To support this system, different pulleys are inserted in the underlying section. For the new developments, this system is no longer needed. Furthermore, the floor no longer needs to be transparent such that a cheaper material can be used.

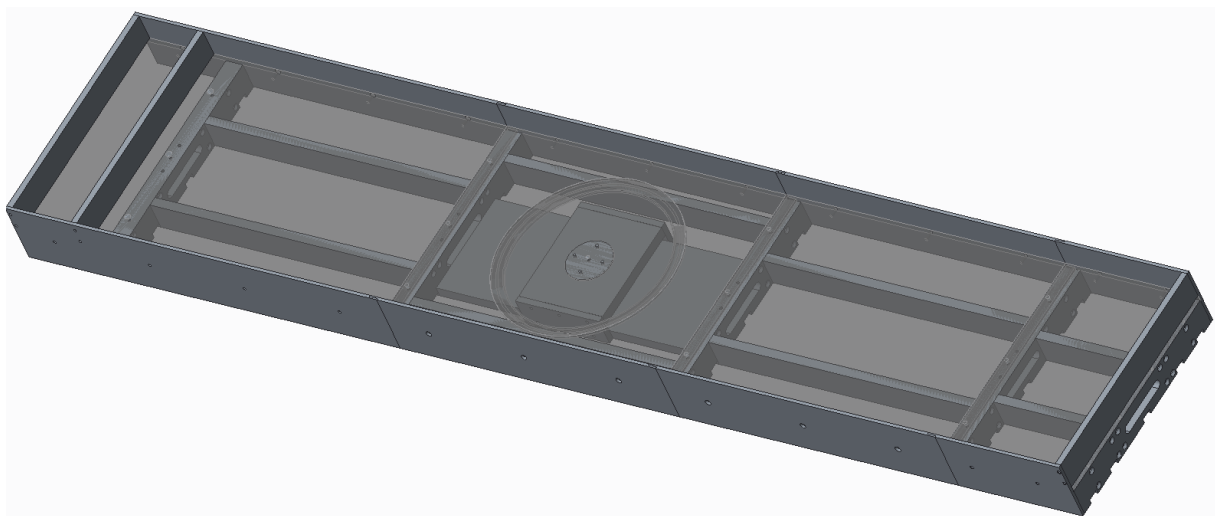


Figure 3-5: Old floor of the water channel

This CAD model of the old floor of the water channel consists of an upper and a lower part. The upper part consists of the wall elements and the lower part (transparent in the figure) makes up the bottom of the measurement area. The lower parts support the upper ones.

For the planned wave experiments, the last section of this old floor is replaced with a new development. To guarantee a smooth reconstruction, the wall elements and the strong cross struts are kept. Hence, the space for the new elements is well defined. Also, the connection elements are not changed.

The new floor of the experiment needs to be applicable for different porous ground models. Hence, the following requirements for the new design were determined:

Table 3-1: Requirements for new floor concept

Requirement	Issue	Concept	Limits
Large floor area	Flow field	Big basin	Width of the channel and length of the floor element
Flexible angle adjustment	Different measuring concepts	Flexible hinge and angle	Depth of the water column and applications
Smooth overlap between channel and porous media section	No production of random turbulence	Rubber material covering the entire ground	Connections between different materials
Plane outflow of tracer fluid underneath the measurement area	No plumes in the experiments	Different volume reduction plates (see 3.3.2)	Inflow
Connection between the new and the old section	Coupling of the floor elements	Similar connector and composition of single elements	Dimensions of old structure
Reduction of dynamic effects	Neglect errors due to oscillations	Strong elements and weights	Space in the channel

The new floor design following the defined requirements above. The construction is split into three subassemblies. This breakdown is needed due to functional and configurational reasons. The underlying part is the first element which is mounted in the channel. The second element is the upper part which is placed on top of it. Once these parts have been set and mounted, they will not change their positions anymore. The last subassembly is the porous media application basin (PMAB). The PMAB will support the attachment of the changeable porous media samples and has a variable pitch mechanism. This setup is independently fixated on the upper and lower segments of the construction. Hence, it is possible to change the PMAB easily or to enlarge functional elements of this part.

In Figure 3-6, the breakdown of the subassemblies is shown. The upper part is enlarged with a small ground plate as a crossover between the old parts and the new ones. The lower part consists of two very

strong lengthwise struts which connect the cross struts of the lower part. Another crossbar is mounted onto these lengthwise connectors. This bar works as a stabilizer for the PMAB.

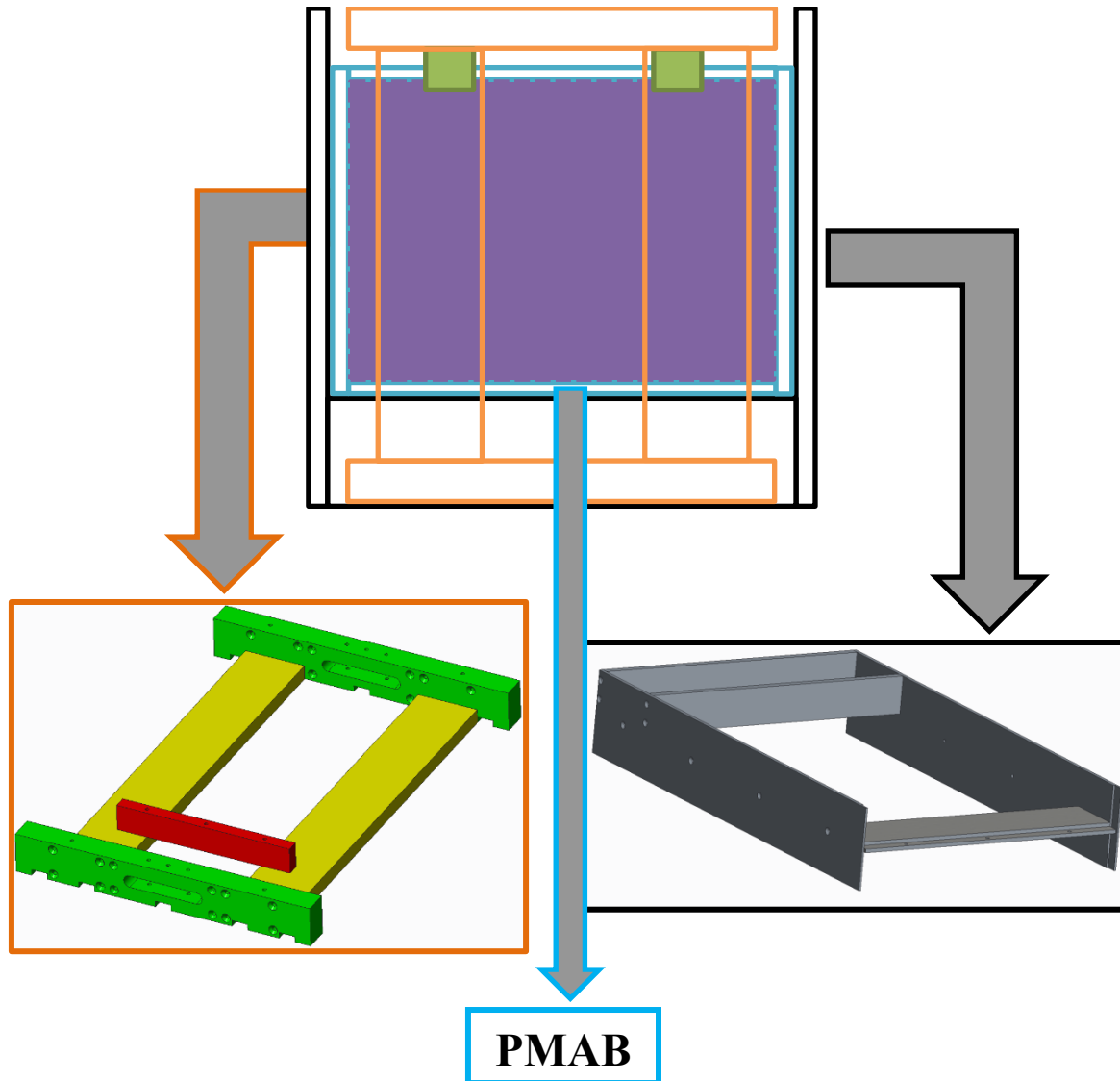


Figure 3-6: Subassemblies of the new floor structure

The upper image shows the schematic plane view of the subassemblies. The orange part is the underlying lower part. In the orange box on the left side, this section is shown as a CAD model consisting of the two (yellow) lengthwise struts, the two (green) crossbars and the (red) stabilizer bar. The black part shows the overlying upper part. The black box on the right side shows a CAD model of this element. Every part in the blue box belongs to the PMAB which is described in detail in 3.3.2. The green boxes represent the fixation mechanism for the PMAB angle selection.

The PMAB is mounted in the front, directly onto the lower section onto the stabilizing bar (red in the figure). At the back, two screws fixate the system via the crossbar (green in the figure). For the use of different angles, the specific angle block is attached at the back.

3.3.2 Porous Media Application Basin (PMAB)

The PMAB was developed mainly for two functions: On the one hand, for the support of the fixation of different permeable ground models, and on the other hand for the realization of different angles of the measurement area. The realization of these functions demands different constructional efforts. The developed concept splits the PMAB into three sections.

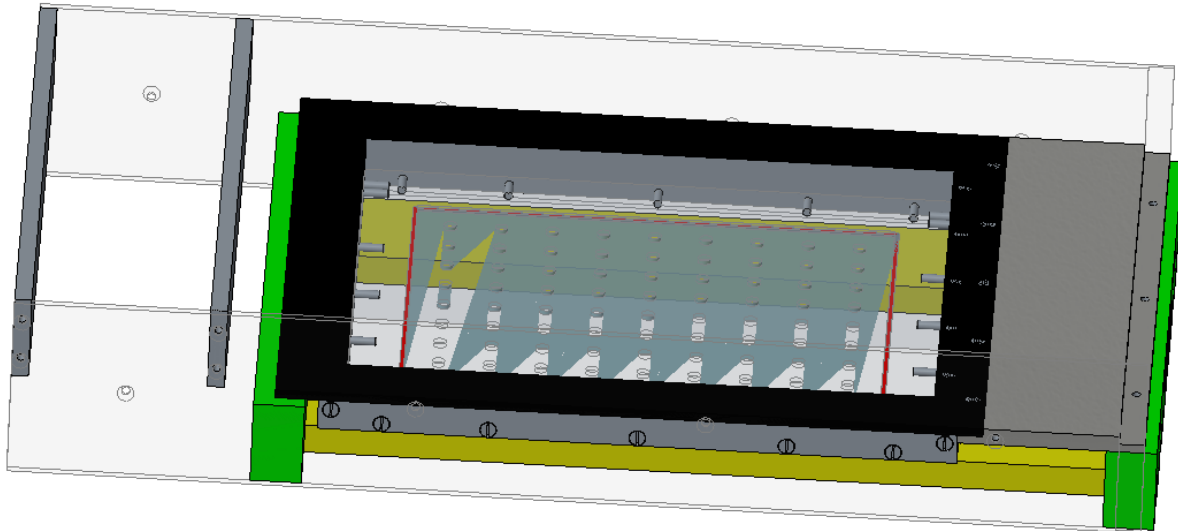


Figure 3-7: CAD model of the PMAB; side view

The CAD model of the PMAB installed in the ground section. The black layer on the top is the rubber mat. Underneath the mat, the frame body is attached. In this frame, a reservoir plate is installed (shown here as transparent in the middle).

The first section is the rubber mat. In Figure 3-7, this is the black colored frame on the top. This mat works as a hinge for the complete PMAB. It is mounted with ten M10 screws at the front (right-hand side in Figure 3-7) to guarantee adequate stability of the changeover between the different sections. In addition to the screws, the rubber mat is fixed with special glue. Several tests showed that the best working glue for this composition of materials is Sikaflex 221. Once set, this one-component polyurethane glue becomes an elastomer, which works perfectly for this setup. Hence, the rubber mat and the underlying frame body are irreversibly glued together.

The second section is the frame body. This part consists of four bars which are screwed together. The front and the back are positioned on the segments of the lower part of the floor construction. The outer sections are variable in their respective positions. The four parts are screwed together at the edges with two M10 screws each (see Figure 3-7). The other 16 M10 screws fixate the reservoir plate.

The third section of the PMAB is the reservoir plate. This plate is the ground of the PMAB and is mounted in the lowest region of the frame body.

The reservoir plate is designed to ensure that the tracer medium is collected and able to flow into the overlying porous media section within a defined area. The reservoir itself is 560 mm long, 470 mm wide and 5 mm high. In Figure 3-8, the two steps in the plate are shown. The inner part enclosed within the first step makes up the reservoir. The plane above the second step can be used for a plate which separates the porous media section and the reservoir. With this, it is possible to define an outflow area underneath the porous media, for example a small cut in the middle of the plane or one specific point.

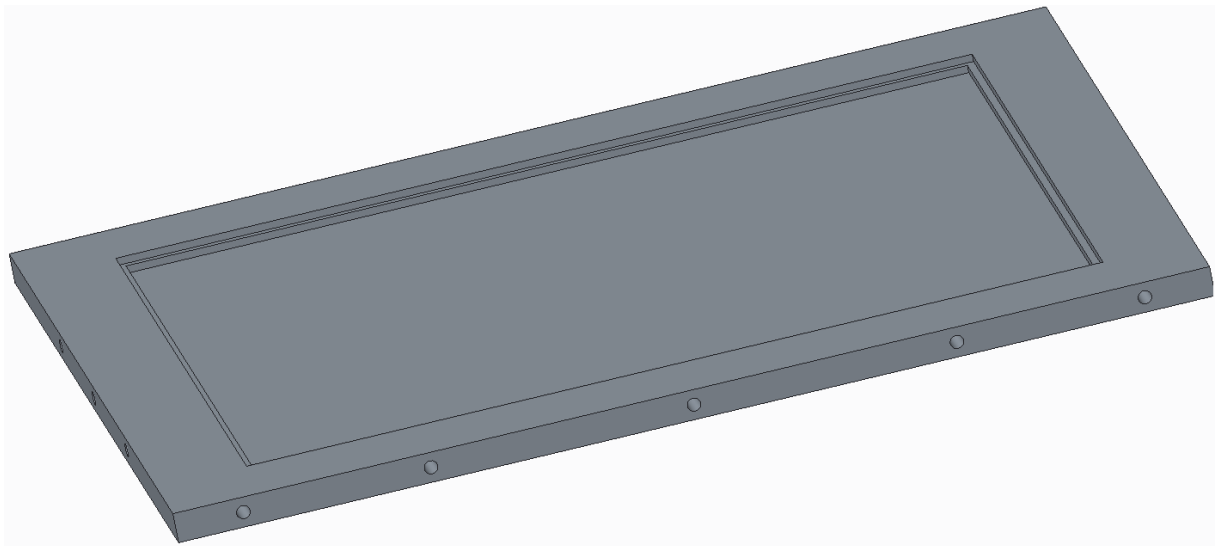


Figure 3-8: Reservoir plate

The plate has two inner steps which make up the reservoir. The steps have a height of 5mm each. The upper step is used for different plates to manipulate the outflow of the reservoir underneath it. The plate has a size of 690 mm x 600 mm.

The reservoir plate is 690 mm long and 600 mm wide. Thus, there is a difference of 60 mm between the inner reservoirs on each side. This plane makes up the bearing surface for the porous media section. Twelve threaded holes are drilled into the surface area. Hence, the porous media model can be screwed onto the reservoir plane. Section 3.4 describes how the model is modified to fit into these holes.

In the main experiments, the outflow out of the reservoir is modified with additional volume-reducing plates. These plates are produced with a 3D-printer (*Ultimaker 2*) with polylactide (PLA).

The volume-reducing plates were developed to reduce the outflow area in the measurement due to the limited field of view. Furthermore, the filling time of the reservoir underneath the porous medium is reduced significantly. The concept of the volume-reducing plate was tested with different test frames.

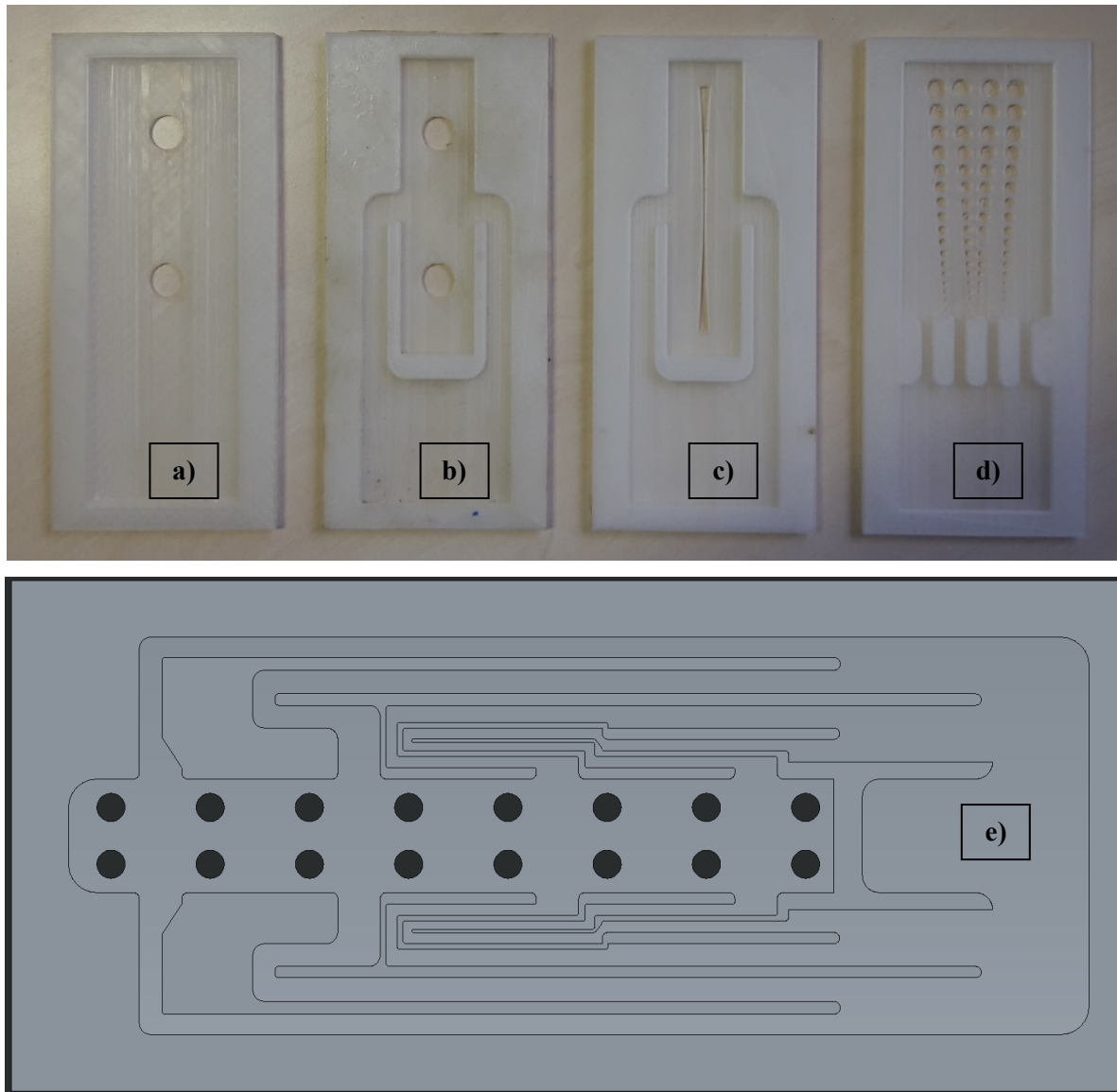


Figure 3-9: Volume-reducing concepts

The different volume-reducing concepts are shown. The inlet into the frames is located in the middle of the free square where the labeling is placed. This inflow is a circular pipe with a diameter of 1 cm. a) is the first configuration as in the measurements of [Groß 2018], b) is an improved version of a), c) is a slit configuration, d) is a cavity array with increasing diameters away from the source zone, e) is the improved volume-reducing plate which is used in the main experiments.

The volume-reducing plate which was finally chosen (see Figure 3-9, e) was designed such that the path for the fluid from the source to the cavities is nearly the same. Experiments have shown that this configuration enables an even outflow of tracer fluid through the permeable ground models which were used in the experiments. Further investigations and other points of views may require other volume-reducing plates.

Another aspect of the planned experiments is the investigation of different slopes. To realize the different slopes, an angle adjustment system was developed. The PMAB has a hinge due to the contact surface of the rubber mat in the front. This flexibility offers a dynamic range of angle adjustments. Due to fixation reasons, the back of the PMAB includes two threaded holes. If no inclination angle is desired, the PMAB is directly mounted to the last crossbar of the underlying section. In the other cases, different angle adjustment blocks (AABs) are needed. In the experiments, three different angle adjustments were planned. Hence, two AAB were produced for each angle. These are produced with two different materials and assemblies, respectively. Four AABs are milled out of blocks of polyoxymethylene (POM). The other two consist of four planes each which were cut out of acrylic glass using a laser cutter system and then screwed together to an AAB.

The shape of an AAB is S-like due to the needed permanent fixation of the PMAB onto the crossbar. It is screwed to the crossbar at the bottom and to the PMAB at the top. The mounting is shown in the following Figure 3-10.

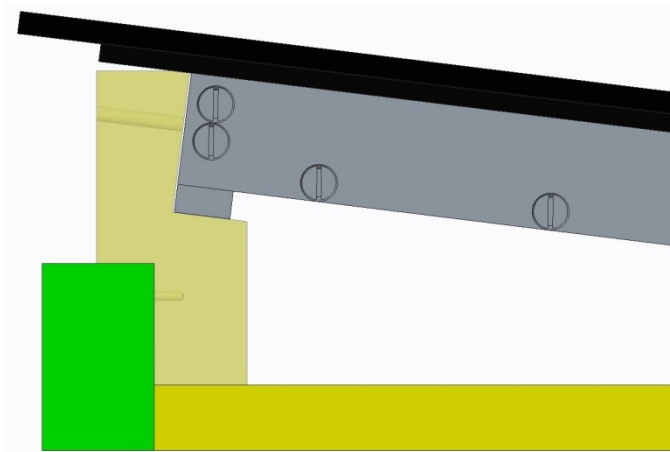


Figure 3-10: Detailed view of the AAB

Detailed view of the AAB in the light-yellow color. The upper part contains a transfixation screw hole which aligns with the threaded hole in the PMAB. Likewise, the lower section contains a threaded hole for the fixation screw from the cross bar.

3.4 Artificial seabed

For the experiments, an artificial seabed material was needed. Due to specific requirements the choice of the right material was very complicated. On the one hand, it was preferable to reproduce the general properties of sand in a fixed bed. On the other hand, a completely new investigation of a new material was not possible. For these reasons, a compromise was made between the specific properties of sand and the available low-cost materials.

The easiest and cheapest way to find a suitable material was the test of different foam mats. This kind of material is produced by expanding synthetic materials or metals. [Beavers and Joseph 1967] used such a metal foam for their investigation of the fluid flow over permeable media. Because metal foams are typically used in filter technologies, their porosity is usually very high (more than 95%). For this reason, choosing metal foam over a synthetic material would not have any advantages. Hence, different synthetic materials were tested concerning the porosity, permeability and flow field under a constant flow. The porosity and permeability measurements took place at the institute of biological science at the University of Rostock. To determine the porosity, several probes of the synthetic material were flooded and weighed and subsequently dried in an oven and weighed again afterwards. The weight difference delivers the solid part of the material and thus the porosity. For the determination of the permeability, an additional experimental setup was assembled.

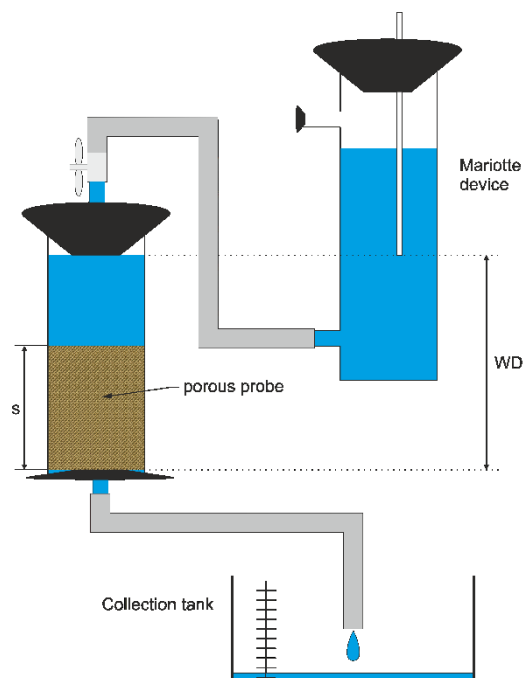


Figure 3-11: Constant head method

The probe in the chamber is subjected to a constant pressure. This is guaranteed with the help of the Mariotte device in the upper right side. Water flows through the porous probe and into the collection tank. The volume of water is measured with time.

With the device shown in Figure 3-11, the time for a specific volume of water to flow into the collection tank is measured. Hence, the volume V , the thickness of the probe s , the surface of the probe A , the measured time t and the height of the water column WD lead to the following expression for the volume flux:

$$\dot{V} = \frac{V * s}{A * WD * t} \quad \text{Eq. (3.1)}$$

In addition to the investigations of the porosity and the permeability of the synthetic materials, the flow field above them under a constant flow condition was measured with a laser doppler anemometer (LDA). Because of the low impact of these measurements, the results are shown in Appendix E.

The two different permeable media which were chosen for the main experiments are identified with the following specific parameters.

Table 3-2: Parameters of the porous materials

Material (5cm thickness)	Hydraulic conductivity [cm/s]	Permeability [m²]	Porosity
10PPI blue	0.33	34.7E-10	0.98
45PPI black	0.22	2,35E-10	0.98
Sandy sediment Hüttelmoor [Schade, personal communication]	NA	(0.04 – 1.13) E-10	0.4

The materials show a very high porosity, which is not comparable to sand (see 2.3.1). Because such porous materials are normally used in filter techniques, the aspired property is usually a maximum surface. For this reason, the porosity reaches a maximum value. For the experiments, the permeability is more important, because the volume flux in and out of the material is of importance for the mixing properties. The permeability of the chosen materials is related to sandy sediments which were found in the measured area Heiligensee Hüttelmoor (see Section 2.3.3).

In the experiment, the artificial seabed plates were adhered to a synthetic material plate. This plate contains 12 cavities which overlap with the thread holes in the reservoir (see 3.3.2). For the experiments, the two plates are screwed together, such that the artificial seabed is fixed onto the floor.

3.5 Measurement concept

Now that every element in the water channel has been explained in detail, the measurement concept itself is described. In the PIV/LIF measurement setting two, cameras and a laser are the main components. The laser is a Nd:YAG (neodymium-doped yttrium aluminium garnet) double pulse laser system with a wavelength of 532 nm (green light). The cameras are two *Dantec Flowsense 2M* with a resolution of 1600x1200 pixels, a pixel size of 7.4 μm and a maximum double image rate of 15 Hz.

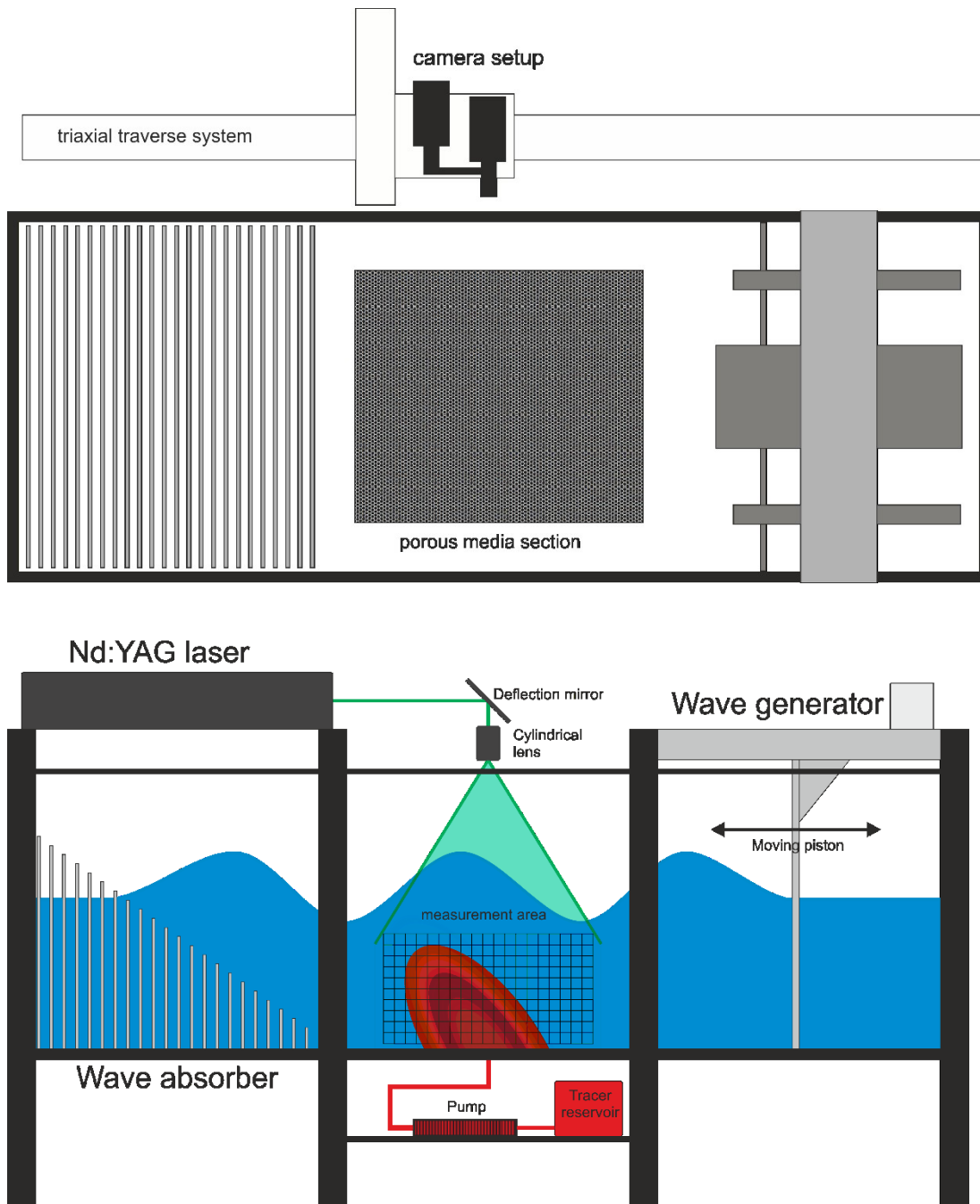


Figure 3-12: Measurement setup

In the upper part, the measurement setup is shown from above with the camera setup and the triaxial traverse system behind the channel. In the lower part, the frontal view is shown with the tracer reservoir underneath the channel and all the described elements within the channel, starting with the wave generator on the right-hand side and ending with the absorber on the left-hand side.

The timing and acquisition were done with the *Dantec Flowmap 1500* system with the *Flowmanager* software. The camera setup is placed on a triaxial traverse system behind the wave channel. Furthermore, this configuration enables movement in all directions. Hence, the measurement area is completely variable. The laser beam is guided via a light guiding arm with deflection mirrors through a cylindrical lens and is spread out into a light sheet from above the channel. This light sheet is guided into the water column with an acrylic glass element. Thus, an undisturbed coupling into the water column is realized. The area of the light sheet defines the maximum measurement area.

On the right side of the wave channel, the waves are produced with the moving piston (see Figure 3-12). They move through the measurement area and are absorbed in the wave absorber section. Underneath the measurement area, the artificial sea bed (see 3.4), which is represented by porous media, is placed. The fixation and construction of this part is described in 3.3.2. The water is filled into the PMAB with the pump system (see 3.2.4), which is placed underneath the flow channel. Furthermore, the reservoir of the tracer with a filling volume of 4 l is arranged next to the system.

During the experiment, the individual parts of the measurement concept are controlled separately. The wave generation is started from a single controller with specific software applications and program codes.

Next, the PIV-LIF setup is controlled with a single computer, which triggers the laser and the cameras. The cavities are opened in a specific time interval based on the rate at which the images are taken. In this setup, the PIV and LIF images are recorded simultaneously. Hence, the velocity and concentration profiles are determined within the same time step.

The last device which has to be started is the tracer pump system. In this case, it is controlled with a laboratory power supply. Hence, every experiment was run with the same volume flux of the tracer medium.

4 Methods

In this chapter, all relevant methods for the realized experiments are explained in detail. At first, the equations and assumptions for the analysis of the wave datasets are given. Furthermore, the determination of the three wave scenarios is described. Further the procedures for every main measurement are explained. In the last sections, the analysis of the results is discussed. This includes the first calculations in *Dynamic Studio* and the further processing in *Matlab*.

4.1 Wave dataset analysis

Ocean waves are complex and are made up of a spectrum of individual wave types. Because of this, it is not possible to determine one specific wave, described by wavelength, amplitude and speed, for the experiments. Hence, the validation of the wave channel experiment relies on specific requirements, which are explained in the following section.

In the Baltic Transcoast project, an acoustic wave and current profiler (AWAC) was placed in the intermediate-water zone in front of the investigation area Heiligensee Hüttelmoor.

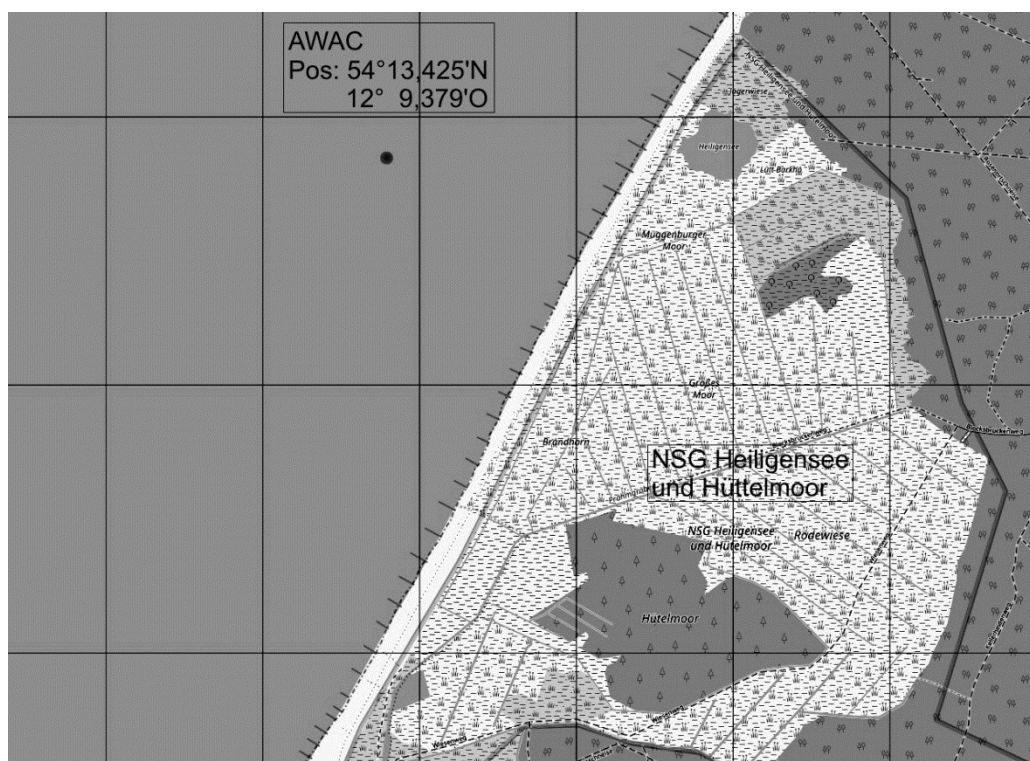


Figure 4-1: Position of the acoustic wave and current profiler

The AWAC is placed in the intermediate-water zone in front of the nature reserve Heiligensee Hüttelmoor. The water depth in this area is between 4 and 5 m. The surrounding sediment is sandy, but the sediment transport is categorized as low.

The position was chosen in this area because of the sufficient water depth and the low sediment transport. Due to the water depth, the impact on the ship traffic and the tourists at the beach is neglectable.

Measurements of the ground structure shows that the sediment transport is very low, such that the sedimentation of the AWAC is low, too. Several control drives need to be added to the device for maintenance and data storage, but with the explained boundary conditions the required number of these drives is reduced to a minimum of four per year.

The AWAC delivers wave datasets day and night at an interval of 1800 s. This acoustic measurement device uses four beams. The first beam is directed in the vertical direction and the other three are arranged around it at a tilt angle of 25° . With this orientation, three orbital velocities at the surface and the distance to the water surface are measured. In addition to these parameters, the stream velocity in the water column is measured in predefined distances from the AWAC. Furthermore, the pressure is measured directly at the device. Because of the measurement technique, the measured orbital velocities are oriented in beam direction. Thus, it is necessary to transform the velocities and analyze them with stochastic theorems. The transformation is dictated by the geometric dimensions of the AWAC (Figure 4-2).

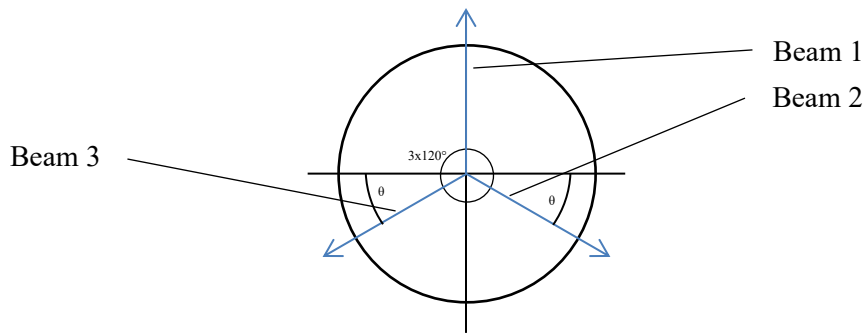


Figure 4-2: Geometrical dimensions of the AWAC

The figure shows the top view of the AWAC. The beams are oriented in a circle with an angle θ of 120° . The tilt angle **A** of the beams amounts to 25° .

In the following equations, the vector $\overrightarrow{U_{mea}}$ represents the measured velocity, \vec{U} the exact orbital velocity and \vec{o} the transformation matrix. This yields the following equation for the orbital velocity of the wave measured with the AWAC:

$$\underline{\underline{o}} \cdot \vec{U} = \overrightarrow{U_{mea}}$$

$$\begin{bmatrix} o_{11} & o_{12} & o_{13} \\ o_{21} & o_{22} & o_{23} \\ o_{31} & o_{32} & o_{33} \end{bmatrix} \begin{bmatrix} u \\ v \\ w \end{bmatrix} = \begin{bmatrix} U_{mea,1} \\ U_{mea,2} \\ U_{mea,3} \end{bmatrix}$$

Eq. (4.1)

$$\begin{bmatrix} u \\ v \\ w \end{bmatrix} = \underline{\underline{o}}^{-1} \begin{bmatrix} U_{mea,1} \\ U_{mea,2} \\ U_{mea,3} \end{bmatrix} \quad \text{Eq. (4.2)}$$

The transformation matrix for this specific case, based on the orientation of the device and the geometrical conditions, yields

$$o = \begin{bmatrix} 0 & \sin(\varphi) & \cos(\varphi) \\ \sin(\varphi) * \cos(\vartheta) & \sin(\varphi) * \sin(\vartheta) & \cos(\varphi) \\ \sin(\varphi) * \cos(\vartheta) & -(\sin(\varphi) * \sin(\vartheta)) & \cos(\varphi) \end{bmatrix}. \quad \text{Eq. (4.3)}$$

Furthermore, the opposite angle is used for the calculation, such that the angles are given by

$$\begin{aligned} \alpha &= 90^\circ - 25^\circ = 65^\circ \\ \vartheta &= 120^\circ - 90^\circ = 30^\circ \end{aligned} \quad \text{Eq. (4.4)}$$

The above equations are used for every single sample and the results are averaged over one burst. In the measurements, one burst consists of 1024 samples.

After the calculation of the orbital velocities at the surface with the above assumptions and equations, the wave parameters near the ground are determined with the *Stokes wave theory* (see chapter 2.4.5). The water depth is calculated with the mean of the wave height measurements of the AWAC. The wave period, amplitude and wave height are determined with the stochastic wave analysis tools from [Ausschuß für Küstenschutzwerke 2002]. These tools rely on the power spectral density function $S(f)$ of the wave frequencies. This leads to the assumption of a spectral moment with the following equation:

$$M_s = \int S(f) f^s df. \quad \text{Eq. (4.5)}$$

This spectral moment M_s (with $s = 0, 1, 2, \dots$) is the basis for different specific parameters. Following [Graw 1995], the significant wave height, which is defined as the height of the maximum this of all waves, is also defined by

$$SWH = WH_{M_0} = 4\sqrt{M_0} \quad \text{Eq. (4.6)}$$

Another significant parameter is the spectral wave period T_{02} . This period gives more weight to the lower wave frequencies than to the higher ones due to the higher energy level of the lower frequency waves. For this reason, it is commonly used in ocean science:

$$T_{02} = \sqrt{\frac{M_0}{M_2}} \quad \text{Eq. (4.7)}$$

The spectral wave period is the square root of the ratio of the spectral moment of the order zero and the spectral moment of the order two. Following [Zanke 2013], another spectral period without specific weighting is defined as

$$T_{01} = \frac{M_0}{M_1} \quad \text{Eq. (4.8)}$$

In this work, the spectral wave period T_{02} was calculated from the AWAC measurement data from half a year in front of the Hüttelmoor. Based on this dataset, the orbital velocity U_Φ one centimeter above the ground was calculated with the *third order Stokes wave theory*. The orbital velocity is connected to the phase angle of the wave. This aspect is considered in the theory. According to this, the velocity values for every phase angle were calculated and after this, the maximum orbital velocity was determined. Due to idealization, a maximum negative value and a maximum positive value occur. These two values are defined by opposite phase angles in the horizontal direction. In the following figure, the distribution of the values of this orbital velocity over half a year is shown.

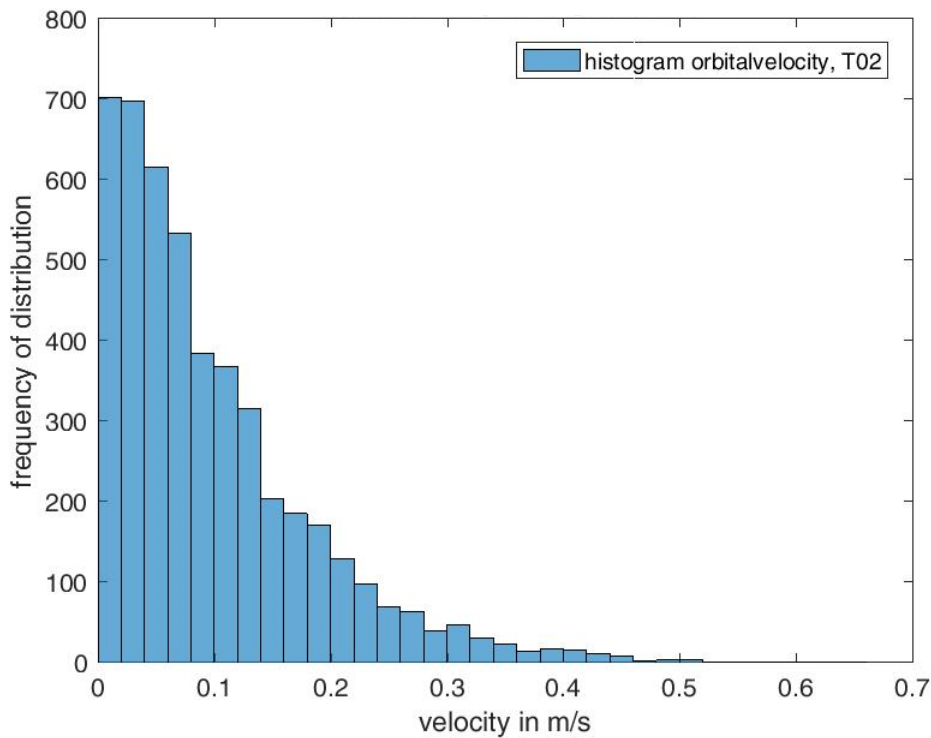


Figure 4-3: Histogram of the orbital velocity

The histogram shows the calculated orbital velocity based on the spectral wave period T_{02} during April until October measured with an AWAC system. The frequency of distribution is given on the y-axis and the maximum velocity on the x-axis.

In Figure 4-3, the frequency of distribution of the calculated orbital velocities are shown. The slow velocities occur more often than the faster ones. This is a common distribution for the considered region the area, water depth and normal weather situations in the southern Baltic Sea. In the wave channel, only one velocity and wave period can be set up. Because of this it is impossible to reproduce such a whole spectrum in the experiments. According to the theory of sediment transport mechanisms, described by [Nielsen 1994], one important factor for diffusion and transport is the orbital velocity near the ground. Because of this, the orbital velocity was chosen as one major factor for the choice of the wave. The other major aspect is the wave period, as test measurements have shown that the mixing and the diffusion of tracer particles are connected to the period of the waves.

In the experiments, three wave scenarios were investigated. The first one aims to reproduce a calmer scenario. For that reason, the orbital velocity has to be very slow, so that it ends up in the left-most side of the histogram in Figure 4-3. Furthermore, the wave period has to be very small, such that small velocities are connected with a small period. Moreover, the wave height should be nearly the same for all scenarios. On the other hand, the wave period cannot be set to be infinitely small due to hardware limitations. If the period is too small, the wave generator performs a kind of vibration, which leads to an undefined movement of the water. For these reasons, a period of less than 2 s was chosen for the first scenario. The second scenario is meant to reproduce a mean wave environment. Thus, a mean wave period of 2.5 s and a mean orbital velocity of 0.1 m/s of the field measurements were realized in the wave channel. The third scenario aims to reproduce a stormy situation. For this, the fastest adjustable orbital velocity was chosen. This is limited by the channel itself. If the speed is too high the forces become too strong and can damage the channel. Furthermore, the ground starts to oscillate if the forces are too strong. Hence, the following parameters were determined for the wave scenarios in the experiments.

Table 4-1: Parameters of the wave scenarios

Scenario	1. Calm scenario	2. Mean scenario	3. Stormy scenario
Wave period	1.99s	2.52s	3.3s
Orbital velocity (max)	0.05m/s	0.1m/s	0.25m/s
Wave type	intermediate	intermediate	intermediate
Ratio of Water depth to wavelength	0.09	0.05	0.07

4.2 Main measurement procedures

The main measurements include 24 single PIV/LIF measurements in the same plane under different conditions. [Kandler 2018] developed the following figure to illustrate the main aspects of the investigation:

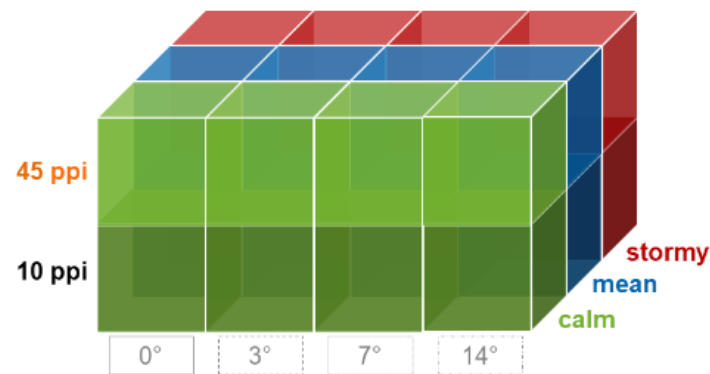


Figure 4-4: Overview of the measurements

The green plane includes 8 measurements with the calm scenario, the blue plane every measurement with the mean wave scenario and the red the stormy scenario. The lower group correspond to the measurements above the 10PPI porous material and the upper part corresponds to the investigations above the 45PPI media. The four columns show the different slope angles during the measurement. The color coding is fixed for the following sections.

The investigation comprises two different permeable seabeds with 12 measurements each: four different slope angles and three wave conditions. Every single experiment was conducted as follows: At first, the water basin was filled. Afterwards, the fluorescent tracer was mixed with the fresh water and the defined volume of *Rhodamin 6G* dissolved in two small water tanks. In the next step, the *Vestosint* particles were mixed into the water basin. To realize the same temperature conditions, the small water tanks with the tracer solution were stored in the water basin. At next, the water was pumped from the water basin into the wave channel, until a water height of 30 cm over the ground model was reached. Afterwards, the wave generator was started. The produced waves have to develop for a time certain period to secure stable conditions. In the experiments, a time period of 10 minutes was enough to reach this state. In the next step, the measurements themselves were started.

The measurement started by filling the tracer from the small tank into a small basin underneath the wave channel. At next, the temperature of the tracer fluid was measured and documented. Afterwards, the measurement was started within the PIV/LIF software. During the time delay until the laser was fully loaded, the tracer setup was prepared. Once the laser beams appeared, the tracer pump was started immediately, such that a maximum time delay of 5 s between the starts of the two systems occurred. After nearly 6 minutes, the second small tracer tank was filled into the tracer basin to secure a continuous

flow of the tracer. During one measurement, 9 l of the *Rhodamin 6G* dissolution was pumped into the measurement area with a volume flux of 0.0154 l/s. One measurement took nearly 14 minutes. With the software, a maximum of 6000 double images for the PIV and 6000 single images for the LIF were taken during one investigation at a frequency of 7.5 Hz.

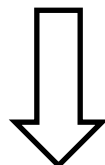
For the following analysis, a calibration of the PIV and the LIF setup was made before the experiments. The PIV calibration was done with a calibration target which was placed in the measurement area. This target has a defined array of points with a distance of 5 mm between each point. With a snapshot of this and the software *FlowManager* of *Dantec Dynamics*, the PIV calibration was finished. The LIF calibration relies on several snapshots with different concentrations of the used tracer solution. In general, the tracers are mixed within 15 minutes in the water channel, which is filled with a constant volume of 4.5 m³ during a constant flow, which is realized with a 5.4 kW radial pump. Afterwards, a snapshot is done for the specific concentration in the system. This procedure is done for at least eleven steps. In this case, it was important that two calibration curves were calculated: the first one for low concentrations between 0 and 50 µg/l and the second one for the region between 50 and 260 µg/l. This was done because of the wide range of the concentration field on the one hand and because of the sensitivity of the software on the other hand. The calibrations steps are listed in Appendix A. Details of the LIF calibration procedure are described in [Kandler 2018].

4.3 Data analysis concepts

The data analysis was done within two steps. At first, the image settings and calculations of the velocity and concentration field are performed within *Dynamic Studio*. Secondly, the calculation and analysis of the diffusion and turbulence is performed via *Matlab*.

4.3.1 Image settings via Dynamic Studio

The first step in the analysis is done with the software *Dynamic Studio 5.1*. This program is specially designed for PIV and LIF investigations and uses validated tools for the analysis. The single steps for every measurement in this investigation are as follows:



Subtraction of the mean reduces the background noise

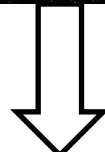
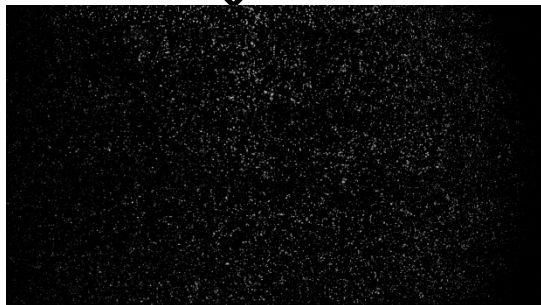
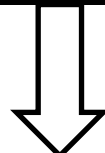
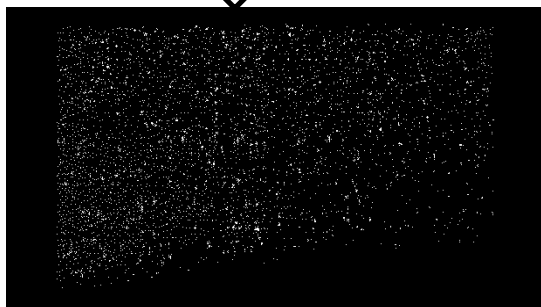


Image balancing leads to an equal illumination



Adaptive PIV generates the velocity vector field

The raw-pictures are captured as double images with a defined time step in between. It is obvious that the background is very bright, and the image seems noisy. The left and right boundaries are subjected to vignetting, such that the edges are black.

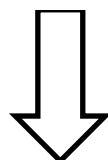
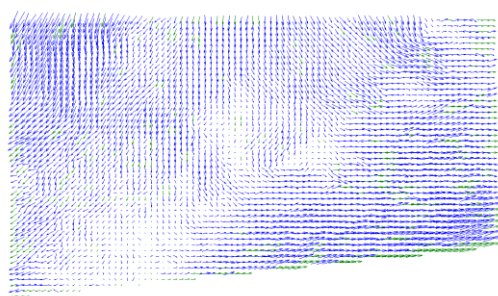
To reduce the background brightness, a mean image of the complete time series is calculated and subtracted from every single image.

After the subtraction of the mean image, the image is less bright in the background and the particles are well defined. This is important for the cross-correlation in a later step. Because of the uneven illumination of the light sheet, due to the long distance through the water, a balancing is needed.

The program calculates an image balance for the complete time series and uses this for every image to balance the light conditions.

After the balancing step, the image is equally illuminated, and the particles are well defined. In addition, the outer boundaries are blacked out. In this example, the slope is blacked out, too. Now the image is prepared for the correlation setup.

The adaptive PIV setup works stepwise by starting with a large interrogation area and ending with a small one.



Masking and export
deliver the database
for final calculations

With the adaptive algorithm, the small interrogation areas are validated with the large ones. For that reason, the final result is more accurate. In the boundary regions, particles leave the measurement area, such that the velocity vectors are normally substituted in this area. The substituted vectors are colored green. In a final step, this vector field is masked again to reject inaccurate vectors at the boundaries.

Furthermore, the *Wall Windowing* function in *Dynamic Studio* was used to reduce the side effects of the boundary regions. For every measurement, the following approaches were made for the adaptive PIV:

Table 4-2: Overview of the specific parameters for the adaptive PIV setup

Parameter	Approach
Grid Step Size	16 x 16 pixels
Minimum Interrogation Area Size	32 x 32 pixels
Maximum Interrogation Area Size	64 x 64 pixels
Peak Height Ratio	1.5
Neighborhood Validation	11 x 11 vectors
Minimum Normalization	0.1
Acceptance Limit	1.0
Particle Detection Limit	5
Desired # of particles/IA	10

The LIF calculation has no further image setting steps. The calibration images were used to define the calibration curve for the measurements. This is used in the LIF analysis sequence to calculate the amount of tracer in the images. The final step includes an *Image Resampling*, which reduces the resolution of the LIF images to the resolution of the vector field from the PIV images. This step is needed because of the post-processing which uses both fields on the same grid for the calculations.

4.3.2 Diffusion analysis in Matlab

The diffusion analysis is based on the LIF analysis of the measurements in *Dynamic Studio*. The resampled LIF images were exported as comma-separated values and loaded as single images into *Matlab*. Each image is interpreted as pixel matrix with a size of 55 x 99 values. Due to masking in *Dynamic Studio*, parts of the image are filled with zeros, for example the left and the right part near the boundaries and the bottom part which includes the slope of the artificial seabed. These zeros are defined as Not a Number (NaNs) to detect the bottom in the image. For this, a column-wise logical request for every row is done.

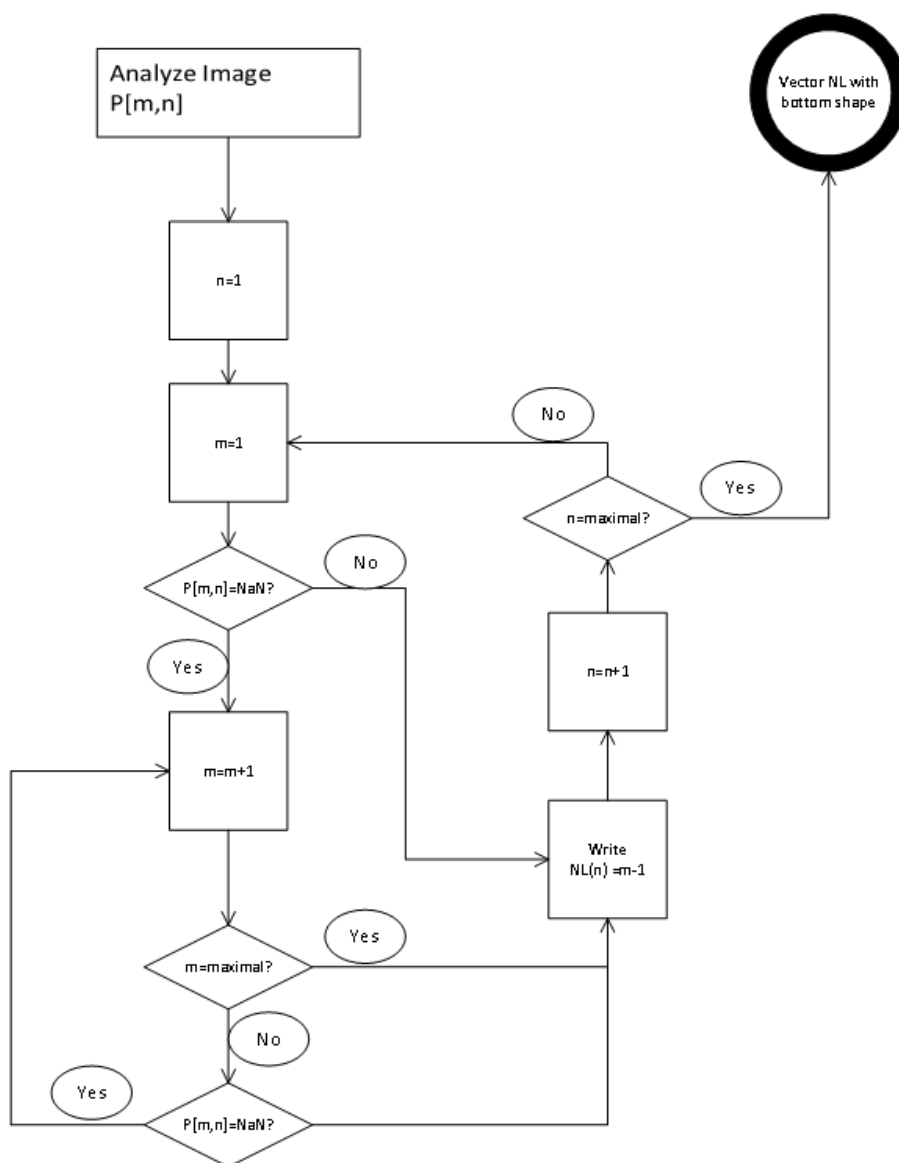


Figure 4-5: Program flow chart

The program flow chart of the analysis of the bottom shape starts with the pixel matrix $P[m,n]$. For every column, each row is checked for the occurrence of NaNs. Once every column has been checked the line NL of the bottom shape is defined.

As mentioned in the program flow chart (see Figure 4-5), the algorithm starts in the first column of the pixel matrix of the image. In this column, the first row is checked for the occurrence of a NaN value. In this specific case, the first row equates to the bottom line of the image. Hence, the row number is equal to the distance from the bottom of the image. If the entry is NaN, then the row number for the specific column is recorded in a new vector. After the scan of every column of the image, the new recorded vector denotes the bottom line of the artificial seabed in the image.

In the next step, the tracking of different concentration lines starts. The tracking algorithm works in the same way as the detection of the bottom line. But in this case defined concentration values are searched. In the experiments, the tracer concentration was 300 $\mu\text{g/l}$, such that the calibration was done up to a maximum of 260 $\mu\text{g/l}$. Initial tests showed that this maximum is not reached. With the algorithm, four concentration lines were tracked:

Table 4-3: Tracking lines of the spread analysis

Label	Percentage	Concentration [$\mu\text{g/l}$]
Boundary10	10	26
Boundary25	25	65
Boundary50	50	130
Boundary75	75	195

The tracking was done image wise. Hence, the result includes a time series of the defined concentration lines for every measurement. To determine the concentration area due to the bottom boundary, the calculated bottom line for every image was subtracted from the concentration lines. These results were used for the analysis of the time-dependent concentration development.

The analysis of the time series was done on the base of the Fourier transformation. Before the decomposition into the frequencies, the mean values of the concentration lines were calculated for every time step. Hence, an averaged concentration time series of the four concentration boundaries for each measurement was enabled. Within the Fourier transformation, the dominant frequencies were determined. Based on this, different low pass filters enabled the investigation of the development of the concentration boundary during the time series.

In addition to the described analysis steps, videos of the concentration and the concentration lines were created. Therefore, a background concentration of 5 $\mu\text{g/l}$ was subtracted from every image.

4.3.3 Turbulence analysis in Matlab

The analysis of turbulent mixing was done with the program *Matlab R2017*. After the calculations in *Dynamic Studio*, the final results were exported as comma-separated values (.csv) and afterwards imported into *Matlab*. This data transfer process guarantees that no information is lost. The data is stored as matrices in the following structure:

$$\begin{bmatrix} \xi(x_{11}, z_{11}) & \xi(x_{12}, z_{12}) & \cdots & \xi(x_{1t}, z_{1t}) \\ \xi(x_{21}, z_{11}) & \cdots & & \\ \vdots & & \ddots & \vdots \\ \xi(x_{B1}, z_{11}) & \cdots & & \\ \xi(x_{11}, z_{21}) & \cdots & & \\ \vdots & & \ddots & \\ \xi(x_{B1}, z_{N1}) & \cdots & & \xi(x_{Bt}, z_{Nt}) \end{bmatrix} \quad \text{Eq. (4.9)}$$

The index ξ includes the velocity components u and w and the concentration c . Furthermore, the indices m and n define the maximum grid points in x - and z -direction. The column includes the single time steps t . In these experiments, the ranges of the indices are

$$\begin{aligned} B &= 1, 2, \dots, 99 \\ N &= 1, 2, \dots, 55 \\ t &= 1, 2, \dots, 6000 \end{aligned} \quad \text{Eq. (4.10)}$$

These matrices build the base for further analysis steps. Next, the velocity and concentration fields were sorted by their phase angles. This is necessary because of the characteristics of the waves. [Groß 2018] and [Kandler 2018] tested different partitionings of the phase angles to find a good agreement between accuracy (maximal division into 360 phase angles) and statistical requirement (minimum division into 4 phase angles) to described the physical aspects as good as possible. Following these requirements [Kandler 2018] ended up with a distribution of to 12 phase angles (see Figure 4-6). Following this division, the phase angles were calculated from the velocity field.

$$\begin{aligned} & \begin{matrix} u > 0 \\ w > 0 \end{matrix} & \varphi &= \tan^{-1}\left(\frac{w}{u}\right) \\ & \begin{matrix} u < 0 \\ w > 0 \end{matrix} \text{ or } \begin{matrix} u < 0 \\ w < 0 \end{matrix} & \varphi &= \tan^{-1}\left(\frac{w}{u}\right) + 180^\circ \\ & \begin{matrix} u > 0 \\ w < 0 \end{matrix} & \varphi &= \tan^{-1}\left(\frac{w}{u}\right) + 360^\circ \end{aligned} \quad \text{Eq. (4.11)}$$

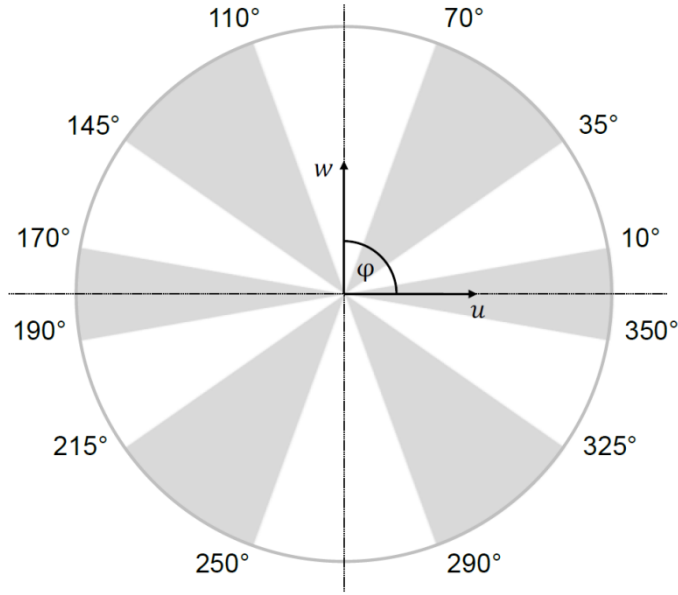


Figure 4-6: Phase angle decomposition [Kandler 2018]

The phase angles were distributed into 12 different phase regions. The section around 0° is equal to the main flow direction of the fluid (in direction of the wave absorber). The orthogonal direction (90°) corresponds to the upwards lift in wave-surface direction. The range of the phase regions depends on the number of elements in the matrices

The calculation of the phase angles and the division leads to 12 phase matrices each for the velocity components and the concentration field. Hence, it is secured that the phase division is equal for every variable. The phase specific matrices w_{ph} , u_{ph} and c_{ph} with $ph = ph_1, ph_2 \dots ph_{12}$ consist of 5445 x 6000 values each. Based on these matrices, the next calculation steps are defined.

4.3.3.1 Calculation of the Reynolds-flux

The Reynolds-fluxes consist of the fluctuation values of the main flow (see 2.5.4). In the case of waves, the fluctuation occurs in every phase. Because of that, the phase specific matrices (see above) are used to define the fluctuations. The phase mean vectors $\langle \xi_{ph} \rangle$ are built as arithmetic means of every row in the phase specific matrices. Thus, for every point of the vector fields phase averaged mean values are calculated. At next, the fluctuating values ξ'_{ph} are calculated as the difference between the momentary value and the phase averaged mean value.

$$\xi'_{ph} = \xi_{ph} - \langle \xi_{ph} \rangle \quad \text{Eq. (4.12)}$$

Then, the phase averaged vertical Reynolds-flux is given as the ensemble average of the phase averaged vertical velocity fluctuations multiplied by the phase averaged concentration fluctuations. For the mean vertical Reynolds-flux, the arithmetic mean of the 12 phase averaged Reynolds-fluxes is calculated.

$$\langle w'c' \rangle = \frac{1}{12} \sum_{ph=1}^{12} \langle w'_{ph} \cdot c'_{ph} \rangle \quad \text{Eq. (4.13)}$$

4.3.3.2 Calculation of the mixing length

The mixing length is calculated following the assumptions from 2.5.3. Hence, the mixing length is defined as

$$l_c = \sqrt{\left| \frac{\langle w'c' \rangle}{\frac{\partial \langle u \rangle}{\partial z} \cdot \frac{\partial \langle c \rangle}{\partial z}} \right|} \quad \text{Eq. (4.14)}$$

In addition to the phase averaged Reynolds-fluxes $\langle w'c' \rangle$, the vertical gradients of the concentration c and horizontal velocity u are needed. Therefor the root mean square of the phase averaged velocity u and concentration c was calculated.

$$\langle \xi \rangle = \sqrt{\frac{1}{12} \sum_{ph=1}^{12} \langle \xi_{ph} \rangle^2} \quad \text{Eq. (4.15)}$$

With $\xi = c, u$ and $ph = ph1, ph2 \dots, ph12$, every phase matrix is used. Additionally, a horizontal averaging was done. Therefor a realignment of the image matrix is needed. Because of the different slope angles of the measurements, a horizontal averaging including the slope would produce errors. With the realignment, the slope is folded down and the image shows a distribution of the concentration and velocity parallel to the ground. In Figure 4-7, an example of [Kandler 2018] of a realignment is shown.

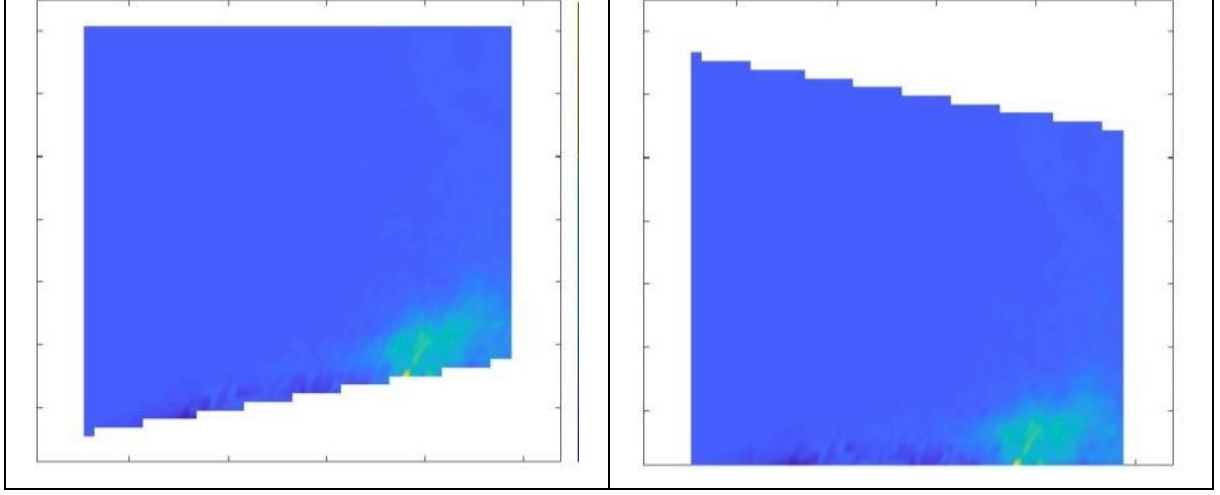


Figure 4-7: Realignment of image matrices

On the left side, the image matrix of the Reynolds-flux diffusion is shown. On the right side, the realignment was done. The single image points are shifted in z-direction depending on the position of the slope. Therefore, the slope occurs on the top of the image.

In the next step, the horizontal averaging is done row-wise. Thus, a new column matrix is built as a base for the calculation of the gradients. It is mentioned that the appearing slope at the top of the image matrix is neglected in the following calculations. The gradients are calculated with a forward difference quotient.

$$\left(\frac{\partial \xi}{\partial z}\right)_{\psi} = \frac{\xi_{\psi+1} - \xi_{\psi}}{z_{\psi+1} - z_{\psi}} \quad \text{Eq. (4.16)}$$

5 Results

In this section the results of the wave tank experiments are shown. Starting with the analysis of the concentration boundary development. Ongoing with a detailed analysis of the Reynolds-fluxes. After this the mixing length for the tracer concentration is investigated. At next, the phase specific Reynolds-fluxes and mixing length is shown. In the last part the wave friction factor, bottom stress and turbulent kinetic energy is analyzed.

5.1 Analysis of the concentration development

The LIF analysis delivers the concentration field of the tracer *Rhodamin 6G* in every measurement. This tracer represents the SGD, which flows out of the seabed in the ocean. In section 4.3.2, the bases for the following analysis are described. The calculated concentration lines of the 10%, 25%, 50% and 75% concentration of the tracer are shown in Figure 5-1 for the measurement with mean wave scenario above the 10PPI permeable bed with 0° slope angle.

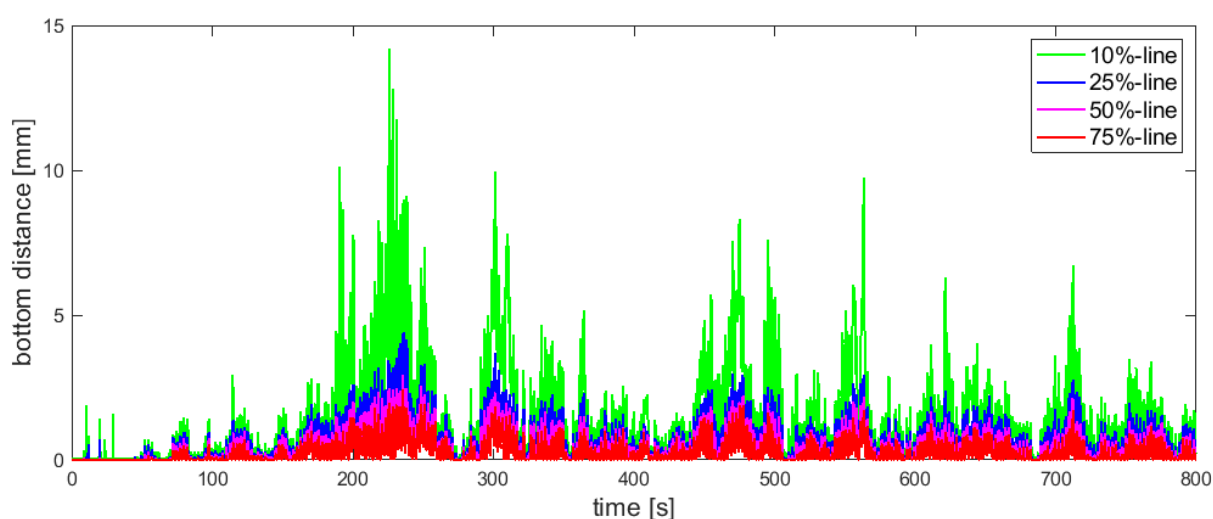


Figure 5-1: Comparison of mean spread behavior

The mean spread is defined by the four boundary concentration lines of 10%, 25%, 50% and 75% in green, blue, magenta and red. On the x-axis the time steps are deposited. On the y-axis the distance of the boundary line from the bottom of the measurement area is shown.

From this Figure 5-1 it is clear that the lowest concentration line reaches the highest distance from the bottom and the highest concentration line the lowest distance from the ground. Furthermore, an increase of the bottom distance during the first 250 s is noticeable. During the experiment the start-up and the end-up processes were observed. It is clear that in the beginning the bottom distances of the boundary lines increase. Moreover, the bottom distance may reach a maximum until it starts to fluctuate around a

constant value. At the time step of 720 s, the inflow of *Rhodamin 6G* was stopped. Thus, a light decrease of the bottom distance may occur in the end-up process.

In the next step, a Fourier analysis of the single time series is done. The result shows which frequencies are dominant in the single signals. In the following Figure 5-2 the amplitude spectrum of the 50% line of the measurement with zero degree slope angle above the 10PPI medium during the mean wave scenario is shown.

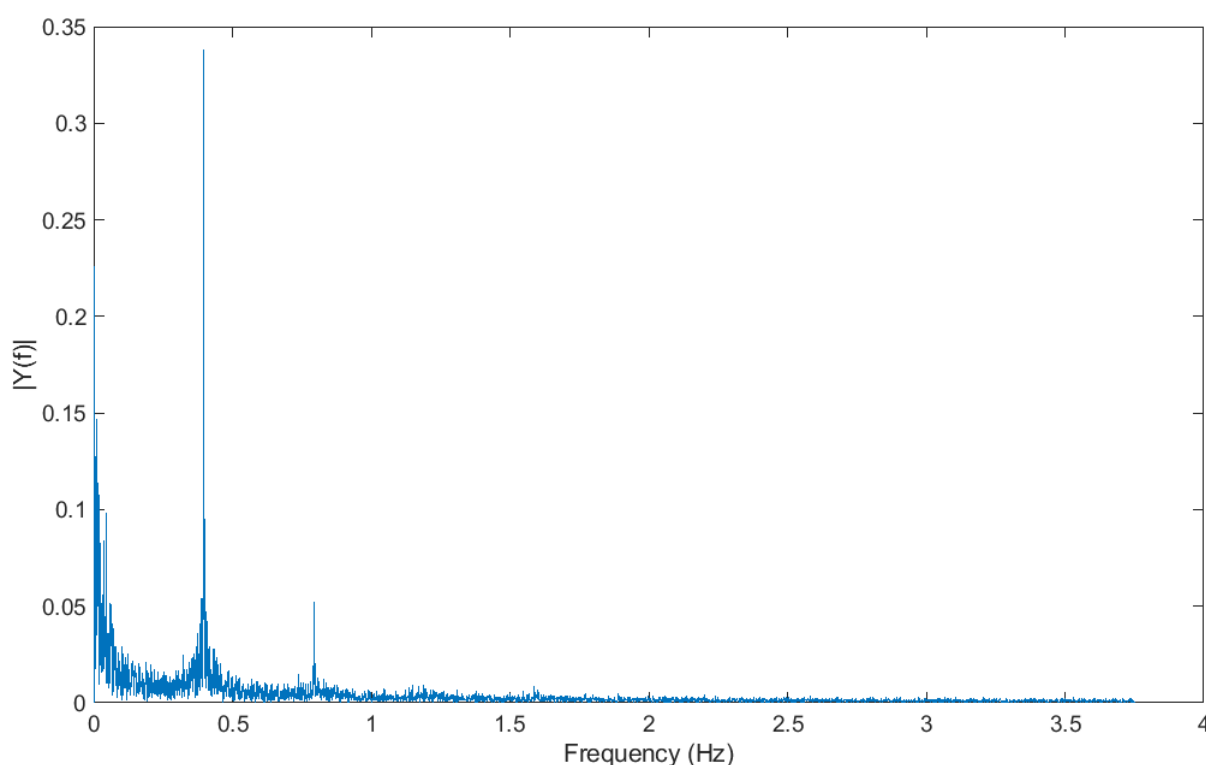


Figure 5-2: Amplitude spectrum of measurement with 10PPI and mean wave scenario, 50% boundary line

In this figure the amplitude spectrum is drawn over the occurring frequencies on the x-axis. This is a result of the fast Fourier transformation.

The Fourier analysis in Figure 5-2 shows the main frequencies of the time signal. There are obviously three dominant peaks in the analysis. The first one occurs nearly 0 Hz. This behavior includes a constant component of the development of the 50% boundary over time. The second peak represents exact the wave frequency. Hence, the main fluctuation of the time signal is equal to the wave frequency. This shows a direct influence of the wave to the mixing of the tracer fluid. The third peak is the double of the wave frequency. In the Appendix B each Fourier analysis of every measurement is printed. Summing up, each Fourier analysis shows the same behavior as the example in Figure 5-2. All are characterized

by a peak near 0 Hz for a constant component, a second peak at the particular wave frequency and a third at the double of the wave frequency.

At next, the constant component will be estimated. For this a low pass filter is laid over the time signal. Considering the frequency analysis, only the very low frequencies are observed. Hence, the increase of the boundary line will be apparent.

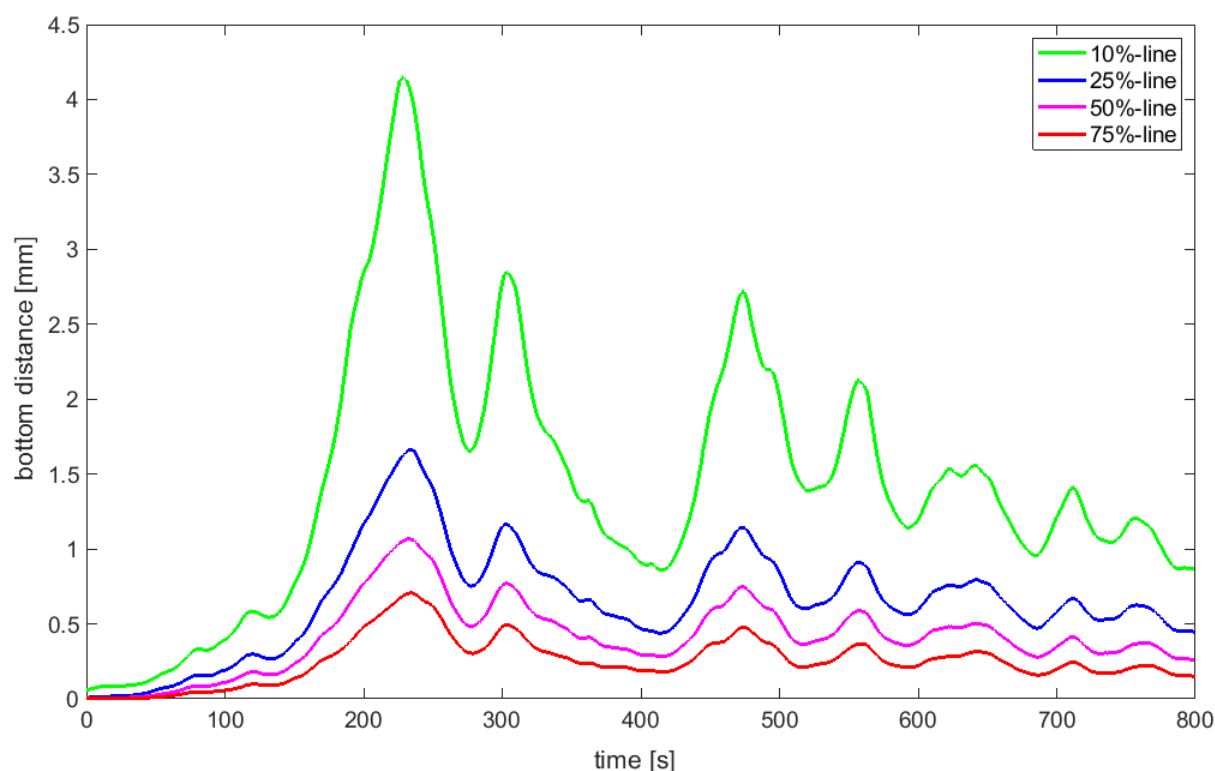


Figure 5-3: Low pass filtered signal of measurement with 10PPI and mean wave scenario at frequency 0.02Hz

On the y-axis the distance of the particular line from the ground is shown. On the x-axis the single time steps are printed. The signals are low pass filtered by a frequency of 0.02 Hz.

The low pass filtered signal in Figure 5-3 shows very clear the development of the single lines from Figure 5-1. In the first part of the time series, the bottom distance increase rapidly until a maximum value is reached around a time step of 200 s. After this, the bottom distance stagnates near a constant value. Estimating this value needs a further low pass filtering at a lower frequency. It is to mention, that the value of the bottom distance decreases with filtering, but comparing Figure 5-1 and Figure 5-3 it is obvious, that the strong fluctuation overly the mean development many times.

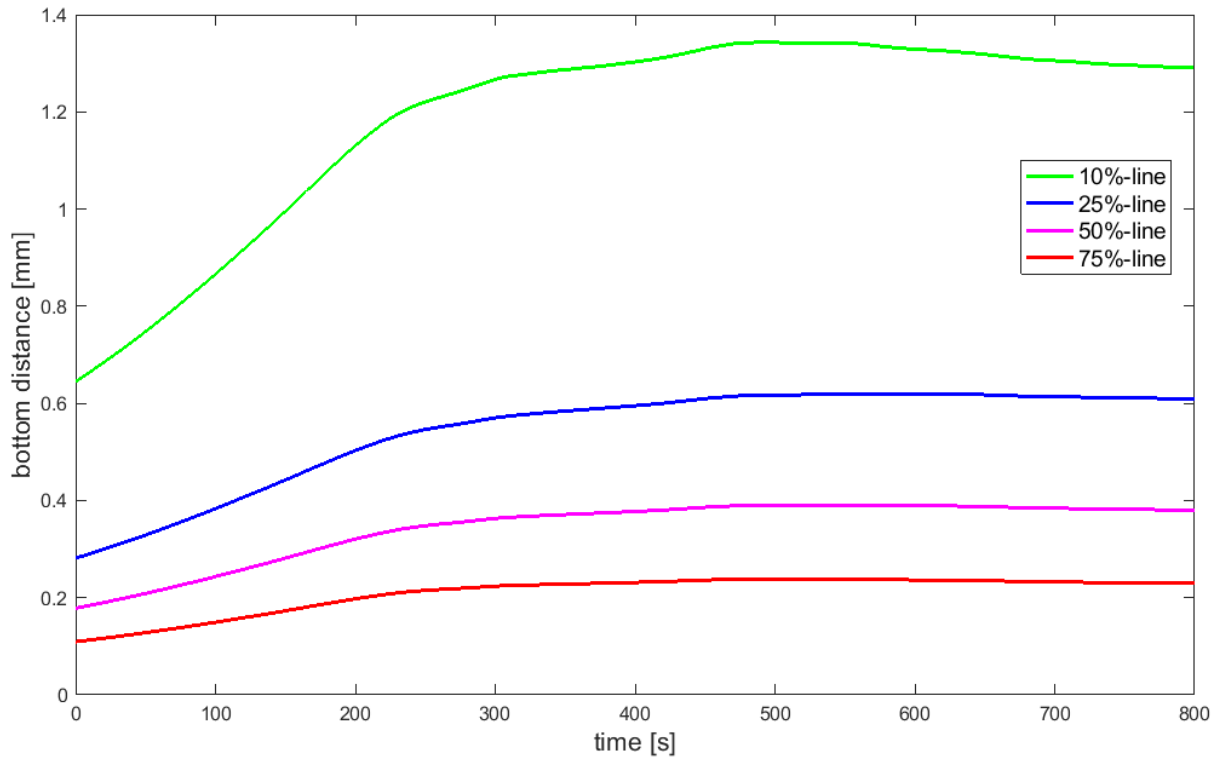


Figure 5-4: Low pass filtered signal of measurement with 10PPI and mean wave scenario at frequency 0.001Hz

On the y-axis the distance of the particular line from the ground is shown. On the x-axis the single time steps are printed. The signals are low pass filtered by a frequency of 0.001 Hz.

Regarding Figure 5-4 the increasing of the different concentration lines is clear. Furthermore, a constant distance can be estimated until a slight decrease in the end of the measurement. The slope of each line increases with lower concentration. Hence, the 10% concentration line has the greatest slope and the 75% concentration line the lowest. Considering the boundary growth rate, which is calculated for each concentration line with the following equation

$$\frac{\partial \gamma_C}{\partial t} = \frac{\gamma_{C,max} - \gamma_{C,min}}{t(\gamma_{C,max}) - t(\gamma_{C,min})} \quad \text{Eq. (5.1)}$$

with $C = 10\%, 25\%, 50\%$ and 75% . The variable γ stand for the bottom distance of the respective concentration line. Comparing the different lines from Figure 5-4 it is obvious, that each line reaches the constant value at the same time point. For that reason, the boundary growth rate increase with the lower concentration line.

In the next step the different wave scenarios are compared on the base of the single analysis steps from above. The low pass filtering at a frequency of 0.001 Hz is done for every single concentration boundary line of each measurement. Furthermore, the 10% diffusion boundaries are plotted for the different wave condition during the same slope angle adjustment.

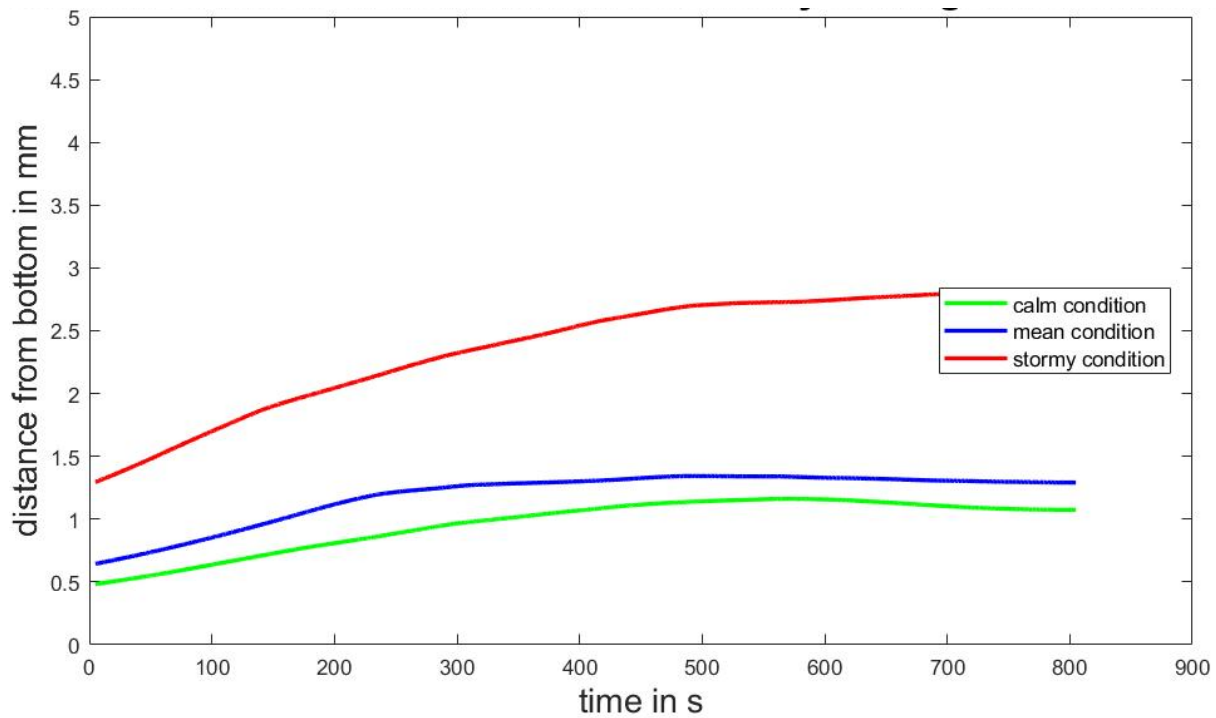


Figure 5-5: Comparison of diffusion during different wave events for measurements with 10PPI and 0° slope angle

On the y-axis the distance from the bottom in mm is plotted over the single time steps on the x-axis. In green the calm wave condition is shown, in blue the mean wave and in red the stormy scenario.

For the 0° slope angle adjustment Figure 5-5 shows a diffusion of the 10% lines as expected. The calm scenario increases slowly and the constant distance from the bottom is the lowest compared to the other two scenarios. On the other hand, in the stormy scenario the bottom distance of the 10% line increases fast and the maximum values are the greatest in this comparison. And the behavior of the mean condition is classed in between the other two scenarios. With the variation of the slope angle adjustment and the ground properties, this expected order is changing.

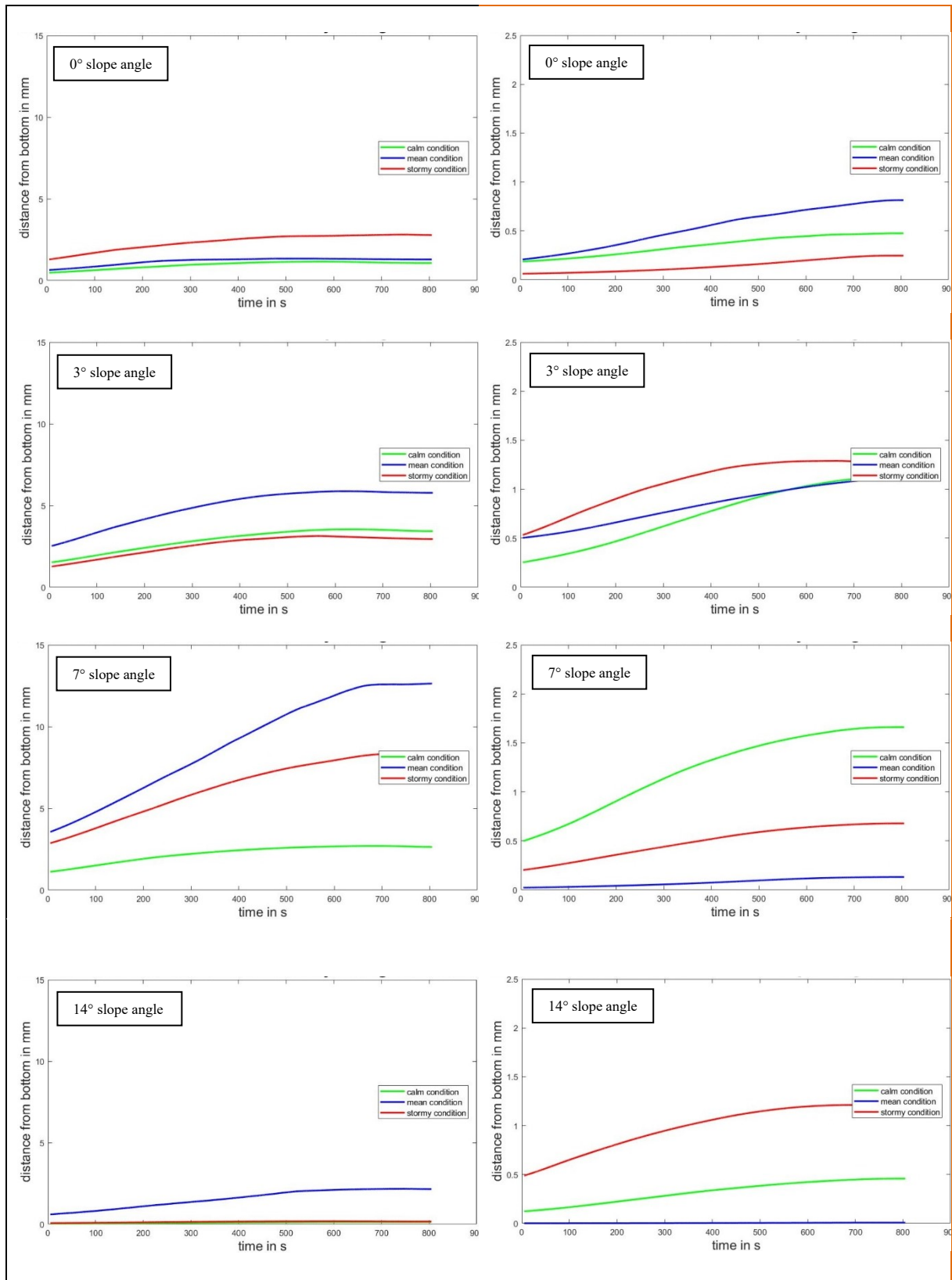


Figure 5-6: Comparison of the diffusion analysis for the 10% line

On the left-hand side, all diffusion lines of the 10% concentration boundary line of the experiments with the 10PPI porous media are shown and on the right-hand side the same for the 45PPI porous media. The scaling of the y-axis is different between the left and the right side. Every single picture includes the diffusion for the three wave scenarios calm, mean and stormy.

In Figure 5-6 the diffusion of the 10% concentration boundary lines for all measurements are shown. On the left-hand side, the measurements with the 10PPI porous media starting with zero slope angle on top and ending with 14° slope angle at the bottom. On the right-hand side, the same is shown with variation of the porous media of 45PPI. The right section is scaled down to a maximum y-axis of 2.5mm, because of the smaller diffusion into the water column.

Firstly, it is clear that the maximum diffusion into the water column of the tracer is much less during the experiments with the 45PPI medium compared to the other. Furthermore, the order of the different wave scenarios is completely different to the experiments with the 10PPI media. This behavior was also observed by [Groß 2018]. For this reason, the influence of the ground properties onto the tracer diffusion is somehow significant.

Secondly, considering only the 10PPI measurements, the different slope angles change the order in which the diffusion of the tracer reaches the water column for the different wave scenarios. The zero degree slope angle measurements show a small diffusion for the calm scenario, a higher diffusion for the mean scenario and the highest for the stormy scenario into the water column. With the change of the slope angle, the mean wave scenario occurs to be the dominant scenario with the highest diffusion not the water column for 3° , 7° and 14° . Moreover, the bottom distance of the boundary lines increases with increasing slope angle until 7° . In the case of 14° slope, the bottom distance of the concentration line decreases immediately. For 3° slope angle the stormy and calm scenario are showing nearly the same behavior. In the other two cases the stormy scenario has a higher ground distance for the concentration line.

Thirdly, considering only the 45PPI measurements, the order of the diffusion into the water column of the wave scenarios may changes randomly. Considering the order of the wave scenarios, it is obvious, that every figure for the 45PPI media shows different behaviors. Furthermore, the order is different to the pendant of the 10PPI media measurement. It is to mention, that the maximum diffusion distance for the 45PPI measurements is 1.5 mm and the difference between the wave scenarios is much less. For this reason, a nearly constant diffusion for the different wave scenarios for the specific slope angle can be estimated.

5.2 Reynolds-flux development and dependencies

The Reynolds-flux model consists of the averaged fluctuation values of the velocity and the concentration. Hence, these fluxes can be estimated as indicator for the turbulent mixing of a tracer fluid into a new environment (see section 2.5.4). In the analysis of the experiments a phase averaged Reynolds-flux development was calculated for the 12 phases. In this chapter firstly a mean phase averaged Reynolds-flux map is shown. At next the specific Reynolds-fluxes for the measurements above the 10PPI permeable seabed are shown. After this the dependence of the fluxes to the boundary growth rate is analyzed.

The mean phase averaged Reynolds-flux for the 10PPI of the mean wave scenario for 0° slope angle measurement is shown in the following Figure 5-7.

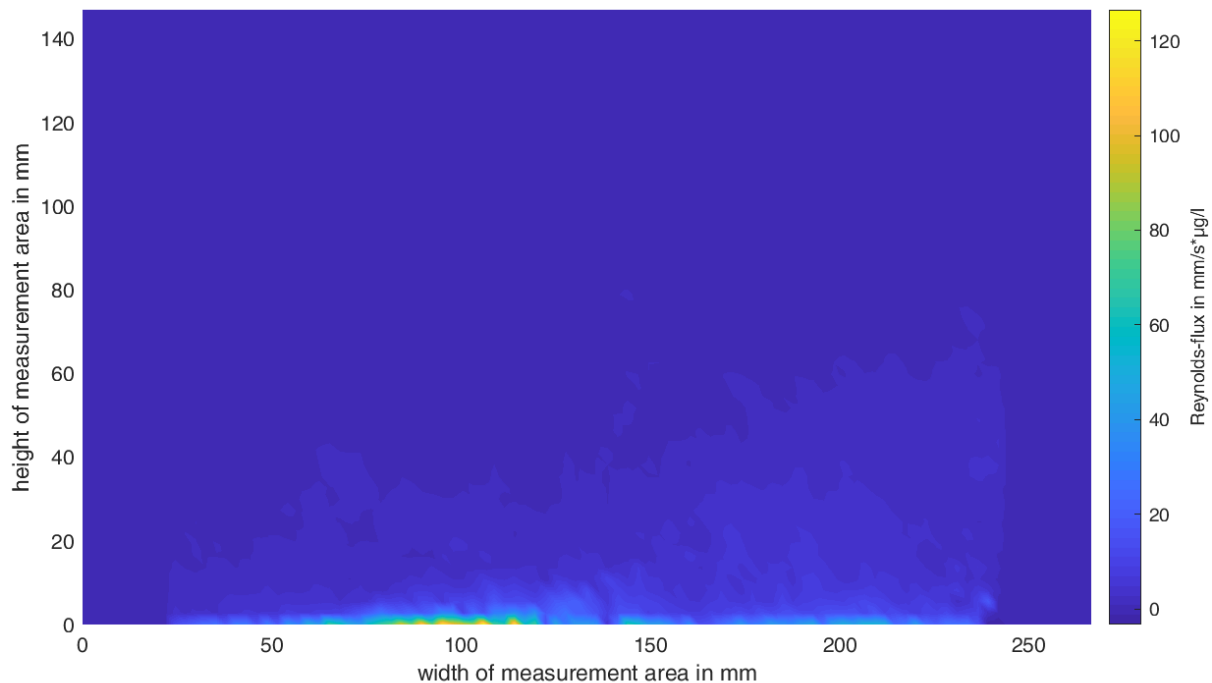


Figure 5-7: Mean phase averaged Reynolds-flux of 10PPI mean 0°

The color plot shows the Reynolds-flux in $\text{mm/s} \cdot \mu\text{g/l}$. The y- and x-axis display the measurement area in mm.

The Reynolds-flux-map marks the highest fluxes directly above the artificial seabed. This highlighted area is very small compared to the whole water column. It is clear, that the gradient in vertical direction is very strong, thus the flux is decreasing near zero very quickly. Considering the horizontal diffusion of the Reynolds-flux, it can be estimated, that in the central area the fluxes are evenly distributed. On the left and right side may boundary effects will occur. Furthermore, in the upper right part of the map, the spread of the flux occurs further into the water column. Hence, the turbulent transport takes place more far away from the ground. In this area it reaches nearly 50% of the measurement area, thus nearly

20% of the water column in this measurement. For the comparison of the single experiments of the vertical development of the Reynolds-fluxes an additional averaging is needed. The center of mass is defined for discrete systems as sum of the single masses multiplied by the position vector of the mass points divided by the total mass.

$$\vec{r}_{xy} = \frac{1}{m_{tot}} \sum_i m_i \vec{r}_i \quad \text{Eq. (5.2)}$$

Considering the Reynolds-flux diffusion of a single measurement (see Figure 5-7), this mass term in this equation is replaced by the Reynolds-flux. Thus, we obtain the center of the phase averaged Reynolds-flux diffusion as integral Reynolds-flux. But the spread of the low fluxes to the upper right leads to a shift of the center of the integral Reynolds-flux to the right side of the Reynolds-flux-map (see Figure 5-7). For this reason, only the parts of the map, which were higher than 50% of the maximum value in each map are considered for the calculation of the center of the integral Reynolds-flux (see Figure 5-8) for the definition of the central point for the averaging. Due to a smooth representation of this point, the averaging is done from 27 mm left and right beside the center of the integral Reynolds-flux.

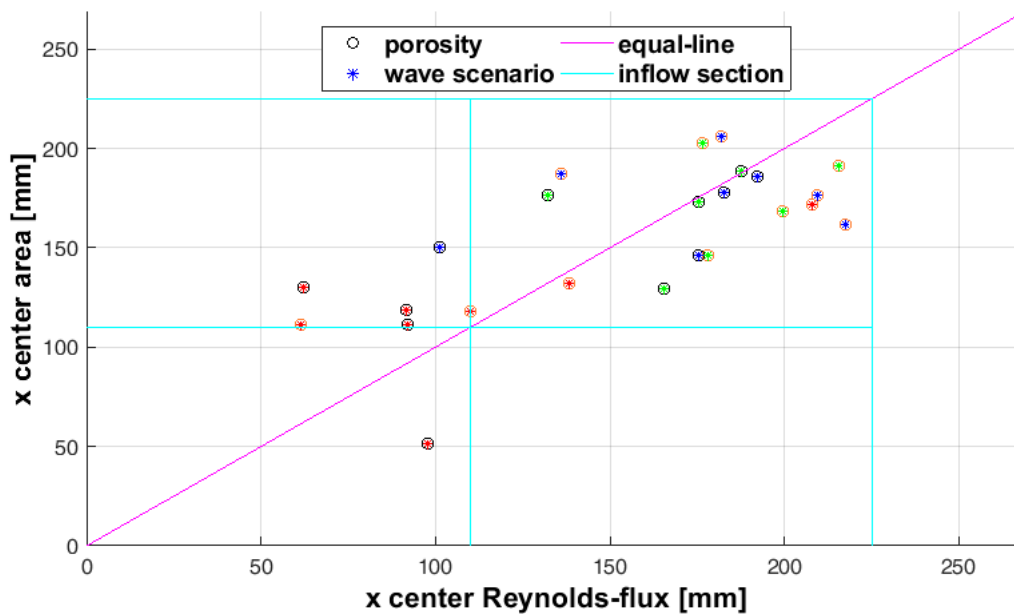


Figure 5-8: Scatter plot of centers for Reynolds-flux hotspots

In the scatter plot, the distribution of the centers of the integral Reynolds-flux in x direction and the centers of the boundary areas in x-direction are compared for every 24 measurements. The circles show the porosity of the medium, thus the orange color defines the 45PPI and the black color the 10PPI. The color of the star in the middle of the circle yields to the wave scenario. In which green is equal to calm, blue to mean and red to stormy (see Figure 4-4). The cyan colored area marks the inflow section. The magenta colored equal-line shows the $f(x) = y$.

The distribution of the centers of the integral Reynolds-fluxes shows, that the centers of the stormy scenarios are oriented to the left side of the measurement area. It is to mention, that the inflow section underneath the porous media is located between 110 mm and 225 mm at the x-axis. Hence, the other measurements are distributed near the center of the inflow area. Especially the calm scenario measurements are close to the center line of 165 mm and are rare distributed in x-direction.

Because of this similarity, the integral phase averaged Reynolds-flux and the calculated mean area of the 10% concentration boundary are compared in the next figure.

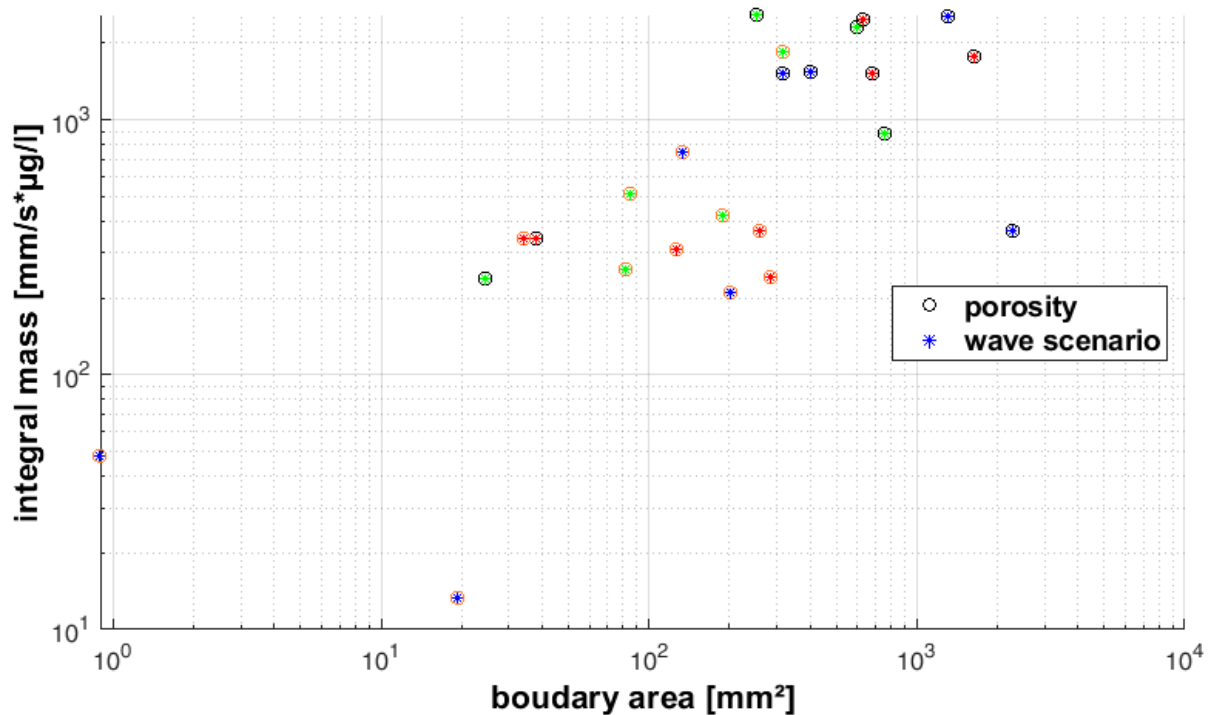


Figure 5-9: Comparison of the integral Reynolds-flux mass and the mean boundary area

On the y-axis the sum of the phase averaged Reynolds-fluxes is drawn on a logarithmic scale. The x-axis includes the boundary area in logarithmic scale. The circles show the porosity of the medium, thus the orange color defines the 45PPI and the black color the 10PPI. The color of the star in the middle of the circle yields to the wave scenario. In which green is equal to calm, blue to mean and red to stormy (see Figure 4-4).

In Figure 5-9 it is shown, that in most cases the higher integral Reynolds-fluxes goes with a bigger concentration boundary area. Hence, a high flux depends directly to a huge concentration field. Furthermore, the boundary areas and the integral Reynolds-fluxes of the 45PPI measurements are less than the 10PPI measurements. Furthermore, the calm scenarios show a less integral Reynolds-flux, than the other scenarios. Moreover, two of the mean wave scenario measurements cause a huge concentration boundary area.

In Figure 5-10 all averaged Reynolds-fluxes for the different measurement above the 10PPI porous medium are shown.

The 10PPI measurements show mainly, that the stormy scenario has the highest fluxes near the ground, followed by the mean scenario and at last the calm one. Furthermore, the decrease of the flux during the stormy scenario is less compared to the other two wave scenarios. Hence, a higher flux in the upper area of the water column occurs. Moreover, the maximum values of the Reynolds-fluxes decrease with the higher slope angles. Considering the 7° slope angle measurements, the mean scenario shows a strong dent near the ground. The reason for this is the occurrence of negative Reynolds-fluxes in the averaged area. Following the behavior of the graph after the dent, the value at the ground may reach the maximum of the stormy wave scenario in the measurements. Hence, a change of the order of magnitudes between the wave conditions may occur. Considering the measurements of the 14° slope angle, this change is obvious. The mean wave scenario shows the highest Reynolds-fluxes and even the slowest decrease of them along the water column.

Considering the differences between the measurements of the two porous medias, it is obvious, that the Reynolds-fluxes upon the 45PPI medium are much less, than over the 10PPI media. For this reason, the Reynolds-fluxes for the 45PPI porous media are not shown in a detailed view here.

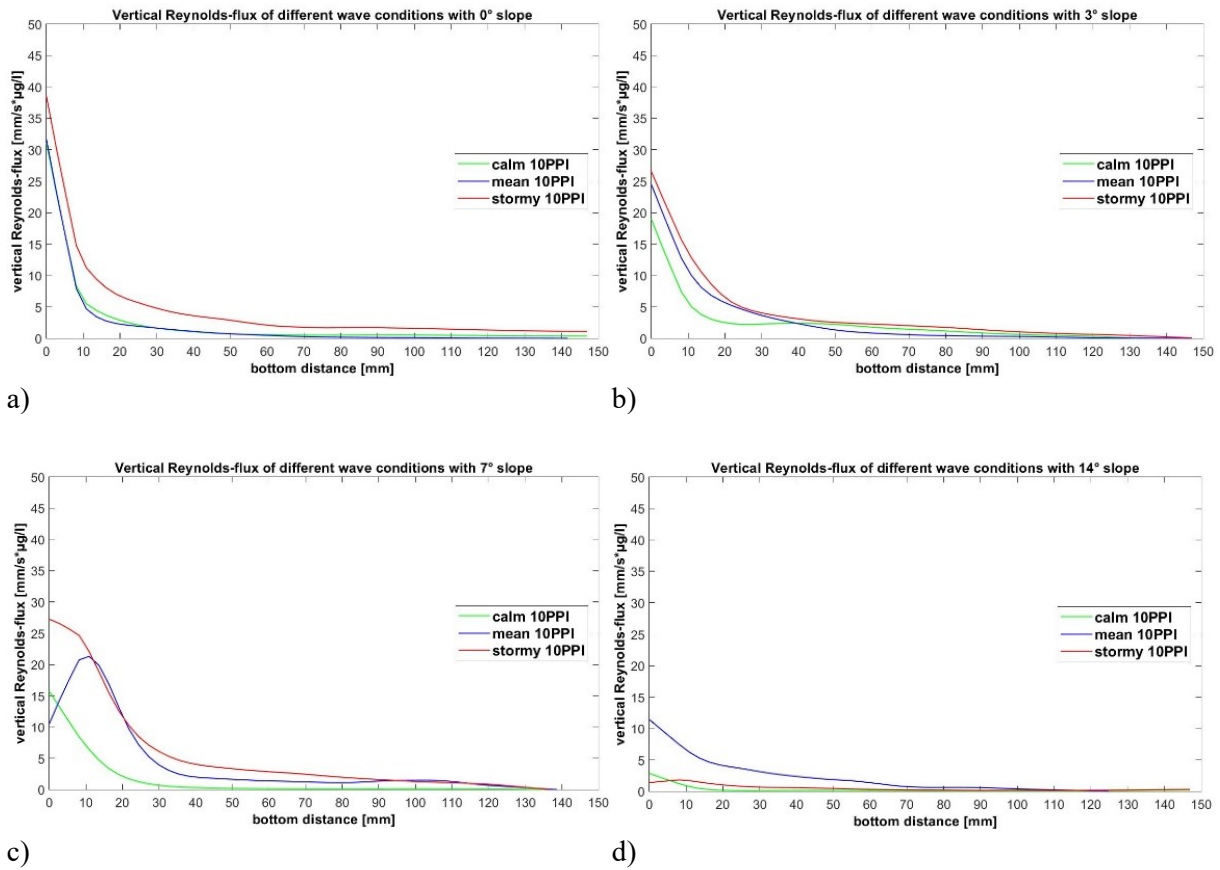


Figure 5-10: comparison of averaged Reynolds-fluxes for the 10PPI measurements

In this figure all averaged Reynolds-fluxes of the experiments with the 10PPI porous medium are shown. Every single image includes the diffusion for the three wave scenarios calm (green), mean (blue) and stormy (red). Starting from a) with 0° slope angle, b) 3° slope angle, c) 7° slope angle and ending up with d) with 14° slope angle.

Considering the spread of the fluxes into the water column, it is seen that the strongest decrease of the fluxes occurs nearly in the same range between 10 and 30 mm bottom distance. The spread itself depends on the wave scenario but comparing the left and the right image it is clear that the spread behavior does not change significantly. Especially the 14° slope angle measurements differ from this expectation. The 45PPI measurement in this case show a stronger decrease down to zero in the range until 20 mm bottom distance.

For the description of the development of the boundary area, a boundary growth rate is calculated (see Eq. 5.1). This rate is defined as the difference quotient of the 10% concentration boundary line over time:

$$\gamma_{10} = \frac{Max(C_{10}) - Min(C_{10})}{t(Max(C_{10})) - t(Min(C_{10}))} \quad \text{Eq. (5.3)}$$

This equation delivers the gradients of the boundary growth which can be estimated in the single images of Figure 5-6. In this figure the low-pass filtered development of the 10% concentration boundary line are plotted for the different porous medias and the wave scenarios.

The rate is due to the gradient between the minimum bottom distance of the concentration boundary line to the maximum development into the water column over time. A scatter plot of this boundary growth rate over the averaged vertical Reynolds-fluxes is shown in Figure 5-11. Due to the minimum of Reynolds-flux and boundary growth rate in the 45PPI measurements, the following figure only includes the parameters of the 10PPI measurements.

The scatter plot leads to the assumption, that an increasing Reynolds-flux leads to an increasing boundary growth rate. A line (red) can be estimated, which shows the gradient of this relation between these two parameters. Furthermore, the stormy scenarios in red color show high Reynolds-fluxes apart from the 14° slope angle measurement. Moreover, the Boundary growth rate in every case the calm scenario shows the weakest rate. In the 0° measurements the rate increases with the stronger wave scenario (calm<mean<stormy). In every other case, always the mean scenario shows the highest boundary growth rate. This is almost comparable to the trends of the line plots in Figure 5-6.

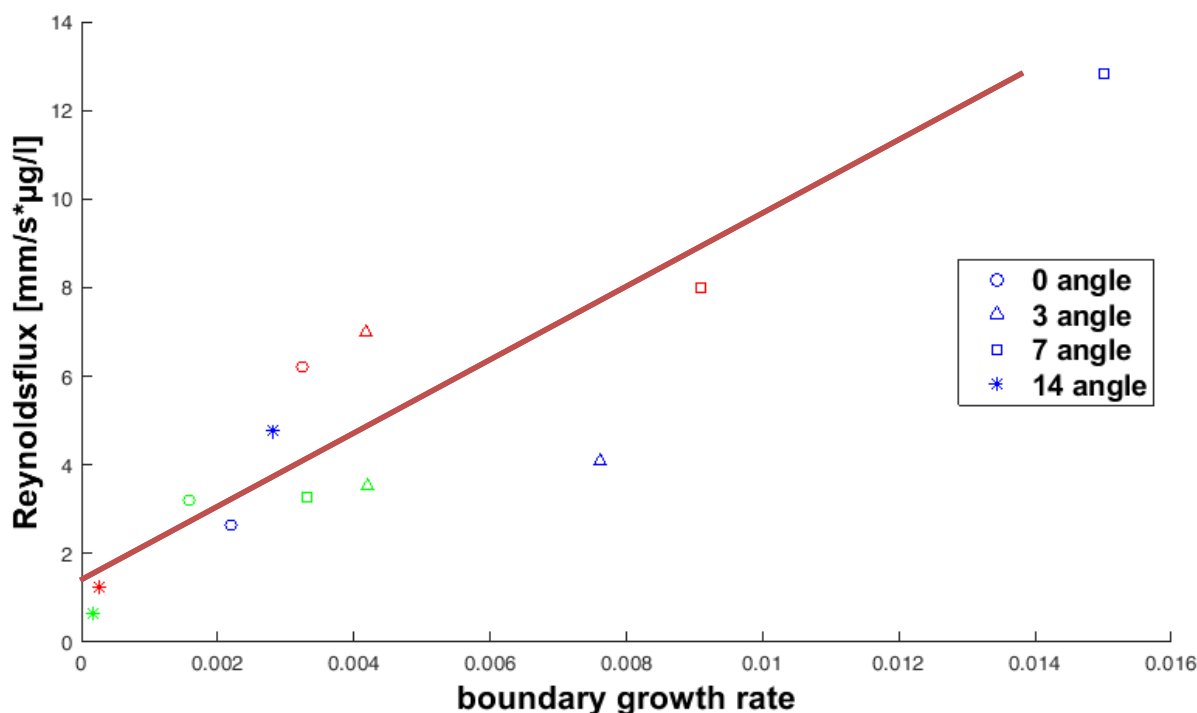


Figure 5-11: Scatter plot of the averaged Reynolds-fluxes of 10PPI and the boundary growth rate

The figure shows the relation between the Reynolds-fluxes on the x-axis and the boundary growth rate on the y-axis. The shown measurements are done with the 10PPI porous medium. The red color indicates the stormy scenario, the blue one the mean scenario and the green the calm wave scenario. The shape of the points is standing out the slope angle of the measurement. The circle corresponds to 0°, the triangle to 3°, the square to 7° and the star correspond to 14° slope angle. With the red line the ratio between the Reynolds-fluxes and the boundary growth rate is marked.

5.3 Mixing length models

The mixing length model is an empirical model for the numerical simulation of turbulent effects in boundary layers. Furthermore, it can be used as model for the turbulent transport of a scalar tracer, like the concentration C . The derivation and background information are given in section 2.5.3. The model consists of the following parameters:

$$l_c = \sqrt{\left| \frac{\langle w'c' \rangle}{\frac{\partial \langle u \rangle}{\partial z} \cdot \frac{\partial \langle c \rangle}{\partial z}} \right|} \quad \text{Eq. (5.4)}$$

For this reason, the single parameters are considered firstly. Then the mixing length development for each measurement is explained.

5.3.1 Concentration gradients

The concentration gradients are calculated with the forward difference quotient in z -direction. Hence, the development of the concentration gradient in vertical direction starting from the bottom is shown in the following figure.

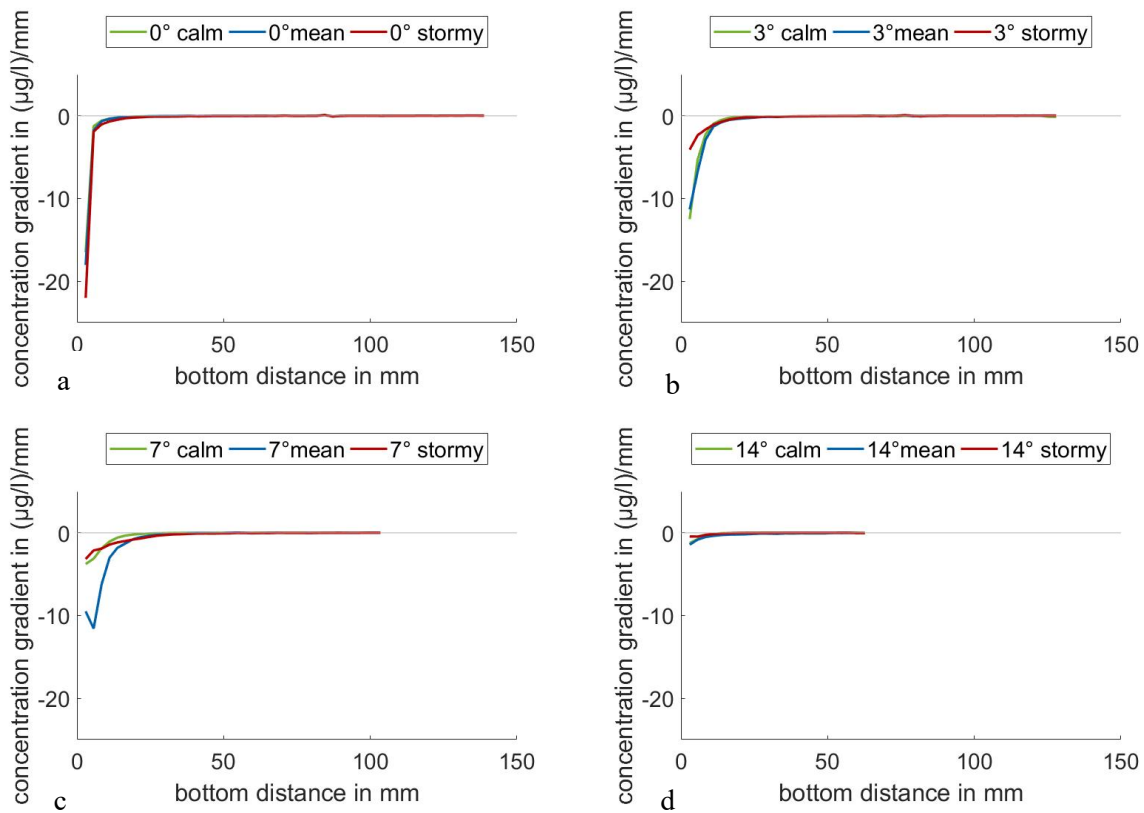


Figure 5-12: Concentration gradients for different wave scenarios of the 10PPI medium

In the single figures a-d the concentration gradient is mentioned on the y-axis over the bottom distance in mm at the x-axis. In a) the 0° slope angle, in b) the 3° slope angle, in c) the 7° slope angle and in d) the 14° slope angle is shown.

Considering the concentration diffusion of the tracer, it is clear that the gradients show always the same development (see Figure 5-12). Because of the inflow from the bottom, the highest concentration is found nearest to the bottom area. Under the wave action, the concentration decreases with higher distance to the bottom. Hence, the vertical gradients must be strong negative near the ground and increase with the bottom distance until the concentration vanishes and the gradient becomes zero. Because of slight background noise in the images, the concentration will not be zero and therefore the gradient will also never be zero. But it is obvious in Figure 5-12, that it is close zero at a bottom distance where the concentration of the tracer starts to vanish.

In the four figures a-d in Figure 5-12 the gradients are smaller with the increasing slope angle. In the case of 0° slope in a), the stormy scenario shows the strongest gradients. Furthermore, the decreasing of the stormy scenario is smaller than for the other two scenarios. In b) the stormy scenario shows the lowest gradients near the bottom, but after 5 mm bottom distance the development is equal to the other two scenarios. Moreover, the calm and mean scenario shows the same behavior from the start at the bottom until the decrease to a zero gradient. The 7° slope angle in figure c) shows almost the same development of the concentration gradient for the calm and stormy scenario. But the stormy condition is defined with a slighter decrease of the gradient with the bottom distance. Furthermore, the mean scenario shows the strongest gradients for this case. In the last figure, the 14° slope angle is plotted. In this case are the concentration gradients very small compared to the other three cases in a), b) and c). For this reason, the development of the gradients for the different wave scenarios is almost the same. The mean scenario may show the strongest concentration gradients in this case.

In summary, the development of the concentration gradients over the bottom distance for the different wave scenarios and slope angles of the 10PPI measurements show no significantly differences between each other. Furthermore, the strength of the gradient decreases with the higher slope angle.

5.3.2 Velocity fields

The calculation of the velocity gradients base on the mean phase averaged velocity fields. These fields show different behavior under the wave scenarios with the two permeable sea beds.

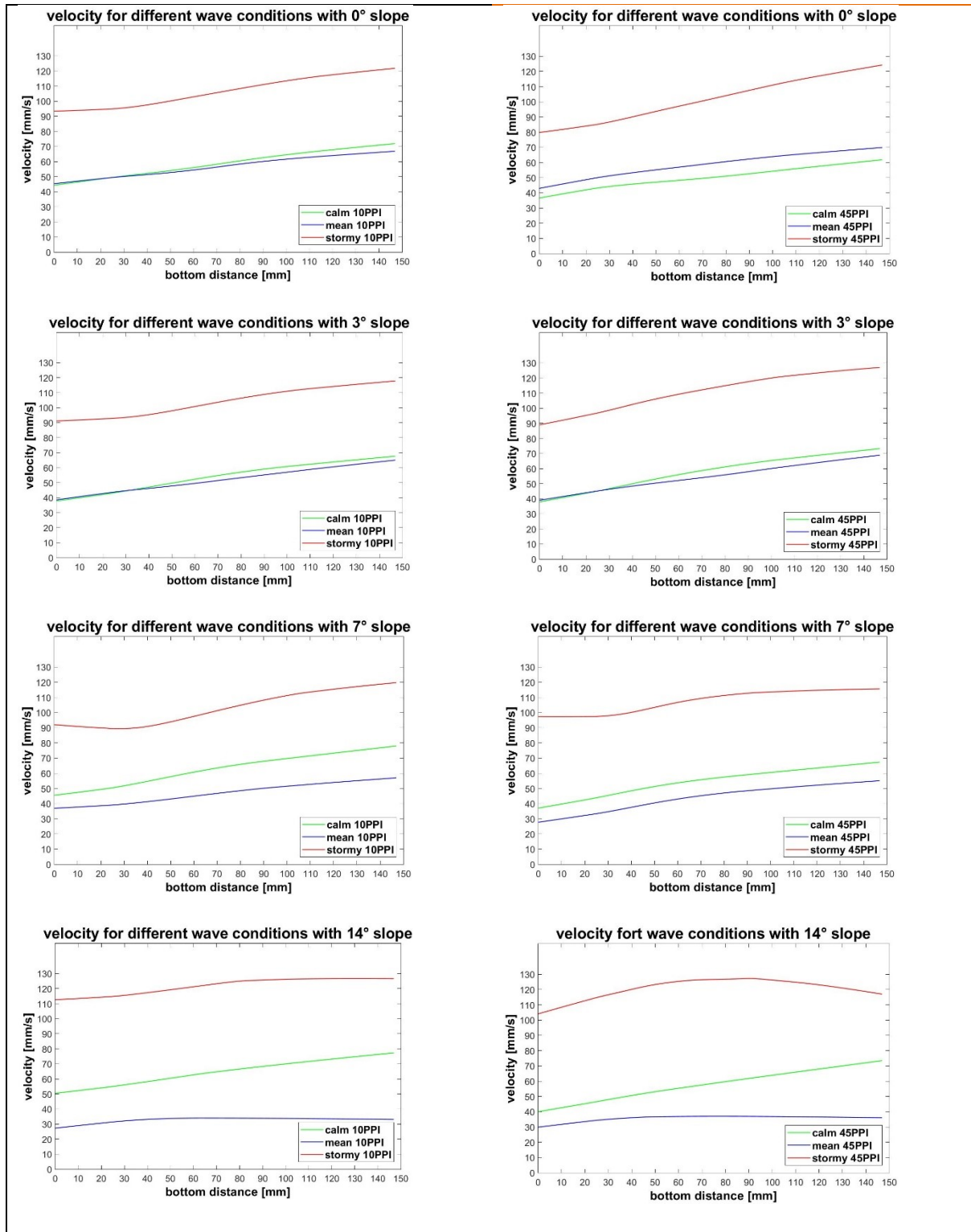


Figure 5-13: Comparison of the phase averaged velocity fields from [Kandler 2018]

On the left-hand side, all phase averaged velocity fields of the experiments with the 10PPI porous media are shown and on the right-hand side the same for the 45PPI porous media. Every single picture includes the development for the three wave scenarios calm (green), mean (blue) and stormy (red). Starting from the upper part with 0° slope angle and ending up with the bottom parts with 14° slope angle.

At first, the left side of the comparison is consolidated. The 10PPI measurements show mainly an increase of the phase averaged velocity field with increasing distance to the ground for every scenario. Furthermore, the calm and mean wave scenario show for the 3° slope angle and for the 0° slope angle nearly the same behavior. In the case of 7° and 14° slope angle, the calm scenario profile is marked with higher velocity compared the profile of the mean scenario. Every profile is defined with a strong increase of the velocity followed by a decrease until a slightly increase follow up. Especially in the stormy scenarios of the 7° slope angle measurement this behavior is observed.

At second, the right side of the comparison is consolidated. The 45PPI measurements show mainly the same behavior of the velocity profiles such as the 10PPI measurements. In the 0° slope angle experiment, the definition case of the wave scenarios is shown. The stormy scenario has much higher velocity values as the mean scenario and the mean scenario has higher values than the calm one. With stronger slope angles, this order changes. For 3° the mean and calm scenarios are mainly the same, but for 7° and 14° the mean scenario velocity profile falls under the calm one.

At last the 10PPI and 45PPI measurements are compared. It is clear that the velocity profiles of the 45PPI measurements differ near the seabed from the 10PPI measurements. In the case of the 0° slope angle, the stormy and the calm scenario start with a 10-15 mm/s lower velocity at the bottom. The mean scenario profile is nearly the same. For the 3° slope angle, the profiles of the 45PPI and the 10PPI measurements are identically. In the case of 7° slope angle, the stormy scenarios show nearly the same course. The velocity profiles of the calm and the mean scenario above the 45PPI seabed show the same shift of 10 mm/s down such as in the 0° slope angle comparison. In the last case of 14° slope angle, this shift occurs for the stormy and calm scenario of the 45PPI measurement. The mean scenario shows the same course for both porous medias.

5.3.3 Velocity gradients

The velocity gradients are built with the forward difference quotient in z-direction. Thus, they are calculated similar to the concentration gradients of section 5.3.1. Because of the high sensibility of the gradients, the velocity fields are smooth by a moving average filter. This leads to fewer fluctuations in the velocity gradients. Furthermore, it is mentioned that because of the moving average filter the velocity profiles are extrapolated to the maximum bottom distance of 150 mm. This distance is not captured by the measurements with different slope angle, because the field of view is not changed. Hence, the 14° slope angle measurements include a maximum bottom distance between 60 and 70 mm.

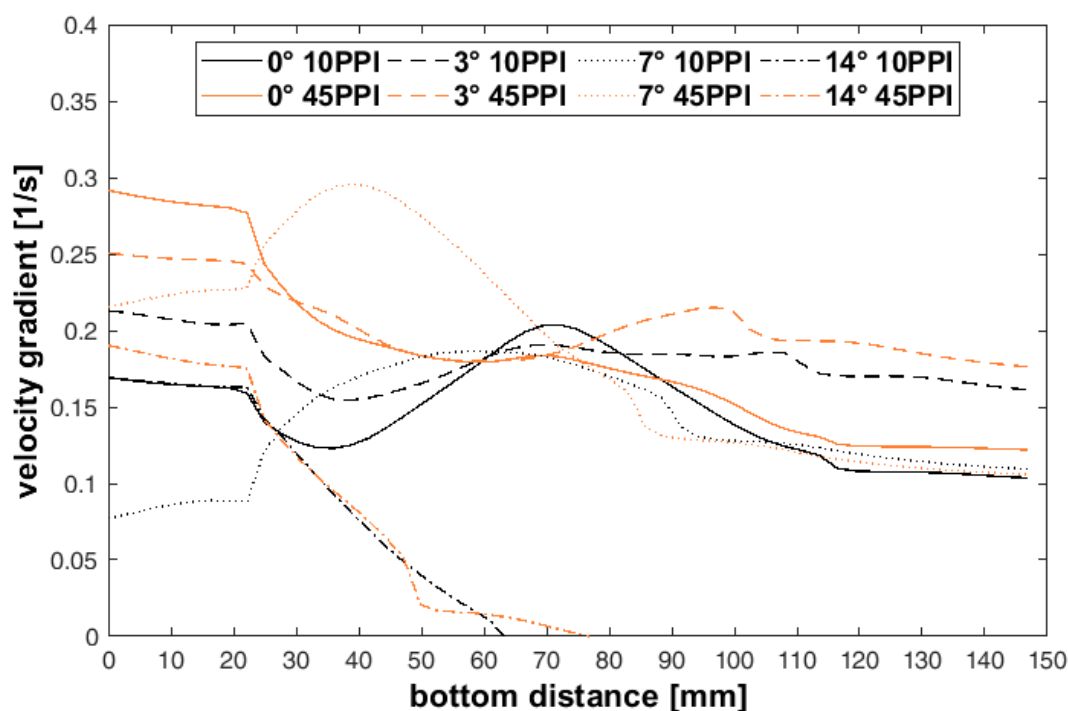


Figure 5-14: Velocity gradients for the mean wave scenario

In the figure the velocity gradients of the mean wave scenario are shown. On the y-axis the gradients in 1/s are plotted over the bottom distance on the x-axis in mm. The solid line illustrates the 0° slope angle, the dashed line the 3° slope, the dotted line the 7° slope and the dashed and dotted line the 14° slope.

The gradients of the mean wave scenario measurements in Figure 5-14 show very specific behavior in the first 20 mm of bottom distance. The profiles are defined by a steady gradient until 20 mm followed by a sharp edge and decreasing of the gradient. Only the 7° profiles show an increase after the sharp edge. After the strong decrease, an increase to a steady value is reached.

5.3.4 Mixing length

Basing on the single parameters explained and described in the chapters above, the mixing length is calculated. Furthermore, a moving average filter is used to smooth these results.

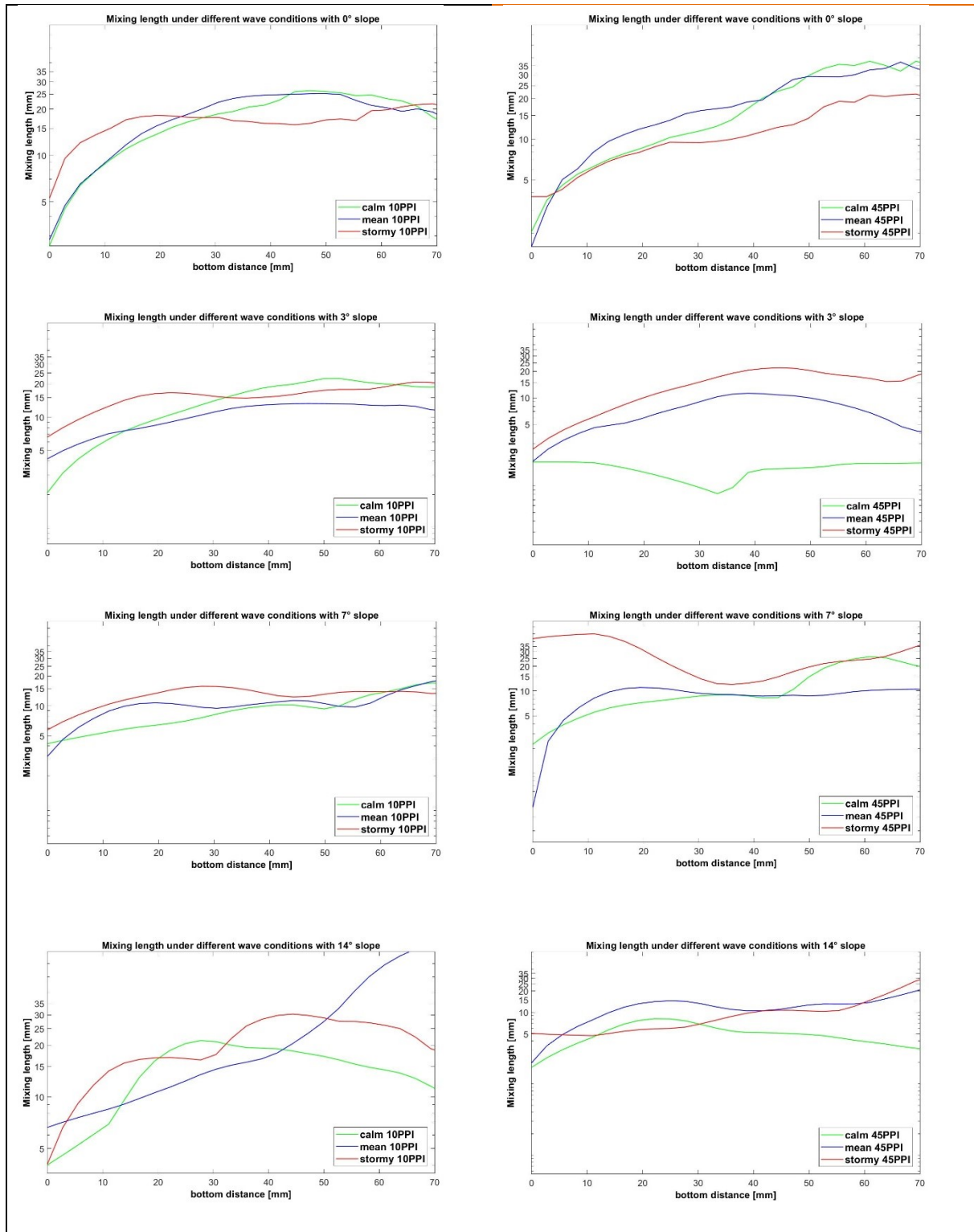


Figure 5-15: Comparison of the Mixing length

On the left-hand side, all averaged mixing length of the experiments with the 10PPI porous media are shown and on the right-hand side the same for the 45PPI porous media. Every single picture includes the development for the three wave scenarios calm (green), mean (blue) and stormy (red). Starting from the upper part with 0° slope angle and ending up with the bottom parts with 14° slope angle.

At first, the left side of the comparison is consolidated. The 10PPI measurements show mainly, an increase of the mixing length with the bottom distance in the first 20 mm distance. After this they may enter a constant value of the mixing length. The starting point differs with the conditions. It is clear that the 14° slope angle measurements show a different development within the wave scenarios. For the other three slope angles the three wave scenarios may end up with the same mixing length. Furthermore, the stormy scenario causes the highest mixing length directly above the seabed. This shows a high fluctuation of a tracer fragment in the boundary zone.

At second, the right side of the comparison is consolidated. The 45 PPI measurements show mainly a slightly increase of the mixing length with the bottom distance. After 10 -25 mm bottom distance the mixing length approximates to a constant value. This value differs between the wave scenarios for every slope angle. Moreover, the stormy scenario shows the highest mixing length near to the bottom, thus they show the same behavior as in the results for the 10PPI measurements.

At third, considering the difference between the 10PPI and the 45PPI measurements for every slope angle. In the case of 0° slope angle, the mixing length shows nearly the same behavior. The mean and calm scenario starts with a mixing length around 1 mm and increase until 15-25 mm far from the bottom. The stormy scenarios starting around 5 mm and end up near 15 mm. In the case of 3° slope angle, the 45PPI measurements show smaller mixing lengths. Furthermore, the differences between the different wave scenarios for the 45PPI measurements are stronger compared to the 10PPI. In the case of the 7° slope angle, the calm and mean wave scenarios show nearly the same development. The stormy event over the 45PPI shows significantly higher mixing lengths than every other experiment. Moreover, it is the only one which shows a decrease of the mixing length with higher bottom distance. In the case of 14° slope angle, the 45PPI measurement shows lower mixing length, but a very constant development over the bottom distance. On the other hand, the 10PPI measurements show high differences between the mixing lengths of the different wave scenarios in the farer distance from the ground.

In conclusion, the mixing length increase in every case with the bottom distance until a maximum is reached. Furthermore, the 45PPI measurements show expected fewer mixing lengths. Moreover, the stormy scenarios have the highest mixing length near the bottom.

In the next figure, the boundary growth rate and the mixing length are considered. For this, the median of each mixing length is plotted to each boundary growth rate. Hence, the effect of the boundary growth on the mixing length is shown. In Figure 5-16 the y-axis marks the boundary growth rate and the x-axis the mixing length. The color of the circle around every point defines the porosity. The color in this circle stand for the wave scenario. The slope angle is not mentioned in this figure.

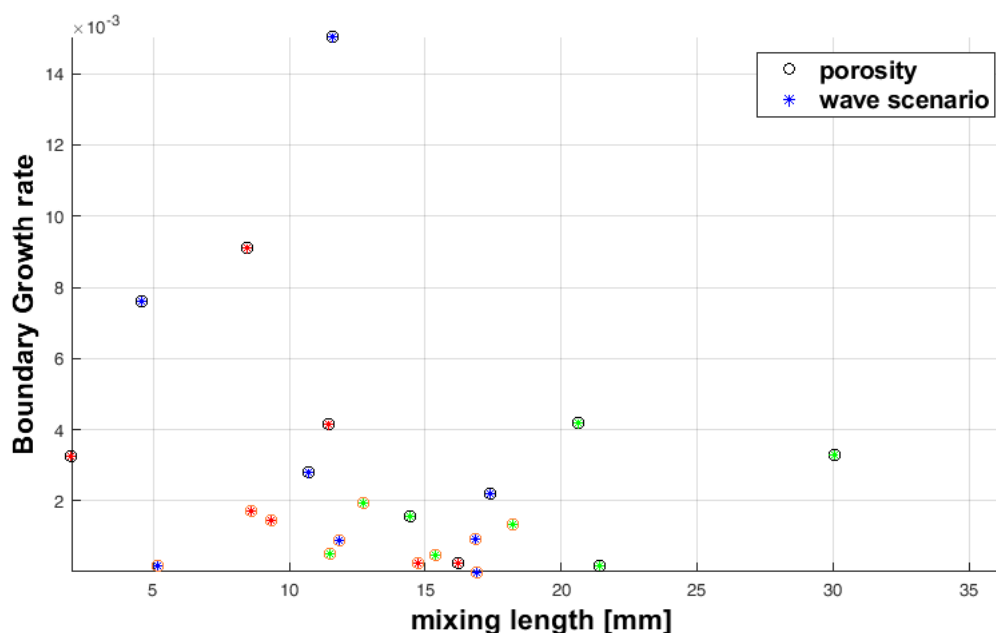


Figure 5-16: Scatter plot of the boundary growth rate over the mixing length

In this figure the boundary growth rate on the y-axis and the mixing length on the x-axis is shown. The circles show the porosity of the medium, thus the orange color defines the 45PPI and the black color the 10PPI. The color of the star in the middle of the circle yields to the wave scenario. In which green is equal to calm, blue to mean and red to stormy (see Figure 4-4).

The scatter plot shows that most of the measurements tends to a mixing length between 10 and 20 mm. Considering the stormy and mean scenarios, they show higher boundary growth rates and small mixing lengths. On the other hand, the calm scenarios tend to larger mixing lengths and small boundary growth rates. Furthermore, the 45PPI measurements have small growth rates and a small variability related to the mixing length.

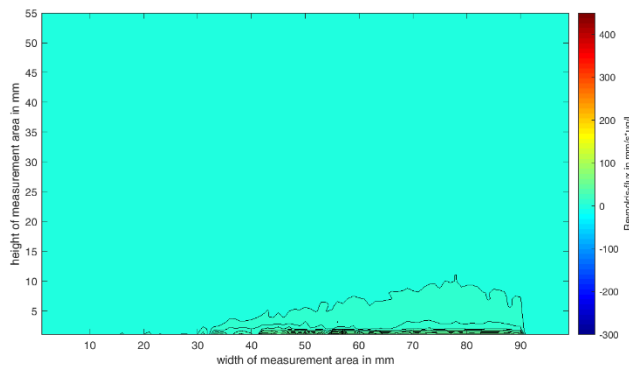
In conclusion, a direct proportionality between the mixing length and the boundary growth rate is not seen. Furthermore, it can be estimated, that with a small boundary growth rate the mixing length tends to increase. Moreover, with a higher permeability, the median mixing length variability tends to decrease.

5.4 Phase specific Reynolds-Fluxes and Mixing length

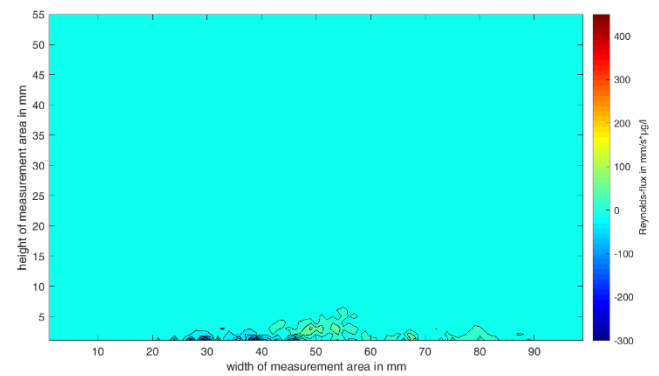
In the aspect of phase depending analysis, the Reynolds-fluxes and the mixing length are considered in this chapter. In the former sections, the averaged, time averaged values of the 12-phase averaged ensembles were considered. Due to the dependencies on the waves, it is necessary to investigate the single phases more in detail.

5.4.1 Phase specific Reynolds-fluxes

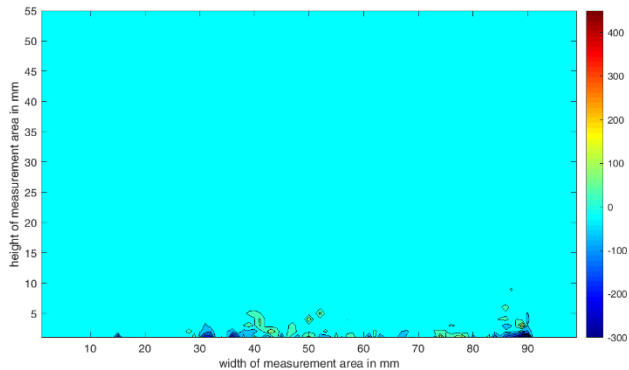
The time series of each measurement is split into 12 phase sections (see Figure 4-6). For every phase section the Reynolds-flux maps were calculated and analyzed separately. The following figures showing the phase averaged Reynolds-fluxes for the measurement with the 10PPI porous medium under the mean wave scenario for 0° slope angle.



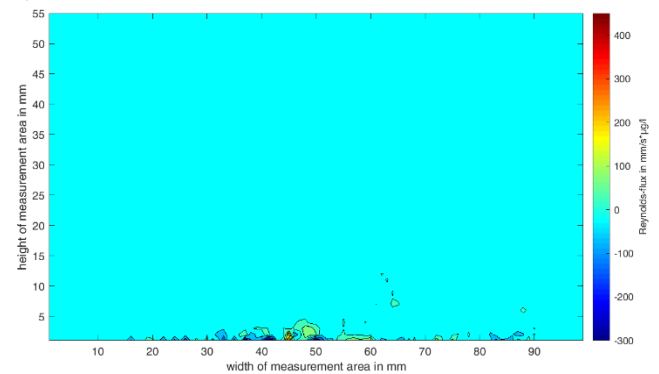
a) Phase 1: 350° - 10°



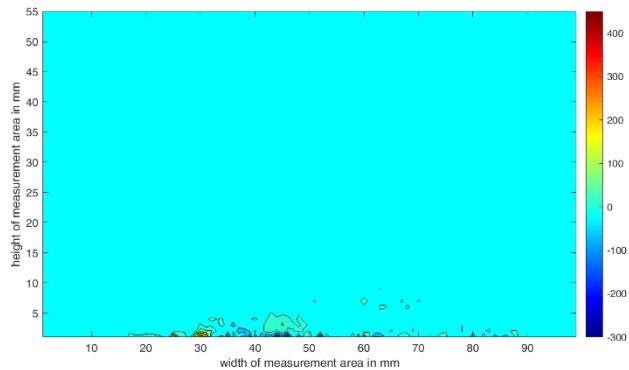
b) Phase 2: 10° - 35°



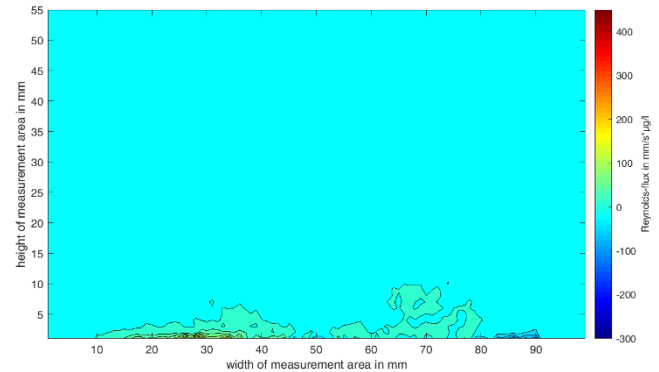
c) Phase 3: 35° - 70°



d) Phase 4: 70° - 110°



e) Phase 5: 110° - 145°



f) Phase 6: 145° - 170°

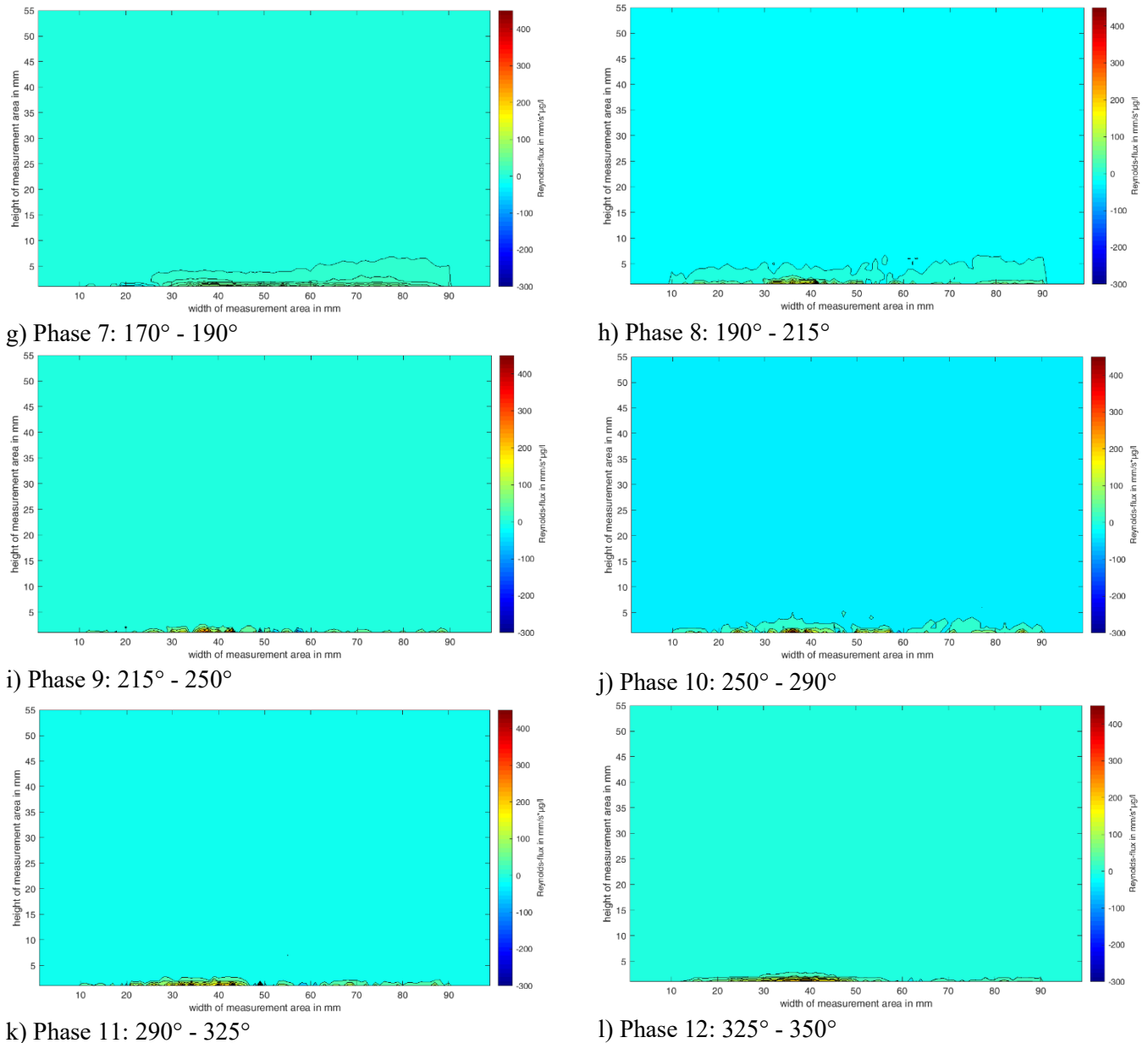


Figure 5-17: Phase averaged Reynolds-flux maps

The 12 Reynolds-flux maps for the measurement with 10PPI porous media, mean wave scenario and 0° slope angle. On the x-axis the width of the measurement area and on the y-axis the height of the area is marked in mm. The left and the right boundary is defined as zero to neglect the boundary effects from the side flow into the measurement area.

The Reynolds-flux maps show over the complete phase sections no significant differences in the distribution into the vertical direction. The flux area is located above the bottom over the complete measurement area. The maximum values are around $500 \text{ mm/s}^2 \cdot \mu\text{g/l}$ and the minimum values are around $-300 \text{ mm/s}^2 \cdot \mu\text{g/l}$. The phases near the horizontal orientation (a), g)) show a smoother distribution of the fluxes in the measurement area than the others. Furthermore, the peak values are much less, and the flux area is higher into the water column. In the other phases, the fluxes are peakwise near the ground with high positive fluxes and high negative ones.

The averaged value of the single maps is calculated in the area of the maximum Reynolds-flux occurrence (described in 5.2). The mean phase value is shown for the 12 phases in a polar diagram to compare the behavior of the different wave conditions onto the phase specific Reynolds-fluxes. The markers in the diagram do not show single measurement points, they only identify the slope angle of the shown measurement. In Figure 5-18 the phase mean values for the three wave scenarios over the 10PPI porous media for the 0° slope angle are plotted.

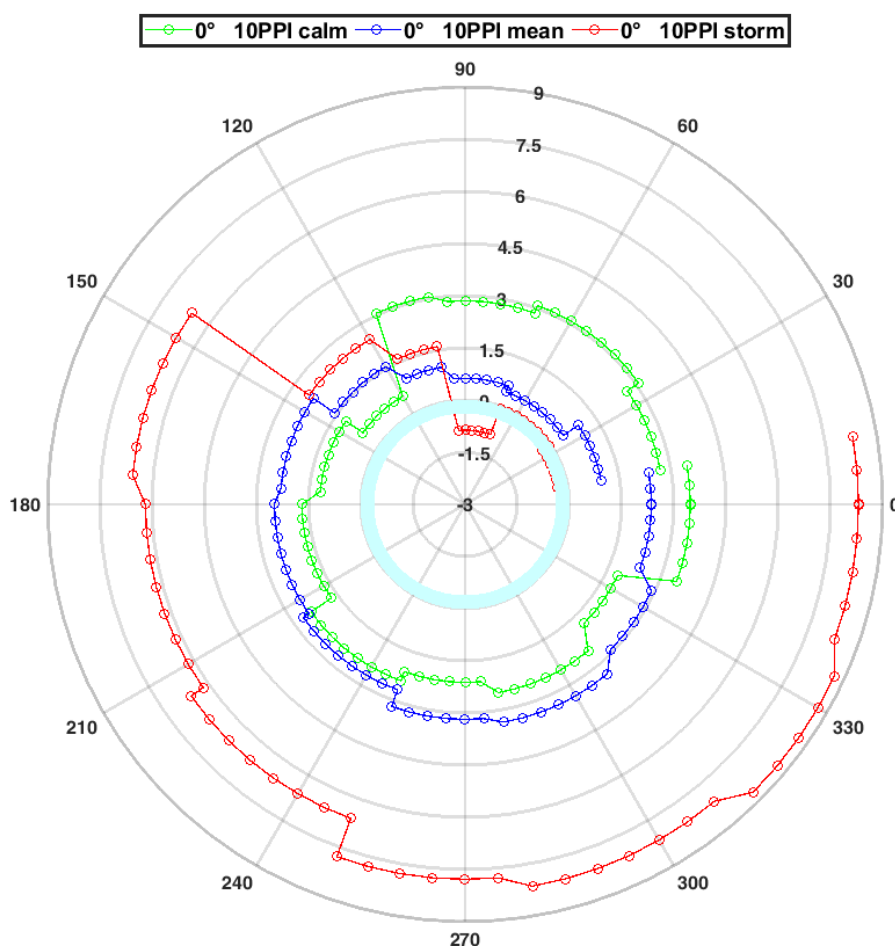


Figure 5-18: Polar diagram of averaged phase specific Reynolds-fluxes

The green color shows the calm wave scenario, the blue the mean wave scenario and the red the stormy wave scenario. The Markers do not show specific points. The phase sections are plotted as equal values. The light blue circle in the middle of the diagram is the zero line. This marks the occurrence of negative Reynolds-fluxes.

The diagram shows the comparison between the three wave scenarios for the phase specific Reynolds-fluxes. The stormy scenario (red) causes the highest fluxes. The mean (blue) causes higher fluxes than the calm (green) one. The mean and the calm scenario do not show significant differences between the phase sections. The mean one has the lowest fluxes between 35° and 120° phase angle. The calm one has the highest fluxes between 330° and 120° phase angle, hence it has contrary Reynolds-flux production compared to the mean scenario. Within the stormy scenario are almost constant between

145° and 10° phase angle. In vertical direction, between 10° and 145° phase angle, the fluxes decrease strongly. Around 90° phase angle also negative fluxes occur.

The slope angle dependencies are shown in Figure 5-19 for the mean wave scenario over the 10PPI porous media.

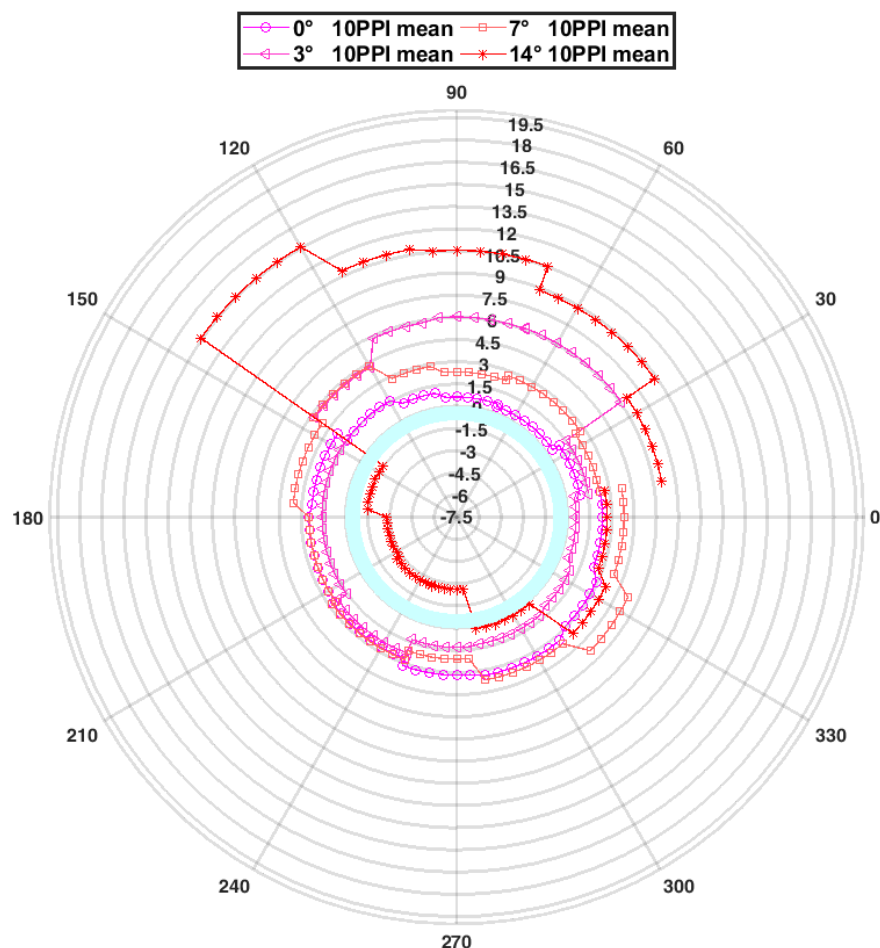


Figure 5-19: Polar diagram of mean wave scenario for 10PPI under different slope angles

The magenta color with circle markers shows 0° slope angle, the dark magenta with triangle markers the 3° slope angle, the light orange color with squared markers the 7° slope angle and the red with star markers the 14° slope angle. The markers do not show specific points. The phase sections are plotted as equal values. The light blue circle in the middle of the diagram is the zero line. This marks the occurrence of negative Reynolds-fluxes.

The 0°, 3° and 7° phase specific Reynolds-fluxes show only slightly differences. They are almost constant over the phases. The 3° and 7° measurements show higher maximum values between 35° and 120° phase angle than the 0° measurement. These three measurements do not show any negative fluxes. The 14° measurement has strong fluctuations between the phase specific Reynolds-fluxes. The highest fluxes occur between 35° and 145° phase angle. Between 145° and 275° also negative fluxes occur. In the rest phase sections, the positive fluxes are low.

5.4.2 Phase specific mixing length

Similar to section 5.4.1 the phase averaged mixing length were calculated. The phase averaged Reynolds-flux and the phase averaged velocity and concentration fields were used in the calculation. In the next figure, the measurement with the mean wave scenario above the 10PPI seabed model with 0° slope angle is considered, such as in section 5.4.1.

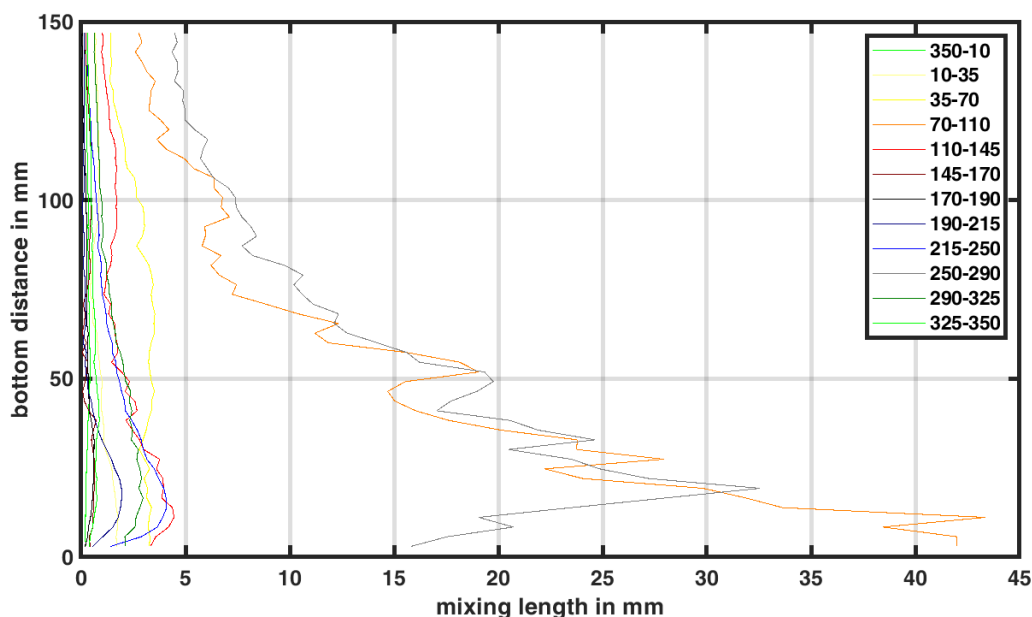


Figure 5-20: Phase specific mixing lengths for measurement 10PPI, 0° slope angle and mean wave scenario

The 12 phase sections are shown in different colors (see legend). On the y-axis the distance from the bottom is plotted.

In Figure 5-20 the phase specific mixing lengths of the 12 phase sections for the measurement above the 10PPI porous media with 0° slope angle and the mean wave scenario are shown. It is clear that two phase sections have significantly higher mixing lengths than the others. The orange colored phase section 4 ($70^\circ - 110^\circ$) is the vertical orientated phase in upwards direction. The grey scaled phase section is the opposite of it, thus the downwards orientated phase section 10 ($250^\circ - 290^\circ$). Moreover, the next four phases with higher mixing lengths are section 3 ($35^\circ - 70^\circ$), 5 ($110^\circ - 145^\circ$) and 9 ($215^\circ - 250^\circ$) and 11 ($290^\circ - 325^\circ$). These four phase sections lie next to the vertical orientated ones. Hence, the vertical phase direction is obviously the one with the significantly highest mixing length. Furthermore, it is seen that the development in y-direction is almost similar between the different phases. Firstly, the mixing length increases until a maximum is reached and secondly it decreases until a constant value. The two phase sections with the highest mixing length do not show a constant value.

In Figure 5-21 the phase specific mixing length for all 24 measurements are compared. To accomplish an overview of this, the median of the phase specific mixing length is calculated.

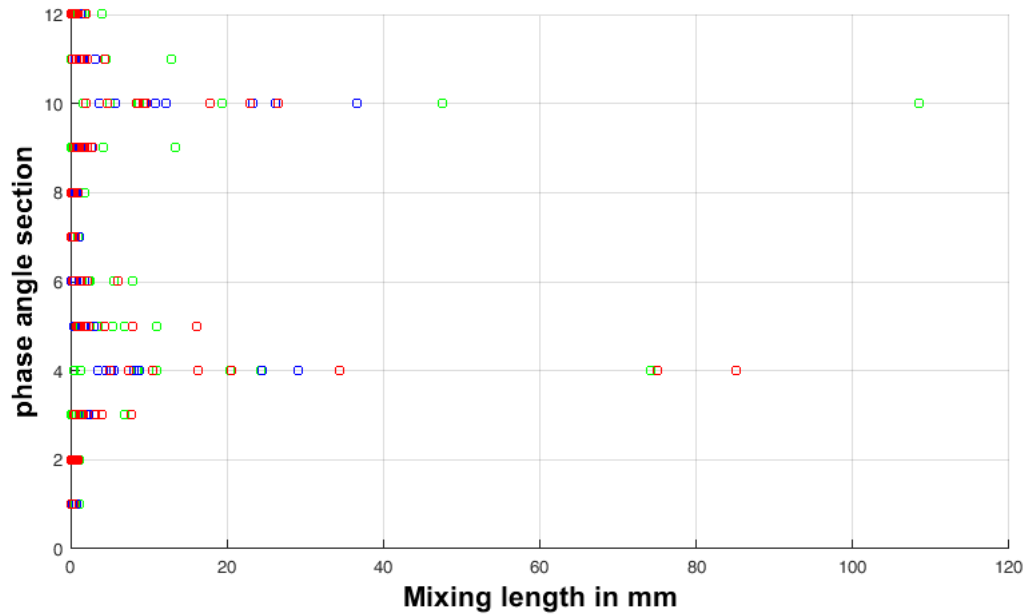


Figure 5-21: Median of phase specific mixing lengths for all measurements

The colors of the circles show the wave scenario. In green the calm scenario, in blue the mean scenario and in red the stormy scenario. On the x-axis the median mixing length is plotted. On the y-axis the phase section is shown:

- | | | | | |
|-----------------|-----------------|----------------|----------------|-----------------|
| 1) 350° - 10° | 2) 10° - 35° | 3) 35° - 70° | 4) 70° - 110° | 5) 110° - 145° |
| 6) 145° - 170° | 7) 170° - 190° | 8) 190° - 215° | 9) 215° - 250° | 10) 250° - 290° |
| 11) 290° - 325° | 12) 325° - 350° | | | |

It is shown, that obviously in the fourth and tenth phase section the highest mixing length occur. Furthermore, the first and seventh phase section have the smallest mixing length of all phase sections. The phases in between increase in direction to the maximum phases and decreases from these to the minimum ones. Hence, the more vertical the phase section is orientated (90° or 270°) the higher is the mixing length. Moreover, the maximum turbulent transport occurs in vertical direction.

5.5 Bottom friction and turbulence

In this section, the wave friction factor is considered as a wave damping factor for the wave scenarios. Furthermore, the bottom stress is calculated and the resulting turbulent kinetic energy is shown.

5.5.1 Bottom Friction factor

The bottom or wave friction factor is depending on the bottom stress. Following [Jonsson 1967], [Corvaro et al. 2016], [Le Roux 2003] and other the relation is defined as follows:

$$\tau_w = \frac{1}{2} * f_w * \rho * U^2 \quad \text{Eq. (5.5)}$$

In Eq. (5.5) the mean velocity U is calculated as the maximum averaged phase velocity. The bottom stress results from general assumption of the near bottom velocity gradient multiplied with the dynamic viscosity:

$$\tau_w = \mu \overline{\frac{du}{dz_{Bottom}}} \quad \text{Eq. (5.6)}$$

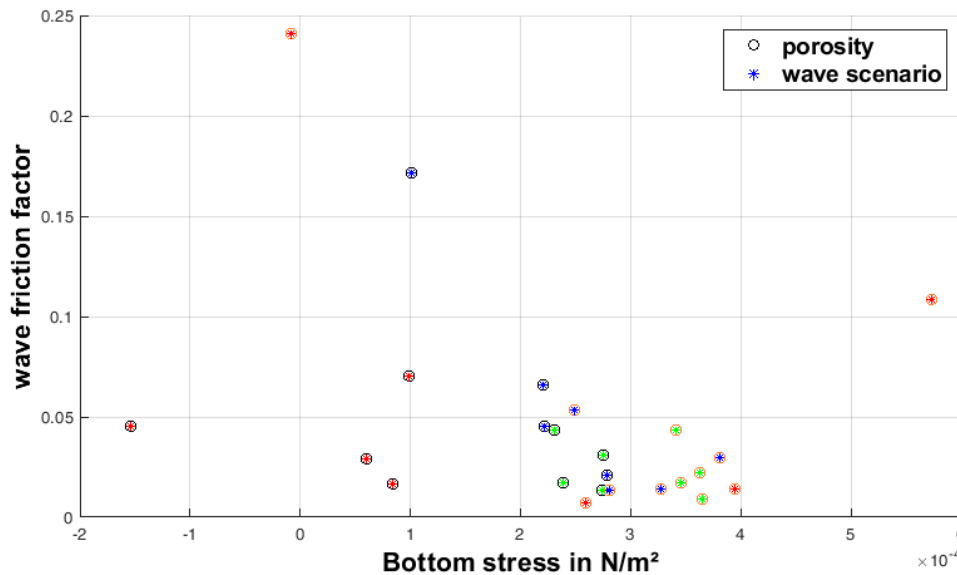


Figure 5-22: Wave friction over bottom stress

On the y-axis the wave friction factor basing on the averaged bottom stress is shown. On the x-axis the belonging bottom stress is shown. The color of the circles stands for the porous medium, thus the orange color includes the 45PPI medium and the black color the 10PPI medium. The color of the star in the circles shows the wave scenario, thus the green color stand for the calm, the blue for the mean and the red for the stormy scenario (see Figure 4-4).

In Figure 5-22 the wave friction factor and the bottom stress are shown. The calm scenarios show two bottom stress regimes, one for the 45PPI (orange) and one for the 10PPI media (black). In these regimes the wave friction differs slightly with respect to the different slope angles. The stormy scenarios show one bottom stress regime for the 10PPI media with one exception with a negative stress due to a negative gradient. The 45PPI media measurements of the stormy scenario show a wide range of bottom stresses with the different slope angles. The mean scenario measurements show the same behavior as the calm scenarios, but the wave friction factor differs more strongly and is in the most cases higher. Furthermore, it is seen, that the 45PPI measurements leads to higher bottom stresses. But in the case of the mean wave scenario, the wave friction factor is strong even like two measurements of the stormy scenario with the 45PPI porous medium. These higher wave friction factors due to strong decrease of the averaged velocity in these cases.

In Figure 5-23 the wave friction factor and the Reynolds-flux are compared. It is shown, that the Reynolds-fluxes are not significantly influenced by the wave friction.

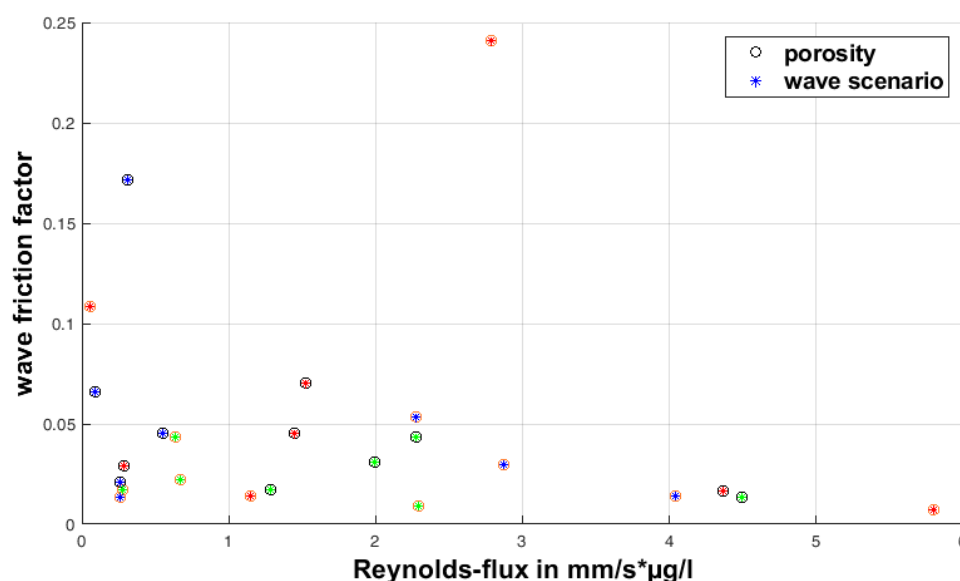


Figure 5-23: Wave friction over Reynolds-flux

On the y-axis the wave friction factor basing on the averaged bottom stress is shown. On the x-axis the belonging Reynolds-flux is shown. The color of the circles stands for the porous medium, thus the orange color includes the 45PPI medium and the black color the 10PPI medium. The color of the star in the circles shows the wave scenario, thus the green color stand for the calm, the blue for the mean and the red for the stormy scenario (see Figure 4-4).

5.5.2 Turbulent Kinetic Energy (TKE)

The turbulent kinetic energy shows the averaged turbulent velocity fluctuation in the flow in all directions. The energy is calculated with the following equation:

$$\text{TKE} = \frac{1}{2} (\overline{(u')^2} + \overline{(w')^2}) \quad \text{Eq. (5.7)}$$

In Figure 5-24 the mean Reynolds-stress is compared with the root mean squares of the median of the phase specific turbulent kinetic energy.

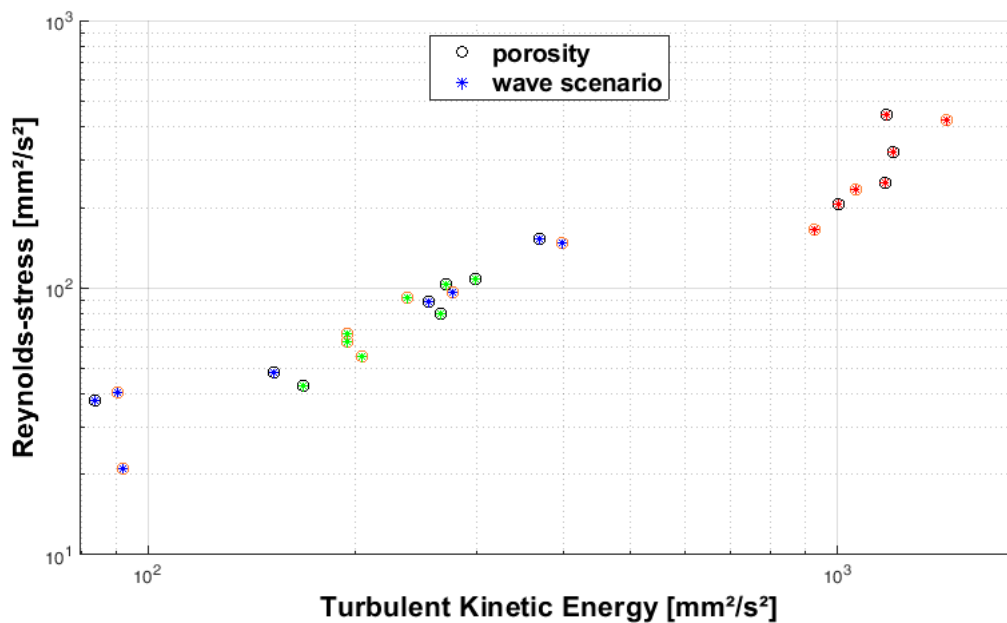


Figure 5-24: Reynolds-stress over turbulent kinetic energy

On the y-axis the Reynolds-stress is shown in logarithmic scale. On the x-axis the TKE is shown in logarithmic scaling. The color of the circles stands for the porosity, thus the orange color marks the 45PPI media and the black color the 10PPI media. Moreover, the color of the star in the circle marks the wave scenario, thus the green star stands for the calm scenario, the blue one for the mean scenario and the red one for the stormy scenario (see Figure 4-4).

In Figure 5-24 a linear dependency of the TKE and the Reynolds-stress is shown. With higher TKE a high Reynolds-stress occurs. Furthermore, the stormy scenarios showing the highest TKE, thus the highest Reynolds-stress. The mean and calm scenario are located in the same regime of TKE and Reynolds-stress. Except for three measurements which show much lower turbulent kinetic energy levels than the others. Moreover, most of the calm scenarios above the 10PPI seabed, showing higher TKE than the 45PPI measurements with the calm scenarios. Furthermore, the measurements above the 10PPI

medias showing mostly the same TKE value for each wave scenario but differ slightly in the Reynolds-stress. Except for the mean wave scenario, here the TKE differs over a wide range.

In Figure 5-25 the median of the phase specific turbulent kinetic energy is shown as polar diagram. It is seen, that the stormy scenarios have the highest energy in every phase section. Furthermore, the mean and calm scenario do not differ significantly from each other (see also Figure 5-24). Moreover, it is obvious, that the horizontal phase sections cause the highest TKE. This behavior is for every measurement the same (see Appendix F). In forward direction (0° phase), the TKE is less than in backward direction (180° phase). This observation is almost the same for every wave scenario and slope angle (see also Figure 5-26, Appendix F).

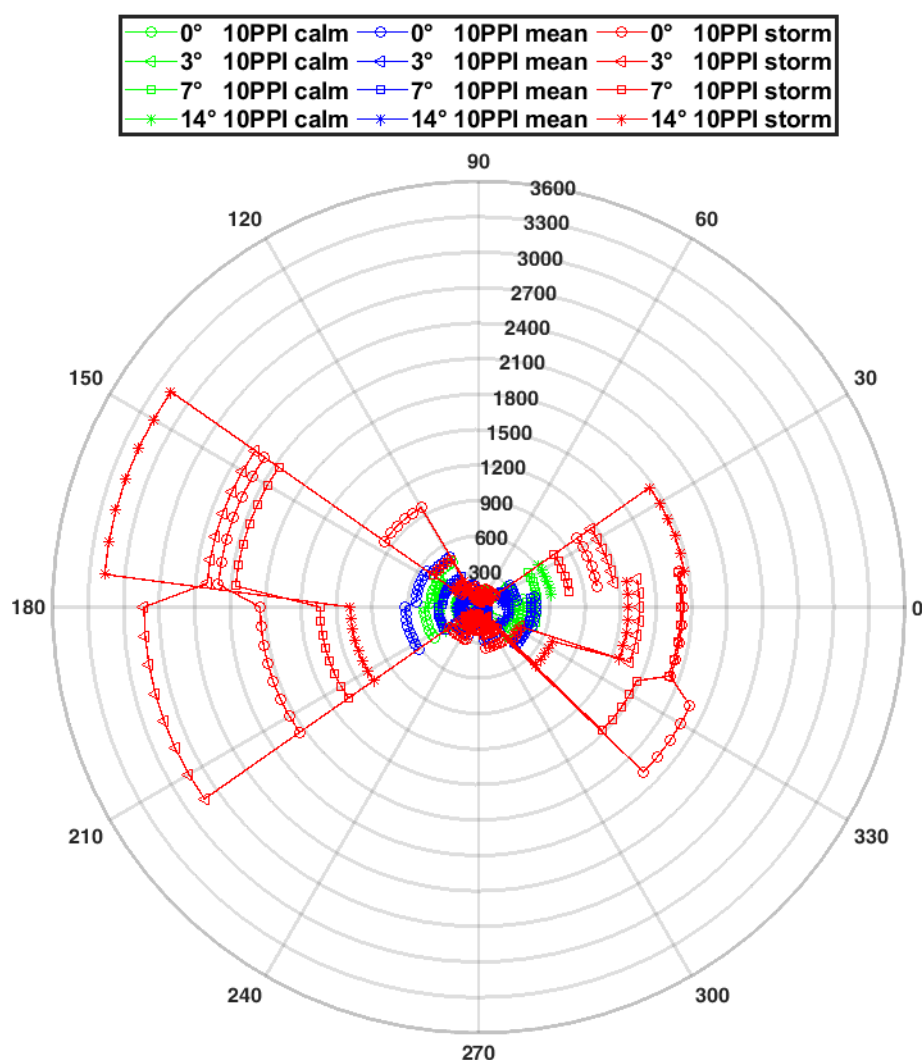


Figure 5-25: Phase specific TKE

In the polar diagram the median of the phase specific turbulent kinetic energy is plotted. The markers do not show single measurement points, they only symbolize the slope angle of the measurement. The results in the diagram are the measurements above the 10PPI porous media section.

For a more detailed view, the median of the phase specific TKE of the measurements with the 10PPI porous media and 0° slope angle are shown as polar plot in Figure 5-26.

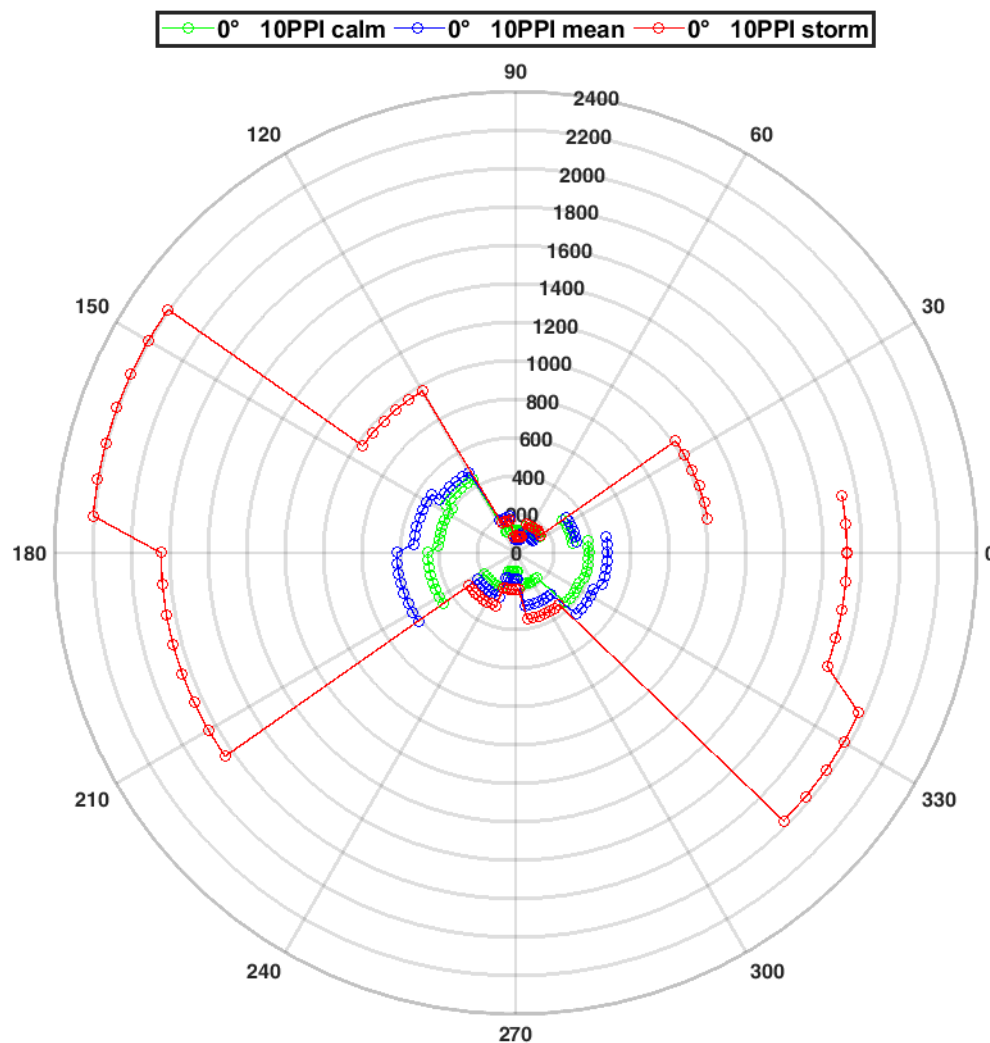


Figure 5-26: Phase specific TKE of 0° slope angle measurements

In the polar diagram the median of the phase specific turbulent kinetic energy is plotted. The markers do not show single measurement points, they only symbolize the slope angle of the measurement.

This figure shows again, that the horizontal phase sections cause the maximum turbulent kinetic energy in the measurements. Furthermore, the stormy scenario has much higher TKE than the other two scenarios. In this case, the mean scenario has higher TKE than the calm one. Moreover, the backward direction (180° phase) shows higher turbulent kinetic than the forward direction (0° phase).

6 Discussion

In the discussion of this work, every section of Chapter 5 is considered. First, the concentration developments for the different experiments are discussed. After this, the Reynolds-fluxes are discussed. In the next part, the mixing length theory for the numerical simulation is analyzed. Furthermore, the phase specific Reynolds-fluxes and mixing lengths are discussed. At last, the wave friction and turbulence are analyzed.

6.1 Concentration boundary development

One main aspect of this work is to understand the mixing and diffusion of a tracer under turbulent wave effects. For this reason, the tracer diffusion was investigated in detail under different aspects. As shown in Figure 5-1, the concentration boundary lines of 10%, 25%, 50% and 75% fluctuate and develop equally. This behavior shows an even inflow condition over the complete time series. If the inflow would stagnate or fluctuate strongly, the higher concentration lines would show peaks in areas where the low concentration line does not change. Furthermore, the low concentration area is much bigger than the high concentration area. This shows that the transport of the tracer is steady and that the tracer is not mixed and transported as fast as the inflow of it.

In the Fourier analysis (Figure 5-2), the frequencies of the concentration development are depicted. Thus, the main impact frequencies are shown, which influence the diffusion of the tracer. It is evident, that the wave frequency has the strongest effect on the diffusion. Moreover, a second order of the wave frequency may influence the fluctuation of the concentration line, too. This overtone occurs due to the construction of the wave generator. The stiffness of the moving plate and the acceleration of this leads to small oscillations of the generator plate in the turning points. But, as seen in the Fourier analysis, these small amplitudes are neglectable in these measurements. The most important information in the frequency analysis is the constant value which occurs. This shows a steady increase of the concentration boundary lines. Hence, the development which was estimated from Figure 5-1 is undermined by the Fourier analysis. Based on these results, the low-pass filtering of the signals shows the development of the boundary lines in detail (Figure 5-3 and Figure 5-4). Hence, the equal growth of the concentration lines is shown. The comparison of these low-pass filtered signals (Figure 5-5) firstly shows that the behavior of the growth rate (definition see 4.3.2) seems to be completely different between the 10PPI and the 45PPI measurements. It is obvious that the 45PPI measurements are identified by a significantly lower tracer inflow into the water column compared to the 10PPI measurements. Hence, the concentration boundary lines show less diffusion into the water column. Moreover, a nearly constant diffusion can be estimated for this permeable sea bed model. This is also seen in Figure 5-11 **Fehler! Verweisquelle konnte nicht gefunden werden.**, where the boundary growth rate of these 45PPI measurements is very low between 0 and 0.002. For this reason, it makes more sense to look at the 10PPI measurements. In the case of a 0° slope angle, the same behavior of the concentration boundaries was

shown for a pointwise inflow area as in the measurements of [Groß 2018]. Considering the different slope angles, the mean wave scenario shows the strongest diffusion into the water column at slopes of 3° , 7° and 14° . Looking at the velocity fields (Figure 5-13), the velocity of the mean scenario is strongly damped when using higher slope angles of 7° and 14° . Hence, in these cases the mean wave causes the lowest averaged velocities near the ground. This leads to the hypothesis that a lower averaged phase velocity leads to greater diffusion of the tracer into the water column. Furthermore, the slope angle has a high impact on the diffusion. In the results for the boundary growth rate (see Figure 5-6), the stronger slope angle leads to a larger spread of the tracer into the water column. Considering the tracer movement in the 0° slope angle experiments, it was shown that the tracer moves with the phase angle of the wave. Thus, in the 180° and 0° phase angles of the wave, the concentration field moves back and forward and in the 90° and 270° phase angles it moves up and down. So, the tracer is pushed into the permeable seabed if the phase angle of the wave is directed towards the ground. When the slope angle of the floor changes the phase angle which is directed towards the ground changes. Furthermore, the fluid accelerates over the slope. For these reasons, the amount of tracer pushed back into the permeable seabed is not the same as in the case of the 0° slope angle. It is seen that the tracer is pushed more up and downhill for the 3° and 7° slopes. Hence, the amount of tracer in the water column is higher, as is the diffusion into the water column. In the case of the 14° slope angle, another extreme situation is reached. The angle of the slope is so strong that the fluid is pushed into the ground model and with it also the tracer. Hence, the tracer fluid is stuck in the ground. In the reverse wave phase, the tracer is pulled out somewhat, but this force is not strong enough to restore the tracer of the seabed before the phase changes again. Only in the case of the mean wave scenario, an outflow of tracer is detected. Considering the velocity fields (see Figure 5-13) of these cases, the wave is damped so strongly, that the averaged velocities are very low compared to the other two wave scenarios. Hence, the tracer which is pushed into the permeable ground is still near the surface of the bed and is removed again with the phase change of the wave. Thus, it remains in the water column and is transported further.

In conclusion, it has been shown that the permeable seabed is responsible on the one hand for the damping of the wave velocity and on the other hand for the capturing of the tracer. In each experiment, the same amount of tracer was pumped into the permeable seabed within the same time interval. But it is shown that in the case of the 45PPI permeable seabed, the diffusion (see Figure 5-6) into the water column is less and that also the total mass (see Figure 5-9) is less than in the case of 10PPI. Hence, the tracer must be stored in the seabed itself.

6.2 Reynolds-flux development

In this section, dependencies of the Reynolds-fluxes are discussed in detail. As discussed before, the Reynolds-fluxes may depend on the amount of tracer in the water column and the velocity fields occurring under the different wave scenarios. The mean phase averaged Reynolds-fluxes are shown in Figure 5-7 and Appendix C. To compare these fluxes, a 55mm stripe was averaged horizontally in the hot spot area (see Figure 5-8) of every measurement. Based on this averaging, the Reynolds-fluxes were compared in Figure 5-10. When considering the averaged Reynolds-flux figures (see Appendix C), it becomes obvious that in the stormy scenarios, Reynolds-flux hot spots occur. These areas are here described as hot spots because of the small horizontal enlargement of the strong inflow fluxes near the ground compared to the other scenarios. To define the central points of these hot spots, the integral Reynolds-fluxes were concretized for the highest 50% of the Reynolds-fluxes. This neglects the low values, which shifts the centers to the right or left side (see Figure 5-8). The centers of the concentration areas and the centers of the integral Reynolds-fluxes are distributed near the equal-line which shows the measurements where the centers are the same. For the case where the center is on the equal-line the transport in the water column is only in vertical direction, because the strongest Reynolds-fluxes near the ground are equal to the strongest tracer fluxes and if the concentration area is in the same position, the tracer is mixed and transported only above the inflow position. If the point is above the equal-line, the center of the area is located to the right of the center of mass, such that the transport of the tracer occurs slightly to the right side of the main inflow section. If the point is below the equal-line, the tracer is shifted to the left side. Hence, in the measurements the tracer is transported mostly in vertical direction, even if the waves push the concentration field strongly to the left or right, depending on the phase of the wave. Especially the calm wave scenarios are aligned in the central part of the physical inflow area. The stormy wave scenarios show a special behavior. They are placed to the left of the physical inflow area. This means that the tracer is pulled through the porous media and guided to another outflow section which does not actually exist. Hence, the wave action has such a strong impact on the velocity and pressure field inside the porous medium, that the transport and mixing of the tracer is guided into several hot spot areas. This leads to the assumption that a pressure field occurs even over a smooth bed which forces the tracer to flow along another direction in the bed.

Considering the whole integrated amount of Reynolds-flux (see Figure 5-9), it can also be seen that the 45PPI measurements have less input into the water column, which was also seen in the averaged boundary surfaces. This behavior corroborates the hypothesis that the less permeable media stores a high amount of tracer in it. Furthermore, it is seen that the boundary area is smaller if the Reynolds-flux mass is lower. This shows that the transport of the tracer is somehow equal in the water column. In the case of the 14° measurement, it is shown that they show the smallest fluxes and areas. The concentration areas are probably not only so small because of the low fluxes. In these cases, the height of the water column is much smaller because of the strong slope angle, compared to the other measurements. But,

because of the shifting of the hot spot to the left side of the observed area, most of the transport and mixing is seen.

Moreover, the stormy and the mean wave scenarios of the 10PPI measurements show the highest integral Reynolds-fluxes (see Figure 5-9). Furthermore, they fluctuate around a value of $2000 \text{ mm/s} \cdot \mu\text{g/l}$. Thus, they reach a maximum. On the other hand, the boundary area is growing. Hence, the Reynolds-fluxes are dependent on the one hand on the amount of tracer which is flowing into the water column. This is obvious, because the Reynolds-fluxes are an indicator of the turbulent transport mechanism of a scalar tracer. If there is less scalar tracer, then the amount of transported tracer is less, too, even if the turbulent behavior is the same. On the other hand, it is seen that the boundary area is more than twice as large as in the other scenarios, but the integral Reynolds-fluxes do not change. Hence, the amount of turbulent flux in these experiments is somehow limited. In fact, the highest turbulence occurs near the bottom because of friction effects with the permeable seabed. When the tracer is in the water column over the complete seabed and the turbulence is nearly zero in the upper water column, the turbulent transport reaches a maximum in each wave scenario.

Considering the comparison of the diffusion (see Figure 5-6) and the comparison of the Reynolds-fluxes (see Figure 5-7), it is seen that the fluxes strongly depend on the diffusion. Most of the figures of the fluxes show the same behavior as the diffusion. For example, in the 0° slope angle measurement above the 10PPI seabed, the highest Reynolds-flux is generated by the stormy wave scenario. Furthermore, the mean and calm scenario show nearly the same development over the water column. For the diffusion lines, the stormy scenario shows the highest spread into the water column and the mean and calm scenario show less diffusion but increase in the same way. Considering additionally the averaged velocity fields (see Figure 5-13), the development is also the same. In some cases, especially for the 3° slope angle measurement above the 10PPI seabed, the diffusion differs from the Reynolds-flux development. Considering the velocity field for this case, it can be concluded that the stormy event may affect the Reynolds-flux so strongly, that the high velocities dominate the other scenarios.

Hence, the amount of tracer inflow regulates the maximum value of the Reynolds-fluxes at the ground and up to which height they occur in the water column. Furthermore, the velocity field influences the value of the Reynolds-flux. Thus, if the velocity is faster, the turbulence is higher, and the Reynolds-flux is higher too.

Another aspect which reduces the averaged Reynolds-fluxes is the occurrence of negative fluxes. In every measurement above the 45PPI seabed and in the measurements using the 7° and 14° slope angles, these negative fluxes are measured (see Appendix C). Mostly, their absolute values are much smaller compared to the positive fluxes, but in some cases, like in the 14° measurements with the stormy scenario, they are equal to the positive Reynolds-fluxes. This yields to a phase averaged concentration

diffusion which is nearly zero in the observed area (see Appendix D). Thus, the negative fluxes occur where the tracer is pushed into the seabed and vanishes from the observed area. This phenomenon was also mentioned by [Groß 2018], where a pointwise outflow area was investigated. In the work of [Groß 2018], a plane seabed was used and the Reynolds-fluxes were positive directly above the outflow area and right beside this section they were negative. Hence, these negative fluxes occur at the boundary sections right beside the main outflow section. During the experiments, the movement of the tracer was observed. In the uplifting phase of the wave, the tracer was pulled out of the seabed and in the downward phase, it was pushed into the porous medium. Thus, if the forces in the downward phase are strong enough, a high amount of tracer is pushed into the ground and causes negative Reynolds-fluxes.

The dependency of the Reynolds-fluxes on the tracer inflow is seen in Figure 5-11. Here, it is clearly seen that the averaged Reynolds-fluxes increase with an increasing boundary growth rate. Hence, the growth rate, which strongly influences the captured area of the tracer fluid, also influences the Reynolds-flux. This is obvious, because if the tracer inflow is low and the concentration field small, no scalar value can be transported. If the growth rate is high, more tracers are in the observation area and can be transported into the water column.

6.3 Mixing length quantities for the scalar transport

The mixing length theory is a model developed to describe the turbulent transport of momentum and scalar tracers in boundary layers. In these experiments, the turbulent mixing and transport of submarine groundwater is considered. In section 5.3, the single components of the mixing length were shown.

First, the concentration gradients (see Figure 5-12) were described for the 10PPI measurements. The tracer is transported and mixed mainly in the vertical direction, as discussed before. Thus, the averaged concentration profiles (see Appendix D) are defined by a high concentration near the ground and a strong decrease in surface direction. This is also seen in the concentration gradients. Furthermore, this behavior is the same for every measurement. Because of the mixing and transport in vertical direction, this result was to be expected.

The next parameter in the mixing length is the velocity gradient. The velocity profiles were already discussed in 6.1. The gradients (see Figure 5-14) alternate strongly, but in a very small range, due to very small changes in the phase averaged velocity profiles (see Figure 5-13). If we imagined a completely smooth velocity profile, the gradient would be constant or would show a slightly decreasing behavior. The shown velocity profiles correspond to the estimated profile for a bottom boundary layer (see 2.7.2) under a steady flow. The stormy scenarios in these measurements show a dent in the profile, which is estimated (see 2.7.3) for a wave-induced velocity field. In the mean and calm scenario, the velocities may be too small for this kind of dent to develop in a range that it is optically detectable. But when considering the gradients for the mean scenario (see Figure 5-14), it is seen that in the first 20 mm above the ground an equal gradient occurs, then a strong decrease followed by an increase. This behavior shows exactly the kind of dent in the velocity profile, which occurs under the influence of a wave-induced velocity field. Hence, the generated waves are comparable to the described ocean waves from the literature.

With the Reynolds-fluxes discussed in 6.2, the mixing length was calculated (see Figure 5-15). It was shown that the stormy wave scenarios cause the greatest mixing length near the ground and that in a distance of 30 mm above the ground, most scenarios show nearly the same mixing length. The 45PPI measurements have smaller mixing lengths because of the smaller averaged velocities, which causes smaller fluctuating parts. The mixing length near the ground is dominated by turbulence, which is higher in the stormy scenarios and above the more permeable seabed.

The scatter plot of the growth rate and the mixing length (see Figure 5-16) showed no significant dependencies between these parameters.

6.4 Phase specific Reynolds-fluxes and mixing length

The phase specific parameters are calculated for the 12 phase sections in these measurements. In the phase specific Reynolds-flux maps (see Figure 5-17), the averaged Reynolds-fluxes for all 12 phase sections of one measurement are shown. Here it is seen that the spatial distribution of the Reynolds-flux does not change significantly within one measurement. But the strength and smoothness of the flux area changes. It is clear that especially the vertical and horizontal phase sections show strong contrary peak values of the fluxes near the ground. Hence, the highest negative and the highest positive Reynolds-fluxes occur next to each other in plume like shapes. Furthermore, it is seen that between phase angles of 0° and 90° the negative flux occurs to the left and the positive one to the right of the hot spot area and between 90° and 180° they change the position. Moreover, this behavior does not occur in the phase angles between 180° and 360° . Furthermore, the Reynolds-flux distribution is smoother in these phases and the negative and positive peaks are not as strong as in the other phase sections.

According to this, the occurrence of negative fluxes is of importance. In the expressions for the Reynolds-flux (see 2.5.4), the flux is negative if one of the components, the velocity fluctuation v' or the concentration fluctuation, is negative and the other one positive. The concentration fluctuation is negative if the tracer concentration in the regarded area decreases. For the velocity fluctuation it is the same. Hence, a negative Reynolds-flux occurs if the velocity fluctuation decreases and the concentration fluctuation increases or the other way around.

For this reason, the occurrence of strong negative and strong positive Reynolds-fluxes in the phase sections shows that the flow of the tracer medium causes also an outflow or backflow of tracer if it is reflected from the porous media. Hence, tracer flows from the water column into the porous media and causes negative concentration fluctuations, but right beside this is the area where tracer vanishes, meaning that tracer flows in the other direction and causes positive fluctuation values. The same phenomenon occurs in the uplifting direction, if the tracer is pulled out of the porous media. Next to this area, tracer is pushed into the porous media because of the conservation of mass.

Now, the median Reynolds-fluxes of each phase section (see Figure 5-18 and Figure 5-19) are considered. The calm and the mean scenario show only slight differences between the phase angles. But the stormy scenario has a stronger impact on the phase specific fluxes. This may occur because of the much higher velocity fluctuations compared to the other two scenarios. Furthermore, it is clear that in the phase sections around 90° the lowest fluxes occur. Thus, the negative fluxes are larger in these sections than in the others. Due to strong uplifting forces, the exchange of the surrounding fluid with the porous media is much higher and causes these negative fluxes.

Different slope angles (see Figure 5-19) show that the impact of low slope angles (3°) is low. Furthermore, in the case of the mean scenario and the 10PPI porous media, the influence of the 7° slope

angle is low, too. But the strong slope angle of 14° shows strong fluctuations over the different phase sections. Here, also negative values occur for the median of the Reynolds-flux around the 90° phase sections. Due to the high slope angle, the vertical uplifting phase is different from 90° . Furthermore, the wave behavior and the velocity fields directly above the seabed have changed compared to the measurements with the slope angle of 0° . Hence, in these special phase sections around 90° it is possible that only negative fluxes occur where tracer fluid is pushed into the porous media.

The phase specific mixing lengths were shown for the measurement with the 0° slope angle with the mean wave scenario above the 10PPI porous media (see Figure 5-20) and as a summary of all measurements in Figure 5-21. It was clearly shown, that the vertical phase sections (around 90° and 270°) cause the highest mixing lengths. In these phase sections, the strongest up- or downward movements of the tracer particles occur due to turbulent fluctuations. This behavior follows from the stronger vertical velocity components in these phases. In the horizontal phase sections, the vertical velocity and the vertical fluctuations are much smaller, such that there is also much less vertical mixing.

6.5 Bottom friction and turbulence

The bottom friction shows the velocity reduction of the fluid near the ground because of the friction caused by the ground shape. With the comparison of the friction factor with the bottom stress, it can be estimated how the velocity changes due to the friction (see Figure 5-22). This figure shows that the different wave scenarios cause nearly the same bottom stresses over the different artificial seabeds. For the calm scenario, also the friction factor differs only slightly, such that the velocity does not change significantly with the different slope angles. Even the stormy scenarios show this behavior, except for two outliers. The mean wave scenario measurements show strong differences in the wave friction factor though. Hence, the wave friction depends on the slope angle. According to this, the velocity fields of the mean wave scenario change strongly (see Figure 5-13). Moreover, the Reynolds-flux does not show any dependencies on the friction factor (see Figure 5-23).

Figure 5-25 considers the phase specific turbulence via the turbulent kinetic energy (TKE). The horizontal and the vertical fluctuations of the velocity components are included in the TKE. Comparing the averaged Reynolds-stresses with the TKE (see Figure 5-24), we expect and see a linear dependency. Furthermore, it is seen that the calm scenarios show a constant TKE value for the two different porous media. The stormy scenarios show the highest TKE, as expected. But the stresses and TKE differ between the different slope angles. This shows an influence of the slope angle on the turbulence. Furthermore, the mean wave scenario measurements show strong fluctuating behaviors of the Reynolds-stress, TKE and slope angle. Most likely the slower velocity of the mean wave scenarios and the higher friction factor cause this behavior.

Considering the phase specific turbulent kinetic energies (see Figure 5-25 and Figure 5-26), it is clear that the phase sections in horizontal directions cause the highest turbulent values. Due to the type of the wave with a strong horizontal velocity component and low vertical velocity components this behavior is as expected, because high velocities cause high velocity fluctuations. Furthermore, the stormy scenario causes the highest values. The calm and mean scenarios do not differ significantly because of the minor velocity differences.

7 Summary and future research

The project "Waves and turbulence on wavy coastal seabeds inducing vertical scalar transport" is part of the graduate school Baltic Transcoast. This graduate school aimed to investigate the interaction between a coastal fen and the Baltic sea.

In this work, the mixing and transport of the submarine groundwater discharge (SGD) was investigated in a defined laboratory experiment. For this, a new wave channel ground model was constructed and produced to facilitate the variation of different parameters for the investigations.

In the experiments, three different parameters were varied. One such aspect was the wave action. Three different wave scenarios were developed and investigated based on field measurements with an acoustic profiler in front of the Hüttelmoor. A calm scenario, a mean scenario and a stormy scenario were extracted from these measurements. The second parameter which was varied was the permeability of the artificial seabed. For the investigations, two different seabed models were used. The last varied parameter was the slope angle of the seabed model. The slope was adjusted using four different angles. In summary, 24 experiments were conducted with varying combinations of these parameters.

In the analysis, the turbulent transport was described with the Reynolds-flux model. Furthermore, the transport mechanism of the tracer is described by signal processing the averaged distribution of different concentration boundaries. Numerical simulations, for example a model of the Baltic Sea, may can be validated by using the mixing length model of [Prandtl 1925]. Based on his theory, the specific mixing lengths of the single measurements were calculated. Moreover, the phase specific values of these parameters were analyzed. Furthermore, the turbulence was determined with the wave friction factor and the behavior of the turbulent kinetic energy.

The results have shown that it is possible to measure the mixing and transport processes over a permeable seabed under defined wave action with the developed experimental setup. Under wave action, in the intermediate water zone, the highest turbulent kinetic energy values occur in the horizontal phase sections. On the other hand, the longest mixing lengths occur in the vertical. Furthermore, the wave friction changes strongly with the slope angle, especially in the mean wave scenario of these experiments. The analysis of the Reynolds-fluxes showed that the Reynolds-flux depends linearly on the boundary growth rate of the tracer. Furthermore, the Reynolds-flux and boundary growth rate increase with stronger slope angles until a maximum is reached at a slope angle of 14° . In these measurements, a strong decrease of both parameters was observed. Especially the mean and stormy wave scenarios give rise to the assumption that a higher boundary growth rate corresponds to a smaller mixing length.

The mixing length theory can be used for numerical simulations of a model of the Baltic Sea. With the experimentally determined averaged mixing lengths this numerical model can be fed with realistic boundary conditions.

In future research, the bottom boundary layer should be investigated in more detail. Thus, a smaller area should be investigated. Furthermore, other artificial seabeds could be tested with a lower permeability. More sophisticated theories could be used to provide a more suitable length scale for the numerical simulations.

References

- AGELINCHAAB, M., TACHIE, M.F., AND RUTH, D.W. 2006. Velocity measurement of flow through a model three-dimensional porous medium. *Phys. Fluids* 18, 1, 017105-1 - 017105-11.
- AIRY, G.B. 1845. *On tides and waves*. Encyclopaedia Metropolitana, London.
- AIRY, G.B. 1952 [reprint. *Tides and waves. A chapter of the encyclopedia Metropolitana, V.V. 1845*. KoHsueh, Nanking.
- ALAZMI, B., AND VAFAI, K. 2001. Analysis of fluid flow and heat transfer interfacial conditions between a porous medium and a fluid layer. *International Journal Heat Mass Transfer* 44, 1735–1749.
- ALLEN, J.R.L. 2001. *Principles of physical sedimentology*. Blackburn Press, Caldwell, NJ.
- ARTHUR, J.K., RUTH, D.W., AND TACHIE, M.F. 2009. PIV measurements of flow through a model porous medium with varying boundary conditions. *J. Fluid Mech.* 629, 343–374.
- AUSSCHUß FÜR KÜSTENSCHUTZWERKE. 2002. *EAK 2002. Empfehlungen für die Ausführung von Küstenschutzwerken*. Die Küste 65.2002. Westholsteinische Verl.-Anst. Boyens, Heide.
- BEAR, J. 2013. *Dynamics of Fluids in Porous Media*. Dover Publ, New York.
- BEAVERS, G.S., AND JOSEPH, D.D. 1967. Boundary conditions at a naturally permeable wall. *Journal of Fluid Mechanics* 30, 1, 197–207.
- BECK, A.J., KELLUM, A.A., LUEK, J.L., AND COCHRAN, M.A. 2016. Chemical Flux Associated with Spatially and Temporally Variable Submarine Groundwater Discharge, and Chemical Modification in the Subterranean Estuary at Gloucester Point, VA (USA). *Estuaries and Coasts* 39, 1, 1–12.
- BESTIER, T. 2015. *Charakterisierung einer Versuchsanlage zur Erzeugung von Oberflächenwellen*, Universität Rostock.
- BOUDREAU, B.P., AND JØRGENSEN, B.B., Eds. 2001. *The benthic boundary layer. Transport processes and biogeochemistry*. Oxford Univ. Press, Oxford.
- BOUSSINESQ, J. 1877. *Essai sur la théorie des eaux courantes*. Imprimerie Nationale, Paris.
- BRINKMAN, H.C. 1949. A calculation of the viscous force exerted by a flowing fluid on a dense swarm of particles. *Appl. Sci. Res.* 1, 1, 27–34.

- BURLEY, S.D., AND WORDEN, R.H. 2003. *Sandstone diagenesis. Recent and ancient*. Reprint series volume 4 of the International Association of Sedimentologists. Blackwell Pub, Malden, MA.
- BURNETT, W.C., AGGARWAL, P.K., AURELI, A., BOKUNIEWICZ, H., CABLE, J.E., CHARETTE, M.A., KONTAR, E., KRUPA, S., KULKARNI, K.M., LOVELESS, A., MOORE, W.S., OBERDORFER, J.A., OLIVEIRA, J., OZYURT, N., POVINEC, P., PRIVITERA, A.M.G., RAJAR, R., RAMESSUR, R.T., SCHOLTEN, J., STIEGLITZ, T., TANIGUCHI, M., AND TURNER, J.V. 2006. Quantifying submarine groundwater discharge in the coastal zone via multiple methods. *The Science of the total environment* 367, 2-3, 498–543.
- BURNETT, W.C., TANIGUCHI, M., AND OBERDORFER, J. 2001. Measurement and significance of the direct discharge of groundwater into the coastal zone. *Jounar of Sea Research*, 46, 109–116.
- BÜSCHING, D.-I.F. 2002. *Küsteningenieurwesen*. Kuesteningenieurwesen, Braunschweig.
- CAROTENUTO, C., AND MINALE, M. 2011. Shear flow over a porous layer. Velocity in the real proximity of the interface via rheological tests. *Phys. Fluids* 23, 6, 063101-1 - 063101-11.
- CLAUSIUS, R. 1885. *Die Potentialfunction und das Potential. Ein Beitrag zur mathematischen Physik*. Barth, Leipzig.
- CORVARO, S., MANCINELLI, A., AND BROCCINI, M., Eds. 2016. *Flow Dynamics of waves propagating over different permeable beds* 1. Int. Conf. Coastal. Eng., Antalya.
- DEMTRÖDER, W. 2006. *Experimentalphysik I*. Springer-Lehrbuch. Springer-Verlag Berlin Heidelberg, Berlin, Heidelberg.
- DIMOTAKIS, P.E. 2005. Turbulent Mixing. *Annu. Rev. Fluid Mech.* 37, 1, 329–356.
- DINGLER, J.R., AND CLIFTON, H.E. Tidal-Cycle Changes in Oscillation Ripples on the Inner Part of an Estuarine Sand Flat 39, 219–233.
- ELLISON, T.H., AND TURNER, J.S. 1959. Turbulent entrainment in stratified flows. *Journal of Fluid Mechanics* 6, 423–448.
- ENGELHARDT, W. v. 1960. *Der Porenraum der Sedimente*. Springer Berlin Heidelberg, Berlin, Heidelberg.
- FEDDERSEN, F. 2012. Observations of the Surf-Zone Turbulent Dissipation Rate. *J. Phys. Oceanogr.* 42, 3, 386–399.

- FENTON, J.D. 1979. A high-order cnoidal wave theory. *J. Fluid Mech.* 94, 129–161.
- FIEDLER, PROF. DR.-ING. H. E. 2003. *Turbulente Strömung*. Technische Universität Berlin, Berlin.
- GOHARZADEH, A., KHALILI, A., AND JØRGENSEN, B.B. 2005. Transition layer thickness at a fluid-porous interface. *Phys. Fluids* 17, 5, 57102.
- GRAW, D.-I.K.-U. 1995. *Wellenenergie. - eine hydromechanische Analyse*. Bericht Nr. 8. Papyrus-Druck GmbH, Berlin.
- GROß, J. 2018. *Bestimmung der Ausbreitungscharakteristik von ausgetretenem Bodengrundwasser in verschiedenen marinen Bodengrenzschichten mittels PIV/LIF Verfahren*. Studienarbeit, Universität Rostock.
- GUILBAULT, G.G., Ed. 1990. *Practical fluorescence*. Modern monographs in analytical chemistry 3. Dekker, New York.
- GUPTA, S.K., AND ADVANI, S.G. 1997. Flow near the permeable boundary of a porous medium: An experimental investigation using LDA. *Exp Fluids* 22, 408–422.
- HEIMBUCH, M. 2014. *Auslegung, Fertigung und Erprobung eines Wellengenerators*. Bachelorarbeit, Universität Rostock.
- HUETTEL, M., ZIEBIS, W., AND FORSTER, S. 1996. Flow-induced uptake of particulate matter in permeable sediments. *Limnology and Oceanography* 41, 2, 309–322.
- IOC, SCOR, AND IAEA. 2004. *Submarine groundwater discharge. Management implications, measurements and effects*. Series on groundwater / IHP-VI 5. UNESCO, Paris.
- JAMES, D.F., AND DAVIS, A.M.J. 2001. Flow at the interface of a model fibrous porous medium. *J. Fluid Mech.* 426, 47–72.
- JONSSON, I.G., Ed. 1967. *Wave Boundary Layers and Friction Factors*. Tenth International Conference on Coastal Engineering, Tokyo.
- KANDLER, L. 2018. *Bestimmung der Transportkoeffizienten von ausgetretenem Bodengrundwasser in der marinen Bodengrenzschicht bei verschiedenen Hangneigungen*. Masterarbeit, Universität Rostock.

- KAROW, N. 2015. *Strömungs- und Strukturmessungen mittels Volumetric Light Field Velocimetry*. Masterarbeit, Universität Rostock.
- KAUFMANN, H. 2015. *Aufbau einer Anlage zur Erzeugung und Absorption von Oberflächenwellen in einem Wasserkanal*. Bachelorarbeit, Universität Rostock.
- KERAMARIS, E., AND PECHLIVANIDIS, G. 2015. The different impact of rods bundle in an inclined open channel incomparison with other permeable beds. *Recent Advances in Fluid Mechanics and Thermal Engineering*, 119–125.
- KOCH, M. 2004. *Skript Allgemeine Hydrologie. 5. Grundwasserhydraulik. 5.2 Der Durchlässigkeitsbeiwert K*. Allgemeine Hydrologie (WS 2004/2005), Kassel.
- KORNEV, N. 2013. *Mathematical Modeling of Turbulent Flows*, Rostock.
- KRAUME, M. 2012. *Transportvorgänge in der Verfahrenstechnik. Grundlagen und apparative Umsetzungen*. VDI Verfahrenstechnik. Springer Vieweg, Berlin.
- LE MÉHAUTÉ, B. 1976. *An introduction to hydrodynamics and water waves*. Springer.
- LE ROUX, J.P. 2003. Wave friction factor as related to the Shields parameter for steady currents. *Sedimentary Geology* 155, 1-2, 37–43.
- LEOTE, C., IBÁÑHEZ, J.S., AND ROCHA, C. 2008. Submarine Groundwater Discharge as a nitrogen source to the Ria Formosa studied with seepage meters. *Biogeochemistry* 88, 2, 185–194.
- LORKE, A., MÜLLER, B., MAERKI, M., AND WÜEST, A. 2003. Breathing sediments: The control of diffusive transport across the sediment–water interface by periodic boundary-layer turbulence. *Limnology and Oceanography* 2003, 48 (6), 2077–2085.
- MALCHEREK, A. 2010. *Gezeiten und Wellen. Die Hydromechanik der Küstengewässer*. Vieweg+Teubner (GWV), s.l.
- MENZEL, P. 2010. *Turbulente Mischungsvorgänge im Nachlauf einer dichtegeschichteten Zylinderumströmung*. Univ., Diss.--Rostock, 2009. Menzel-Verl., Kühlungsborn.
- MIEGEL, K., THOMAS GRAEFF, BENNY SELLE, THOMAS SALZMANN, CHRISTIAN FRANCK, AND AXEL BRONSTERT. 2016. Untersuchung eines renaturierten Niedermoores an der mecklenburgischen Ostseeküste - Teil I: Systembeschreibung und hydrologische Grundcharakterisierung. *Hydrologie und Wasserbewirtschaftung/ BfG* 60, 4, 242–258.

- MOORE, W.S. 2010. The effect of submarine groundwater discharge on the ocean. *Annual review of marine science* 2, 59–88.
- MORAD, M.R., AND KHALILI, A. 2009. Transition layer thickness in a fluid-porous medium of multi-sized spherical beads. *Exp Fluids* 46, 2, 323–330.
- NEREM, R.S., BECKLEY, B.D., FASULLO, J.T., HAMLINGTON, B.D., MASTERS, D., AND MITCHUM, G.T. 2018. Climate-change-driven accelerated sea-level rise detected in the altimeter era. *Proceedings of the National Academy of Sciences of the United States of America* 115, 9, 2022–2025.
- NIELSEN, P. 1994. *Coastal bottom boundary layers and sediment transport*. Advanced series on ocean engineering 4. World Scientific, Singapore u.a.
- NITSCHKE, W., AND BRUNN, A. 2006. *Strömungsmesstechnik*. VDI-Buch. Springer-Verlag Berlin Heidelberg, Berlin, Heidelberg.
- NOLTING, W. 2009. *Quantenmechanik - Grundlagen*. Grundkurs Theoretische Physik 5/1, Ed. 7. Springer, Berlin.
- OCHOA-TAPIA, A. 1995. Momentum transfer at the boundary between a porous medium and a homogeneous fluid. II. Comparison with experiment. *International Journal Heat Mass Transfer* 38, 14, 2647–2655.
- PEDERSEN, G.K., GRUE, J., AND LIU, P.L.F., Eds. 2004. *PIV and water waves*. Advances in coastal and ocean engineering v. 9. World Scientific Pub. Co, Singapore, Hackensack, N.J.
- PRANDTL, L. 1925. Bericht über Untersuchungen zur ausgebildeten Turbulenz. *Z. angew. Math. Mech.* 5, 136–139.
- PRANDTL, L., EHRHARD, P., ETLING, D., MÜLLER, U., RIEDEL, U., AND SREENIVASAN, K.R. 2012. *Führer durch die Strömungslehre. Grundlagen und Phänomene*. Springer Vieweg, Wiesbaden.
- PRECHT, E., AND HUETTEL, M. 2003. Advective pore-water exchange driven by surface gravity waves and its ecological implications. *Limnology and Oceanography* 48, 4, 1674–1684.
- RAPAGLIA, J., KOUKOULAS, S., ZAGGIA, L., LICHTER, M., MANFÉ, G., AND VAFEIDIS, A.T. 2012. Quantification of submarine groundwater discharge and optimal radium sampling distribution in the Lesina Lagoon, Italy. *Journal of Marine Systems* 91, 1, 11–19.

- ROBINSON, C., LI, L., AND BARRY, D.A. 2007. Effect of tidal forcing on a subterranean estuary. *Advances in Water Resources* 30, 4, 851–865.
- RUSCH, A., HUETTEL, M., AND FORSTER, S. 2000. Particulate Organic Matter in Permeable Marine Sands—Dynamics in Time and Depth. *Estuarine, Coastal and Shelf Science* 51, 4, 399–414.
- SALMON, R. 2018. *Introduction to Ocean Waves*. Scripps Institution of Oceanography, San Diego.
- SANTOS, I.R.S., BURNETT, W.C., CHANTON, J., MWASHOTE, B., SURYAPUTRA, I.G.N.A., AND DITTMAR, T. 2008. Nutrient biogeochemistry in a Gulf of Mexico subterranean estuary and groundwater-derived fluxes to the coastal ocean. *Limnol. Oceanogr.* 53, 2, 705–718.
<https://pdfs.semanticscholar.org/a49b/942794e9665ffc5a7da55e9db9114298ede5.pdf>.
- Schade, personal communication.
- SCHUBERT, R. 2006. *Die Zukunft der Meere - zu warm, zu hoch, zu sauer. Sondergutachten*. Wissenschaftlicher Beirat der Bundesregierung Globale Umweltveränderungen (WBGU), Berlin.
- SIMMONS, C.T. 2008. Henry Darcy (1803–1858). Immortalised by his scientific legacy. *Hydrogeol J* 16, 6, 1023–1038.
- SLOMP, C.P., AND VAN CAPPELLEN, P. 2004. Nutrient inputs to the coastal ocean through submarine groundwater discharge. Controls and potential impact. *Journal of Hydrology* 295, 1-4, 64–86.
- SMYTH, C. 2002. Coherent Doppler Profiler measurements of near-bed suspended sediment fluxes and the influence of bed forms. *J. Geophys. Res.* 107, C8.
- SPEKTRUM. 2000. *Lexikon der Geowissenschaften*.
<http://www.spektrum.de/lexikon/geowissenschaften>. Accessed 18 January 2016.
- SPURK, J.H., AND AKSEL, N. *Strömungslehre. Einführung in die Theorie der Strömungen*. Springer-Lehrbuch.
- STIERSTADT, K. 2010. *Thermodynamik. Von der Mikrophysik zur Makrophysik*. Springer-Lehrbuch. Springer-Verlag Berlin Heidelberg, Berlin, Heidelberg.
- STOKES, G.G. 2009. On the Theory of Oscillatory Waves. In *Mathematical and physical papers. Volume I*, G. G. STOKES, Ed. Cambridge University Press, Cambridge, 197–229.

- TACHIE, M.F., JAMES, D.F., AND CURRIE, I.G. 2003. Velocity measurements of a shear flow penetrating a porous medium. *J. Fluid Mech.* 493, 319–343.
- TANIGUCHI, M., ISHITOBI, T., AND SHIMADA, J. 2006. Dynamics of submarine groundwater discharge and freshwater-seawater interface. *J. Geophys. Res.* 111, C1.
- TURNER, J.S. 1986. Turbulent entrainment: the development of the entrainment assumption, and its application to geophysical flows. *J. Fluid Mech.* 173, 431–471.
- WALKER, D.A. 1987. A fluorescence technique for measurement of concentration in mixing liquids. *Journal of Physics E: Scientific Instruments* 20, 217–224.
- WALLIS, G.B. 1967. Use of the Reynolds Flux Concept for Analysing One-Dimensional Two-Phase Flow. Part 1. Derivation and Verification of Basic Analytical Techniques. *International Journal Heat Mass Transfer* 11, 445–458.
- ZANKE, U. 2013. *Hydraulik für den Wasserbau*. Springer, Berlin, Heidelberg.
- ZARE, R.N. 2012. My life with LIF: a personal account of developing laser-induced fluorescence. *Annual review of analytical chemistry (Palo Alto, Calif.)* 5, 1–14.

Appendix

Appendix A: List of LIF-Calibration steps

The LIF-calibration workflow enhances the capturing of several concentration maps in the measurement plane. For the experiments in this work, 11 calibration steps were defined. In every single step, 10 pictures were captured for the specific concentration of Rhodamine 6G in the wave channel. Each of the ensembles is averaged to reduce failures. Because of light intensity fluctuations, which can occur during the measurements, all calibration steps were done for 100% Laser intensity and for 50% Laser intensity. Furthermore, the linear approximation of the calibration curve was split into two areas. One enhanced the low concentration fields from 0 until 80 $\mu\text{g/l}$ and the other one the high concentration fields from 80 until 260 $\mu\text{g/l}$. This procedure guarantees, that the resolution of the post processing steps in the software application is more precisely.

In the workflow, the Rhodamine 6G solution is filled into the water tank, then the complete water is mixed with the radial pump for 15 minutes. After this, the water solution is calm down before the calibration pictures are captured. For the calibration steps the following solutions were used:

step	Rhodamine 6G solution (...) in ml	Concentration in $\mu\text{g/l}$ in 4,5m ³ water in the tank system
1	0	0
2	10	10
3	20	20
4	30	30
5	40	40
6	50	50
7	80	80
8	110	110
9	140	140
10	200	200
11	260	260

Appendix B: Frequency analysis

Calm scenarios

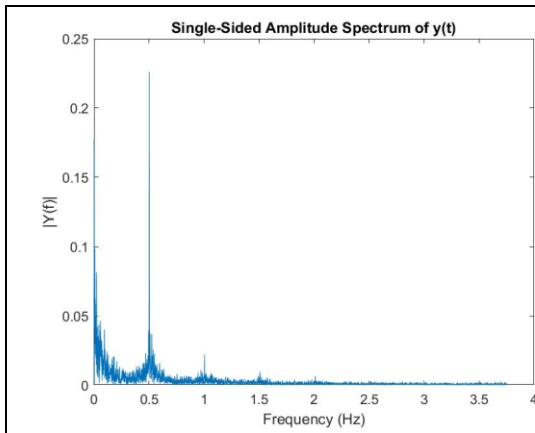


Figure 7-1: frequency analysis measurement 10PPI, 0° slope

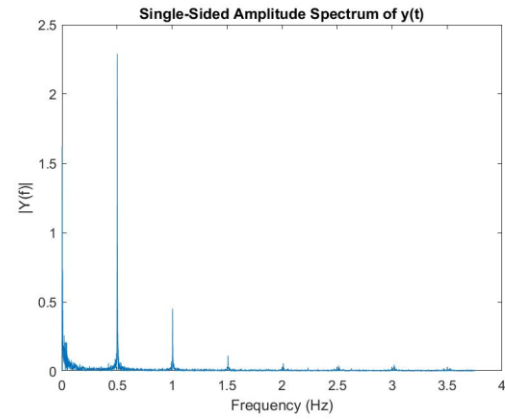


Figure 7-2: frequency analysis measurement 10PPI, 3° slope

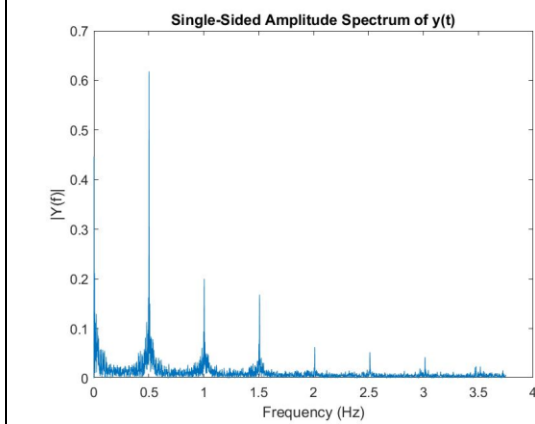


Figure 7-3: frequency analysis measurement 10PPI, 7° slope

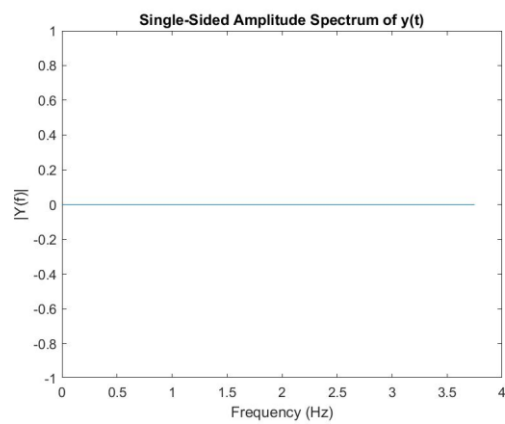


Figure 7-4: frequency analysis measurement 10PPI, 14° slope

Every frequency analysis was done for the 50% concentration line. For this reason, the 14° slope angle measurement is empty, because of the less high concentration in during the measurement.

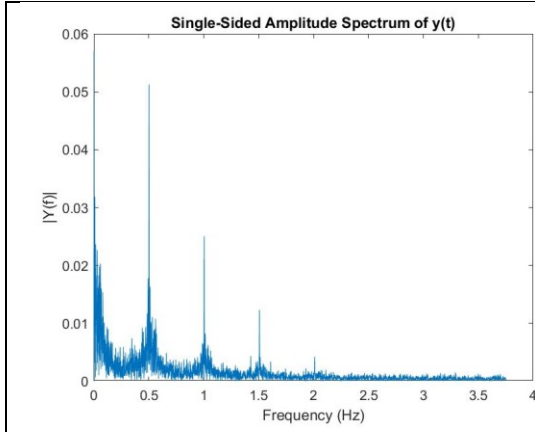


Figure 7-5: frequency analysis measurement 45PPI, 0° slope

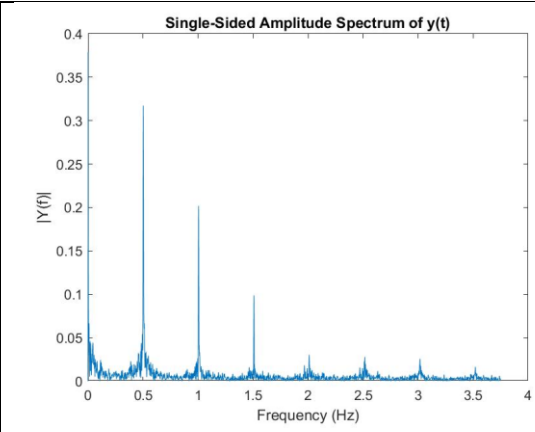


Figure 7-6: frequency analysis measurement 45PPI, 3° slope

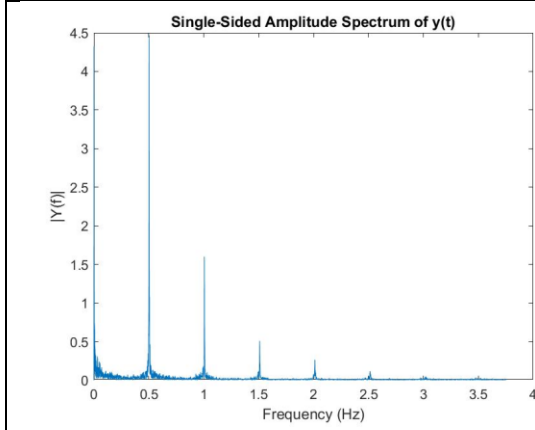


Figure 7-7: frequency analysis measurement 45PPI, 7° slope

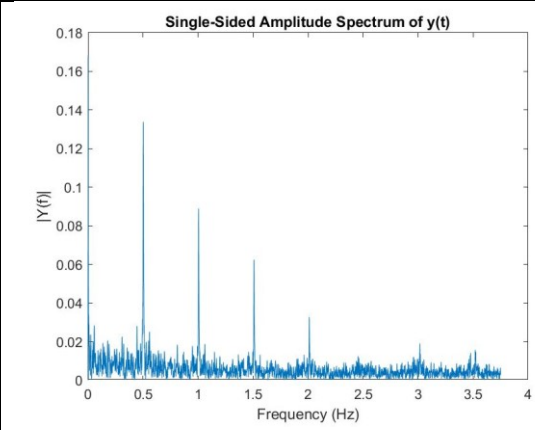


Figure 7-8: frequency analysis measurement 45PPI, 14° slope

Mean scenarios

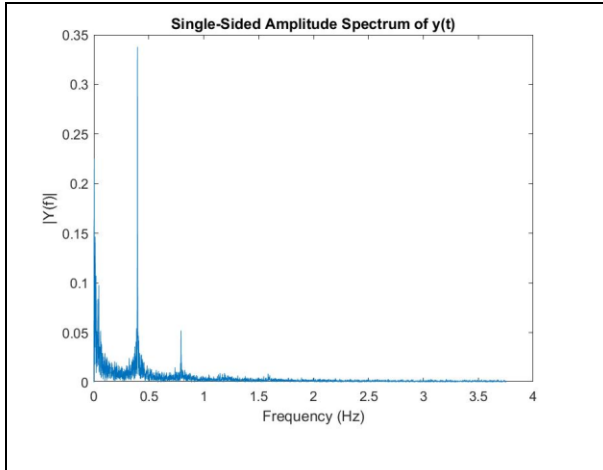


Figure 7-9: frequency analysis measurement 10PPI, 0° slope

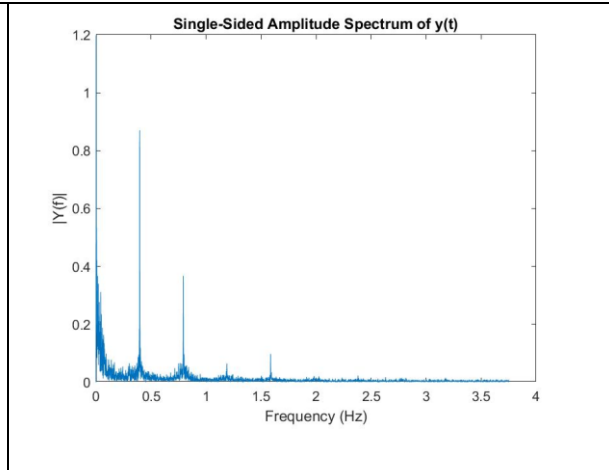


Figure 7-10: frequency analysis measurement 10PPI, 3° slope

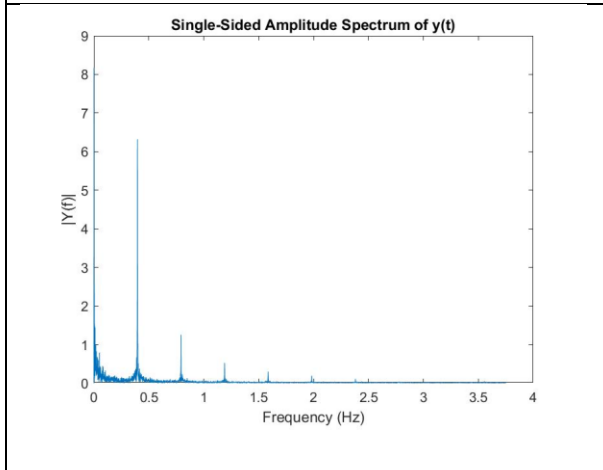


Figure 7-11: frequency analysis measurement 10PPI, 7° slope

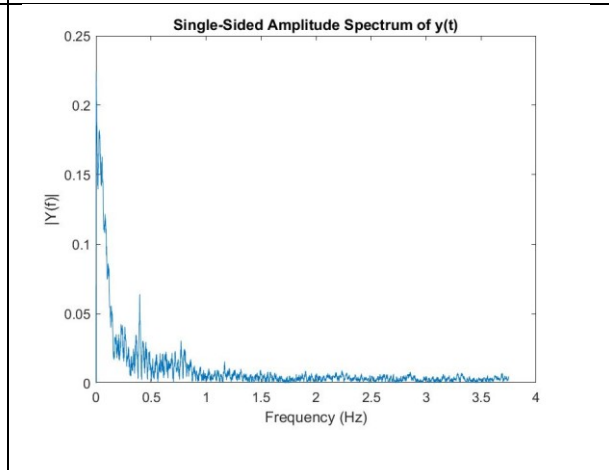


Figure 7-12: frequency analysis measurement 10PPI, 14° slope

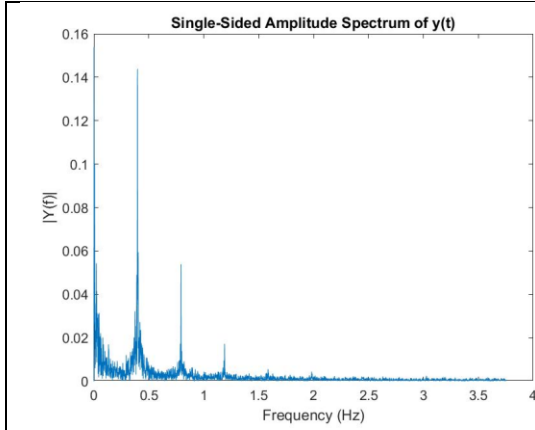


Figure 7-13: frequency analysis measurement 45PPI, 0° slope

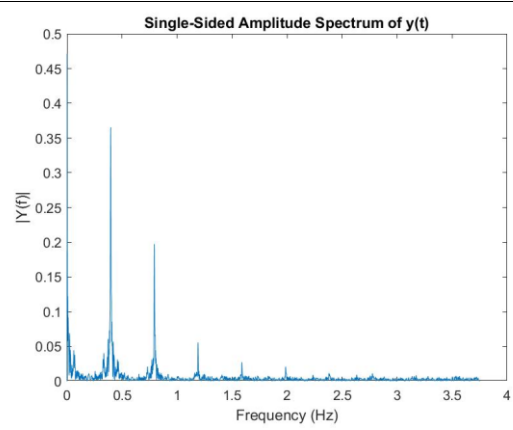


Figure 7-14: frequency analysis measurement 45PPI, 3° slope

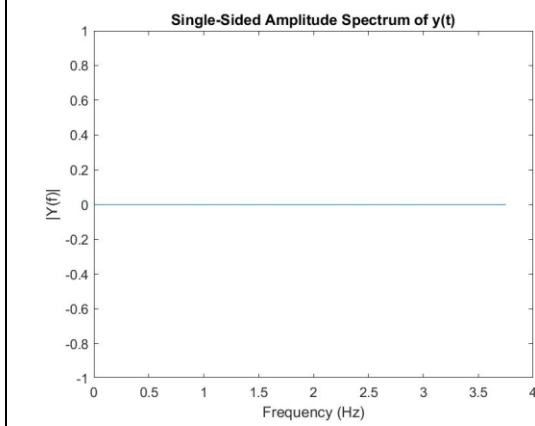


Figure 7-15: frequency analysis measurement 45PPI, 7° slope

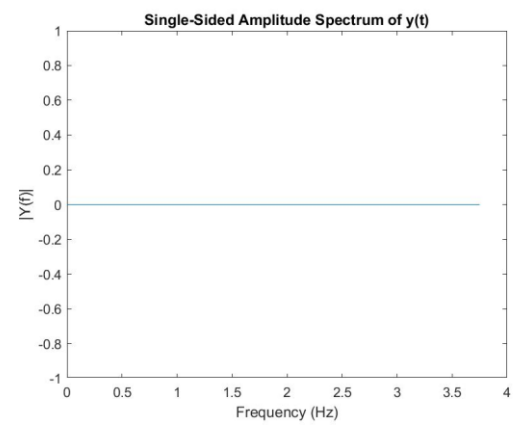
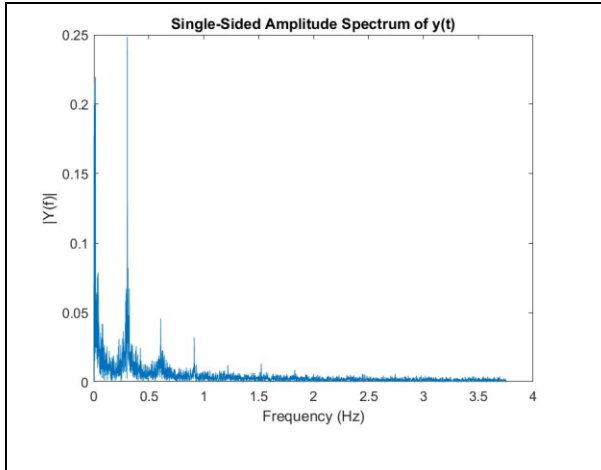
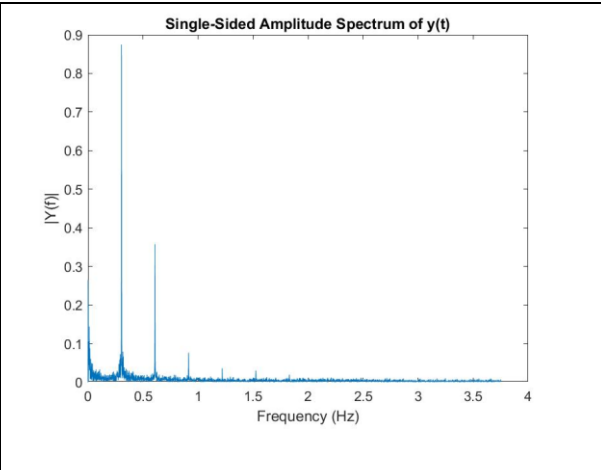
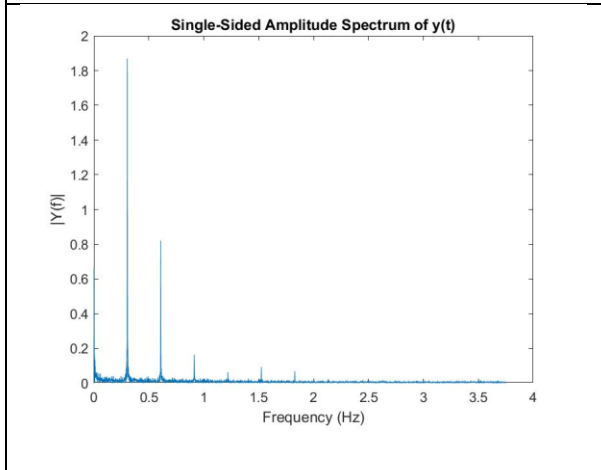
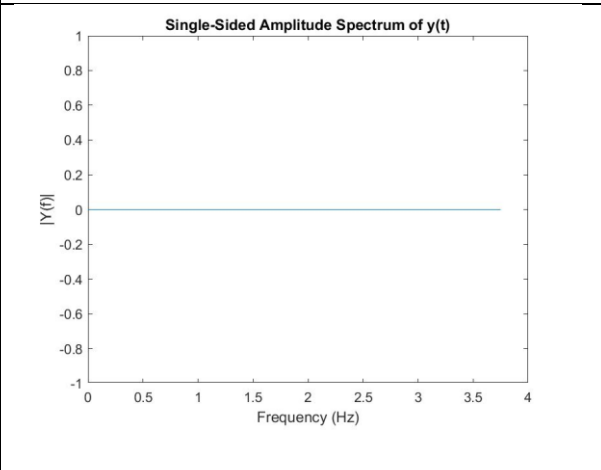


Figure 7-16: frequency analysis measurement 45PPI, 14° slope

Every frequency analysis was done for the 50% concentration line. For this reason, the 7° and 14° slope angle measurements are empty, because of the less high concentration in during the measurement.

Stormy scenarios**Figure 7-17: frequency analysis measurement 10PPI, 0° slope****Figure 7-18: frequency analysis measurement 10PPI, 3° slope****Figure 7-19: frequency analysis measurement 10PPI, 7° slope****Figure 7-20: frequency analysis measurement 10PPI, 14° slope**

Every frequency analysis was done for the 50% concentration line. For this reason, the 14° slope angle measurement is empty, because of the less high concentration in during the measurement.

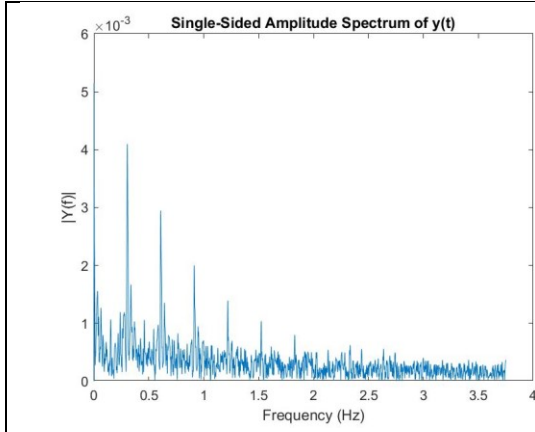


Figure 7-21: frequency analysis measurement 45PPI, 0° slope

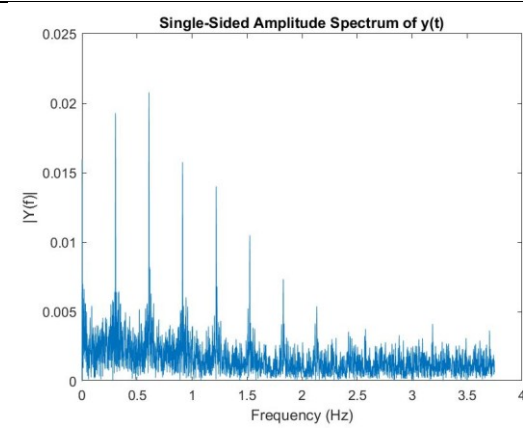


Figure 7-22: frequency analysis measurement 45PPI, 3° slope

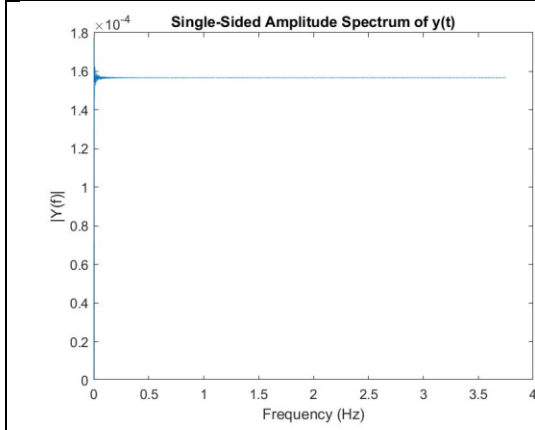


Figure 7-23: frequency analysis measurement 45PPI, 7° slope

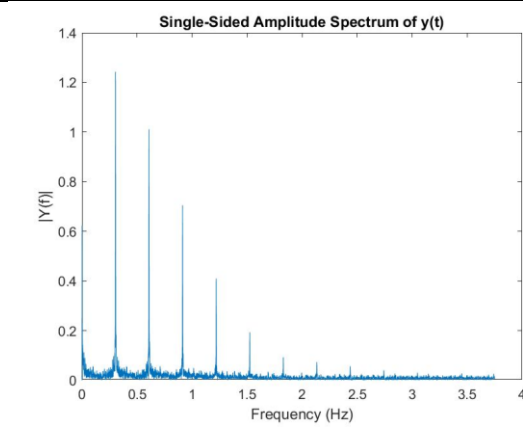


Figure 7-24: frequency analysis measurement 45PPI, 14° slope

Every frequency analysis was done for the 50% concentration line. For this reason, the 7° slope angle measurement is empty, because of the less high concentration in during the measurement.

Appendix C: Reynolds-flux diffusions

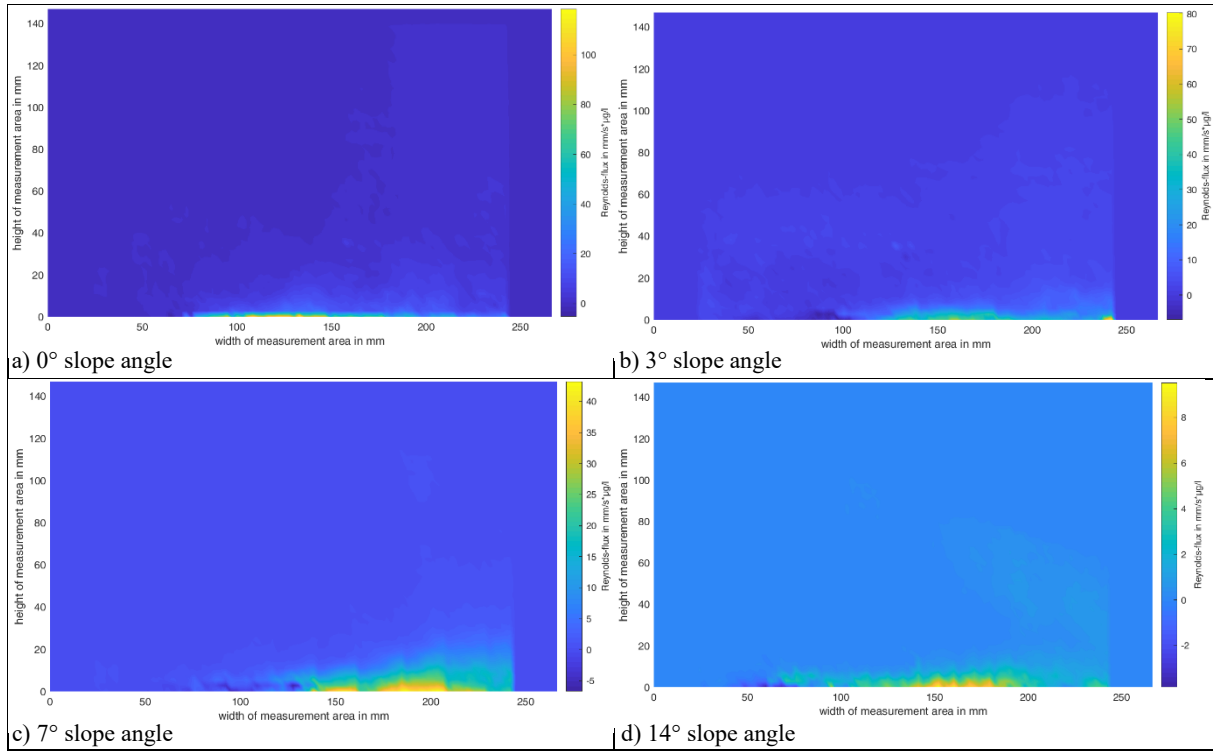


Figure 7-25: Reynolds-flux diffusion for the calm scenarios and the 10PPI porous media

The four images show the Reynolds-flux diffusion for the four different slope angles. With a) 0° slope angle, b) 3° slope angle, c) 7° slope angle and d) 14° slope angle.

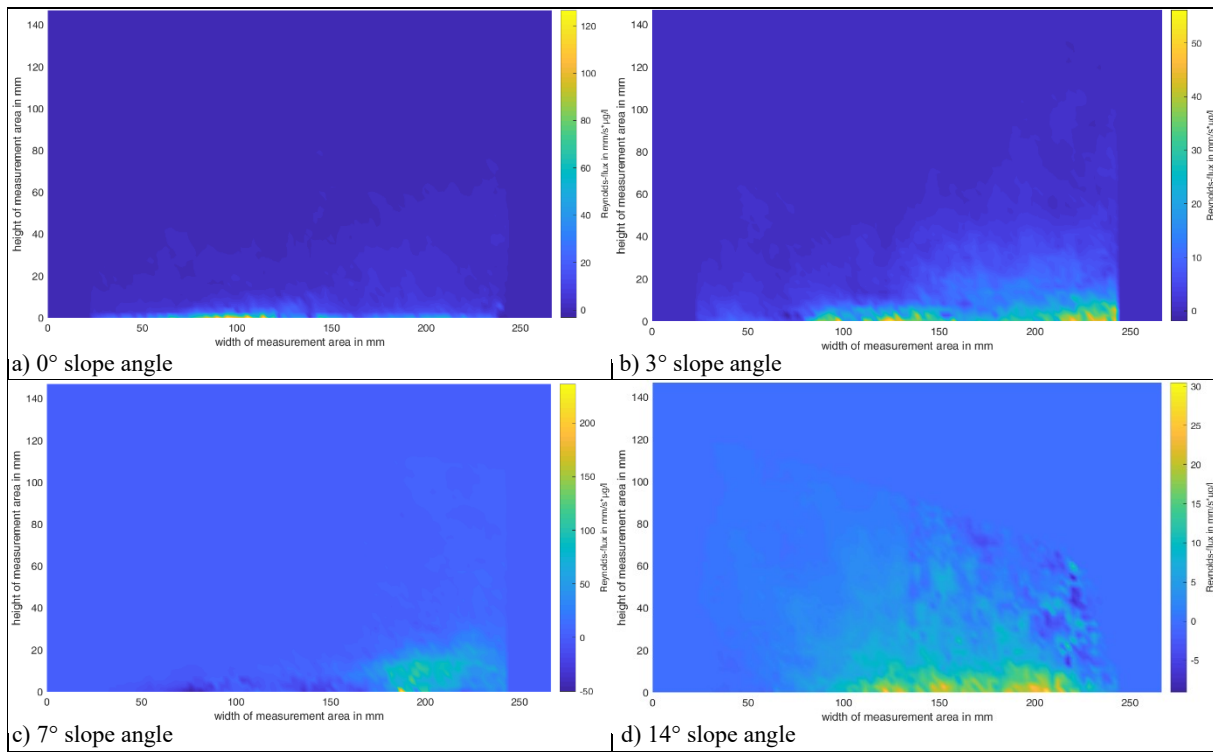


Figure 7-26: Reynolds-flux diffusion for the mean scenarios and the 10PPI porous media

The four images show the Reynolds-flux diffusion for the four different slope angles. With a) 0° slope angle, b) 3° slope angle, c) 7° slope angle and d) 14° slope angle.

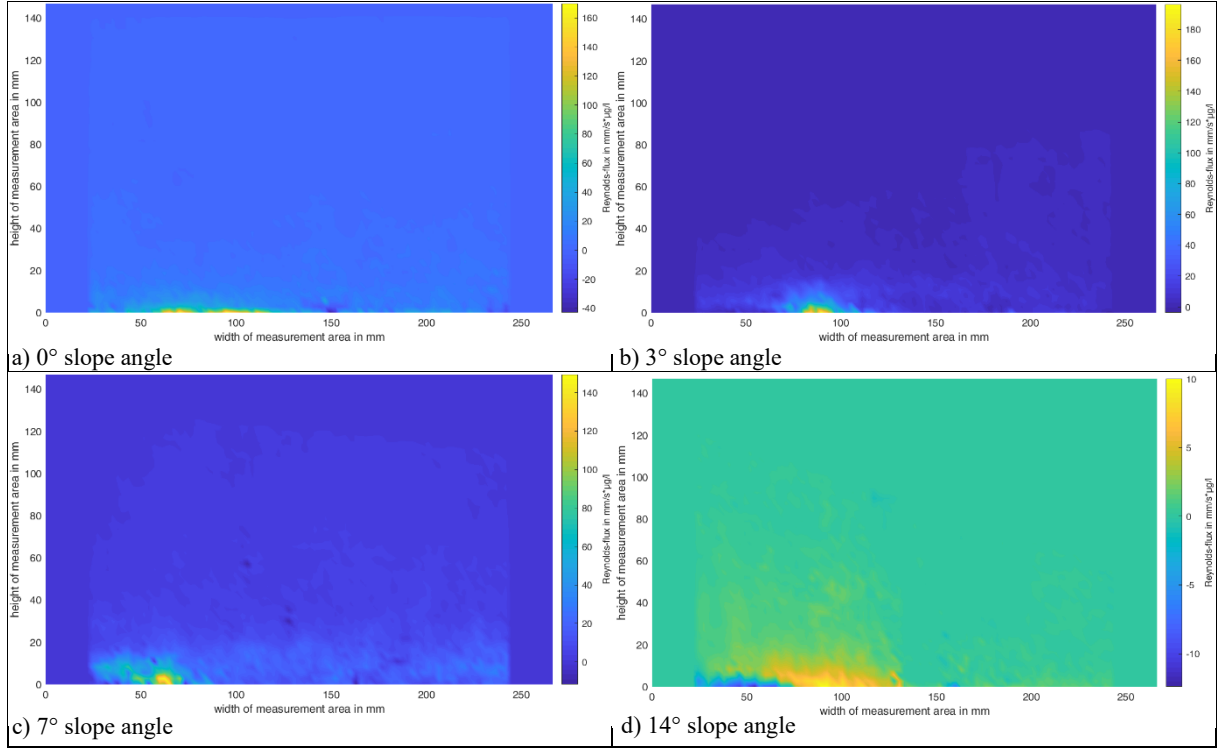


Figure 7-27: Reynolds-flux diffusion for the stormy scenarios and the 10PPI porous media

The four images show the Reynolds-flux diffusion for the four different slope angles. With a) 0° slope angle, b) 3° slope angle, c) 7° slope angle and d) 14° slope angle.

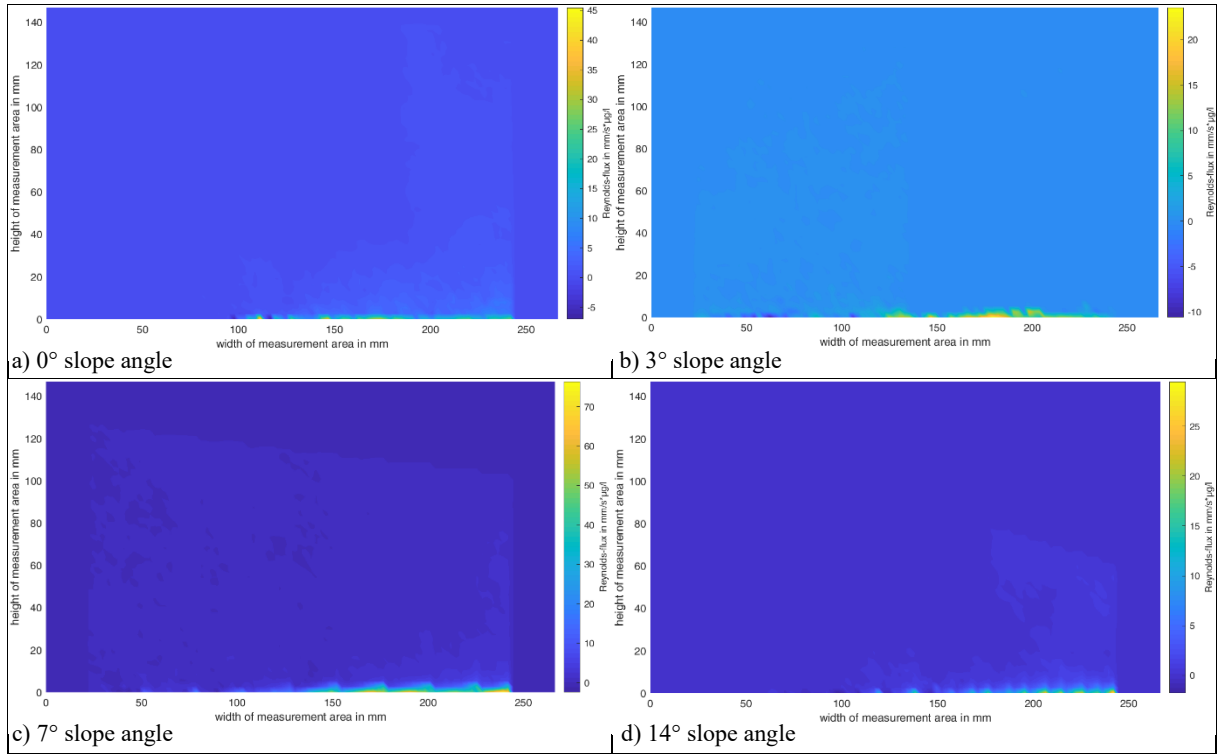


Figure 7-28: Reynolds-flux diffusion for the calm scenarios and the 45PPI porous media

The four images show the Reynolds-flux diffusion for the four different slope angles. With a) 0° slope angle, b) 3° slope angle, c) 7° slope angle and d) 14° slope angle.

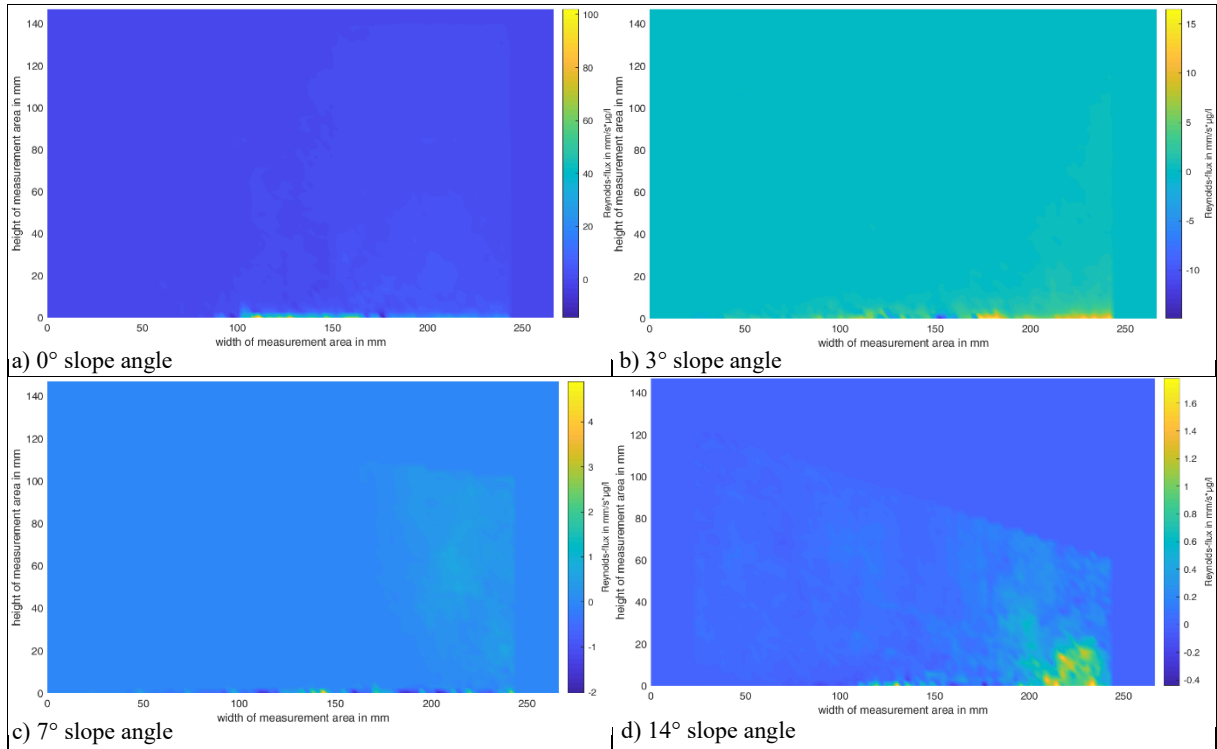


Figure 7-29: Reynolds-flux diffusion for the mean scenarios and the 45PPI porous media

The four images show the Reynolds-flux diffusion for the four different slope angles. With a) 0° slope angle, b) 3° slope angle, c) 7° slope angle and d) 14° slope angle.

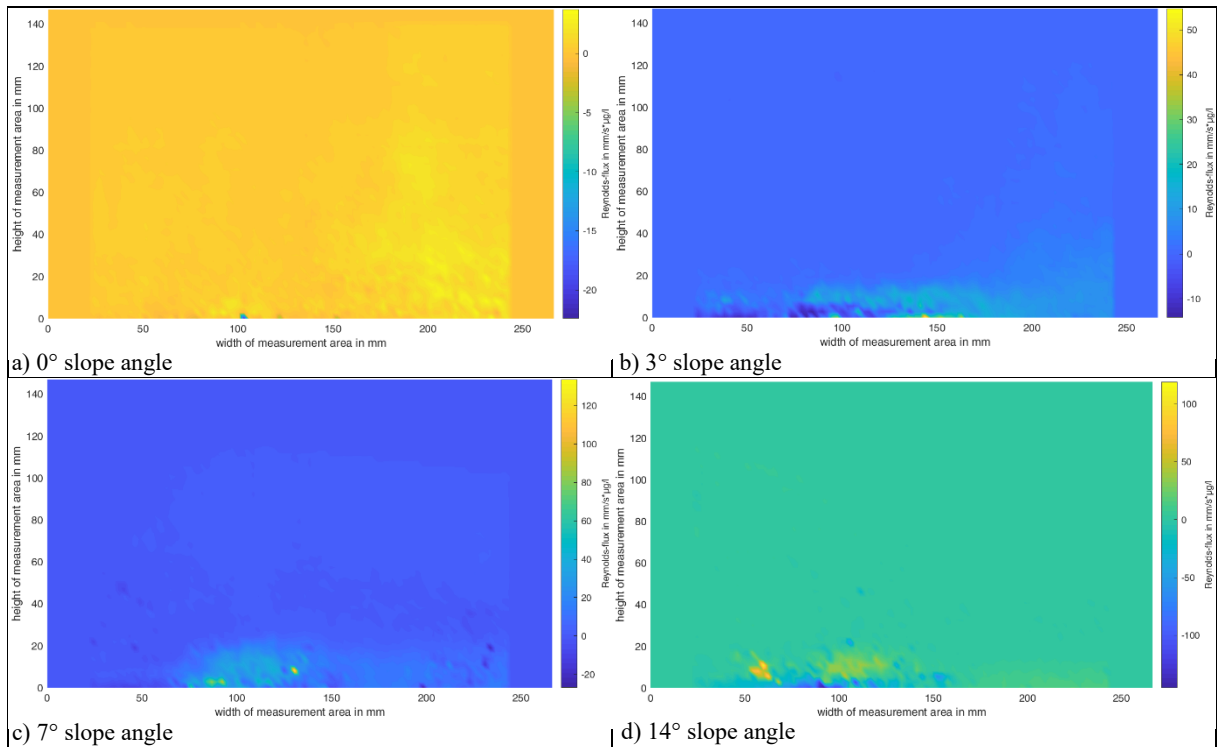


Figure 7-30: Reynolds-flux diffusion for the stormy scenarios and the 45PPI porous media

The four images show the Reynolds-flux diffusion for the four different slope angles. With a) 0° slope angle, b) 3° slope angle, c) 7° slope angle and d) 14° slope angle.

Appendix D: Concentration maps

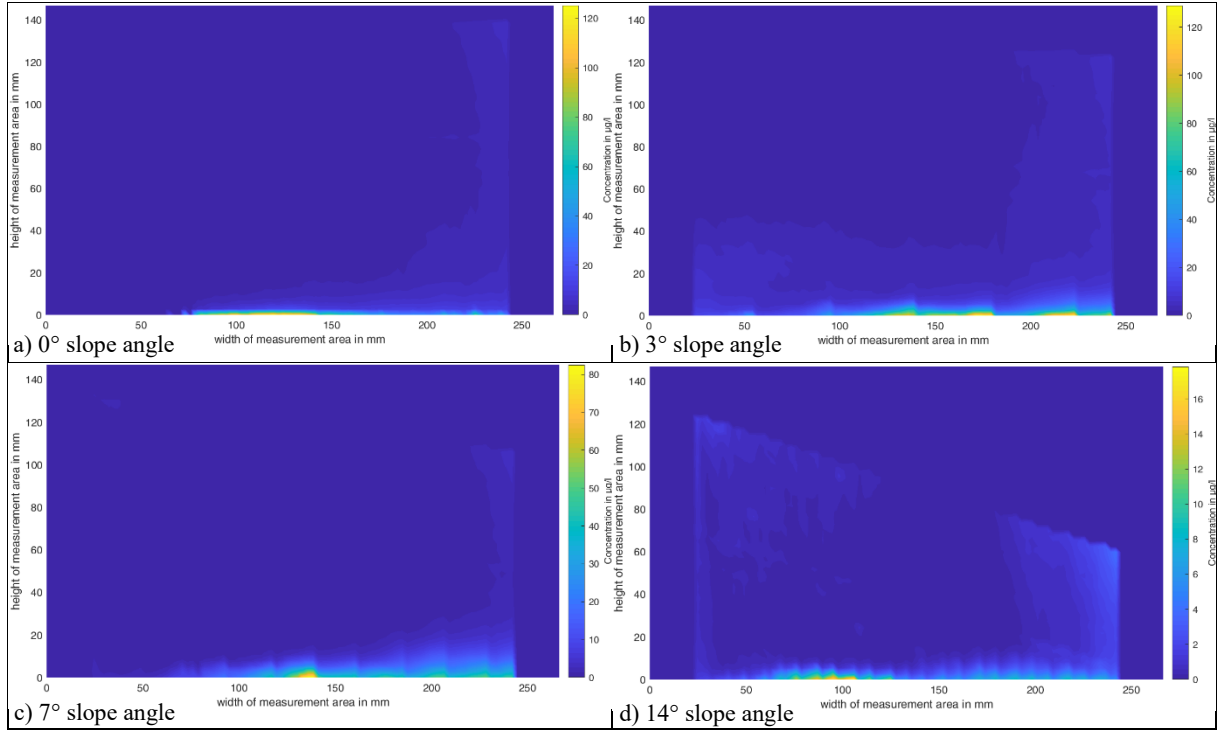


Figure 7-31: Concentration maps for the calm scenarios and the 10PPI porous media

The four images show the Reynolds-flux diffusion for the four different slope angles. With a) 0° slope angle, b) 3° slope angle, c) 7° slope angle and d) 14° slope angle.

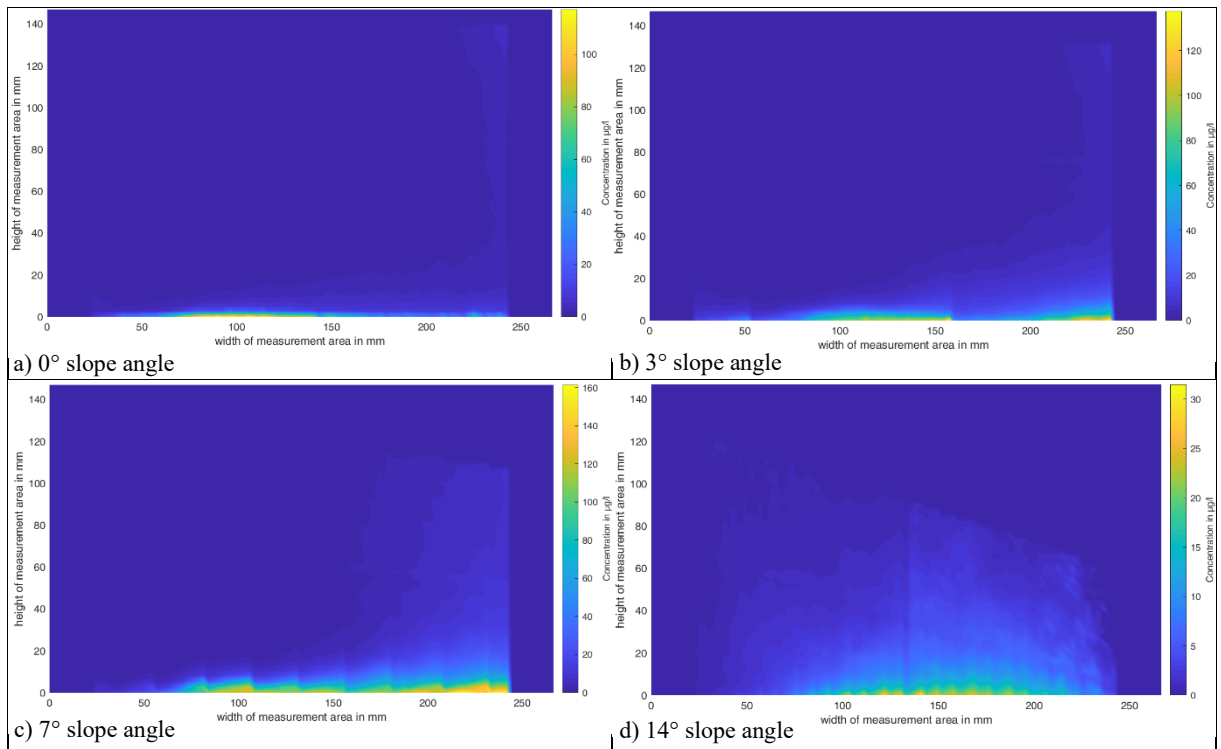


Figure 7-32: Concentration maps for the mean scenarios and the 10PPI porous media

The four images show the Reynolds-flux diffusion for the four different slope angles. With a) 0° slope angle, b) 3° slope angle, c) 7° slope angle and d) 14° slope angle.

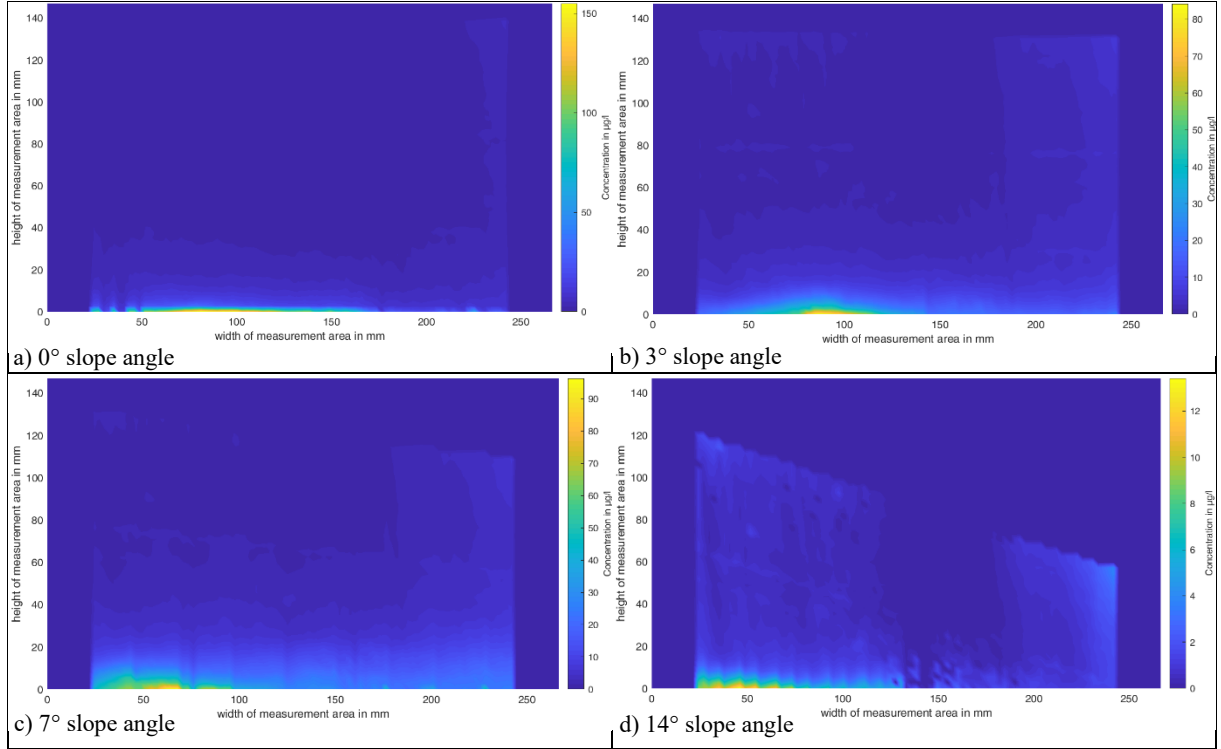


Figure 7-33: Concentration maps for the stormy scenarios and the 10PPI porous media

The four images show the Reynolds-flux diffusion for the four different slope angles. With a) 0° slope angle, b) 3° slope angle, c) 7° slope angle and d) 14° slope angle.

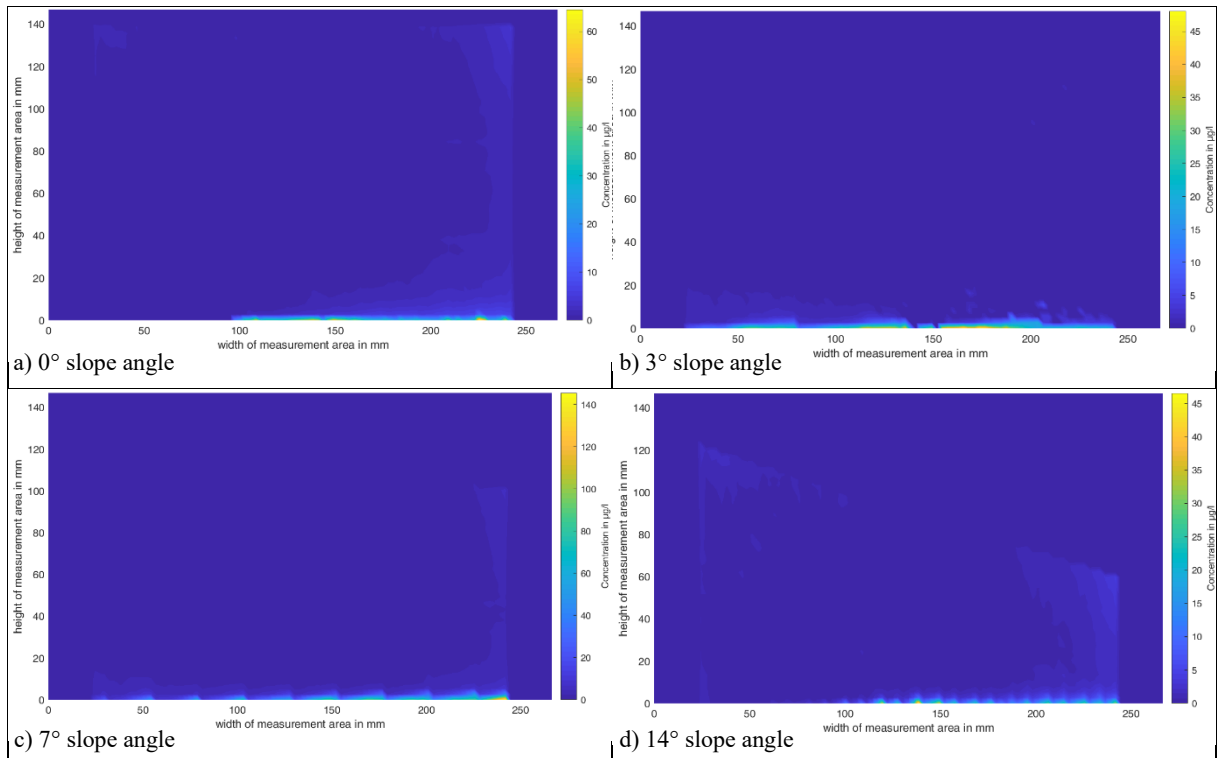


Figure 7-34: Concentration maps for the calm scenarios and the 45PPI porous media

The four images show the Reynolds-flux diffusion for the four different slope angles. With a) 0° slope angle, b) 3° slope angle, c) 7° slope angle and d) 14° slope angle.

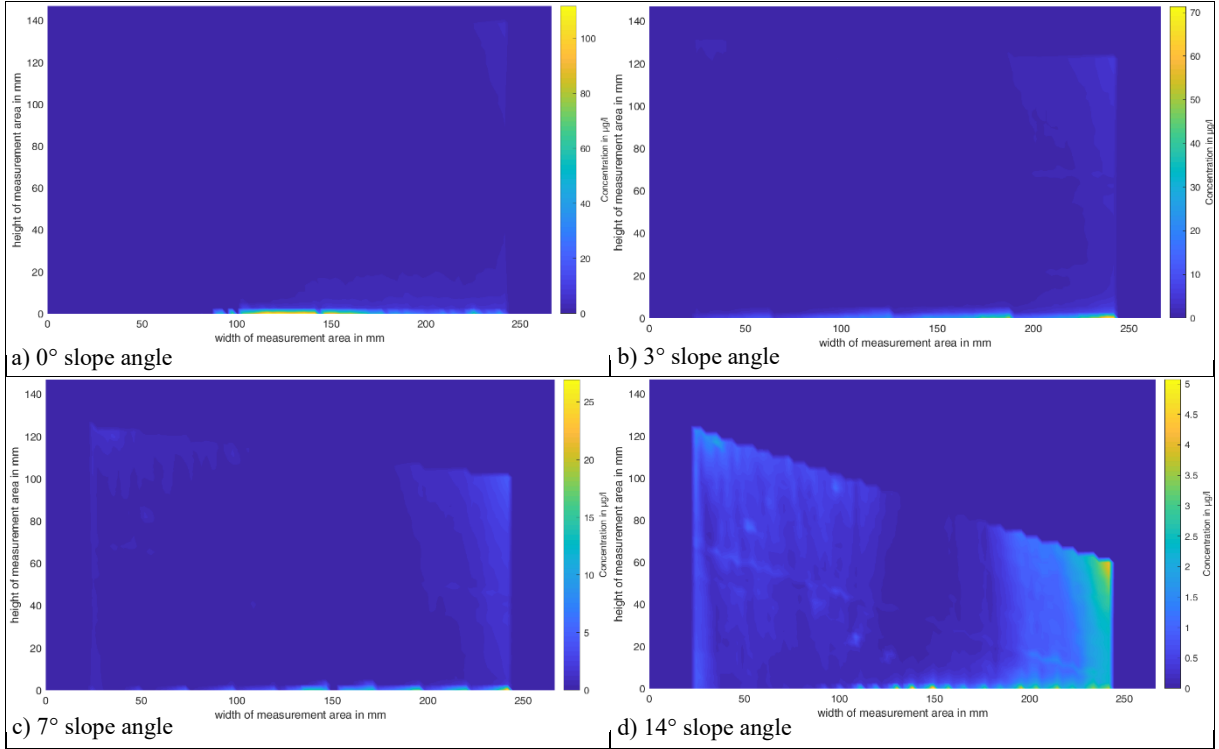


Figure 7-35: Concentration maps for the mean scenarios and the 45PPI porous media

The four images show the Reynolds-flux diffusion for the four different slope angles. With a) 0° slope angle, b) 3° slope angle, c) 7° slope angle and d) 14° slope angle.

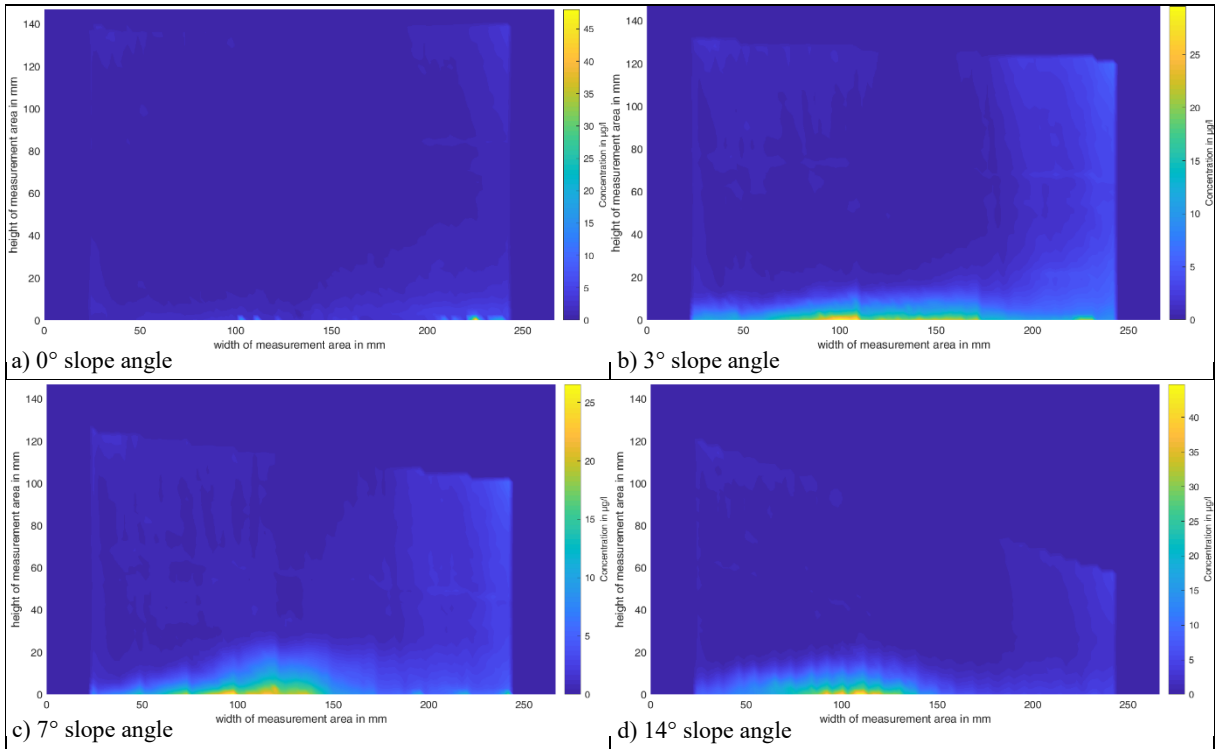


Figure 7-36: Concentration maps for the stormy scenarios and the 45PPI porous media

The four images show the Reynolds-flux diffusion for the four different slope angles. With a) 0° slope angle, b) 3° slope angle, c) 7° slope angle and d) 14° slope angle.

Appendix E: LDA results

Four transects above each porous medium were conducted in the LDA measurements. In the following figures, the dashed line shows the velocity in the middle of the channel, the green line the profile directly above the crossover between the porous medium and the mattress, the blue line the profile 60 mm behind the green line in flow direction and the red line 160 mm behind the green line above the porous medium. Every measurement was conducted with the same stream characteristics: a steady current with a volume flux of $140 \text{ m}^3/\text{h}$. The measurement grid includes 20 points above the ground with a distance between the points of 1 mm and 70 points with a distance between the points of 5 mm following the bottom near grid.

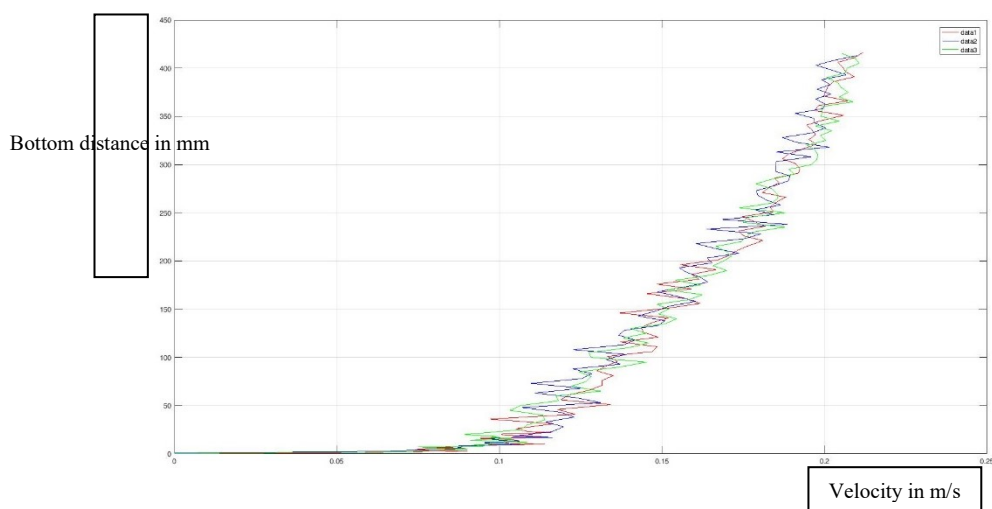


Figure 7-37: LDA velocity profiles of the 45PPI porous media

In the figure the four different velocity profiles (description see above) are shown in m/s at the x-axis. On the y-axis the bottom distance in mm is shown.

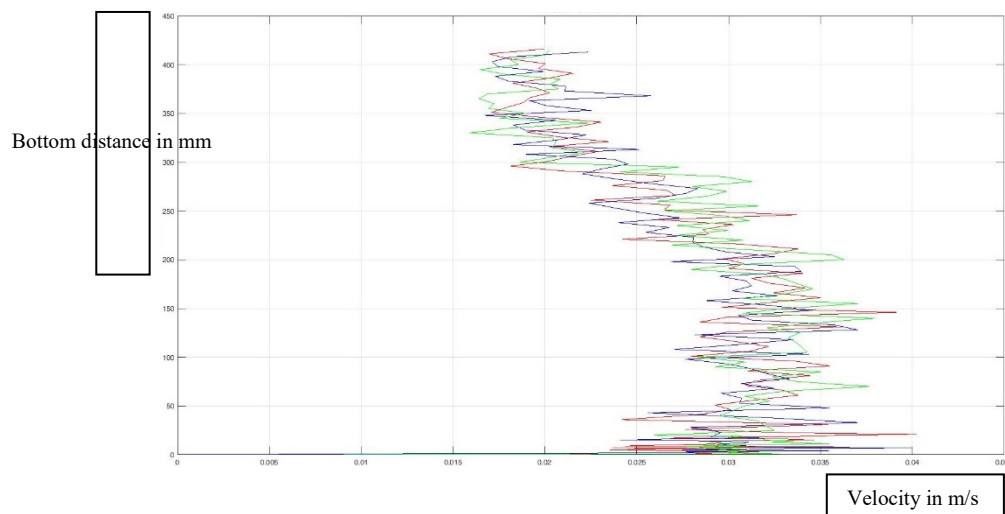


Figure 7-38: LDA turbulence profiles of the 45PPI porous media

In the figure the four different turbulence profiles for the different velocity profiles (description see above) are shown in m/s at the x-axis. On the y-axis the bottom distance in mm is shown.

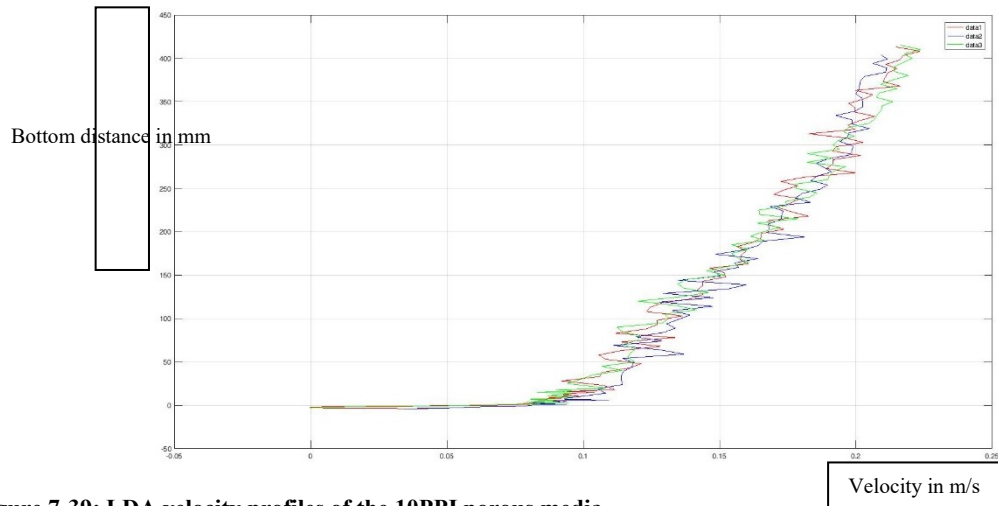


Figure 7-39: LDA velocity profiles of the 10PPI porous media

In the figure the four different velocity profiles (description see above) are shown in m/s at the x-axis. On the y-axis the bottom distance in mm is shown.

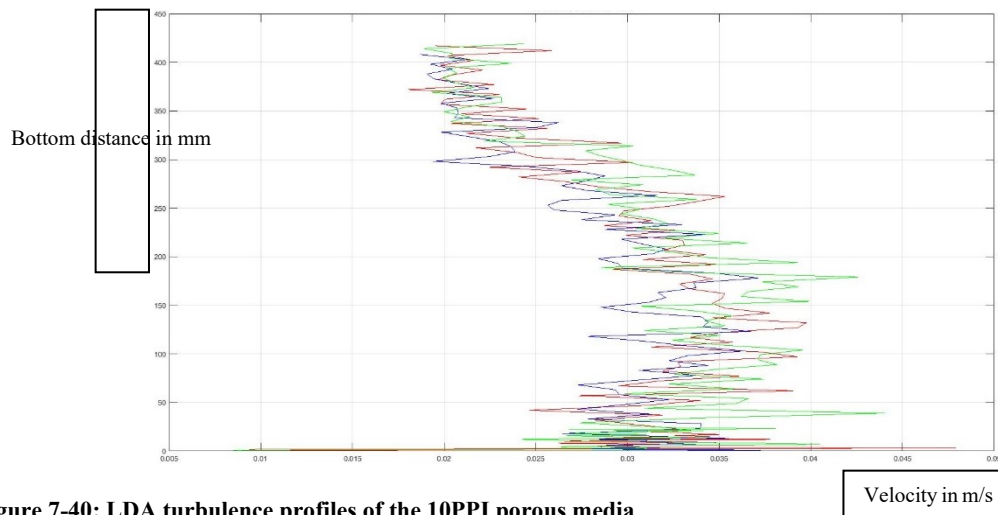


Figure 7-40: LDA turbulence profiles of the 10PPI porous media

In the figure the four different turbulence profiles for the different velocity profiles (description see above) are shown in m/s at the x-axis. On the y-axis the bottom distance in mm is shown.

Appendix F: Phase specific TKE

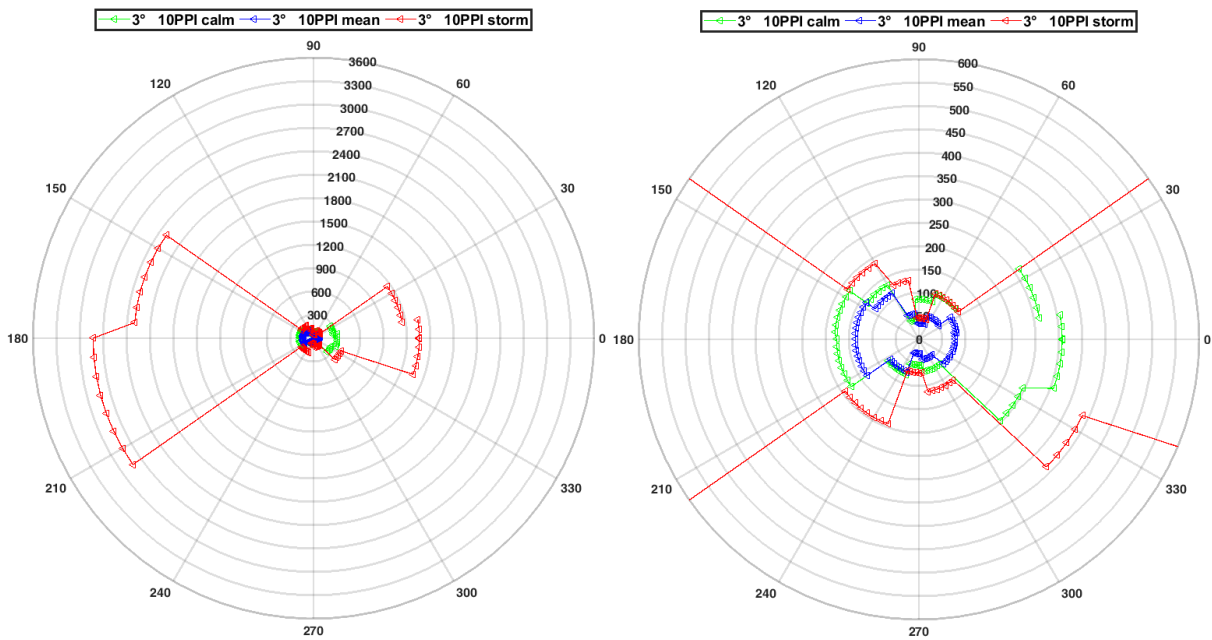


Figure 7-41: Phase specific TKE of 3° slope angle and 10PPI porous medium
On the left the maximum values are shown and on the right a detail view of the small values is focused. The points in the figures do not represent a measurement point, they show only the value of the slope angle.

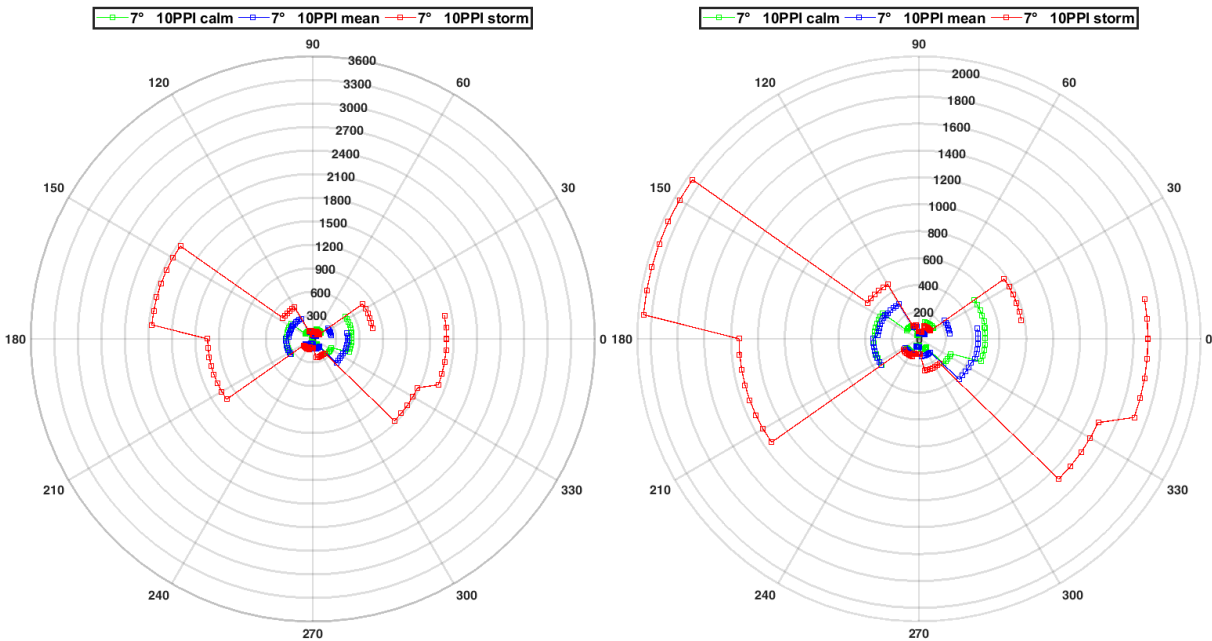


Figure 7-42: Phase specific TKE of 7° slope angle and 10PPI porous medium
On the left the maximum values are shown and on the right a detail view of the small values is focused. The points in the figures do not represent a measurement point, they show only the value of the slope angle.

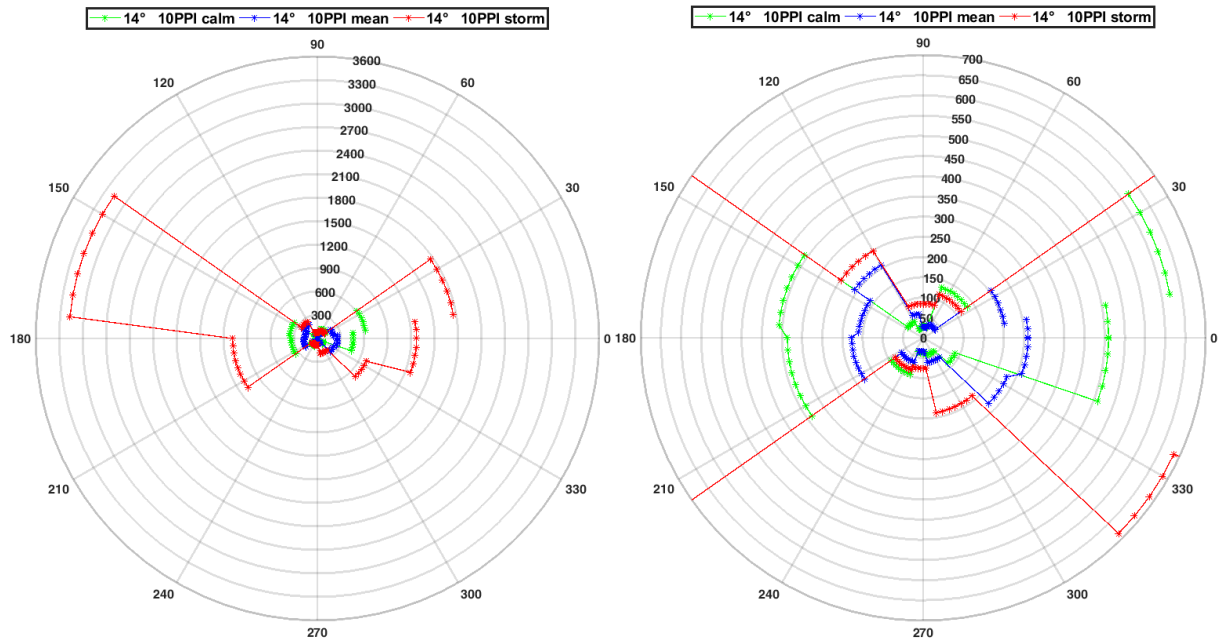


Figure 7-43: Phase specific TKE of 14° slope angle and 10PPI porous medium

On the left the maximum values are shown and on the right a detail view of the small values is focused. The points in the figures do not represent a measurement point, they show only the value of the slope angle.

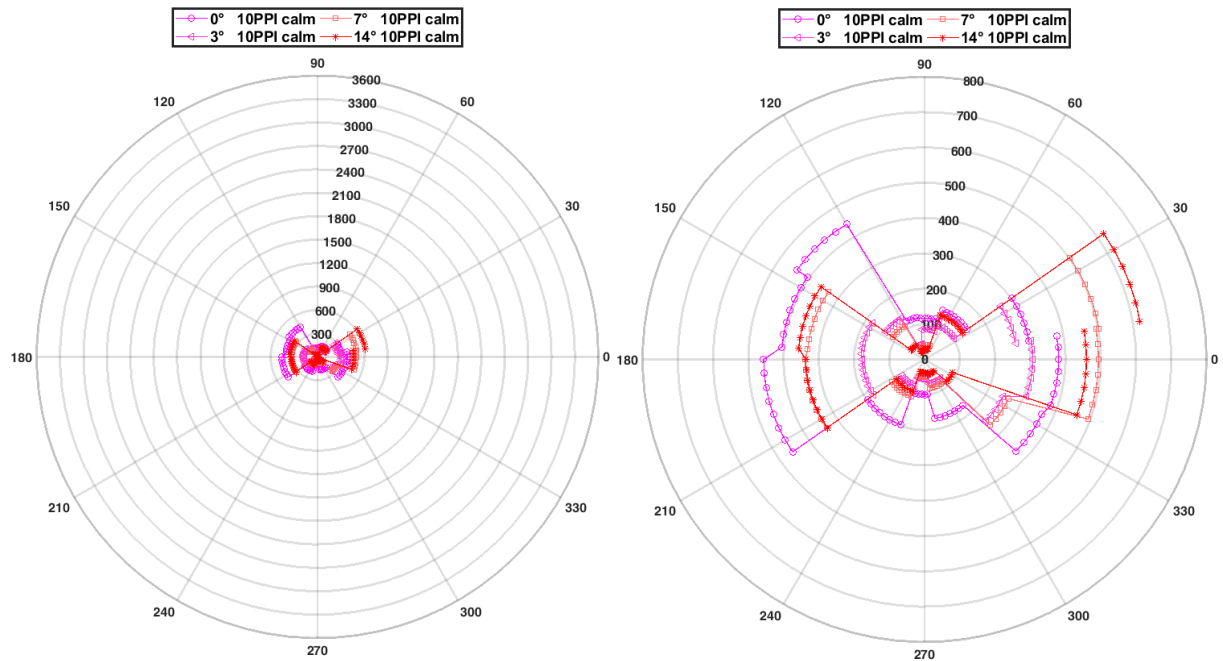


Figure 7-44: Phase specific TKE of the calm wave scenario and 10PPI porous medium

On the left the maximum values are shown and on the right a detail view of the small values is focused. The points in the figures do not represent a measurement point, they show only the value of the slope angle.

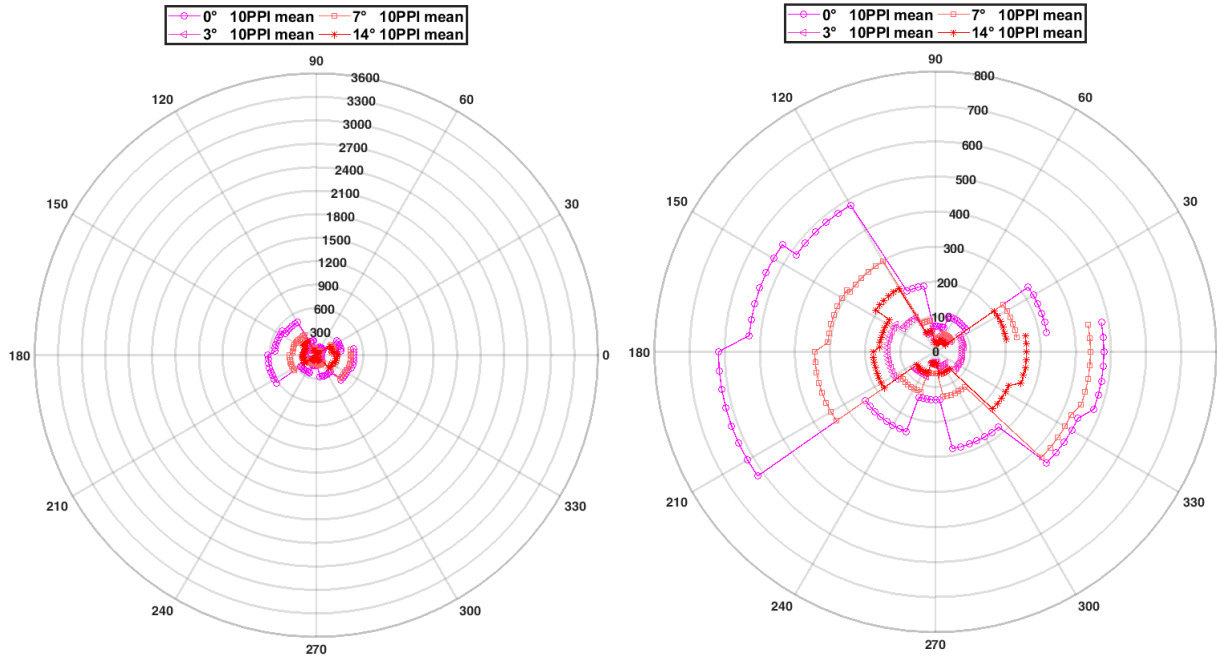


Figure 7-45: Phase specific TKE of the mean wave scenario and 10PPI porous medium

On the left the maximum values are shown and on the right a detail view of the small values is focused. The points in the figures do not represent a measurement point, they show only the value of the slope angle

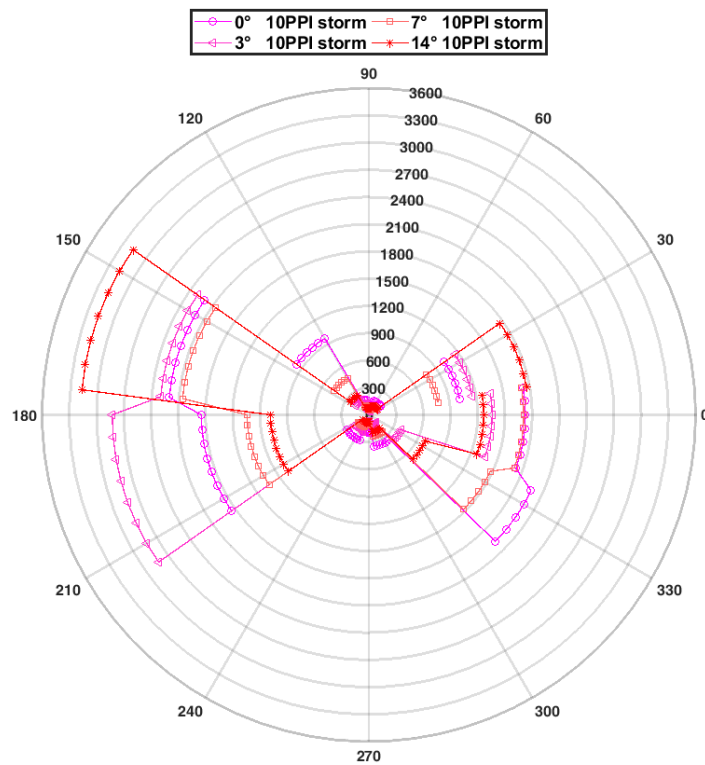


Figure 7-46: Phase specific TKE of the stormy wave scenario and 10PPI porous medium

The points in the figures do not represent a measurement point, they show only the value of the slope angle